Durham University

Durham E-Theses

Improved Treatment of Hard Radiation in New Physics Processes at the LHC

ALEXANDRA HANNAH WILCOCK

How to cite:

WILCOCK, ALEXANDRA HANNAH (2015) Improved Treatment of Hard Radiation in New Physics Processes at the LHC. Doctoral thesis, Durham University.

Use policy

The full-text may be used and/or reproduced, and given to third parties in any format or medium, without prior permission or charge, for personal research or study, educational, or not-for-profit purposes provided that:

- a full bibliographic reference is made to the original source
- a https://etheses.durham.ac.uk/id/eprint/11268/ is made to the metadata record in Durham E-Theses
- the full-text is not changed in any way

The full-text must not be sold in any format or medium without the formal permission of the copyright holders.

Please consult the full Durham E-Theses policy for further details.

Academic Support Office, The Palatine Centre, Durham University, Stockton Road, Durham, DH1 3LE
e-mail: e-theses.admin@durham.ac.uk Tel: +44 0191 334 6107
https://etheses.durham.ac.uk

Improved Treatment of Hard Radiation in New Physics Processes at the LHC

Alexandra Wilcock

A Thesis presented for the degree of
Doctor of Philosophy

Institute for Particle Physics Phenomenology
Department of Physics
University of Durham

August 2015

Improved Treatment of Hard Radiation in New Physics Processes at the LHC

Alexandra Wilcock

Submitted for the degree of Doctor of Philosophy
August 2015

Abstract

Despite the continued success of the Large Hadron Collider, no clear evidence for the existence of new BSM particles has been identified to date, pushing the bounds on their masses to ever higher values. As such, increasing efforts have been made to constrain all remaining regions of parameter space where light new particles could still exist. To do so reliably requires accurate Monte Carlo simulations of signal events, often in the case that hard radiation is produced together with the new particles. In this thesis, we focus on using matrix-element corrections based on the POWHEG formalism to improve the simulation of hard radiation produced in new physics events. The corrections have been implemented within the Herwig++ Monte Carlo event generator, both for squark-antisquark production at the LHC and a wide range of decay modes that occur in beyond the Standard Model physics scenarios. Taking supersymmetry as a test case, we find that corrections applied to radiation generated during either the production or decays of new particles each impact on the reach of analysis strategies sensitive to high transverse momentum jets, with the most important effect occurring when the former correction is applied in scenarios featuring a compressed new particle mass spectrum. Finally, we investigate the sensitivity of the LHC to supersymmetric scenarios using monotop signatures of a single top quark produced together with missing transverse energy. We present analysis strategies sensitive to compressed regions of parameter space, and compare their expected reach at the next run of the LHC to those of more traditional search strategies.

Declaration

The work in this thesis is based on research carried out at the Institute for Particle Physics Phenomenology, Department of Physics, University of Durham, England. This work has been carried out in collaboration with Prof. P. Richardson, the wider Herwig++ collaboration and Dr. B. Fuks. Parts of this thesis have been previously published:

1. The work undertaken in Chapter 2 has been published as:
   P. Richardson and A. Wilcock, *Monte Carlo Simulation of Hard Radiation in Decays in Beyond the Standard Model Physics in Herwig++*, *Eur.Phys.J.* **C74** (2014) 2713, [arXiv:1303.4563].

2. The work undertaken in Chapter 5 has been published as:
   B. Fuks, P. Richardson, and A. Wilcock, *Studying the sensitivity of monotop probes to compressed supersymmetric scenarios at the LHC*, *Eur.Phys.J.* **C75** (2015) 308, [arXiv:1408.3634].

No part of this thesis has been submitted elsewhere for any other degree or qualification.

Copyright © 2015 by Alexandra Wilcock.
"The copyright of this thesis rests with the author. No quotations from it should be published without the author's prior written consent and information derived from it should be acknowledged".

Acknowledgements

Firstly I would like to thank my supervisor Peter Richardson for his patient help and guidance over the duration of this research, without which this work would not have been possible. I am also deeply grateful to Simon Plätzer for his help during the later part of my PhD and for his seemingly endless drive and energy.

I would also like to extend my gratitude to the other members of the Herwig++ collaboration for all their help, especially David Grellscheid for his patient assistance with computing issues. I also thank Benjamin Fuks for his extended collaboration.

I gratefully acknowledge financial support from the Science and Technology Facilities Council for the duration of my studies and additional support from the European Union via MCNet PITN-GA-2012-315877, which allowed me to travel widely to useful conferences and schools.

Finally, thank you to my fellow IPPP students for their friendship and entertaining lunchtime conversations, and to all members of the IPPP who have made my time here so enjoyable. And last but not least, thanks to my friends and family, in particular my parents and brother, for their amazing support over the years.

I may not have gone where I intended
to go, but I think I have ended
up where I needed to be.
Douglas Adams

Contents

Abstract **ii**

Declaration **iii**

Acknowledgements **iv**

1 Introduction **1**

1.1 Supersymmetry 5

1.1.1 Motivations for physics beyond the Standard Model 5

1.1.2 Introduction to supersymmetry 8

1.1.3 The particle content of the MSSM 10

1.1.4 Searching for supersymmetry at the LHC 13

1.2 Calculations in perturbative QCD 16

1.2.1 Hard scattering formalism 16

1.2.2 Next-to-leading order calculations 18

1.3 Monte Carlo event generators 21

1.3.1 Overview 22

1.3.2 Parton showers 24

1.4 Combining higher-order matrix elements and parton showers 34

1.4.1 Combining LO matrix elements and parton showers 36

1.4.2 Combining NLO matrix elements and parton showers 37

1.4.3 The POWHEG formalism 39

1.4.4 Matrix-element corrections 45

1.4.5 Truncated and vetoed parton showers 47

2 Matrix-element corrections to the decays of BSM particles 49

2.1 Top quark decays 50

2.1.1 Implementation in Herwig++ 50

2.1.2 Validation and results 54

2.2 Decays of BSM particles 58

2.3 Results 60

2.3.1 Randall-Sundrum graviton 60

2.3.2 The Constrained Minimal Supersymmetric Standard Model . . 62

2.4 Summary 68

3 Matrix-element corrections to stop-antistop production 70

3.1 Validation 71

3.1.1 Setup 71

3.1.2 Validation of leading-order amplitudes 72

3.1.3 Validation of matrix-element corrections 73

3.2 Parton-level results 76

3.2.1 Setup 76

3.2.2 Effect of the correction 77

3.2.3 Effect of the truncated shower 78

3.2.4 Division of the real-emission phase space 85

3.2.5 Combining corrections to stop production and decay 89

3.3 Effect of the correction on exclusion boundaries 94

3.4 Summary 102

4 Matrix-element corrections to squark-antisquark production 104

4.1 Treatment of on-shell contributions 105

4.2 Validation 113

4.2.1 Setup 113

4.2.2 Validation of leading-order amplitudes 113

4.2.3 Validation of matrix-element corrections 115

4.3 Comparison of on-shell subtraction methods 120

4.3.1 Setup 120

4.3.2 Dependence on the width 121
4.3.3 Dependence on the phase-space cutoff 125
4.3.4 Comparison of on-shell subtraction methods 127
4.4 Parton-level results 131
4.4.1 Setup 131
4.4.2 Effect of the correction 131
4.4.3 Combining corrections to squark production and decay 133
4.5 Summary 138

5 Constraining compressed SUSY scenarios with monotop signatures 140
5.1 Monte Carlo simulations 141
5.1.1 Signal processes 141
5.1.2 Background processes 143
5.2 Event selection strategies 146
5.2.1 Object reconstruction 146
5.2.2 Leptonic monotops 147
5.2.3 Hadronic monotops 148
5.3 Results 150
5.3.1 Leptonic monotops 150
5.3.2 Hadronic monotops 154
5.3.3 Comparison to existing bounds 156
5.4 Summary 158

6 Summary and conclusions 159

A. Technical details 161
A.1 Matrix-element corrections in the MATCHBOX framework 161

B. Additional plots 166
B.1 Validation of matrix-element corrections to $\tilde{q}\tilde{q}^*$ production 166

List of Figures

1.1 One-loop contributions to the Higgs boson mass from fermion and scalar fields. 6

1.2 Branching of the quark i into a collinear gluon k and the final-state quark j. 25

2.1 Effect of the POWHEG style ME correction on the Dalitz distribution of the decay $t \to Wbg$. 55

2.2 Comparison of distributions generated with no ME correction, to those generated using the preexisting or new POWHEG style ME correction to the decay $t \to Wb$. 57

2.3 Effect of the POWHEG style ME correction on the dijet invariant mass distribution formed when the lightest RS graviton decays into jets. . . 61

2.4 Effect of the POWHEG style ME correction on the Dalitz distribution of the decay $\tilde{u}_L \to u\,\tilde{\chi}_1^0 g$. 64

2.5 Effect of the POWHEG style ME correction on the transverse momentum distribution of the second hardest jet produced during the decay $\tilde{u}_L \to u\,\tilde{\chi}_1^0$. 65

2.6 Effect of the POWHEG style ME correction on the Dalitz distribution of the decay $\tilde{g} \to \tilde{t}_1\,\bar{t}g$. 66

2.7 Effect of the POWHEG style ME correction on the transverse momentum distribution of the third hardest jet produced during the decay $\tilde{g} \to \tilde{t}_1\,\bar{t}$. 67

3.1 Comparison of LO $m_{\tilde{t}_1\tilde{t}_1^*}$ and $p_{T,\tilde{t}_1}$ distributions generated using the MATCHBOX and internal Herwig++ setups. 73

3.2 Comparison of $m_{\tilde{t}_1\tilde{t}_1^*}$, $p_{T,\tilde{t}_1}$ and $p_{T,\tilde{t}_1\tilde{t}_1^*}$ distributions generated using the ME correction implementations in MATCHBOX and POWHEGBOX. . 74

3.3 Comparison of $p_{T,\tilde{t}_1\tilde{t}_1^*}$ distributions generated with and without the POWHEG style ME correction. 77

3.4 Comparison of ME corrected $m_{\tilde{t}_1\tilde{t}_1^*}$, $p_{T,\tilde{t}_1}$, $p_{T,\tilde{t}_1\tilde{t}_1^*}$ and $\Delta R(\tilde{t}_1\tilde{t}_1^*, j_1)$ distributions generated with and without the truncated shower, and with the direct shower approach described in Section 3.2.3. 81

3.5 As in Figure 3.4, now including improvements to the direct shower approach. 84

3.6 Effect of the different phase-space restriction schemes on ME corrected distributions of $m_{\tilde{t}_1\tilde{t}_1^*}$, $p_{T,\tilde{t}_1}$, $p_{T,\tilde{t}_1\tilde{t}_1^*}$ and $\Delta R(\tilde{t}_1, \tilde{t}_1^*)$. 86

3.7 Effect of the different phase-space restriction schemes on ME corrected distributions of p_{T,j_1} and p_{T,j_2}. 88

3.8 Distributions of p_{T,j_1}, p_{T,j_2}, p_{T,b_1} and E_T^{miss} for the benchmark scenario $(m_{\tilde{t}_1}, m_{\tilde{\chi}_1^+}) = (700, 200)$ GeV. Results were generated with either no ME corrections, or ME corrections applied to the top squark production, decays or both. 91

3.9 As in Figure 3.8, but for the compressed benchmark scenario $(m_{\tilde{t}_1}, m_{\tilde{\chi}_1^+}) = (225, 180)$ GeV. 93

3.10 Comparison of the 95% CL exclusion limits set by the ATLAS collaboration search for direct top squark pair production, with those derived using Herwig++ signal events without POWHEG style ME corrections. 98

3.11 Comparison of the 95% CL exclusion limits set using Herwig++ signal events generated either without ME corrections, or with ME corrections applied to the top squark production, decays or both. 99

3.12 As in Figure 3.10, but with POWHEG style ME corrections applied during the production and decays of the top squarks in the Herwig++ events. 101

4.1 Real-emission Feynman diagrams with potentially on-shell gluinos. . . 105

4.2 Comparison of LO $m_{\tilde{u}_L\tilde{u}_L^*}$ and $p_{T,\tilde{u}_L}$ distributions generated using the MATCHBOX and internal Herwig++ setups. 114
4.3 Comparison of $m_{\tilde{u}_L\tilde{u}_L^*}$, $p_{T,\tilde{u}_L}$, $p_{T,\tilde{u}_L\tilde{u}_L^*}$ and $m_{\tilde{u}_L^*q}$ distributions generated using the MATCHBOX and POWHEGBOX implementations of POWHEG style ME corrections with diagram removal. 116
4.4 As in Figure 4.3, but using the DS0 diagram subtraction method. . . 118
4.5 As in Figure 4.3, but using the DSII diagram subtraction method. . 119
4.6 Numerical dependence of the combined q_ig and $\bar{q}_ig$-initiated contributions to the real-emission cross section for the process $pp \to \tilde{q}_i\tilde{q}_i^*$ on the parameter $\Gamma_{\tilde{g}}/m_{\tilde{g}}$, calculated using diagram subtraction. . . . 122
4.7 Dependence of the $p_{T,\tilde{u}_L\tilde{u}_L^*}$ distribution on the parameter $\Gamma_{\tilde{g}}/m_{\tilde{g}}$ in the DS0, DSI, DSI′ and DSII schemes. 124
4.8 Dependence of the $p_{T,\tilde{u}_L\tilde{u}_L^*}$ distribution on the parameter Δ in the DSI and DSI′ schemes. 126
4.9 Comparison of $m_{\tilde{u}_L\tilde{u}_L^*}$, $p_{T,\tilde{u}_L}$, $p_{T,\tilde{u}_L\tilde{u}_L^*}$ and $m_{\tilde{u}_L^*q}$ distributions generated either using diagram removal or the DS0, DSI, DSI′ and DSII diagram subtraction procedures. 128
4.10 Comparison of $p_{T,\tilde{u}_L\tilde{u}_L^*}$ distributions generated with and without ME corrections in the DSI′ scheme. 132
4.11 Distributions of $p_{T,j1}$, $p_{T,j2}$, $p_{T,j3}$ and E_T^{miss} for the benchmark scenario $(m_{\tilde{g}}, m_{\tilde{u}_L}) = (2.4, 1.8)$ TeV. Results were generated with either no ME corrections, or with ME corrections applied during the squark production, decays or both. 134
4.12 As in Figure 4.11, but for the compressed benchmark scenario $(m_{\tilde{g}}, m_{\tilde{q}}) = (700, 650)$ GeV. 136

5.1 Distributions of m_T^W and E_T^{miss} for the leptonically decaying monotop signal scenarios and dominant background processes. 151
5.2 LHC sensitivity to the leptonically decaying monotop signal induced by $(\tilde{t}_1, t, \tilde{g})$ production in compressed supersymmetric scenarios. . . . 152
5.3 LHC sensitivity to the leptonically decaying monotop signal induced by $(\tilde{t}_1, t, \tilde{\chi}_1^0)$ production in compressed supersymmetric scenarios. . . . 153

5.4 Distributions of m_{bjj} for the hadronically decaying monotop signal scenarios and dominant background processes. 153
5.5 Same as Figure 5.2, but for the hadronically decaying monotop signal. 155
5.6 Same as Figure 5.3, but for the hadronically decaying monotop signal. 155
5.7 Comparison of the bounds derived using monotop probes with those set by the ATLAS and CMS collaborations using more traditional search strategies. 157

B.1 Comparison of $m_{\tilde{d}_R\tilde{d}_R^*}$, $p_{T,\tilde{d}_R}$, $p_{T,\tilde{d}_R\tilde{d}_R^*}$ and $m_{\tilde{d}_R^* d}$ distributions generated using the MATCHBOX and POWHEGBOX implementations of ME corrections with the DS0 diagram subtraction scheme for the mass splitting $(m_{\tilde{g}}, m_{\tilde{d}_R}) = (1.9, 1.8)$ TeV. 166
B.2 As in Figure B.1, but for $\tilde{c}_R\tilde{c}_R^*$ production with the mass splitting $(m_{\tilde{g}}, m_{\tilde{c}_R}) = (1.9, 1.8)$ TeV. 168
B.3 As in Figure B.1, but for $\tilde{s}_L\tilde{s}_L^*$ production with the mass splitting $(m_{\tilde{g}}, m_{\tilde{s}_L}) = (2.4, 1.8)$ TeV. 169

List of Tables

1.1 Summary of the gauge and mass eigenstates of the superpartners and Higgs sector of the MSSM. 12

2.1 List of two-body decay spin structures for which the POWHEG style ME correction has been implemented. 59

2.2 List of two-body decay colour flows for which the POWHEG style ME correction has been implemented. 59

2.3 Masses of the SUSY particles relevant to the decays studied in Section 2.3.2. 63

3.1 Summary of the selection criteria imposed in the ATLAS collaboration search for direct top squark pair production. 96

5.1 Cross sections and number of events surviving all selection criteria for the simulated background processes and two representative monotop signals. 145

Chapter 1

Introduction

The Standard Model of particle physics (SM) provides a remarkably successful framework for describing fundamental particles and their interactions. However, despite its continued success in the face of intense experimental scrutiny, it is widely believed that the Standard Model is not the complete theory of everything. This motivates the search for an extension to the Standard Model, and a plethora of new physics theories has been postulated. The most studied set of beyond the Standard Model (BSM) scenarios are the class of weak scale supersymmetric theories [1, 2]. Supersymmetry (SUSY) is motivated by the observation that it is the only non-trivial extension to the Poincaré group which gives rise to a consistent interacting quantum field theory. It unambiguously predicts the existence of a partner with opposite spin statistics for each of the Standard Model particles, and there is theoretical motivation to believe that at least some of these new superparticles should be accessible at current collider energy scales.

However, no clear evidence of supersymmetry has been observed to date, and exclusion limits on the masses of the strongly interacting superparticles are being pushed to and beyond the TeV scale [3, 4]. Corners of parameter space where these high bounds can be evaded are becoming increasingly appealing and well scrutinized. One such area is the region occupied by compressed spectra supersymmetric scenarios in which the mass splittings between the superpartners accessible at the LHC are small. In this case, the SM objects produced during the decays of superparticles are soft, and only a relatively small amount of missing transverse energy

is expected in events. Consequently, the kinematic quantities traditionally used to identify supersymmetric events and reduce the SM background become less effective, making these scenarios more difficult to exclude.

To constrain compressed spectra scenarios, new analysis techniques have been developed which rely on the production of a hard SM object together with a pair of superpartners. The introduction of the SM object leads to recoil of the superparticle pair, increasing the amount of missing transverse energy in events. Studies and experimental searches have been performed for a range of SM objects, for example a photon or top quark, but the most investigated scenario is that of monojet signatures where the additional SM object is a hard jet originating from initial-state radiation (ISR).

The limits on new physics that are set by these monojet searches are clearly sensitive to the way in which hard (high-transverse momentum) Quantum Chromodynamic (QCD) radiation is treated during the simulation of the SUSY signal events. In a typical Monte Carlo event generator, fixed-order matrix elements describing the partonic scattering process are combined with parton showers that simulate the emission of QCD radiation from coloured particles in the event[1]. Traditionally, the hard process is described at leading order (LO) in perturbation theory, while the parton shower utilizes an approximation that is exact only for soft and collinear radiation. Consequently, high transverse momentum emissions are not well described using this basic event generation setup. However, much effort has been made in recent years to improve the simulation of hard radiation in Monte Carlo event generators, with several techniques now widely available. In one approach, known as matrix-element (ME) matching, the hardest emission in each event is distributed using the next-to-leading order (NLO) real-emission correction to the matrix element of the hard process. As such, the hardest emission is now described with leading-order accuracy. This method may be further improved, in an approach known as NLO matrix-element matching, such that the description of suitably inclusive observables is promoted to NLO accuracy, in addition to the improvement in the description of

[1]Typically, a QED parton shower simulating the emission of photons is also included. However, in this work we restrict our study to the effects of QCD radiation only.

the hardest emission.

The main purpose of this thesis is to study the impact of using higher-order matrix elements to improve the simulation of hard radiation produced in new physics events. To this end, we consider matrix-element matching based on the POsitive Weight Hardest Emission Generator (POWHEG) formalism [5]. While the POWHEG formalism deals with NLO matrix-element matching, we only implement ME matching in which inclusive observables are accurate to leading order. This choice is motivated by the limited availability of NLO virtual corrections for processes involving BSM particles. The matching prescription, which we refer to as a POWHEG style matrix-element correction, has been implemented within the Herwig++ Monte Carlo event generator [6, 7].

Hard radiation may be generated in BSM events either during the production or decay of particles. In the latter case, we consider the application of matrix-element corrections to a range of decays that appear in both supersymmetry and alternative new physics scenarios. Previously, the POWHEG formalism has been successfully applied to a number of decays involving Standard Model and new physics particles [8–11]. In addition, a similar approach based on generic spin structures has been used to apply matrix-element corrections to hard radiation in SM and BSM particle decays in the PYTHIA 6 event generator [12].

When considering radiation emitted during the production stage of the event, we study only the production of squark-antisquark pairs at the LHC. This production process is a test case that marks the beginning of the development of an automated method for implemented POWHEG style matrix-element corrections in Herwig++. In future, it is envisaged that the correction will be available for a wide range of BSM production processes. The motivation for this choice of test case comes from the fact that the production of the strongly interacting superpartners, the squarks and gluinos, presents one of the most promising channels for discovering SUSY at the LHC. As such, accurate predictions for their production cross sections and observable distributions are crucial. The leading-order cross section predictions for squark-antisquark production, calculated for example in Ref. [13], have been known for some time. The NLO predictions are now also widely available, having first been

determined in the case of five degenerate light-flavour squarks [14–17] and then more recently calculated for a completely general squark mass spectrum [11, 18]. In addition to fixed-order calculations, in Ref. [11] the NLO accurate matrix elements have been matched to parton showers following the POWHEG prescription. The POWHEG approach has also been previously applied to alternative hard production processes in SUSY models [19–24].

This thesis is organised as follows. The remainder of Chapter 1 is devoted to introductory information relevant to later chapters. A brief summary of the main principles of supersymmetry and the minimal supersymmetric extension to the SM is given in Section 1.1. In Section 1.2, we outline the general structure of fixed-order NLO calculations in perturbative QCD. A brief review of the main components of Monte Carlo event generators is then given in Section 1.3, along with a more detailed discussion of the parton-shower algorithm in Herwig++. Finally, matching NLO calculations and parton showers using the POWHEG formalism is described in Section 1.4, with technical details relevant to our POWHEG style matrix-element correction included both in this section and in Appendix A.1.

In Chapter 2, we consider the impact of improving the simulation of hard radiation generated during the decays of BSM particles. In Section 2.1, our implementation of the POWHEG style matrix-element correction is described in full for the example of top quark decays. Details of the full range of decay modes for which the correction is implemented are then given in Section 2.2. In Section 2.3, the impact of the correction on the decay of the lightest graviton in the Randall-Sundrum model [25] and a selection of decays in the Constrained Minimal Supersymmetric Standard Model is presented, before our results are summarized in Section 2.4.

In Chapters 3 and 4, we turn our attention to the application of the matrix-element correction to the production of squark-antisquark pairs at the LHC. In Chapter 3 we focus on the case of top squarks. After validation of our matrix-element correction algorithm in Section 3.1, we study the impact of the correction on parton-level distributions[2] in Section 3.2. Having done so, in Section 3.3 the effect

[2]We use the term parton level to refer to events that include the simulation of some or all of the parton-shower evolution, but exclude the effects of hadronization and the underlying event.

of including matrix-element corrections in simulations used to constrain compressed spectra scenarios is illustrated, considering also the combination of corrections applied during the production and decays of the top squarks. Finally, Section 3.4 summarizes the findings of this chapter.

Matrix-element corrections to squark-antisquark production are addressed for all remaining squark flavours in Chapter 4. We begin in Section 4.1 with a detailed discussion of techniques used to deal with real-emission contributions containing a heavy, on-shell intermediate particle. Our matrix-element correction approach is then validated in Section 4.2, with additional results available in Appendix B.1. The various methods for removing on-shell contributions to the real-emission matrix element are compared in Section 4.3, before the effect of the matrix-element correction on parton-level results is presented in Section 4.4. Conclusions are drawn in Section 4.5.

In Chapter 5, we move away from the matrix-element corrections relevant to monojet based search strategies, and consider instead monotop signatures consisting of a single top quark produced in association with missing transverse momentum. We investigate the possibility of using monotop probes at the LHC to gain sensitivity to two simplified supersymmetric scenarios with compressed spectra. To do so, we make use of Monte Carlo simulations of both the new physics signals and SM background processes, using the technical setup described in Section 5.1. In Section 5.2, we present analysis strategies sensitive to compressed regions of parameter space. The reach of these strategies for our two simplified model scenarios is illustrated in Section 5.3, before the chapter is summarized in Section 5.4.

Finally, in Chapter 6 we summarize the thesis.

1.1 Supersymmetry

1.1.1 Motivations for physics beyond the Standard Model

The Standard Model of particle physics is a consistent theoretical framework which describes elementary particles and their interactions. Within it is contained Quantum Chromodynamics, the theory describing the strong interaction of quarks and

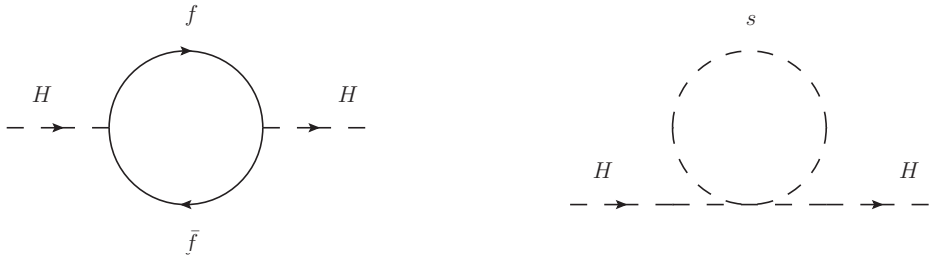

Figure 1.1: One-loop contributions to the Higgs boson mass from fermion (left) and scalar (right) fields.

gluons, and a unified picture of electromagnetic and weak interactions [26–28]. Over the past 50 years, it has been subjected to a barrage of experimental tests and has successfully explained almost all existing high energy physics data. However, it fails to provide satisfactory answers to a number of fundamental questions. Perhaps the most obvious shortcoming is its inability to describe gravitational interactions. At the scale at which quantum gravitational effects become important, *i.e.* the reduced Planck scale $\bar{M}_{Pl} = 2.4 \times 10^{18}$ GeV, it is necessary to describe gravity using a quantum field theory (QFT) approach. However, attempts to do so are typically plagued by issues of non-renormalizability, and so a robust theory of quantum gravity is yet to be formulated. In addition, given the complexity of nature at the weak scale, it seems likely that new physics exists beyond that which is encompassed in the Standard Model, in the unexplored 16 orders of magnitude below $\bar{M}_{Pl}$. In fact, postulating that no new physics effects are present between the weak and reduced Planck scales gives rise to a significant conceptual problem with the Standard Model, known as the hierarchy problem. The hierarchy problem refers to the sensitivity of the Higgs mass to high energy phenomena. In a theory with an ultraviolet (UV) energy cutoff Λ, the one-loop correction to m_H^2 arising from a fermion loop in the Higgs propagator, as illustrated in the left-hand side of Figure 1.1, is [29]

$$\delta m_H^2 = -\frac{\lambda_f^2}{8\pi^2}[\Lambda^2 + \text{terms logarithmic in } \Lambda], \tag{1.1.1}$$

where λ_f is the Yukawa coupling of the fermion to the Higgs boson. Through renormalization, the regulated divergent terms in Eq. 1.1.1 can be absorbed into a redefinition of the Higgs mass. However, if one assumes that no new physics is

present below the reduced Planck scale, *i.e.* $\Lambda = \bar{M}_{Pl}$, huge cancellation is required between the bare Higgs mass parameter and the one-loop contribution in order to arrive at a renormalized mass that agrees with the experimentally observed value [30], $m_H = 125.09 \pm 0.21$ (stat.) $\pm$ 0.11 (syst.) GeV. While not technically inconsistent, this level of fine-tuning is theoretically unpleasant. It is more appealing to imagine that new physics effects are introduced at a lower energy scale, $\Lambda \approx 1$ TeV, such that the bare and renormalized Higgs mass parameters are of the same order of magnitude. If this new physics takes the form of a new complex scalar field, an additional contribution to m_H^2 exists. This correction, shown in the right-hand side of Figure 1.1, is [29]

$$\delta m_H^2 = \frac{\lambda_s}{16\pi^2}[\Lambda^2 + \text{terms logarithmic in } \Lambda], \tag{1.1.2}$$

where λ_s is the coupling of the new scalar to the Higgs boson. As such, the systematic cancellation of contributions to m_H^2 that depend quadratically on the cutoff parameter Λ, and therefore the elimination of the hierarchy problem, can be achieved by introducing two new complex scalar fields for every fermion in the Standard Model and requiring $\lambda_f^2 = \lambda_s$.

Two further aspects of nature not incorporated in the Standard Model of particle physics are that of dark matter and dark energy. Fundamental particles described by the Standard Model account for less than 5% of the total energy content of the Universe. The remainder exists in terms of dark matter (27%) and dark energy (68%), and no suitable candidate for either exists within the Standard Model framework. Finally, experimental observations of neutrino oscillations set non-zero bounds on neutrino masses. The Standard Model predicts massless neutrinos and so must be augmented with some mechanism through which they may obtain a mass.

Given these and further unmentioned limitations, the Standard Model is typically viewed as a low energy limit of some larger theory. Consequently, many theories attempting to describe physics beyond the Standard Model have been developed over the years. One of the most popular candidates is weak scale supersymmetry [1, 2]. In the following section, the main ideas and motivations for supersymmetry will be outlined and the additional particle content predicted by the minimal supersymmetric extension to the Standard Model (MSSM) introduced. Having done so, typical

collider signatures for SUSY and the corresponding search strategies employed at the LHC will be outlined. Details are limited to those relevant for later chapters of this thesis. Pedagogic introductions to the theoretical construction and collider signatures of SUSY can be found, for example, in Refs. [29, 31].

1.1.2 Introduction to supersymmetry

Supersymmetric theories postulate the existence of a symmetry relating fermionic and bosonic degrees of freedom. Schematically, this symmetry can be expressed in terms of a SUSY operator, Q, which when acting on a fermionic state transforms it into a bosonic state and visa versa,

$$Q\,|\text{fermion}\rangle = |\text{boson}\rangle \quad \text{and} \quad Q\,|\text{boson}\rangle = |\text{fermion}\rangle\,. \tag{1.1.3}$$

It is clear from the nature of these transformations that the generators of supersymmetry are fermionic spin-1/2 operators. Through the introduction of such generators, the Poincaré algebra which encapsulates the space-time symmetries of the SM may be extended in a non-trivial way [32], *i.e.* such that the Poincaré and SUSY generators have non-zero commutation relations.

In fact, the addition of SUSY generators is the only possible non-trivial extension to the Poincaré group that gives rise to a consistent relativistic QFT [32]. The addition of bosonic generators (*i.e.* those that preserve the spin of the state they act on) is ruled out by the Coleman-Mandula no-go theorem [33], while the Haag-Lopuszanski-Sohnius theorem [32] limits the possible fermionic generators to only those which generate supersymmetry. The SUSY generators satisfy the following anticommutation and commutation relations that, together with the Poincaré algebra, form the Super-Poincaré algebra [31]

$$\{Q, \bar{Q}\} = 2\sigma_\mu P^\mu, \tag{1.1.4}$$

$$[M^{\mu\nu}, Q] = -i\sigma^{\mu\nu} Q, \tag{1.1.5}$$

$$\{Q, Q\} = \{\bar{Q}, \bar{Q}\} = 0, \tag{1.1.6}$$

$$[P^\mu, Q] = [P^\mu, \bar{Q}] = 0, \tag{1.1.7}$$

where Q and $\bar{Q}$ are the generators of supersymmetry, related through $Q^\dagger = \bar{Q}$, P^μ are the generators of spacetime translations and $M^{\mu\nu}$ are the generators of Lorentz transformations[3].

Supersymmetric extensions to the SM are constructed by embedding each SM particle as a component field in a supermultiplet. Also contained within each supermultiplet is a superpartner field related to the SM one through a SUSY transformation. As such, these superpartners have identical properties to their SM counterparts with the exception of spin, where they differ by a half integer. This symmetry between fermionic and bosonic degrees of freedom naturally gives rise to the equality of coupling constants that was required in order to solve the hierarchy problem introduced in the previous section. The Lagrangian of the theory may then be constructed from the supermultiplets by including all possible renormalizable terms that are consistent with the symmetries of the theory. Finally, the Lagrangian may be expanded in terms of the component fields to obtain the Feynman rules of the theory. These can be found for the minimal supersymmetric extension to the Standard Model in, for example, Ref. [34].

It is clear that supersymmetric theories, in their most basic form, cannot represent a realistic model of Nature. The equality of SM particle and superpartner properties, so crucial in the solution to the hierarchy problem, raises a significant issue. If the masses and gauge couplings of the superpartners are identical to their SM counterparts, the superpartners should be being produced copiously at current collider experiments. However, the superpartners are yet to be observed [3, 4], leading to the conclusion that SUSY, if it exists, cannot be an exact symmetry of Nature. By breaking SUSY, the masses of the superpartners can be greater than the SM particles, therefore accounting for their non-observation. While details of the SUSY-breaking mechanism are unknown, the form of the additional SUSY-breaking terms in the Lagrangian can be constrained by requiring that they do not disrupt the cancellation of the quadratically divergent contributions to the Higgs mass. The resulting procedure in known as soft SUSY-breaking.

[3] $\sigma^\mu = (\mathbf{1}, \sigma^i)$, $\bar{\sigma}^\mu = (\mathbf{1}, -\sigma^i)$ and $\sigma^{\mu\nu} = \frac{1}{4}(\sigma^\mu\bar{\sigma}^\nu - \sigma^\nu\bar{\sigma}^\mu)$, where σ^i are the Pauli matrices.

In the MSSM, no mechanism for SUSY breaking is assumed and instead the Lagrangian is simply augmented with the most general combination of soft SUSY-breaking terms. With the inclusion of these terms, the Lagrangian for the MSSM contains some 124 parameters [35]. Such a model is of limited use to experimental searches and so it is often helpful to consider a constrained form, the CMSSM, in which the number of new parameters is reduced. The reduction is obtained by assuming high scale universality (at $m_{\mathrm{GUT}} \approx 10^{16}$ GeV) of the SUSY-breaking masses of the gauginos ($m_{1/2}$) and scalars (m_0), and of the trilinear SUSY-breaking couplings[4] (A_0). In addition to these parameters, to fully define the CMSSM it is also necessary to specify the ratio of the vacuum expectation values of the two Higgs doublets ($\tan\beta$) and the sign of a parameter μ that appears in the Lagrangian. The low scale parameters of the model, relevant to phenomenological studies, can then be obtained through renormalization group running of these high scale parameters.

1.1.3 The particle content of the MSSM

In the minimal supersymmetric extension to the SM, two types of supermultiplets are required - chiral and vector supermultiplets. The SM fermions are contained within the former, with the left and right-handed components of each Dirac fermion embedded separately in left and right-handed chiral supermultiplets, thus allowing them to transform differently under electroweak gauge transformations. Each chiral supermultiplet also contains a spin-0 complex scalar superpartner. The superpartners of the SM quarks and leptons are referred to as the squarks and sleptons respectively. They are typically denoted by *e.g.* $\tilde{q}_L$ for the superpartner of the left-handed quark, where the subscript indicates the chiral nature of the SM partner.

The Higgs boson is embedded within the spin-0 component field of a chiral supermultiplet, with its superpartner the higgsino, $\tilde{H}$, providing the spin-1/2 component. In fact, it is necessary to extend the Higgs sector to include two such supermultiplets, one which couples to up-type quarks and one which couples to down-type

[4]The trilinear soft SUSY-breaking terms describe the coupling of three scalar fields and take the form $\mathcal{L}_{\mathrm{tri}} = A_0 \lambda \phi_i \phi_j \phi_k$.

quarks and charged leptons. These multiplets have differing values of weak hypercharge such that the total higgsino contribution to the gauge anomaly is zero. After electroweak symmetry breaking, an extended Higgs sector remains in the MSSM with two charged and three neutral scalar bosons. Finally, the SM gauge bosons are contained within the spin-1 component fields of vector supermultiplets. Their superpartners are spin-1/2 fermions called the gauginos. The superpartner of the gluon is known as the gluino ($\tilde{g}$) and, prior to electroweak symmetry breaking, the partners of the electroweak W and B gauge bosons are the winos and bino, ($\tilde{W}^{0,\pm}$ and $\tilde{B}$ respectively).

When both SUSY and electroweak symmetry are broken, mixing occurs between the electroweak gauginos and the higgsinos, such that the gauge eigenstates do not correspond with the mass eigenstates of the theory. The bino, neutral wino and neutral higgsinos mix to form four neutral superpartners, the neutralinos $\tilde{\chi}_i^0$. The remaining charged winos and higgsinos similarly mix to form two positively and two negatively charged superpartners, known as the charginos $\tilde{\chi}_i^\pm$. Supersymmetry breaking also gives rise to mixing in the squark and slepton sectors. The mass eigenstates of the squarks and sleptons are determined by diagonalizing three 6×6 mixing matrices for the up-type squarks, down-type squarks and charged sleptons, and one 3×3 matrix for the sneutrinos. In practice however, off-diagonal terms in the mixing matrix are proportional to the Yukawa coupling constants, and so significant mixing only occurs between pairs of third generation sfermions. For example, the left and right-handed stops, $\tilde{t}_L$ and $\tilde{t}_R$, mix to form the mass eigenstates[5] $\tilde{t}_1$ and $\tilde{t}_2$. The lightest of these, $\tilde{t}_1$, is typically the lightest of all the squarks. The gauge and mass eigenstates of the new superpartners and Higgs sector content of the MSSM is summarized in Table 1.1.

In the most general form of the supersymmetric Lagrangian, terms appear which violate either lepton number (L) or baryon number (B) conservation. The existence of such terms is not compatible with experimental constraints that arise, for example, from the non-observation of proton decay. If the lepton and baryon number violating

[5]By convention, mass eigenstates are numbered in terms of increasing mass.

		Gauge eigenstates	Mass eigenstates
Scalars	Squarks	$\tilde{u}_L$, $\tilde{u}_R$, $\tilde{d}_L$, $\tilde{d}_R$,	same
		$\tilde{c}_L$, $\tilde{c}_R$, $\tilde{s}_L$, $\tilde{s}_R$,	same
		$\tilde{t}_L$, $\tilde{t}_R$, $\tilde{b}_L$, $\tilde{b}_R$	$\tilde{t}_1$, $\tilde{t}_2$, $\tilde{b}_1$, $\tilde{b}_2$
	Sleptons	$\tilde{\nu}_e$, $\tilde{\nu}_\mu$, $\tilde{\nu}_\tau$	same
		$\tilde{e}_L$, $\tilde{e}_R$, $\tilde{\mu}_L$, $\tilde{\mu}_R$,	same
		$\tilde{\tau}_L$, $\tilde{\tau}_R$	$\tilde{\tau}_1$, $\tilde{\tau}_2$
	Higgs bosons	H_u^0, H_d^0, H_u^+, H_d^-	h^0, H^0, A^0, $H^\pm$
Fermions	Gluino	$\tilde{g}$	same
	Charginos	$\tilde{W}^+$, $\tilde{W}^-$, $\tilde{H}_u^+$, $\tilde{H}_d^-$	$\tilde{\chi}_1^\pm$, $\tilde{\chi}_2^\pm$
	Neutralinos	$\tilde{B}$, $\tilde{W}^0$, $\tilde{H}_u^0$, $\tilde{H}_d^0$	$\tilde{\chi}_i^0$, $i = 1, 2, 3, 4$

Table 1.1: Summary of the gauge and mass eigenstates of the superpartners and Higgs sector of the MSSM.

terms were present in the Lagrangian with non-negligible couplings, the lifetime of the proton would be extremely short and in contradiction with the experimentally observed limit[6] which is in excess of 10^{33} years [36]. In the MSSM, these problematic terms are eliminated through the addition of a new Z_2 symmetry called R-parity. The R-parity of a particle with spin s is defined as

$$P_R = (-1)^{3(B-L)+2s}. \tag{1.1.8}$$

Accordingly, SM particles have even R-parity ($P_R = +1$), while the R-parity of the superpartners is odd ($P_R = -1$). The conservation of R-parity has a huge impact of the phenomenology of SUSY processes. Firstly, only even numbers of supersymmetric particles can be produced in the collisions of SM particles (*i.e.* at

[6]This limit applies to the decay of the proton into a lepton plus meson final state.

current collider experiments). These sparticles, with the exception of the lightest supersymmetric particle (LSP), can decay through a number of stages, with each decay vertex involving an even number of superparticles. The decay proceeds until the only sparticles remaining in the event are an even number of LSPs. Finally, the LSP is stable, and can provide a suitable candidate for non-baryonic dark matter if it is also electrically and colour neutral.

1.1.4 Searching for supersymmetry at the LHC

Due to the strong theoretical motivation for studying SUSY, searches for sparticle production have been one of the main emphases of the BSM program during Run 1 of the LHC, continuing on from studies previously performed at LEP and the Tevatron. In R-parity conserving models, such as the MSSM, sparticles produced in high energy collisions would decay though a number of stages to produce SM objects (*e.g.* leptons, photons, jets) and the LSP. Throughout the course of this work, we will assume the LSP is the lightest neutralino $\tilde{\chi}_1^0$. The neutralino only interacts weakly and as such would evade detection at collider experiments. This typically leads to a significant imbalance in the combined transverse momentum of the visible final-state particles when compared with the colliding protons in events in which sparticles are produced. The magnitude of this quantity, E_T^{miss}, has traditionally been the most important kinematic quantity employed in discriminating SUSY events from the SM background, since in the latter, normally only a small amount of E_T^{miss} is present[7]. The classic experimental signature studied in SUSY searches is therefore a number of SM objects accompanied by a significant amount of missing transverse energy.

Many searches for sparticles have been performed at the LHC by both the general purpose experiments, ATLAS [3] and CMS [4]. Given the huge number of SUSY models and size of the associated parameter spaces, these searches must be done in a quasi model-independent manner if they are to efficiently probe the likelihood of a supersymmetric extension to the SM. As such, data is often interpreted in terms

[7]Missing transverse momentum in SM events arises due to neutrino production and detector effects.

of simplified models in which only a small subset of the superpartners have masses that are kinematically accessible at the LHC. This severely restricts the number of viable decay modes so that sparticles typically decay in only one or two steps and into a limited number of final states. In this simplified setup, the remain degrees of freedom in the parameter space, often the masses of the sparticles, can be varied to produced exclusion bounds like those found in Refs. [3, 4].

A large fraction of this thesis will be concerned with the impact of an improved treatment of hard radiation on LHC searches for SUSY particles, with the focus being on squark-antisquark production. Searches for squark production are particularly relevant at the LHC (and other hadron colliders) owing to the large production cross sections associated with coloured interactions. In addition, the lightest top squark can be considerably lighter than the other squarks and so should in principle be easily accessible at the LHC[8], despite the relative reduction in the production cross section when compared directly to light-flavour squark production[9].

In our study of squark-antisquark production, we will rely heavily on simplified models in which only the squarks and a subset of the gauginos are accessible at the LHC. In the case of light-flavour squark production, we focus on the decay mode $\tilde{q} \to q\tilde{\chi}_1^0$ which is often considered in experimental studies, see for example Refs. [37,38]. In the case of top squark production, the equivalent decay mode is not kinematically accessible in all regions of phase space. In the region $m_{\tilde{t}_1} > m_t + m_{\tilde{\chi}_1^0}$, the decay mode $\tilde{t}_1 \to t\tilde{\chi}_1^0$ is expected to dominate, but as the difference between the stop and neutralino masses decreases, the 3-body decay $\tilde{t}_1 \to bW\tilde{\chi}_1^0$ and then the flavour changing mode $\tilde{t}_1 \to c\tilde{\chi}_1^0$ and 4-body decay $\tilde{t}_1 \to bff'\tilde{\chi}_1^0$ become dominant. In later chapters, we will consider simplified models that probe a number of different regions of the stop and neutralino mass plane.

The regions of parameter space that exhibit small mass splittings between the superpartners accessible at the LHC are of particular relevance to this work. In

[8]Arguably, if the top squark is not accessible at the LHC, supersymmetry no longer provides a suitable solution to the hierarchy problem introduced in Section 1.1.1.

[9]This reduction arises due to the negligible top quark content in the parton distribution functions of the proton at the LHC.

these so called compressed supersymmetric scenarios, sparticles decay as before into the LSP and a collection of SM objects. However, now the SM objects are typically not energetic enough to be identified by the trigger algorithms used at the LHC. In addition, since sparticles are minimally produced in pairs, the two LSPs arising from the sparticle decays will be produced in an approximately back-to-back configuration, such that the amount of E_T^{miss} in events will be significantly reduced. This means that the event selection criteria which in uncompressed scenarios gave good discrimination between SUSY events and the SM background, are now less efficient. Furthermore, poor trigger efficiencies are expected from algorithms that rely solely on the amount of E_T^{miss} in events [39,40]. Classical search strategies based on the presence of numerous jets and leptons and a large amount of missing energy therefore have poor sensitivity to compressed supersymmetric scenarios.

These difficulties have lead to the development of non-standard analysis techniques, such as those which search for a monojet signature consisting of a single hard jet and missing transverse energy[10]. Such a signature can arise when superparticles are produced in association with a hard jet originating from initial-state radiation and all the decay products of the sparticles are soft or invisible. The introduction of an additional hard jet causes recoil of the sparticles which serves to increase the amount of E_T^{miss} in events. When combined with the requirement of a hard jet, this quantity can be used to achieve good efficiency in trigger algorithms and discrimination from SM backgrounds. As was previously stated, in this work we are interested in improving the treatment of high transverse momentum radiation in SUSY events. Consequently, monojet search strategies are of particular interest since their reach will be highly sensitive to any change in the description of hard radiation.

Events with single jets and missing transverse momentum have been interpreted in terms of SUSY particle production for over 30 years now, starting with data recorded at the UA1 experiment [41], see for example Ref. [42]. Since then, the

[10]In analogy with monojet systems, signatures comprising of missing transverse energy produced in association with an alternative SM object, for example an energetic photon, have also been used to constrain sparticle production at the LHC. In Chapter 5, monotop signatures in which the SM particle is a top quark, will be studied in the context of compressed spectrum SUSY scenarios.

use of monojet probes in searches for new physics scenarios has received significant attention[11] and has been effective at constraining compressed spectra SUSY scenarios, in particular the existence of light top squarks [45, 46], and alternative new physics models [47, 48]. In Chapter 3, a monojet-type search for light top squarks in compressed spectra scenarios will be used to assess the effect of different treatments of hard radiation in stop-antistop production.

1.2 Calculations in perturbative QCD

Methods for improving the treatment of hard radiation in Monte Carlo simulations typically make use of higher-order QCD contributions to the matrix elements of the hard process. As such, aspects of calculations within perturbative QCD will be relevant in later chapters and so are briefly reviewed in the following section. In Section 1.2.1, the salient points about the strong coupling constant, QCD factorization theorem and the connection between hadronic and partonic cross sections will be discussed. The treatment of next-to-leading order contributions in perturbative QCD calculations will then be outlined in Section 1.2.2, including a brief introduction to the Catani-Seymour dipole subtraction formalism.

1.2.1 Hard scattering formalism

Quantum Chromodynamics is a non-abelian SU(3) gauge theory, included within the framework of the Standard Model, that describes the strong interactions experienced by coloured particles and mediated by gluons. The scale dependence of the QCD coupling constant, α_s, that arises after renormalization of ultraviolet divergences in the theory, may be expressed as

$$\beta(\alpha_s) = \mu_R^2 \frac{\partial \alpha_s(\mu_R^2)}{\partial \mu_R^2}. \tag{1.2.9}$$

In QCD, the β-function appearing in the left-hand side of Eq. 1.2.9 is negative. As such, at high energies, or equivalently at short distance scales, the coupling constant

[11] See for example Refs. [43] and [44], for studies at the Tevatron and LHC respectively.

is small. This behaviour is known as asymptotic freedom. Conversely, at low energies the coupling constant becomes large - a phenomenon known as confinement. Confinement forbids the observation of free quarks and gluons and leads to the formation of colour-singlet hadrons, which are the experimentally observable states. In Eq. 1.2.9, the scale on which the coupling constant depends is an unphysical scale introduced during renormalization, known accordingly as the renormalization scale μ_R.

Interactions at hadron colliders in general depend on both high and low energy scales. According to QCD factorization theorem[12], the treatment of these two regimes can be separated such that the cross section for a hadronic scattering process may be written as

$$\sigma^{\text{had}}_{h_1 h_2 \to n} = \sum_{a,b} \int dx_a dx_b f_a^{h_1}(x_a, \mu_F) f_b^{h_2}(x_b, \mu_F) d\sigma_{a,b\to n}. \tag{1.2.10}$$

Here $d\sigma_{a,b\to n}$ is the differential partonic cross section describing the scattering of partons[13] a and b into n final-state particles. The characteristic scale of the partonic interaction, Q, is large and so the associated value of the coupling constant is small. Consequently, $d\sigma_{a,b\to n}$ is calculable within perturbation theory and may be written as an expansion in terms of α_s, such that Eq. 1.2.10 becomes

$$\begin{aligned}\sigma^{\text{had}}_{h_1 h_2 \to n} \\ = \sum_{a,b} \int dx_a dx_b f_a^{h_1}(x_a, \mu_F) f_b^{h_2}(x_b, \mu_F) \sum_{m=0}^{\infty} (\alpha_s(\mu_R^2))^{k+m} d\sigma^{(m)}_{a,b\to n}\left(x_a, x_b, \frac{Q^2}{\mu_F^2}, \frac{Q^2}{\mu_R^2}\right),\end{aligned} \tag{1.2.11}$$

where k is the order in α_s of the LO contributions to the partonic cross section. Each term in the perturbative expansion can be computed using, for example, Feynman diagrams.

The long range physics effects in the hadronic cross section are encapsulated in non-perturbative parton distribution functions (PDFs), $f(x, \mu_F)$. These describe

[12]Only the factorization of inclusive cross sections for deep inelastic scattering and Drell-Yan processes has been proven. For all other hadronic collisions, factorization is taken as an ansatz.

[13]The term parton refers to the fundamental particles that are the constituents of hadrons, *i.e.* the quarks, antiquarks and gluons.

the dynamics of partons within a given hadron, for example, $f_a^{h_1}(x_a, \mu_F)$ can be interpreted as the probability of finding within hadron h_1, a parton of type a that carries a fraction x_a of the total hadron momentum. The functions are universal, however, can not be calculated perturbatively and must instead be extracted from fits to experimental data[14].

In addition to the momentum fraction x, the PDFs depend on an unphysical factorization scale, μ_F, which can be thought of as defining the transition between the hard and soft regimes. The exact choice of this scale, as with the renormalization scale, is somewhat arbitrary. To avoid large logarithms, the factorization and renormalization scales are typically set equal to some momentum scale characteristic of the hard scattering process. Formally, the hadronic cross section in Eq. 1.2.11 is independent of both scales when calculated to all order in perturbation theory. However if the perturbative expansion is truncated, some residual dependence of the cross section on μ_R and μ_F will remain. In this case, an estimate of the size of the unknown higher-order contributions may be obtained by varying the values of μ_R and μ_F used in the calculation. As such, renormalization and factorization scale variation is typically used to estimate the level of theoretical uncertainty associated with a calculation.

1.2.2 Next-to-leading order calculations

The cross section for a partonic hard scattering process can be expanded perturbatively in powers of the strong coupling constant, that is

$$d\sigma = \sum_{m=0}^{\infty} (\alpha_s(\mu_R^2))^{k+m} d\sigma^{(m)}. \tag{1.2.12}$$

Taking only the first term in the perturbative expansion, *i.e.* the $m = 0$ term, corresponds to the leading-order result. Leading-order calculations provide an order of magnitude estimate for the total cross section and rough predictions for the shapes

[14] Although the PDFs cannot be calculated perturbatively, the functions at a given x and μ_F^2 may be evolved to lower values of x and higher values of μ_F^2 using by the perturbatively calculable DGLAP equations [49–51].

of some observables. Often, this level of accuracy is insufficient and it is necessary to include further terms in the expansion so as to achieve a reasonable description of data and better control of the theoretical uncertainties.

In the next-to-leading order prediction for $d\sigma$, both the first and second terms in Eq. 1.2.12 must be included. The new terms present at NLO arise from taking into account processes that contribute with an additional factor of α_s as compared with the lowest order interaction. These terms can be divided into contributions in which an additional parton has been radiated from the lowest order process and contributions in which a virtual parton has been exchanged between particles present at LO. As such, the NLO cross section may be written as

$$d\sigma^{\mathrm{NLO}} = \mathcal{B}(\Phi_n)d\Phi_n + \mathcal{V}(\Phi_n)d\Phi_n + \int \mathcal{R}(\Phi_{n+1})d\Phi_{n+1}. \tag{1.2.13}$$

Here $\mathcal{B}$ corresponds to the LO or Born matrix element squared[15], present also in the lowest order expansion, while $\mathcal{R}$ and $\mathcal{V}$ are the real and virtual corrections that contribute with one higher power of α_s. Since the real-emission contribution corresponds to the radiation of an additional parton, it is evaluated in the real-emission phase space Φ_{n+1}. The virtual or 1-loop contribution is defined, as for the Born process, in the phase-space element Φ_n.

The real-emission contribution in Eq. 1.2.13 is infrared (IR) divergent in regions of phase space where the additional emitted parton is either soft (*i.e.* has vanishing energy) or is emitted collinear to one of the particles involved in the Born process[16]. The virtual term is also divergent in the IR limit[17], but contributes to the cross section with the opposite sign. The Bloch-Nordsieck [52] and Kinoshita-Lee-Nauenberg [53,54] theorems guarantee that the IR singularities arising from integration of soft and collinear real-emission configurations will cancel with those arising

[15]Throughout this thesis, relevant flux factors will be absorbed into the definitions of $\mathcal{B}$, $\mathcal{V}$ and $\mathcal{R}$ such that, for example, the partonic LO cross section is $\sigma^{\mathrm{LO}} = \int \mathcal{B}(\Phi_n)d\Phi_n$.

[16]Collinear singularities occur only for pairs of massless collinear particles.

[17]The virtual contribution is also divergent in the ultraviolet limit, *i.e.* in the limit of large loop momentum. These divergences can be dealt with by first regularizing them and then renormalizing the theory.

from virtual loop integrals[18] when considering infrared-safe observables[19]. This cancellation occurs order-by-order in perturbation theory, such that each higher-order correction is independently finite.

The numerical evaluation of Eq. 1.2.13 as it stands, is not possible. While the total result is finite, the cancellation of IR singularities occurs between terms with different final-state multiplicities. This issue is overcome in the subtraction formalism by introducing a subtraction term, $\mathcal{C}(\Phi_{n+1})$. The subtraction term accurately reproduces the singular structure of the real-emission contribution in the soft and collinear regions of phase space, and is by design analytically integrable over the one-particle phase space of the unresolved parton Φ_R, defined through $\Phi_{n+1} = \Phi_R \Phi_n$. Eq. 1.2.13 may then be rewritten as

$$d\sigma^{\mathrm{NLO}} = \mathcal{B}(\Phi_n) d\Phi_n + \left[\mathcal{V}(\Phi_n) + \int \mathcal{C}(\Phi_{n+1}) d\Phi_R \right] d\Phi_n + \left[\mathcal{R}(\Phi_{n+1}) - \mathcal{C}(\Phi_{n+1}) \right] d\Phi_{n+1}. \tag{1.2.14}$$

Through the introduction of the subtraction term, both square brackets in Eq. 1.2.14 are now separately finite, with $\mathcal{C}(\Phi_{n+1})$ providing local cancellation of singular contributions in the real-emission term and $\int \mathcal{C}(\Phi_{n+1}) d\Phi_R$ allowing for analytic cancellation of singularities in the virtual term. The total cross section is unaffected by the procedure and numerical integration over the n and $n+1$ body phase-space elements is now possible.

Different formulations of the exact form the subtraction terms have been developed in, for example, the Catani-Seymour (CS) dipole formalism [55, 56] and the Frixione-Kunszt-Signer (FKS) [57] and antenna [58,59] subtraction approaches. The first of these methods will be relevant to later sections of this thesis, and so will be briefly outlined below. More details can be found in Refs. [55] and [56] for the case

[18] In fact, there is a class of real-emission divergences, arising from collinear emissions from initial-state or identified final-state partons, that are not cancelled by singularities appearing in the virtual term. Instead, these divergences are dealt with through a redefinition of the PDFs which introduces a mass factorization counter term into Eq.1.2.13. This term will not be made explicit but is assumed to be absorbed into the virtual contribution.

[19] An observable $\mathcal{O}$ is infrared safe if it fulfils the property $\mathcal{O}(\Phi_{n+1}) \to \mathcal{O}(\Phi_n)$ in the limit that one of the particles in the $n+1$ body phase space becomes soft or collinear to another particle.

of massless and massive partons respectively.

Construction of the subtraction term in the CS dipole formalism (and other approaches) is based on the factorized form of real-emission amplitudes evaluated in the soft or collinear limits. This allows the IR singular structure of the real-emission contribution to be encoded in a sum of terms, each of which is the convolution of a Born-level matrix element and a universal function. Schematically, the subtraction term is

$$\mathcal{C} = \sum_{\text{dipoles}} \mathcal{B} \otimes V_{\text{dipole}}, \tag{1.2.15}$$

where V_{dipole} are the universal dipole splitting functions. Each term in Eq. 1.2.15 defines a dipole function, $\mathcal{D}_{ij,k}$, that describes the behaviour of the real-emission matrix element in the singular regions of phase space where the emitted parton j becomes soft or collinear to the emitting parton i. The dipole functions also depend on a spectator parton k which is colour connected to the emitted parton.

For each dipole function, a kinematic mapping between the $n+1$ and n body phase spaces is required. The emitter particle and unresolved parton are combined into a single on-shell particle $\tilde{ij}$, while the momentum of the spectator particle is reshuffled to account for the recoil of the emission. Once this mapping has be established, the one-particle phase space required for the analytic integration of the dipole may be determined.

1.3 Monte Carlo event generators

While fixed-order calculations can provide predictions for high momentum transfer scattering processes involving a limited number of partons, collision data recorded at experiments like the LHC typically involves multiple high and low energy scatterings which give rise to a huge number of final-state hadrons. Monte Carlo event generators aim to bridge this gap between perturbative calculations and experimental observations by simulating, for a given theoretical model, all elements of a high-energy collision. As such, Monte Carlo event generators play a crucial role in the search of BSM physics signals, the measurement of SM parameters and the design of future experiments. A comprehensive review of Monte Carlo event generators is

available in Ref. [60]. In the following section, a brief review of the main components of a Monte Carlo event generator will be given, followed in Section 1.3.2 by a more in-depth description of the parton-shower stage of the event. Only collisions involving initial-state hadrons will be discussed[20] and all generator specific information applies to the Herwig++ event generator [6].

1.3.1 Overview

The complete simulation of high-energy hadronic collisions is only feasible due to QCD factorization. This allows the different stages of the event to be simulated separately, each with their own tailored mathematical and computational tools. The different stages are characterized by the associated scale of momentum transfer, and are outlined below.

- **Hard process**: At the highest momentum transfer scale, partonic constituents of the colliding hadrons scatter into a small number of fundamental final-state particles, in a stage of the event known as the hard process. The cross section for this process has traditionally been calculated at LO in perturbation theory although, as will be discussed in Section 1.4, it is possible to increase the accuracy to NLO and this is fast becoming the norm for SM processes. The cross section is integrated with standard Monte Carlo techniques, using pseudo-random numbers to determine the particles, momenta and colour flow of the process and sampling the integrand over the available phase space. The momentum transfer and colour flow of the hard process sets the initial conditions for the next stage of the event - the parton shower.

- **Parton shower**: The parton-shower stage of the event perturbatively evolves particles involved in the hard process from the high momentum transfer scale of the scattering to an IR cutoff scale. This evolution typically leads to the emission of additional QCD radiation and provides a connection between the

[20] In lepton collisions, treatment of the initial-state parton shower, PDFs and underlying event is no longer necessary. This leads to significant simplification of the event generation process.

hard and soft regimes. The procedure is separated into an initial-state shower describing radiation from the colliding partons, and a final-state shower accounting for the evolution of coloured particles produced in the hard process. The emission of QED radiation from charged particles is simulated in a similar way.

- **Decays of fundamental particles**: The decays of unstable particles produced in the hard process, for example top quarks or top squarks, are treated separately from their production by making use of the narrow width approximation. In the simulation of BSM events, the narrow width approximation is often invoked in scenarios where it is not strictly applicable. To improve the accuracy in these cases, an additional weight factor is available in Herwig++ which aims to take into account finite width effects, see Ref. [61] for more details. In addition, the correct treatment of spin correlations between the production and decay stages is obtained by using the algorithm described in Ref. [62]. Finally, unstable coloured particles that are produced in the hard process will typically initiate parton showers both during their production and decay. The treatment of hard radiation in both these stages will be the subject of subsequent chapters.

- **Multiple partonic interactions**: In parallel to the hard process, additional interactions can take place between pairs of initial-state partons not involved in the hard scattering. For the large centre-of-mass energies found at the LHC, the probability of this occurring is high. These interactions are treated separately from the hard process, and may be modelled as perturbative $2 \to 2$ QCD scattering processes when their characteristic scale is above the IR cutoff. As with the hard process, these additional interactions initiate parton showers making them a source of extra soft and semi-hard jets in events. Additional scatters that occur in the non-perturbative regime are also included, see Refs. [6, 63] for more details.

- **Hadronization**: The parton-shower evolution of particles involved in the hard process and additional scatters terminates at an IR cutoff scale, typically taken

to be $\mathcal{O}(1)$ GeV. At this scale, the formation of hadrons from colour connected systems of partons is simulated in a process known as hadronization. This process cannot be described perturbatively and so a phenomenological model containing a number of universal parameters is used. The values of these parameters are tuned by comparing the results of Monte Carlo simulations to experimental data. In Herwig++, the particular hadronization model used is the cluster model, as described in Ref. [64]. Motivated by colour preconfinement, colour connected partons present at the end of the parton shower are formed into colour-singlet clusters. These clusters have a universal mass distribution typically peaked around a few GeV. As such, they are too massive to correspond directly to one of the known hadrons, but are assumed instead to decay into pairs of hadrons.

- **Hadron decays**: Finally, hadrons produced during the hadronization stage of the event are not necessarily stable on collider timescales and therefore their decays into stable particles must be simulated. The decays of unstable colourless fundamental particles, such as the τ lepton[21], are also simulated at this stage. The treatment of hadron and tau decays is described for Herwig++ in Refs. [6, 65]. Decays are simulated using experimentally measured branching ratios and matrix-element descriptions of the distributions of the decay products. Spin correlations between the different decays are included where possible and in particular are treated consistently for τ lepton decays.

1.3.2 Parton showers

In Monte Carlo event generation, the hard scattering process is simulated using fixed-order matrix elements, typically at leading or next-to-leading order. Given the complexity involved in calculating these matrix elements, the addition of further terms in the perturbative expansion is not an efficient method for including

[21]The decay of colourless SUSY particles is handled prior to the parton shower, alongside the decays of coloured fundamental particles. This allows for the correct treatment of any coloured particles produced during the decay.

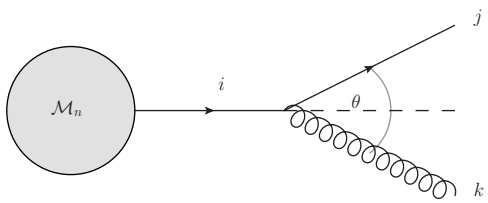

Figure 1.2: Branching of the quark i into a collinear gluon k and the final-state quark j.

important higher-order contributions. Higher-order corrections due to additional emissions are formally suppressed by factors of the strong coupling constant, however, there exist kinematic configurations for which this suppression is overcome by a logarithmic enhancement of the cross section. These contributions must be resummed to all orders in perturbation theory so as to obtain reliable predictions when considering anything other than the most inclusive observables. In Monte Carlo event generators, this resummation is performed by the parton-shower stage of the event, which will be the subject of the following section.

The all-order resummation of exact higher-order corrections is not possible and so an approximation is used that is accurate in the enhanced regions of phase space only. We begin by discussing the origin of this so-called parton-shower approximation in the context of collinear emissions. The formulation of the parton shower in terms of an iterative algorithm and the treatment of soft singularities will then be outlined briefly. Finally, Herwig++ specific details about the starting scale of the parton shower and kinematic reconstruction procedure will be given. These will be relevant to discussions appearing in later chapters.

Collinear emissions and the parton-shower approximation

For processes in which a final-state quark emits a gluon, as illustrated in Figure 1.2, the matrix element contains a propagator factor

$$\frac{1}{(p_j + p_k)^2 - m_j^2} = \frac{1}{2z(1-z)E_i^2(1 - v\cos\theta)}, \tag{1.3.16}$$

where p_i and p_j are the momenta of the quark before and after the branching, p_k is the momentum of the emitted gluon and m_j the mass of the quark. The energy carried by the splitting parton, E_i, is divided between the quark and gluon according to $E_j \simeq zE_i$ and $E_k \simeq (1-z)E_i$. The velocity of the final-state quark is $v = |\vec{p}_j|/E_j$, while θ is the angle between the final-state quark-gluon pair. The form of this propagator illustrates the divergent nature of the matrix elements of such processes. Singularities occur in two distinct kinematic regions: the soft limit in which the energy fraction of the gluon is small (*i.e.* $z \to 1$) and, for $m_j = 0$, the collinear limit in which $\theta \to 0$. As was discussed in Section 1.2.2, when considering infrared-safe observables these soft and collinear singularities cancel with those arising from virtual corrections. However, for some observables large-logarithmic terms will remain after the cancellation has taken place. The purpose of the parton shower is to resum such logarithms to all orders in perturbation theory.

To introduce the parton-shower algorithm with which this resummation is performed, we begin by considering logarithms arising from collinear branchings only. The effects of soft singularities will be incorporated later. In the collinear limit, the squared matrix element for the process shown in Figure 1.2, with massless quarks, is

$$|\bar{\mathcal{M}}_{n+1}|^2 = \frac{8\pi\alpha_s}{t} C_F \frac{1+z^2}{1-z} |\bar{\mathcal{M}}_n|^2, \tag{1.3.17}$$

where $t = p_i^2$ is the mass of the off-shell splitting quark, C_F is the Casimir of the fundamental representation of SU(3) and we have summed over the spins of the final-state particles. The n body process before gluon emission is described by the squared matrix element $|\bar{\mathcal{M}}_n|^2$, where summation over the spins of the final-state particles has again been performed. The colour factor and z-dependence of Eq. 1.3.17 define a universal unregularized Altarelli-Parisi splitting function, $P_{q\to qg}(z)$. The splitting functions for Standard Model branchings in the massless limit are given by

$$\begin{aligned} P_{q\to qg}(z) &= C_F \frac{1+z^2}{1-z}, \\ P_{g\to q\bar{q}}(z) &= T_R(z^2 + (1-z)^2), \\ P_{g\to gg}(z) &= C_A \left[\frac{z}{1-z} + \frac{1-z}{z} + z(1-z) \right], \end{aligned} \tag{1.3.18}$$

where T_R and C_A are the trace and Casimir invariants in the fundamental and

adjoint representations of SU(3) respectively[22]. Finally, the $n+1$ body phase space also factorizes such that the cross section for the process shown in Figure 1.2 is

$$d\sigma_{n+1} \approx d\sigma_n \frac{\alpha_s}{2\pi} \frac{dt}{t} \hat{P}_{q\to qg}(z) dz, \tag{1.3.19}$$

where $\hat{P}_{q\to qg}$ is now the splitting function after averaging over the azimuthal angle of the emitted parton[23]. From Eq. 1.3.19, we see that the cross section for processes involving a collinear emission factorizes into the cross section for the process with no splitting and a universal function describing the emission.

The above picture may be easily extended to the case with multiple coloured particles in the hard process, for example the process $e^+e^- \to q\bar{q}$. The interference between contributions in which a gluon is emitted from either the quark or antiquark is negligible in the collinear limit. As such, Eq. 1.3.19 is simply modified to now include a sum of universal splitting functions, each one of which describes an emission from a different particle in the hard process. This allows the evolution of different particles to be treated independently.

The Altarelli-Parisi splitting functions can be used as the building blocks of an iterative algorithm. The final state shown in Figure 1.2, *i.e.* after a single collinear emission, is treated as the new hard process from which a second collinear splitting can be generated. The emissions are ordered in terms of an evolution variable, in this case the virtuality of the emitting parton, t, that decreases with each subsequent emission. Any variable k that satisfies $\frac{dt}{t} = \frac{dk}{k}$ may be used, and common alternatives to the virtuality are the transverse momentum of the emitted parton or the angle between the branched pair of partons.

To construct the parton-shower algorithm, a more probabilistic interpretation of the splitting functions is necessary. As such, we may express the probability of a

[22]The splitting functions applicable to the case of massive partons and additional branchings possible in SUSY processes can be found, for example, in Ref. [6].

[23]In general, the splitting functions do depend on the azimuthal angle of the emitted parton and these angular correlations are accounted for in the Herwig++ parton-shower algorithm. However, for simplicity they are neglected in this discussion.

parton i undergoing a branching in the infinitesimal range t to $t + dt$ as

$$d\mathcal{P} = \frac{\alpha_s}{2\pi}\frac{dt}{t}\int_{\sqrt{t^{\min}/t}}^{1-\sqrt{t^{\min}/t}} \sum_{j,k} \hat{P}_{i\to jk}(z)dz, \tag{1.3.20}$$

where all possible splittings $i \to jk$ are summed. In order to produce physically meaningful distributions it has been necessary to impose a resolution criterion that limits the transverse momenta of emissions to be greater than an IR cutoff, $p_T^{\min}$, typically chosen to be $\mathcal{O}(1\,\text{GeV})$. This is motivated by the observation that a pair of exactly collinear partons is experimentally indistinguishable from the single parent parton before splitting. This limit on the transverse momentum translates into a lower bound on the evolution variable, $t^{\min}$, which defines the scale at which the parton-shower evolution terminates and non-perturbative effects are considered to be significant. The resolution criterion also restricts the z integration range such that the integral in Eq. 1.3.20 is finite.

While Eq. 1.3.20 expresses the probability of producing a resolvable emission, the probability of producing no resolvable emission in the range t to $t + dt$ may be constrained through unitarity to be $(1 - d\mathcal{P})$. This encapsulates both contributions arising from unresolvable emissions with $p_T < p_T^{\min}$, and those from enhanced virtual corrections. Extending this non-emission probability to a finite range of the evolution variable, we obtain the Sudakov form factor

$$\Delta(t_1, t_2) = \exp\left(-\int_{t_2}^{t_1} \frac{\alpha_s}{2\pi}\frac{dt}{t}\int_{\sqrt{t^{\min}/t}}^{1-\sqrt{t^{\min}/t}} \sum_{j,k} \hat{P}_{i\to jk}(z)dz\right). \tag{1.3.21}$$

This expresses the probability of parton i evolving from a high scale, t_1, to a low scale, t_2, without producing a resolvable emission.

Monte Carlo implementation

Using the Sudakov form factor introduced in Eq. 1.3.21, it is possible to construct a simple parton-shower algorithm as follows. Working separately for each coloured particle produced in the hard process, collinear emissions are generated by solving,

for t_1, the equality[24]

$$\Delta(t^{\max}, t_1) = \mathcal{R}. \tag{1.3.22}$$

Here $\mathcal{R}$ is a pseudo-random number uniformly distributed in the range $[0, 1]$ and $t^{\max}$ is the starting scale of the parton shower. Any emission not satisfying $t_1 > t^{\min}$ is discarded. Additional random numbers are then used to generate a value of z according to the splitting function and a value of the azimuthal angle, ϕ, which is uniformly distributed in the range $[0, 2\pi]$. For each parton produced in the branching, the process is repeated with the starting scale of the shower replaced by the scale of the previous splitting, *i.e.* using $\Delta(t_1, t_2)$ and solving for t_2. This evolution continues for each parton independently, until the scale drops below the cutoff value $t^{\min}$.

The above process is sufficient when describing emissions generated from final-state particles. However in the case of initial-state branchings, a modified algorithm is required. In Monte Carlo event generators, the hard process is generated first therefore fixing the flavour and momenta of the initial-state partons involved. A parton shower based on the algorithm used for final-state particles would extract a parton from the colliding hadron and run a forward evolution towards the hard process. As such, the partons at the end of the shower evolution would typically not have flavour and momentum matching those required by the hard process. This would result in a highly inefficient procedure. Instead, the initial-state shower evolution is effectively performed backwards, starting from the partons involved in the hard process and evolving them back to partons extracted from the colliding hadrons. As such, the backwards evolution is generated using the modified Sudakov form factor

$$\Delta(t_1, t_2) = \exp\left(- \int_{t_2}^{t_1} \frac{\alpha_s}{2\pi} \frac{dt}{t} \int_{\sqrt{t^{\min}/t}}^{1-\sqrt{t^{\min}/t}} \sum_{j,k} \hat{P}_{i\to jk}(z) \frac{x/z f_j^h(x/z, t)}{x f_i^h(x, t)} dz \right). \tag{1.3.23}$$

The ratio of the PDFs in Eq. 1.3.23 ensures that unphysical values of the momentum fraction x are avoided. Finally if an initial-state emission is generated, the

[24]Typically, Eq. 1.3.22 is not analytically tractable. To overcome this, radiation is instead generated using a simple overestimated branching probability for which the analog to Eq. 1.3.22 can be easily solved. The correct branching probability is then restored using the veto algorithm, a good description of which may be found in Ref. [66].

corresponding value of z is now determined using $x/z f_j(x/z, t)\hat{P}_{i\to jk}(z)$.

Soft singularities

The parton-shower algorithm described in the previous section can be used to resum the leading logarithms associated with collinear branchings. However, soft emissions give rise to an additional class of enhanced contributions that must also be resummed. In the Herwig++ event generator, this is done through angular ordering of the parton-shower emissions, exploiting the properties of QCD coherence [67,68], as will be outlined in this section.

In the soft limit, the matrix element describing a process with an additional emission factorizes into a universal eikonal function and the matrix element for the process with no soft emission. However, the interference between different matrix elements contributing to the soft emission process is such that this factorization does not persist beyond the level of the matrix element. At the level of the cross section, the factor accounting for the soft emission depends on the momenta of all the external particles. Therefore, the soft emission cannot be viewed as having been emitted from any given particle, but rather as having come from the scattering process as a whole. This prohibits the treatment of emissions from different particles as independent processes, something that is vital to the parton-shower algorithm.

However, the picture of independent evolution can be restored by making use of colour coherence. To illustrate this phenomenon, consider the example of a quark radiating a relatively hard and collinear gluon, as shown in Figure 1.2. The probability of a subsequent soft gluon being radiated from this process has contributions arising from emissions from either the collinear gluon or the final-state quark. If the soft gluon is emitted at an angle wider than that associated with the collinear branching[25], interference between the two contributions is largely destructive. Neglecting colour suppressed terms, the combined contribution of emissions from each of the collinear pair of partons is equivalent to the contribution corresponding to the

[25] *i.e.* at an angle larger than the opening angle between the emitting member of the collinear pair and its colour connected partner. For emissions from the collinear gluon, the assignment of a colour partner is not unique. This will be discussed in more detail in the next section.

soft gluon being emitted by the branching parent quark (*i.e.* quark i in Figure 1.2). Schematically, a wide-angle soft gluon cannot resolve the individual partons in the collinear pair and so is sensitive only to the sum of their colour charges, *i.e.* the colour charge of the parent quark. Therefore, it can effectively be viewed as having branched from the parent quark, before the collinear emission. As such, soft enhancements can be incorporated into a collinear parton-shower algorithm simply by ordering the parton-shower emissions in terms of the opening angle of the splittings, giving rise to an angular-ordered parton-shower algorithm.

By employing the angular-ordered prescription, the Herwig++ parton shower resums leading collinear and leading-colour soft logarithms. A further class of universal higher-order corrections may also be incorporated in the parton shower through the choice of renormalization scale. By using the transverse momentum of the emission as the argument of the strong coupling constant during the parton-shower evolution, these subleading but phenomenologically important logarithms are resummed to all orders [69]. Whilst technically a higher-order consideration, this choice of scale in the running coupling has a significant impact of the multiplication rate of partons in the shower and cluster mass distributions arising during hadronization.

Starting scale of the parton shower

A component missing from the parton-shower prescription detailed so far is the starting value of the shower-evolution variable. As was discussed in the previous section, enhanced contributions due to soft emissions are taken into account in Herwig++ by ordering radiation in terms of a decreasing angular variable. Each branching must occur at a lower value of the angular variable than the one associated with the opening angle of the emitting parton and its colour connected partner. As such, the maximum allowed value of the angular variable depends on the colour flow in the hard process. The colour flow is determined in the large N_c limit[26] by associating a (anti)colour line to each particle that transforms under the (anti)fundamental representation of SU(3) and a pair of lines, one with colour and one with anticolour, to

[26]Here N_c represents the number of colours.

particles transforming under the adjoint representation. As such, quarks involved in the hard process have only one possible colour connected partner, while for gluons a choice must be made between the partners connected via the colour and anticolour lines. For correct treatment of colour factors in the splitting functions, the gluon partner is chosen at random with an equal probability of selecting each of the two possibilities.

Having assigned colour partners, the starting scale of the shower evolution variable is determined for each colour connected pair using the prescription detailed in Ref. [70], taking into account whether the particles are in the initial or final state. Radiation from each member of the pair is constrained to populate a distinct region of phase space. The regions are required to be non-overlapping and to meet smoothly in the soft limit. By doing so, the full soft region of phase space is populated and no double counting of radiation occurs. Some ambiguity exists in how this division of phase space is performed, but in all cases, in addition to the regions populated by emissions from each of the colour connected pair, there will typically be some region of phase space which is completely unpopulated by the parton shower. The presence of this region, known as the dead zone, will be illustrated explicitly in Chapter 2. The phase space within the dead zone corresponds to (relatively) hard emissions, *i.e.* those which are neither soft nor collinear.

An additional constraint on the transverse momentum of emissions is also imposed by default in the Herwig++ angular-ordered shower. Shower emissions must have transverse momentum below some upper value, $p_T^{\max}$, which depends on the nature of the hard process. For hard scatterings that produce coloured particles, the minimum transverse mass[27] of all the final-state coloured particles is used. In the case that no coloured particles exist in the final state, $p_T^{\max}$ is set equal to the invariant mass of the colour-singlet system. Alternatively, the option exists in Herwig++ to set $p_T^{\max}$ equal to the factorization scale of the hard process. Finally for parton showers initiated from particle decays, the maximum transverse momentum is equal to the mass of the decaying particle. The limit on the transverse momentum

[27]The transverse mass is defined as $m_T = \sqrt{m^2 + p_T^2}$.

of emissions is necessary to ensure no double counting of configurations[28] and to restrict the application of the parton-shower approximation to the regions of phase space in which it is valid.

Kinematic reconstruction

After the parton-shower evolution has terminated, the momenta of all particles involved are calculated from the values of the shower variables generated at each splitting. Particles produced in the final branching step of the shower are constrained to be on their constituent mass shells such that partons involved in the hard process develop a virtual mass. The momenta of all final-state progenitors[29] and their subsequent emissions are then rescaled by a common factor that is determined by requiring the total centre-of-mass energy of the system to be unchanged by the parton shower. A similar rescaling procedure is used for initial-state progenitors, where now different kinematic quantities are preserved based on whether the colour connected partner to the progenitor is in the initial or final state. Further details of this process can be found in Ref. [6].

When an external matrix-element generator is interfaced to the angular-ordered parton shower in Herwig++, care must be taken with regards to the kinematic reconstruction if the simulation of the hard scattering process involves higher-order corrections. In this case, the additional parton in real-emission configurations generated by the external matrix-element generator will always be interpreted in the parton-shower algorithm as a final-state emission. However, the final-state kinematic reconstruction procedure gives unphysical results when applied to hard process final states containing two massive particles and a hard additional parton that actually originated from initial-state radiation. In this case, the massive particles

[28] A very hard parton-shower emission would cause significant recoil of the hard process such that particles involved in the hard process would be boosted to higher transverse momenta. This is indistinguishable from a hard process with high transverse momentum particles from which a softer emission is produced.

[29] The term progenitor is used to refer to any particle (be it in the hard process, subsequent decays of unstable particles or additional scatterings) that initiates a parton shower.

produce only a small amount of radiation, while the additional parton can build up a considerable virtual mass. By rescaling the momenta of all final-state progenitors democratically, the energies of the massive particles can be significantly decreased, giving rise to unphysical distributions. This phenomenon was pointed out in Ref. [71] for the case of top quark pair production. To account for this, an alternative final-state kinematic reconstruction procedure is available in the Herwig++ shower. In this scheme, the momenta of the progenitor with the largest virtual mass and the combined system of all other progenitors are rescaled by a common factor to restore energy conservation. Then working in the rest frame of the combined system, the momenta of the remaining progenitors are rescaled to preserve the total energy of the system in this frame. In this way, the invariant mass of the combined system of progenitors is preserved. The effect of the different choices of kinematic reconstruction procedure will be investigated for the case of stop-antistop production in Chapter 3.

1.4 Combining higher-order matrix elements and parton showers

Monte Carlo event generators provide a link between theoretical models and experimental signatures. As such, it is important that the simulation is performed with the highest possible accuracy so that results correctly reflect the underlying physics. The parton-shower algorithm, by which additional QCD radiation is produced, makes use of an approximation which is valid only in the soft and collinear regions of phase space. Consequently, the production of hard radiation is not accurately described by the parton shower. This can pose a problem, for example, in searches for BSM scenarios where often the event selection criteria require the presence of hard jets in each event. In particular, signal predictions in monojet based compressed spectra SUSY searches, introduced in Section 1.1.4, are highly sensitive to the way in which hard parton-shower radiation is generated. The parton shower alone cannot be relied upon to produce sufficiently accurate predictions in this case.

In recent years, improving the simulation of hard radiation within Monte Carlo

event generators has been the subject of extensive work. Currently, two main techniques are available - matrix-element merging and matrix-element matching. In the former, matrix-element level event samples are generated in which the final-state particles in the hard process are produced together with differing numbers of additional partons, j. That is, in addition to generating the hard process $pp \to X$, the processes $pp \to X + (1, 2, ..., i, ..., n)j \ \forall \ i \leq n$ are also simulated at fixed order. The event samples are then merged with the parton shower so that multiple hard emissions in each event are now described using fixed-order matrix elements, not the parton-shower splitting kernels. Several prescriptions exist for performing this merging procedure, see for example Refs. [72–75], which each ensure that no double counting of radiation takes place.

In this work, we focus exclusively on the latter technique of matrix-element matching. In this approach, the real-emission contribution to the NLO matrix element of the hard process is used to generate the hardest extra parton in each event. The resulting configuration is then matched to the parton-shower stage of the event to simulate additional softer radiation in such a way that double counting of emissions is avoided. In some prescriptions, a further modification is also made which ensures that the Born configuration is simulated with NLO accuracy. Multiple formalisms exist for performing matrix-element matching. We will mention briefly the MC@NLO approach [76, 77] and the phase-space slicing technique previously implemented in Herwig++ [78], but focus predominantly on the POsitive Weight Hardest Emission Generator or POWHEG approach suggested in Ref. [5]. We will use this formalism to implement a POWHEG inspired matrix-element correction in which the description of both the hardest parton-shower emission and the Born process are accurate to LO.

In this section, we begin by considering the combination of LO matrix elements with the parton shower in Section 1.4.1, before extending the prescription to NLO matrix-element matching in Section 1.4.2. Having done so, details of the POWHEG formalism will be given in Section 1.4.3, along with a brief outline of the MC@NLO prescription. This will be followed in Section 1.4.4 by an introduction to the POWHEG style matrix-element corrections relevant to this work, and a short

review of the phase-space slicing approach which has previously been used to implement ME corrections in Herwig++. Finally, details specific to the application of the POWHEG formalism to angular-ordered parton showers will be given in Section 1.4.5. A more in-depth description of the POWHEG formalism can be found, for example, in Ref. [79].

1.4.1 Combining LO matrix elements and parton showers

Before discussing the matching of NLO calculations with a Monte Carlo parton shower, it is instructive to first consider the action of the parton shower on a LO calculation. To this end, we consider an generic infrared-safe observable $\mathcal{O}$. The expectation value of the observable is

$$\langle \mathcal{O} \rangle = \int d\Phi_n \mathcal{B}(\Phi_n) \left[\Delta(p_T^{\max}, p_T^{\min}) \mathcal{O}(\Phi_n) + \int_{p_T^{\min}}^{p_T^{\max}} d\mathcal{P}(p_T) \Delta(p_T^{\max}, p_T) \mathcal{O}(\Phi_{n+1}) \right], \tag{1.4.24}$$

where only the first parton-shower splitting has been included. Here we are considering a parton shower ordered in terms of the transverse momentum of the emitted parton, p_T. The Born matrix element squared, including the relevant flux and parton luminosity factors[30], is represented by $\mathcal{B}(\Phi_n)$. The phase space of the $2 \to n$ LO process is represented by Φ_n, while Φ_{n+1} is the configuration after an emission from the Born process. More concretely, we define

$$d\Phi_n = \frac{dx_a}{x_a} \frac{dx_b}{x_b} (2\pi)^4 \delta^4 \left(x_a P_a + x_b P_b - \sum_{i=1}^{n} p_i \right) \prod_{i=1}^{n} \frac{d^3 \vec{p}_i}{2E_i (2\pi)^3}, \tag{1.4.25}$$

where x_a and x_b are the momentum fractions of the incoming partons, P_a and P_b are the momenta of the incoming hadrons and $p_i = (E_i, \vec{p}_i)$ is the momentum of the outgoing particle i. In general, the $n+1$ body phase space will depend on the splitting channel through which the emission took place, however the splitting channel index has been suppressed in the following discussion for the sake of clarity. Furthermore, in the following we abbreviate $\mathcal{O}(\Phi_n)$ to $\mathcal{O}_n$. In the notation of Eq. 1.4.24, the

[30] The parton luminosity is defined as $\mathcal{L} = x_a f_a^{h_1}(x_a, \mu) x_b f_b^{h_2}(x_b, \mu)$, where $f^h(x, \mu)$ is the PDF of hadron h, as introduced in Section 1.2.1.

Sudakov form factor for the parton shower is[31]

$$\Delta(p_T^{\max}, p_T) = \exp\left(-\int_{p_T}^{p_T^{\max}} d\mathcal{P}(\tilde{p_T})\right). \tag{1.4.26}$$

The first term in Eq. 1.4.24 represents the case in which no radiation is generated by the parton shower above the IR cutoff scale, while the second term is the scenario where an emission is produced at a scale p_T. On continuing the parton-shower evolution, terms describing the production of multiple emissions would also be present. Observables that are insensitive to the additional radiation produced by the parton shower, *i.e.* those for which $\mathcal{O}_n = \mathcal{O}_{n+1}$ throughout phase space, are predicted with LO accuracy and the square bracket in Eq. 1.4.24 integrates to one. As such, the parton shower does not effect the total cross section of the hard scattering. This property is referred to as the unitarity of the parton shower. Observables which are sensitive to the hardest parton-shower emission are predicted with the accuracy of the parton-shower splitting kernels, *i.e.* leading-logarithmic accuracy.

1.4.2 Combining NLO matrix elements and parton showers

In the most naïve combination of an NLO cross section with the parton shower, one finds that the prediction for the observable $\mathcal{O}$ is

$$\begin{aligned}\langle\mathcal{O}\rangle = &\int d\Phi_n \left[\mathcal{B}\left(\Phi_n\right)+\mathcal{V}\left(\Phi_n\right)\right]\left[\Delta\left(p_T^{\max}, p_T^{\min}\right)\mathcal{O}_n + \int_{p_T^{\min}}^{p_T^{\max}} d\mathcal{P}(p_T)\Delta\left(p_T^{\max}, p_T\right)\mathcal{O}_{n+1}\right] \\ &+ \int d\Phi_{n+1}\left[\mathcal{R}(\Phi_{n+1})\mathcal{O}_{n+1} - \mathcal{C}(\Phi_{n+1})\mathcal{O}_n\right],\end{aligned} \tag{1.4.27}$$

where again we consider a shower ordered in terms of the transverse momentum of the emissions and only the splitting giving rise to the hardest emission has been considered. Here the subtraction term required to render the virtual contribution

[31] In relation to the notation used for final-state emissions in Section 1.3.2, the exponent $d\mathcal{P}(p_T)$, referred to in the following as as the parton-shower splitting kernel, is $d\mathcal{P}(p_T) = \frac{\alpha_s}{2\pi}\frac{dp_T^2}{p_T^2}\int dz \sum_i \hat{P}_i(z)$. When applied to initial-state emissions, an additional factor of $\frac{\mathcal{L}_{n+1}}{\mathcal{L}_n}$ is present in the splitting kernel, where $\mathcal{L}_n$ ($\mathcal{L}_{n+1}$) is the parton luminosity before (after) the splitting.

finite is included in $\mathcal{V}(\Phi_n)$ implicitly. Note that no showering of the real-emission contribution is necessary since we are concerned with the generation of at most one emission. Expanding this expression to $\mathcal{O}(\alpha_s^{k+1})$, where k is the order in α_S of the Born process, gives

$$\begin{aligned}\langle\mathcal{O}\rangle = &\int d\Phi_n \left[\mathcal{B}(\Phi_n) + \mathcal{V}(\Phi_n)\right]\mathcal{O}_n + \int d\Phi_n \mathcal{B}(\Phi_n) \int_{p_T^{\min}}^{p_T^{\max}} d\mathcal{P}(p_T)\left[\mathcal{O}_{n+1} - \mathcal{O}_n\right] \\ &+ \int d\Phi_{n+1}\left[\mathcal{R}(\Phi_{n+1})\mathcal{O}_{n+1} - \mathcal{C}(\Phi_{n+1})\mathcal{O}_n\right].\end{aligned} \tag{1.4.28}$$

The contributions relating to the parton-shower splitting kernel are problematic. The term $\mathcal{B}(\Phi_n)d\mathcal{P}(p_T)\mathcal{O}_{n+1}$ corresponds to a resolvable emission generated by the parton shower which is already accounted for by the real-emission contribution to the prediction, $\mathcal{R}(\Phi_{n+1})\mathcal{O}_{n+1}$. Furthermore, the expansion of the Sudakov form factor $\Delta\left(p_T^{\max}, p_T^{\min}\right)$ in Eq. 1.4.27 gives rise to the spurious term $\mathcal{B}(\Phi_n)d\mathcal{P}(p_T)\mathcal{O}_n$ which leads to double counting of virtual contributions.

In addition to the double counting, another issue is present in Eq. 1.4.27. The subtraction term appearing on the second line of the equation must contribute towards the prediction for the observable for n parton configurations so that it exactly cancels the subtraction term that has been absorbed into the virtual contribution. This means that the combination of terms contributing to $\mathcal{O}_{n+1}$ and $\mathcal{O}_n$ are not separately finite.

Taking into account both issues, consistent matching of the NLO matrix element and parton shower can be obtained by beginning the parton-shower evolution from the modified cross section[32]

$$\begin{aligned}d\sigma_{\text{mod}}^{\text{NLO}} = &\left[\mathcal{B}(\Phi_n) + \mathcal{V}(\Phi_n) + \mathcal{B}(\Phi_n)\int_{p_T^{\min}}^{p_T^{\max}} d\mathcal{P}(p_T)\right] d\Phi_n \\ &- \mathcal{B}(\Phi_n)d\mathcal{P}(p_T)d\Phi_n + \left[\mathcal{R}(\Phi_{n+1}) - \mathcal{C}(\Phi_{n+1})\right] d\Phi_{n+1},\end{aligned} \tag{1.4.29}$$

[32]Note that the third term on the first line and first term on the second line of Eq. 1.4.29 contribute to the n and $n+1$ body configurations respectively, since no integration over the radiative phase-space variables is included for the latter term.

and including an additional bridging contribution to the expectation value of the observable

$$\int d\Phi_{n+1}\mathcal{R}(\Phi_{n+1})\left[\mathcal{O}_n - \mathcal{O}_{n+1}\right]\Theta(p_T^{\min} - p_T). \tag{1.4.30}$$

For infrared-safe observables, the contribution in Eq. 1.4.30 does not effect the NLO accuracy of predictions that are insensitive to additional radiation or the resummation properties of the parton shower [80].

After these modifications have been made, the expectation value of the observable $\mathcal{O}$ becomes

$$\begin{aligned}\langle\mathcal{O}\rangle^{\text{matched}} = &\int d\Phi_n\bar{\mathcal{B}}\left(\Phi_n\right)\left[\Delta\left(p_T^{\max}, p_T^{\min}\right)\mathcal{O}_n + \int_{p_T^{\min}}^{p_T^{\max}} d\mathcal{P}(p_T)\Delta\left(p_T^{\max}, p_T\right)\mathcal{O}_{n+1}\right] \\ &+\left[\int d\Phi_{n+1}\mathcal{R}\left(\Phi_{n+1}\right)\Theta(p_T - p_T^{\min}) - \int d\Phi_n\mathcal{B}(\Phi_n)\int_{p_T^{\min}}^{p_T^{\max}} d\mathcal{P}(p_T)\right]\mathcal{O}_{n+1} \\ &+\int d\Phi_{n+1}\left[\mathcal{R}\left(\Phi_{n+1}\right)\Theta(p_T^{\min} - p_T) - \mathcal{C}\left(\Phi_{n+1}\right)\right]\mathcal{O}_n,\end{aligned} \tag{1.4.31}$$

where

$$\bar{\mathcal{B}}\left(\Phi_n\right) = \mathcal{B}\left(\Phi_n\right) + \mathcal{V}\left(\Phi_n\right) + \mathcal{B}(\Phi_n)\int_{p_T^{\min}}^{p_T^{\max}} d\mathcal{P}(p_T). \tag{1.4.32}$$

Up to $\mathcal{O}(\alpha_s^{k+2})$ corrections, the third line in Eq. 1.4.31 may be absorbed into the prefactor so that now

$$\begin{aligned}\bar{\mathcal{B}}\left(\Phi_n\right) = &\mathcal{B}\left(\Phi_n\right) + \mathcal{V}\left(\Phi_n\right) + \mathcal{B}(\Phi_n)\int_{p_T^{\min}}^{p_T^{\max}} d\mathcal{P}(p_T) \\ &+\int d\Phi_R\left[\mathcal{R}\left(\Phi_{n+1}\right)\Theta(p_T^{\min} - p_T) - \mathcal{C}\left(\Phi_{n+1}\right)\right],\end{aligned} \tag{1.4.33}$$

where the radiation variables of the additional emitted parton, Φ_R, have be factorized such that $d\Phi_{n+1} = d\Phi_n d\Phi_R$.

1.4.3 The POWHEG formalism

In the POWHEG matching prescription, the ratio of the differential real-emission and Born-level cross sections[33] is used as the parton-shower splitting kernel during the

[33]In practice, the real-emission and Born cross sections in the ratio are stripped of their respective factors of α_s. A single factor of α_s, evaluated at the transverse momentum scale of the

generation of the hardest emission, *i.e.*

$$\int_{p_T^{\min}}^{p_T^{\max}} d\mathcal{P}(p_T) = \int d\Phi_R \frac{\mathcal{R}\left(\Phi_{n+1}\right)}{\mathcal{B}\left(\Phi_n\right)} \Theta(p_T - p_T^{\min}). \tag{1.4.34}$$

In the right-hand side of Eq. 1.4.34, the radiative phase space of the additional emitted parton is limited to emissions with transverse momenta greater than $p_T^{\min}$ by the inclusion of the function $\Theta(p_T - p_T^{\min})$. In the following, this Heaviside function will be translated into explicit limits on the phase-space integral without rewriting $d\Phi_R$ in terms of the transverse momentum of the emission.

Making the substitution in Eq. 1.4.34 leads to considerable simplification of the approach detailed in Section 1.4.2, such that the expectation value of $\mathcal{O}$ is now

$$\begin{aligned} \langle \mathcal{O} \rangle^{\text{POWHEG}} = \int d\Phi_n \bar{\mathcal{B}}\left(\Phi_n\right) \Bigg[& \Delta\left(p_T^{\max}, p_T^{\min}\right) \mathcal{O}_n \\ & + \int_{p_T^{\min}}^{p_T^{\max}} d\Phi_R \frac{\mathcal{R}\left(\Phi_{n+1}\right)}{\mathcal{B}\left(\Phi_n\right)} \Delta\left(p_T^{\max}, p_T\right) \mathcal{O}_{n+1} \Bigg], \end{aligned} \tag{1.4.35}$$

where

$$\bar{\mathcal{B}}\left(\Phi_n\right) = \mathcal{B}\left(\Phi_n\right) + \mathcal{V}\left(\Phi_n\right) + \int d\Phi_R \left[\mathcal{R}\left(\Phi_{n+1}\right) - \mathcal{C}\left(\Phi_{n+1}\right)\right]. \tag{1.4.36}$$

As such, the total cross section and suitably inclusive observables are generated with NLO accuracy, while the hardest shower emission is distributed with LO accuracy.

The Sudakov form factor, $\Delta(p_T^{\max}, p_T)$, used to generate the hardest emission in the POWHEG formalism is given by

$$\Delta(p_T^{\max}, p_T) = \exp\left(- \int_{p_T}^{p_T^{\max}} d\Phi_R \frac{\mathcal{R}(\Phi_{n+1})}{\mathcal{B}(\Phi_n)} \right). \tag{1.4.37}$$

In practice, Eq. 1.4.37 is modified to include dipole functions, $\mathcal{D}_i$, thus allowing the singular behaviour of the real-emission matrix element in different phase-space regions to be isolated. Eq. 1.4.37 becomes a product of Sudakov form factors,

$$\Delta(p_T^{\max}, p_T) = \prod_i \exp\left(- \int_{p_T}^{p_T^{\max}} d\Phi_R \frac{\mathcal{D}_i}{\sum_j \mathcal{D}_j} \frac{\mathcal{R}(\Phi_{n+1})}{\mathcal{B}(\Phi_n)} \right). \tag{1.4.38}$$

emission, is then included in the numerator of the splitting kernel. This allows for resummation of phenomenologically important but subleading corrections as discussed in Section 1.3.2.

As discussed in Section 1.2.2, each dipole function approximates the behaviour of the real-emission matrix element in some singular limit, *i.e.* when the emitted parton becomes soft or collinear to one of the particles in the Born process. An emission can be simulated according to Eq. 1.4.38 by generating a value of p_T for each form factor in the product using the method described in Section 1.3.2. The form factor giving rise to the hardest emission is selected and the associated dipole then fixes the kinematic mapping between Φ_n and Φ_{n+1}.

Aside - The MC@NLO method

The original matrix-element matching prescription, dubbed MC@NLO [76, 77], can be derived in a similar way to the POWHEG formalism by instead taking the bridging contribution to be

$$\int d\Phi_{n+1}\mathcal{C}^{(A)}(\Phi_{n+1})\left[\mathcal{O}_n - \mathcal{O}_{n+1}\right]\Theta(p_T^{\min} - p_T), \tag{1.4.39}$$

and writing the parton-shower splitting kernels as

$$\mathcal{B}\left(\Phi_n\right)\int_{p_T^{\min}}^{p_T^{\max}} d\mathcal{P}(p_T) = \int d\Phi_R\mathcal{C}^{(A)}\left(\Phi_{n+1}\right)\Theta(p_T - p_T^{\min}). \tag{1.4.40}$$

Then, representing the subtraction term present in the NLO calculation now with $\mathcal{C}^{(S)}(\Phi_{n+1})$, the expectation value of the observable $\mathcal{O}$ becomes

$$\begin{aligned}\langle\mathcal{O}\rangle^{\text{MC@NLO}} = \int d\Phi_n\bar{\mathcal{B}}\left(\Phi_n\right)\Bigg[&\Delta\left(p_T^{\max}, p_T^{\min}\right)\mathcal{O}_n \\ &+ \int_{p_T^{\min}}^{p_T^{\max}} d\Phi_R\frac{\mathcal{C}^{(A)}\left(\Phi_{n+1}\right)}{\mathcal{B}\left(\Phi_n\right)}\Delta\left(p_T^{\max}, p_T\right)\mathcal{O}_{n+1}\Bigg] \\ &+ \int d\Phi_{n+1}\left[\mathcal{R}\left(\Phi_{n+1}\right) - \mathcal{C}^{(A)}(\Phi_{n+1})\right]\mathcal{O}_{n+1},\end{aligned} \tag{1.4.41}$$

where

$$\bar{\mathcal{B}}\left(\Phi_n\right) = \mathcal{B}\left(\Phi_n\right) + \mathcal{V}\left(\Phi_n\right) + \int d\Phi_R\left[\mathcal{C}^{(A)}\left(\Phi_{n+1}\right) - \mathcal{C}^{(S)}\left(\Phi_{n+1}\right)\right] \tag{1.4.42}$$

and

$$\Delta(p_T^{\max}, p_T) = \exp\left(-\int_{p_T}^{p_T^{\max}} d\Phi_R\frac{\mathcal{C}^{(A)}(\Phi_{n+1})}{\mathcal{B}(\Phi_n)}\right). \tag{1.4.43}$$

The first and second lines in Eq. 1.4.41 correspond to events originating from a Born-like n parton hard process, commonly referred to as shower or S-events. The real-emission like $n+1$ parton configurations generated by the terms on the third line are known as hard or H-events. The parton-shower splitting kernel $\mathcal{C}^{(A)}$ and NLO subtraction term $\mathcal{C}^{(S)}$ have the same phase-space factorization and may both be written in terms of a sum of dipole contributions. However, their functional form away from the singular limits may differ, and typically the parton-shower kernel will include a cutoff that limits the upper scale of the shower evolution variable. As such, the upper limits in the integration of the splitting kernels in Eqs. 1.4.41, 1.4.42 and 1.4.43 are reduced from $p_T^{\max}$ to some physically motivated choice of parton-shower starting scale, p_T^{hard}, which is typically similar to the factorization scale. By doing so, the resummation is limited to the region of phase space where the parton-shower approach is appropriate.

Finally, we note that the integrand in the third line of Eq. 1.4.41 is not guaranteed to be positive. The weights of H-events can become negative if the parton-shower approximation of the real-emission term exceeds the true value. While the presence of negative weights affects the efficiency of the Monte Carlo simulation, typically these contributions do not lead to an unacceptable reduction in performance.

Division of the real-emission phase space

In the original POWHEG formalism, the emission generated by the POWHEG correction must populate the entire radiative phase space in order to achieve LO accuracy for the hardest emission. As such, the starting scale of the parton-shower evolution is equal to the hadronic centre-of-mass energy, $p_T^{\max} = \sqrt{s}$, and the real-emission matrix element is exponentiated beyond the scale where the parton-shower approach is valid. Furthermore, observables sensitive to the real-emission configuration are enhanced by the artificial K-factor[34] $\bar{\mathcal{B}}(\Phi_n)/\mathcal{B}(\Phi_n)$ which, although formally an NNLO effect, is not guaranteed to be small[35].

[34]We use the term K-factor to refer to the ratio of the NLO to LO cross sections.

[35]See for example Ref. [81], where the resulting K-factor in Higgs boson production via gluon fusion was found to be approximately 2.

The unphysical choice of parton-shower starting scale can be corrected through the division of the real-emission matrix element into shower and hard components [5] according to

$$\mathcal{R}^S = f(p_T, p_T^{\max}, p_T^{\text{hard}})\mathcal{R} \quad \text{and} \quad \mathcal{R}^H = \mathcal{R} - \mathcal{R}^S, \tag{1.4.44}$$

where now the former is identified with the parton-shower splitting kernel. The function $f(p_T, p_T^{\max}, p_T^{\text{hard}})$ is designed such that it:

- vanishes for large values of p_T thus limiting the resummation scale of the parton shower to $\mathcal{O}(p_T^{\text{hard}})$;
- tends to unity in the soft/collinear limit such that $\mathcal{R}^s(\Phi_{n+1})$ encapsulates the full singular behaviour of the real-emission matrix element.

On performing the division of $\mathcal{R}$, Eq. 1.4.35 becomes

$$\begin{aligned}\langle\mathcal{O}\rangle^{\text{POWHEG}} = \int d\Phi_n \bar{\mathcal{B}}\left(\Phi_n\right) \Bigg[& \Delta\left(p_T^{\max}, p_T^{\min}\right)\mathcal{O}_n \\ & + \int_{p_T^{\min}}^{p_T^{\max}} d\Phi_R \frac{\mathcal{R}^S\left(\Phi_{n+1}\right)}{\mathcal{B}\left(\Phi_n\right)} \Delta\left(p_T^{\max}, p_T\right)\mathcal{O}_{n+1}\Bigg] \\ & + \int_{p_T^{\min}}^{p_T^{\max}} d\Phi_{n+1}\mathcal{R}^H\left(\Phi_{n+1}\right)\mathcal{O}_{n+1},\end{aligned} \tag{1.4.45}$$

where

$$\bar{\mathcal{B}}\left(\Phi_n\right) = \mathcal{B}\left(\Phi_n\right) + \mathcal{V}\left(\Phi_n\right) + \int d\Phi_R \left[\mathcal{R}^S\left(\Phi_{n+1}\right) - \mathcal{C}\left(\Phi_{n+1}\right)\right] \tag{1.4.46}$$

and

$$\Delta(p_T^{\max}, p_T) = \prod_i \exp\left(-\int_{p_T}^{p_T^{\max}} d\Phi_R \frac{\mathcal{D}_i}{\sum_j \mathcal{D}_j} \frac{\mathcal{R}^S(\Phi_{n+1})}{\mathcal{B}(\Phi_n)}\right). \tag{1.4.47}$$

Therefore, by choosing the function f to have a sharp cutoff,

$$f_{\text{sharp}}(p_T, p_T^{\max}, p_T^{\text{hard}}) = \Theta(p_T^{\text{hard}} - p_T), \tag{1.4.48}$$

the upper scale in the Sudakov form factor is reduced from $p_T^{\max}$ to p_T^{hard}, limiting the resummation of the real-emission contribution to scales less than p_T^{hard}. All radiation above this scale is included by the finite hard component, $\mathcal{R}^H$, which is generated as a separate $n+1$ body hard process. In doing so, the artificial K-factor $\bar{\mathcal{B}}(\Phi_n)/\mathcal{B}(\Phi_n)$ is no longer applied to the hard regions of the real-emission phase space.

Restricting the phase space of the hardest parton-shower emission with a sharp cutoff gives rise to a discontinuity in the distribution of the restricted variable, in this case the transverse momentum of the emitted parton. Formally, this amounts to an NNLO effect, but can have a non-negligible impact on observables. To solve this problem, f may instead be chosen to be a function that vanishes smoothly. In Ref. [81] the function

$$f_{\text{hfact}}(p_T, p_T^{\text{max}}, p_T^{\text{hard}}) = \Theta(p_T^{\text{max}} - p_T)\frac{(p_T^{\text{hard}})^2}{(p_T^{\text{hard}})^2 + p_T^2}, \tag{1.4.49}$$

was first used for the phase-space restriction. This function, referred to from now on as the hfact profile, has been adopted for a number of processes implemented within the PowhegBox program [82]. Naïvely, this function appears to fulfil the necessary criteria - it smoothly vanishes in the high p_T limit and approaches unity as $p_T \to 0$. However, as discussed in Ref. [83], this approach can run into difficulties in the soft collinear limit where the function may not approach unity sufficiently quickly to preserved the Sudakov resummation. Furthermore by reaching zero only in the infinite p_T limit, results produced using this approach tend to reflect those produced using the original Powheg formalism with $\mathcal{R}^S = \mathcal{R}$, unless p_T^{hard} is significantly less than the factorization scale.

An alternative function referred to as the resummation profile,

$$f_{\text{resum}}(p_T, p_T^{\text{max}}, p_T^{\text{hard}}) = \Theta(p_T^{\text{hard}} - p_T)P(p_T/p_T^{\text{hard}}, \rho), \tag{1.4.50}$$

where,

$$P(x,\rho) = \begin{cases} 0 & \text{if } x > 1, \\ \frac{(1-x)^2}{2\rho^2} & \text{if } 1-\rho < x \leq 1, \\ 1 - \frac{(1-2\rho-x)^2}{2\rho^2} & \text{if } 1-2\rho < x \leq 1-\rho, \\ 1 & \text{if } x \leq 1-2\rho, \end{cases} \tag{1.4.51}$$

was suggested in Ref. [84]. The function is zero for all values of p_T greater than the natural starting scale of the shower, unity in the low p_T region and interpolates quadratically between these two regimes. The range of p_T over which the transition occurs may be controlled via the parameter ρ, with $f = 1 \;\; \forall \;\; p_T/p_T^{\text{hard}} < 1 - 2\rho$.

For suitable choices of ρ, this ensures that the full real-emission matrix element is used in the splitting kernel in the Sudakov region.

1.4.4 Matrix-element corrections

The matrix-element correction approach that is the subject of this work is equivalent to a POWHEG correction in which the Born configuration is generated according to the differential cross section $\mathcal{B}(\Phi_n)$, rather than $\bar{\mathcal{B}}(\Phi_n)$. In this case, the expectation value of the observable $\mathcal{O}$ is

$$\langle\mathcal{O}\rangle^{\mathrm{ME}} = \int d\Phi_n \mathcal{B}\left(\Phi_n\right)\left[\Delta\left(p_T^{\max}, p_T^{\min}\right)\mathcal{O}_n + \int_{p_T^{\min}}^{p_T^{\max}} d\Phi_R \frac{\mathcal{R}\left(\Phi_{n+1}\right)}{\mathcal{B}\left(\Phi_n\right)}\Delta\left(p_T^{\max}, p_T\right)\mathcal{O}_{n+1}\right]. \tag{1.4.52}$$

As such, the hardest emission in the parton shower is still distributed according to the full real-emission matrix element. However, inclusive observables that would in the POWHEG approach be accurate to NLO, are now only described at LO accuracy. Furthermore, the absence of the full NLO calculation for the Born configuration means there is no reduction in the uncertainties associated with the choice of factorization and renormalization scales.

Division of the real-emission phase space

As with the full POWHEG approach, the upper p_T boundary of the phase space of the ME corrected emission may be limited to a more natural scale. In this case, Eq. 1.4.52 becomes

$$\begin{aligned}\langle\mathcal{O}\rangle^{\mathrm{ME}} = \int d\Phi_n \mathcal{B}\left(\Phi_n\right)\Bigg[&\Delta\left(p_T^{\max}, p_T^{\min}\right)\mathcal{O}_n \\ &+ \int_{p_T^{\min}}^{p_T^{\max}} d\Phi_R \frac{\mathcal{R}^S\left(\Phi_{n+1}\right)}{\mathcal{B}\left(\Phi_n\right)}\Delta\left(p_T^{\max}, p_T\right)\mathcal{O}_{n+1}\Bigg] + \int_{p_T^{\min}}^{p_T^{\max}} d\Phi_{n+1}\mathcal{R}^H\left(\Phi_{n+1}\right)\mathcal{O}_{n+1}.\end{aligned} \tag{1.4.53}$$

Unlike in the full POWHEG correction, no discontinuity is present in the transverse momentum distribution, even when employing the sharp cutoff to the real-emission matrix element defined in Eq. 1.4.48. However considering Eq. 1.4.53, it is clear that the LO accuracy of the integrated cross section has been destroyed by the division

of the real-emission phase space. To restore unitarity, the Born configuration in Eq. 1.4.53 is modified to

$$\mathcal{B}'(\Phi_n) = \mathcal{B}(\Phi_n) - \int_{p_T^{\min}}^{p_T^{\max}} d\Phi_R \mathcal{R}^H \left(\Phi_{n+1}\right). \tag{1.4.54}$$

The replacement $\mathcal{B} \to \mathcal{B}'$ will be referred to throughout as a LoopSim correction, owing to similarities between this approach and those proposed in Ref. [85]. The function $\mathcal{B}'$ may be viewed as an approximation to the NLO accurate function $\bar{\mathcal{B}}$ in which the virtual contribution has been replaced using $\mathcal{V} \approx -\int \mathcal{R} d\Phi_R$.

One of the motivations for the original POWHEG formalism was the absence of negative weights as compared with the MC@NLO approach. In the LoopSim ME correction introduced here, it is again possible for negative weights to arise. In fact, in our implementation the two terms in Eq. 1.4.54 are simulated as separate n parton contributions, the second of which will have negative weights. This impacts on the efficiency of the simulation but typically not at an unacceptable level.

A more detailed discussion of the LoopSim correction as implemented within the MATCHBOX framework in the Herwig++ event generator is available in Appendix A.1.

Finally, we note that matrix-element corrections represent the original [86, 87] and simplest method of improving the parton shower using information from full QCD matrix elements. Consequently, an alternative implementation of ME corrections, based on phase-space slicing, has been available within the Herwig++ event generator for a number of processes[36] for some time. In this phase-space slicing approach, two types of correction are required [78]. The first, called the hard ME correction, populates the dead zone of the parton-shower phase space using the exact matrix element describing an additional emission from the hard process. In the second, soft ME correction, existing parton-shower emissions are corrected again using the full real-emission matrix element. This correction is applied to all shower emissions for which there is no previous splitting with higher transverse momentum. The POWHEG style ME correction that has been implemented in this work

[36]See Ref. [6] for a summary of available processes and further details on the ME correction implementation.

has two significant advantages over the original phase-space slicing method. Firstly, it is easily extendable to full NLO matrix-element matching if and when automated calculations of NLO virtual contributions become available. In addition to this, the POWHEG style correction is considerably easier to implement within the Herwig++ event generator, given that no knowledge of the phase-space boundaries of the dead zone is required.

1.4.5 Truncated and vetoed parton showers

In POWHEG based matching procedures, once the hardest shower emission has been generated using a splitting kernel proportional to the real-emission matrix element, all further parton-shower emissions are simulated using the normal parton-shower splitting kernels. For the case in which the parton-shower emissions are ordered in terms of decreasing transverse momentum, this amounts simply to applying the parton-shower algorithm to the hard process including the first emission, with a starting scale set by the transverse momentum of the POWHEG emission[37].

For parton showers in which the emissions are ordered in terms of an angular evolution parameter, such as the default shower in Herwig++, the highest transverse momentum emission is not necessarily produced first. In this case, starting the normal parton shower from the scale defined by the POWHEG emission would miss a class of emissions which have a larger value of the angular evolution parameter but smaller transverse momentum than the POWHEG emission. The impact of this soft, wide-angle radiation is typically thought to be small and so is often neglected. This assumption allows matrix-element event generators that specialize in the implementation of the POWHEG correction, for example POWHEGBOX, to be easily interfaced to angular-ordered parton showers. This is done using the same procedure as for the transverse-momentum ordered showers with an additional veto on any subsequent parton-shower emission which is generated with transverse momentum greater than

[37]We use the term POWHEG emission to refer to the parton-shower emission that is generated using the Sudakov form factor in Eq. 1.4.37, both for the full POWHEG and ME correction approaches.

that of the POWHEG emission.

However to correctly reconcile angular ordering with the POWHEG formalism, a vetoed and truncated component of the shower must be introduced which simulates the missing soft wide-angle radiation. This amounts to an angular-ordered shower that is initiated at a scale determined from the underlying Born process, in which any emission with transverse momentum exceeding that of the POWHEG emission is discarded. The evolution of the shower is stopped, or truncated, when the angular evolution parameter reaches the value corresponding to the POWHEG emission. The POWHEG emission is then inserted into the chain, and the normal shower is used to continue the evolution from this scale down to the non-perturbative cutoff scale, again discarding emissions with transverse momentum greater than that of the POWHEG emission. Currently, the consistent inclusion of a truncated shower is only available in internal implementations of the POWHEG formalism, such as those included in the Herwig++ event generator[38].

In the case that the phase space of shower-type POWHEG emissions has been restricted, as described in Section 1.4.3, the shower evolution of events generated with the hard real-emission matrix element, $\mathcal{R}^H$, must also be included. These events require no truncated shower and are showered freely, with the parton-shower starting scale fixed at the maximum value defined by the particular parton-shower convention.

More details of the truncated and vetoed parton showers present in Herwig++ can be found in Ref. [88].

[38]It is important to note that there may be regions of the parton-shower phase space that are not correctly populated even in the case that a specialist POWHEG matrix-element generator is interfaced to a transverse-momentum ordered parton shower. This is due to the ambiguity in the definition of transverse momentum within the shower, and clearly advocates the use of a fully integrated Monte Carlo approach in which parameter definitions can be easily communicated between the different stages of the program.

Chapter 2

Matrix-element corrections to the decays of BSM particles

The production of high transverse momentum radiation in BSM processes will affect the topology of new physics events and therefore the expected experimental signature at collider experiments. Radiation produced during the hard scattering processes is of particular importance in scenarios which feature small mass splittings between the new BSM particles. As was discussed in Section 1.1.4, searches for these compressed spectra scenarios can benefit from considering events in which final-state BSM particles recoil against hard initial-state radiation. The emission of radiation in the subsequent decays of the new particles could either enhance or reduce the sensitivity of these search strategies and so must be accurately accounted for.

In this chapter, the impact of improving the simulation of hard radiation using a POWHEG style ME correction is studied for a range of decays relevant to BSM physics searches. The chapter is organised as follows. In Section 2.1, our implementation of the ME correction within the Herwig++ event generator is described for the example of top quark decay. In addition, the effect of applying the correction to this decay is studied and compared with results generated using an alternative matrix-element correction based on phase-space slicing [89]. This allows us to validate our algorithm. In Section 2.2, details are given of the decay modes for which the correction has been implemented. The impact of the correction on the decay of

the lightest graviton in the Randall-Sundrum model [25] is studied in Section 2.3.1 and results for two decays in the CMSSM are presented in Section 2.3.2. Finally, our findings are summarized in Section 2.4.

2.1 Top quark decays

In this section, we describe the implementation of the POWHEG style ME correction for the example of a top quark decaying to a W-boson and a bottom quark. We make use of the existing Herwig++ matrix elements for leading-order top quark decay and modify the shower such that the hardest emission is distributed according to the full real-emission matrix element. Application of the POWHEG correction to top quark decays in Herwig++, along with top quark-antiquark production in e^+e^- collisions, has been previously studied in Ref. [8] for massless bottom quarks. Here the physical mass of the bottom quark is used throughout.

2.1.1 Implementation in Herwig++

Matrix elements

At leading order, the spin and colour-averaged squared matrix element for the decay of a top quark into a bottom quark and a W-boson is given by

$$|\bar{\mathcal{M}}_B|^2 = \frac{g^2}{4m_W^2}\left(m_t^4 + m_b^4 - 2m_W^4 + m_t^2 m_W^2 + m_b^2 m_W^2 - 2m_t^2 m_b^2\right), \tag{2.1.1}$$

where m_t, m_b and m_W are the masses of the top quark, bottom quark and W-boson respectively and g is the weak interaction coupling constant. The relevant CKM factor has been set equal to 1. The spin and colour-averaged squared matrix element for the $\mathcal{O}(\alpha_s)$ real-emission correction to the decay $t \to Wb$ is

$$|\bar{\mathcal{M}}_R|^2 = g^2 g_s^2 C_F \left\{ -\frac{|\bar{\mathcal{M}}_B|^2}{g^2}\left(\frac{p_b}{p_b{\cdot}p_g} - \frac{p_t}{p_t{\cdot}p_g}\right)^2 + \left(\frac{p_t{\cdot}p_g}{p_b{\cdot}p_g} + \frac{p_b{\cdot}p_g}{p_t{\cdot}p_g}\right)\left(1 + \frac{m_t^2}{2m_W^2} + \frac{m_b^2}{2m_W^2}\right) - \frac{1}{m_W^2}\left(m_t^2 + m_b^2\right)\right\}, \tag{2.1.2}$$

where g_s is the strong coupling constant, C_F is the Casimir invariant in the fundamental representation of SU(3) and p_t, p_b, p_W and p_g are the momenta of the top quark, bottom quark, W-boson and gluon.

Kinematics

Decays of fundamental particles are performed in the rest frame of the parent particle, in this case the top quark. In this frame, we are free to choose the orientation of the W-boson to be along the negative z-direction and so, at leading order, the bottom quark is orientated along the positive z-direction. In general, the orientation of the decay products in the three-body final state of a real-emission configuration is chosen such that the emitting parton absorbs the transverse recoil coming from the emission of the gluon, while the spectator particle, the W-boson, continues to lie along the negative z-direction. However, when the radiation originates from the top quark, the bottom quark effectively acts as the emitting particle such that we remain in the rest frame of the parent. Therefore for emissions from both the top and the bottom quarks, the momenta of the decay products are:

$$p_W = \left(E_W, 0, 0, -\sqrt{E_W^2 - m_W^2}\right); \tag{2.1.3}$$

$$p_b = \left(E_b, -p_T \cos\phi, -p_T \sin\phi, \sqrt{E_b^2 - p_T^2 - m_b^2}\right); \tag{2.1.4}$$

$$p_g = \left(E_g, p_T \cos\phi, p_T \sin\phi, \sqrt{E_g^2 - p_T^2}\right); \tag{2.1.5}$$

where E_x is the energy of particle x, and p_T and ϕ are the transverse momentum and azimuthal angle of the gluon.

Phase space

The Lorentz invariant phase-space element of the additional emitted gluon, $d\Phi_R$, is obtained from the relation

$$d\Phi_3 = d\Phi_2 d\Phi_R, \tag{2.1.6}$$

where

$$d\Phi_n = (2\pi)^4 \delta^4 \left(p_t - \sum_{i=1}^{n} p_i\right) \prod_{i=1}^{n} \frac{d^3\vec{p}_i}{2E_i(2\pi)^3}, \tag{2.1.7}$$

and $\vec{p}_i$ is the three-momentum of particle i. We choose to parameterize the radiative phase space in terms of the transverse momentum, p_T, rapidity, y, and azimuthal angle, ϕ, of the gluon and so find

$$\mathrm{d}\Phi_R = J dp_T dy d\phi, \tag{2.1.8}$$

where the Jacobian factor, J, is [1]

$$J = \frac{1}{8\pi^3} \frac{m_t^2 p_T |\vec{p}_W|^2}{\lambda(m_t^2, m_W^2, m_b^2)[|\vec{p}_W|(m_t - p_T \cosh y) - E_W p_T \sinh y]}. \tag{2.1.9}$$

Dipole functions

The Sudakov form factor used to generate the POWHEG corrected emission[2] is

$$\Delta(p_T^{\max}, p_T) = \prod_i \exp\left(- \int_{p_T}^{p_T^{\max}} 4\pi\alpha_s(\tilde{p}_T^2) \frac{\mathcal{D}_i}{\sum_j \mathcal{D}_j} \frac{|\bar{\mathcal{M}}_R|^2}{|\bar{\mathcal{M}}_B|^2} J d\tilde{p}_T dy d\phi \right), \tag{2.1.10}$$

where now the factor of g_s^2 has been removed from the expression for $|\bar{\mathcal{M}}_R|^2$ in Eq. 2.1.2. Considering Eq. 2.1.10, the final components required for the implementation of the POWHEG style ME correction are the dipole functions, $\mathcal{D}_i$, which each describe the singular behaviour of the real-emission matrix element for a particular enhanced kinematic configuration. We use the functions defined in the Catani-Seymour subtraction scheme [55, 56] to describe the singular behaviour resulting from emissions from the decay products. The dipole used to describe radiation from the top quark is as follows,

$$\mathcal{D}_i = \frac{-4\pi C_F \alpha_s}{E_g^2} |\bar{\mathcal{M}}_B|^2. \tag{2.1.11}$$

It contains only soft enhancements since, in the top quark rest frame, collinear enhancements are suppressed. In practice, the absolute magnitude of the dipole functions are used in Eq. 2.1.10 to ensure that the parton-shower splitting kernel is always positive.

Matrix-element correction algorithm

Using the above information, the hardest emission in the shower can be generated according to Eq. 2.1.10 using the veto algorithm, which proceeds as follows:

[1] $\lambda(x, y, z) = \sqrt{x^2 + y^2 + z^2 - 2xy - 2xy - 2yz}$.

[2] We note that restricting the phase space of shower-type POWHEG emissions, as discussed in Section 1.4.4, is not necessary in the case of particle decays since the starting scale of the shower is naturally limited by the masses of the particles involved.

1. Trial values of the radiative phase-space variables are generated. The transverse momentum of the emission is generated by solving

$$\Delta^{\text{over}}\left(p_T^{\max}, p_T\right) = \exp\left(-\int_{p_T}^{p_T^{\max}} \frac{d\tilde{p}_T}{\tilde{p}_T} \frac{\alpha_s^{\text{over}}}{2\pi} C \int_{y_{\min}}^{y_{\max}} dy \int_0^{2\pi} \frac{d\phi}{2\pi}\right) = \mathcal{R}, \tag{2.1.12}$$

   where $p_T^{\max} = \frac{(m_t - m_W)^2 - m_b^2}{2(m_t - m_W)}$ is the maximum possible p_T of the gluon. The upper and lower bounds on the gluon rapidity, $y_{\max}$ and $y_{\min}$, are chosen to overestimate the true rapidity range, while α_s^{over} overestimates the true value of the strong coupling constant evaluated at the scale of the emission. The constant C is chosen such that the integrand in Eq. 2.1.12 always exceeds the integrand of the true Sudakov form factor, and $\mathcal{R}$ is a random number distributed uniformly in the range $[0, 1]$. Values of y and ϕ are generated uniformly in the ranges $[y_{\min}, y_{\max}]$ and $[0, 2\pi]$ respectively;

2. If the trial value of the transverse momentum does not satisfy $p_T \geq p_T^{\min}$, no radiation is generated and the decay products are hadronized directly;

3. If $p_T \geq p_T^{\min}$, the momenta of the W-boson, bottom quark and gluon are calculated using the generated values of the radiative variables. Doing so yields two possible values of E_W, which must both be retained and used in the remainder of the calculation. If the resulting momenta do not lie within the physically allowed region of phase space, the configuration is rejected, the maximum allowed transverse momentum is updated to $p_T^{\max} = p_T$ and the algorithm returns to step 1;

4. Events within the physical phase space are accepted with a probability given by the ratio of the integrands of the true and overestimated form factors, *i.e.* events are accepted if

$$\frac{\alpha_s(p_T^2)}{\alpha_s^{\text{over}}} \frac{16\pi^3 J p_T}{C} \frac{\mathcal{D}_i}{\sum_j \mathcal{D}_j} \frac{|\bar{\mathcal{M}}_R|^2}{|\bar{\mathcal{M}}_B|^2} > \mathcal{R}', \tag{2.1.13}$$

   where $\mathcal{R}'$ is a random number in the range $[0, 1]$. If the event is rejected, we set $p_T^{\max} = p_T$ and return to step 1;

Using this procedure, a trial emission is generated for each Sudakov form factor in the product in Eq. 2.1.10 and the one giving rise to the highest p_T emission is

selected. The existing Herwig++ framework is then used to generate the remainder of the parton shower, including the truncated and vetoed component introduced in Section 1.4.5.

2.1.2 Validation and results

To validate our implementation of the algorithm described in Section 2.1.1, Dalitz style plots were generated for the decay $t \to Wbg$ and are shown in Figure 2.1. The Dalitz variables, x_W and x_g, were defined by the relation $x_i = \frac{2E_i}{m_t}$, where E_i is the energy of particle i in the rest frame of the top quark. The left-hand panel in Figure 2.1 shows the distribution obtained when the POWHEG style ME correction is applied. In this case, x_g is the energy fraction of a gluon generated using the full real-emission matrix element. The distribution on the right-hand side of Figure 2.1 was instead generated using the uncorrected parton shower, limited to a single emission, such that x_g is the energy fraction of a gluon produced using the parton-shower splitting kernels. In both distributions, the black outline indicates the physical phase-space boundaries. The enclosed area is divided into a section populated by radiation from the bottom quark (above the green dashed line), sections populated by radiation from the top quark (below the blue dotted lines) and the dead zone (between the blue dotted and green dashed lines), which corresponds to hard gluon radiation and is not populated by the parton shower. These boundaries correspond to the theoretical limits of the Herwig++ parton shower with symmetric phase-space partitioning, described in Ref. [70], in which the starting values of the shower evolution variables for the top and bottom quarks are chosen such that the volumes of phase space accessible to emissions from each quark are approximately equal.

As expected, in both plots a high density of points is observed in the region $x_g \to 0$, corresponding to soft gluon emissions. The ME corrected distribution also has a concentration of points along the upper physical phase-space boundary where x_W is maximal and emissions are collinear to the bottom quark. The density of points along the upper boundary is reduced in the uncorrected distribution, and instead a concentration is present along the lower boundary of the bottom quark emission region. As discussed in Ref. [70], the parton-shower approximation agrees

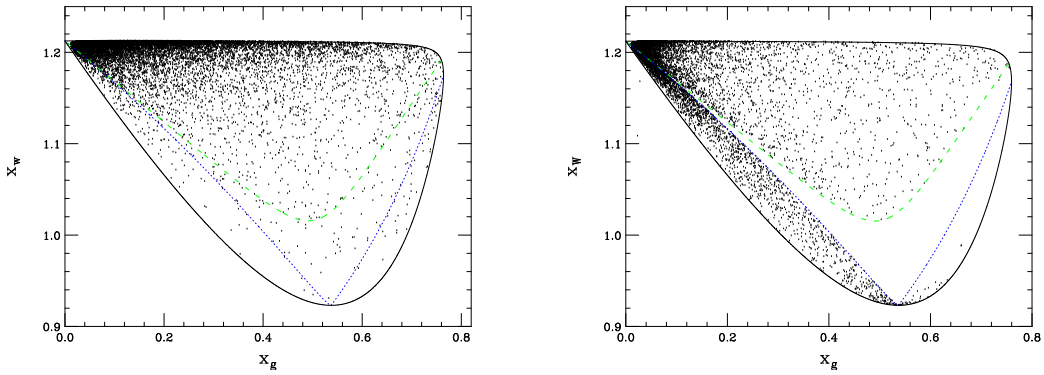

Figure 2.1: Dalitz distributions for the decay $t \to Wbg$ with (left) and without (right) the POWHEG style ME correction. The black outline indicates the physically allowed region of phase space. In the uncorrected parton-shower approach, the region above the green dashed line is populated with radiation from the bottom quark and the regions below the blue dotted lines are populated with radiation from the top quark. These boundaries correspond to the limits of the parton shower with symmetric phase-space partitioning.

with the true splitting probability for the case of collinear radiation from the bottom quark, but overestimates it elsewhere in this emission region. The factor by which the parton-shower approximation exceeds the exact real-emission matrix element increases towards the lower boundary of the region, and therefore we see an excess of points in that area. The parton-shower distribution also has a high density of points in the top quark emission region for $x_g \lesssim 0.53$, again caused by the parton-shower approximation overestimating the true splitting probability in this area. In general, we find that the parton shower produces areas of high emission density which do not correspond to physically enhanced regions of phase space, and therefore has a tendency to produce too much hard radiation. On the other hand, the ME corrected emission is distributed according to the exact real-emission matrix element and so correctly populates the physically enhanced regions of phase space with no additional spurious high density regions. Finally, we also see that the ME corrected distribution fills the dead zone of the parton-shower phase space that is not populated by shower emissions.

To further study the impact of the POWHEG style ME correction to top quark de-

cays, $e^+e^- \to t\bar{t}$ events were generated and analysed as in Ref. [89]. The production of the top-antitop pair was simulated at leading order using the built-in implementation in Herwig++ version 2.6 [90]. The full evolution of the parton shower was simulated, but the effects of hadronization were neglected. Events were generated at a centre-of-mass energy close to the $t\bar{t}$ threshold, $\sqrt{s} = 360\,\text{GeV}$, in order to minimize the effects of radiation generated during the production of the top-antitop pair. The top quarks were forced to decay leptonically, either at leading order or including, for the decay $t \to Wb$, the POWHEG style or preexisting ME correction based on phase-space slicing [89]. The events were analysed using the Rivet framework [91]. Final-state particles, excluding the decay products of the W-boson, were clustered into three jets using the FASTJET [92] implementation of the e^+e^- k_T algorithm [93]. Events were discarded if they contained a jet with transverse momentum $p_{T,j} < 10\,\text{GeV}$ or the minimum jet separation[3], ΔR , did not satisfy $\Delta R \geq 0.7$. Differential distributions of ΔR and $\log(y_{32})$, where y_{32} is the value of the jet resolution parameter[4] at which a three jet event is classified as a two jet event, were plotted and are shown in the left and right-hand panels in Figure 2.2. The bottom panel in each plot shows the ratio of distributions generated either with no ME correction or using the original phase-space slicing technique to the one generated with the POWHEG style ME correction. For both observables, the uncertainty in the results due to limited statistics is indicated by error bars in the distributions, except for the central values in the ratio plots where this uncertainty is instead shown by a yellow error band.

Distributions generated with and without the POWHEG style ME correction applied to the top quark decays are shown by the black solid and blue dashed lines in Figure 2.2 respectively. The red dotted lines in Figure 2.2 show the distributions obtained when the preexisting ME correction is used. In this phase-space slicing approach, both hard and soft matrix-element corrections must be included. The

[3] $\Delta R = \min_{ij} \sqrt{\Delta\eta_{ij}^2 + \Delta\phi_{ij}^2}$, where the indices i, j run over the three hardest jets and $i \neq j$. $\Delta\eta_{ij}$ and $\Delta\phi_{ij}$ are the differences in pseudorapidity and azimuthal angle of jets i and j respectively.

[4] $y_{32} = \frac{2}{s} \min_{ij} \left(\min\left(E_i^2, E_j^2\right)(1 - \cos\theta_{ij})\right)$, where the indices i, j run over the three hardest jets with $i \neq j$. E_i is the energy of jet i and θ_{ij} the polar angle between jets i and j.

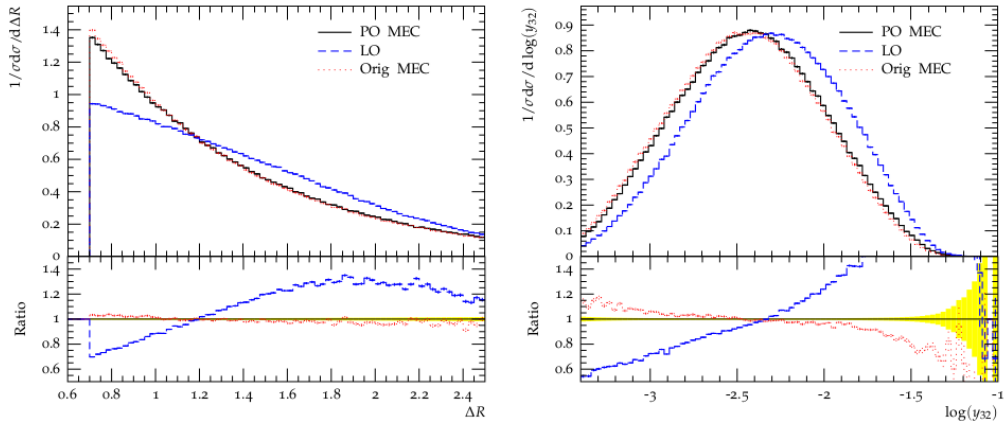

Figure 2.2: Comparison of distributions generated with no ME correction to those generated using the preexisting or new POWHEG style ME correction to the decay $t \to Wb$. Parton-level $e^+e^- \to t\bar{t}$ events were generated at $\sqrt{s} = 360\,\text{GeV}$. The left-hand plot shows the distribution of the minimum jet separation, ΔR, and the right-hand plot shows the logarithm of the jet measure, y_{32}.

hard ME corrections use the $t \to Wbg$ matrix element to distribute emissions in the dead zone of parton-shower phase space, while soft matrix-element corrections use the real-emission matrix element to correct parton-shower emissions that lie outside the areas of phase space where the shower approximation is valid, *i.e.* away from the soft and collinear limits. Applying these corrections ensures that the hardest emission in the shower is generated according to the exact real-emission matrix element, therefore, we expect a high level of agreement between results generated using the POWHEG style and original ME corrections.

Considering the plots in Figure 2.2, we see that applying either type of matrix-element correction has the effect of softening both the ΔR and $\log(y_{32})$ distributions. This is the result of the corrections reducing the number of high p_T emissions generated within the parton-shower phase space, as was observed in Figure 2.1. The magnitude of the observed effect illustrates the importance of matching the parton shower to the exact matrix element in high p_T regions. As expected, the distributions generated using the POWHEG style and original matrix-element corrections are very similar, although for both variables the POWHEG style correction yields slightly harder distributions. The differences between the distributions are

the result of a number of subtle variations between the POWHEG style and original matrix-element correction schemes. Firstly in the original approach, events in the dead zone are generated using the fixed-order real-emission matrix element only, without any Sudakov suppression, and subsequent showering of the resulting configuration is simulated starting from the $1 \to 3$ process. However in the POWHEG style approach, the real-emission configuration is interpreted in terms of a parton-shower splitting and incorporated into the evolution of the shower, which begins from the Born configuration as outlined in Section 1.4.5. In addition to this, the soft matrix-element correction in the original approach is applied to all emissions in the parton shower which are the hardest so far. Normally this leads to the correction of both the hardest emission and a number of other emissions with large values of the evolution parameter, but smaller transverse momenta. These differences all contribute to the disparity between the POWHEG style and original ME corrected distributions, although it is unclear which has the dominant effect. The difference between the POWHEG style and original matrix-element corrected results is, however, small. As such, the agreement between the two approaches serves to further validate the implementation of our POWHEG style ME correction. Finally, we note that the POWHEG style approach is preferable to the original matrix-element correction scheme since it is significantly simpler to implement in Herwig++.

2.2 Decays of BSM particles

Having outlined and validated our implementation of POWHEG style ME corrections for the case of top quark decays, we now turn our attention to decays involving BSM particles. The POWHEG style ME correction has been implemented within the Herwig++ event generator for a range of decays that occur in most of the well studied BSM scenarios. The leading-order and real-emission matrix elements are calculated using the internal Herwig++ implementation of the HELAS formalism [94], thereby allowing spin correlations to be correctly incorporated through the algorithm described in Ref. [62]. The singular nature of the real-emission matrix element is partitioned using dipole functions defined as in the Catani-Seymour subtraction

Incoming	Outgoing
Scalar	Scalar Scalar
Scalar	Scalar Vector*
Scalar	Fermion Fermion
Fermion	Fermion Scalar
Fermion	Fermion Vector*
Vector	Scalar Scalar
Vector	Fermion Fermion
Tensor	Fermion Fermion
Tensor	Vector Vector*

Table 2.1: Spin combinations for which the POWHEG style ME correction has been implemented. Corrections to the decays marked * are not included for massive coloured vector particles.

Incoming	Outgoing
0	$3\ \bar{3}^{\dagger}$
0	$8\ 8^{\dagger}$
3	3 0
$\bar{3}$	$\bar{3}$ 0
3	3 8
$\bar{3}$	$\bar{3}$ 8
8	$3\ \bar{3}$

Table 2.2: Colour flows for which the POWHEG style ME correction has been implemented. For tensor particles, corrections are only included for colour flows marked †.

scheme [55, 56] when describing radiation from the decay products, and a spin-independent soft contribution for emissions from the decaying particle. The latter is defined in analogy to the function in Eq. 2.1.11, modifying the colour factor to reflect the colour flow of the decay.

Table 2.1 shows the combinations of incoming and outgoing spins for which the correction has been included, and each spin structure is implemented for the colour flows given in Table 2.2. However, two limitation apply. Firstly, no models with coloured tensor particles have been considered and therefore decays involving incoming tensor particles are limited to the colour flows in which the tensor is a colour singlet. In addition, the Fermion-Fermion-Vector, Scalar-Scalar-Vector and Tensor-Vector-Vector decays are not implemented in the case of massive coloured

vector particles, although the corrections for massless coloured vector particles have been included[5].

2.3 Results

2.3.1 Randall-Sundrum graviton

In the remainder of the chapter we investigate the impact of applying POWHEG style ME corrections to the decays of BSM particles, beginning in this section with the decay of the lightest graviton in the Randall-Sundrum (RS) model. To this end, we make use of the RS type model [25] implemented within Herwig++, see Ref. [95] for more details. Proton-proton collisions were simulated in which the lightest graviton, G, was produced as a resonance and allowed to decay via $G \to gg$ or $G \to q\bar{q}$ for $q = u, d, s, c, b$. The mass of the graviton was chosen to be $m_G = 2.23\,\text{TeV}$ which, at the time of writing, corresponded to the lower bound on the allowed graviton mass for the coupling $k/\bar{M}_{Pl} = 0.1$ [96]. Events were generated at a centre-of-mass energy of $\sqrt{s} = 8\,\text{TeV}$ and include simulation of the full parton shower, hadronization and the underlying event. The default values of the renormalization and factorization scales in Herwig++ version 2.6 were used, along with the default PDF set CTEQ5L [97].

To study the impact of the POWHEG style ME correction to the decay of the graviton, an analysis based on an ATLAS collaboration search for new phenomena in dijet distributions [98] was implemented within the Rivet framework. Jets were constructed using the FASTJET [92] implementation of the anti-k_T algorithm [99] with the energy recombination scheme and a distance parameter $R = 0.6$. Events with less than two jets satisfying $|y_i| < 4.4$ were discarded, where y_i is the rapidity in the pp centre-of-mass frame of the ith hardest jet. In the dijet centre-of-mass frame formed by the two hardest jets, the rapidities of those jets, y_* and $-y_*$, where determined from $y_* = \frac{1}{2}(y_1 - y_2)$. Events not satisfying $|y_*| < 0.6$ and $|y_{1,2}| < 2.8$

[5] At the time of implementation, attempts to calculate well-defined dipoles describing quasi-collinear radiation from massive vector bosons were unsuccessful. While the dipoles have now been determined, corrections to these modes remain absent.

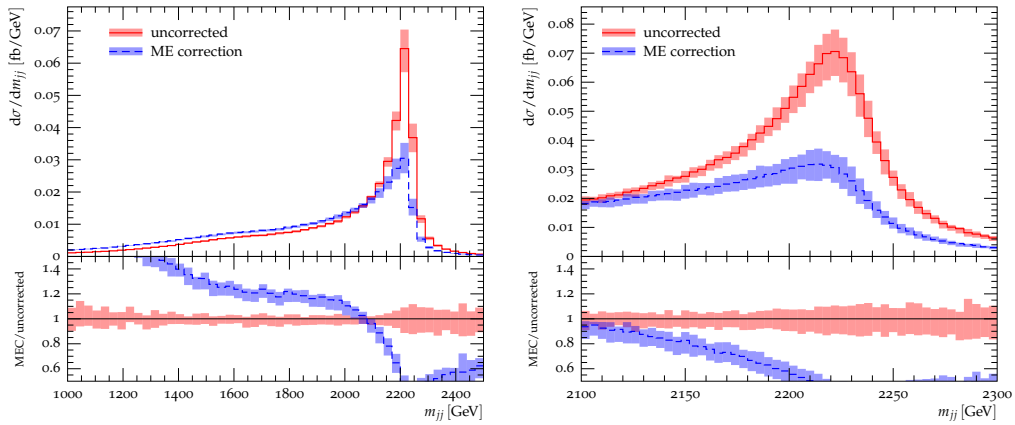

Figure 2.3: Dijet invariant mass distributions for the lightest RS graviton decaying to jets. The left-hand plot shows the distribution in the full range $1.0\,\text{TeV} \leq m_{jj} \leq 2.5\,\text{TeV}$, while the right-hand plot emphasises the effect on the peak region $2.1\,\text{TeV} \leq m_{jj} \leq 2.3\,\text{TeV}$. The mass of the graviton was $m_G = 2.23\,\text{TeV}$ and the coupling $k/\bar{M}_{Pl} = 0.1$. LHC events were simulated with $\sqrt{s} = 8\,\text{TeV}$. The uncertainty bands were generated by varying the event tune parameters in the ME corrected (blue) and uncorrected (red) distributions respectively.

were discarded. The dijet invariant mass, m_{jj}, was determined from the vector sum of the momenta of the two hardest jets, and events were required to satisfy $m_{jj} > 1.0\,\text{TeV}$.

The dijet mass distribution after the above selection criteria were applied is shown in the left-hand plot in Figure 2.3. The red solid line shows the invariant mass distribution in the case that no ME correction was included, while the blue dashed line shows the result obtained when the POWHEG style ME correction to the graviton decay was applied. From Figure 2.3, we see that including the POWHEG style correction causes a decrease of $\mathcal{O}\,(40\%)$ in the number of events in the region $2.1\,\text{TeV} \leq m_{jj} \leq 2.3\,\text{TeV}$. This effect is highlighted in the right-hand plot in Figure 2.3, which shows the dijet mass distribution in this range. In the uncorrected approach, the majority of the graviton's momentum will be carried by the two partonic decay products. When the POWHEG style correction is applied, the momentum is instead distributed between the partonic decay products and the POWHEG corrected emission, such that a significant fraction of the graviton's mo-

mentum is missed when the invariant mass of only the hardest two jets is considered. Therefore, we see a shift in the dijet mass distribution to lower values of m_{jj} when the ME correction is applied.

The central values of the dijet mass distributions were generated using the optimum set of tuned perturbative and non-perturbative parameters (event tune) found in Ref. [9]. To give an estimate of the uncertainty arising from our choice of event tune, the dijet mass distributions were generated at ten points in the event tune parameter space and error bands were created showing the maximum and minimum values from the resulting set of distributions. A description of the varied parameters can be found in Ref. [9] and their values at each of the ten points are given in Table 2 of Ref. [9]. The resulting error bands are shown in blue and red for the distributions with and without the ME correction respectively. The impact of the POWHEG style correction is still clearly evident once this uncertainty has been taken into account.

2.3.2 The Constrained Minimal Supersymmetric Standard Model

In addition to the results presented in Section 2.3.1, the effect of the POWHEG style ME correction has also been studied in the context of the CMSSM model. To this end, we consider a scenario with the high scale parameters $m_0 = 1220\,\text{GeV}$, $m_{1/2} = 630\,\text{GeV}$, $\tan\beta = 10$, $A_0 = 0$ and $\mu > 0$. This point lies just outside the exclusion limits set by the ATLAS experiment in Ref. [100], which at the time of writing provided the most stringent constraint on the CMSSM parameter space. The corresponding weak scale parameters and decay modes were calculated using ISAJET 7.80 [101], and the resulting masses of the SUSY particles relevant to this study are given in Table 2.3. The Herwig++ implementation of the MSSM model [95] was used to generate LHC pp collisions at a centre-of-mass energy of $\sqrt{s} = 8\,\text{TeV}$. Here we focus on the effect of the correction to the parton shower and so hadronization and the underlying event were not simulated[6]. In the following

[6] As in Section 2.3.1, we use the default values of the renormalization and factorization scales and the CTEQ5L PDF set.

$m_{\tilde{u}_L}$	$m_{\tilde{g}}$	$m_{\tilde{t}_1}$	$m_{\tilde{\chi}_1^0}$
1812.91 GeV	1546.56 GeV	1278.14 GeV	279.22 GeV

Table 2.3: Masses of the SUSY particles relevant to the decays studied in Section 2.3.2. Values were obtained using ISAJET 7.80 with the high scale parameters $m_0 = 1220\,\text{GeV}$, $m_{1/2} = 630\,\text{GeV}$, $\tan\beta = 10$, $A_0 = 0$ and $\mu > 0$.

sections, the impact of the POWHEG style correction on two archetypal decays is presented. In both cases, the decaying SUSY particle is pair produced in the hard process and the two subsequent decays are then analysed separately in the rest frame of the decaying particle. Dalitz style distributions were produced, as described in Section 2.1.2, for both the POWHEG corrected emission and an emission generated using the uncorrected parton-shower splitting kernel. In addition, for each decay mode the transverse momentum distribution of the hardest jet not originating from a decay product was also studied. To do so, the full parton shower was generated, with and without the POWHEG style correction, and the visible final-state particles originating from each decay were clustered into jets using the FASTJET implementation of the anti-k_T algorithm with the energy recombination scheme and $R = 0.4$. Jets with transverse momentum $p_{T,j} \leq 20\,\text{GeV}$ or pseudorapidity $|\eta| > 4.0$ were discarded. Each decay was required to have at least $n + 1$ jets passing the selection criteria, where n is the number of visible decay products.

Matrix-element corrections to $\tilde{u}_L \to u\,\tilde{\chi}_1^0$

Events were generated in which a left-handed up squark-antisquark pair was produced and then decayed according to $\tilde{u}_L \to u\,\tilde{\chi}_1^0$, and the equivalent conjugate mode. Dalitz style distributions with and without the ME correction were produced and are shown in the left and right-hand plots in Figure 2.4. The black outline indicates the kinematic limits of phase space and the green dashed and blue dotted lines are the boundaries of the emission regions in the uncorrected parton shower with the most symmetric choice of shower phase-space partitioning. Emissions from the up quark populate the area above the green dashed line, while the regions below the blue dotted lines are filled by emissions from the $\tilde{u}_L$. The area between the green

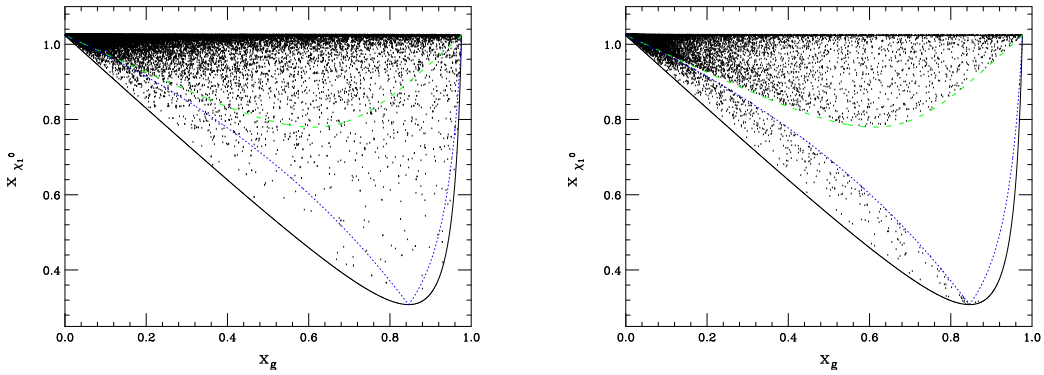

Figure 2.4: Dalitz distributions for the decay $\tilde{u}_L \to u\,\tilde{\chi}_1^0 g$ with (left) and without (right) the POWHEG style ME correction. The black outline indicates the physically allowed region phase space. In the uncorrected parton-shower approach, the region above the green dashed line is populated with radiation from the up quark and the regions below the blue dotted lines are populated with radiation from the $\tilde{u}_L$. These boundaries correspond to the limits of the parton shower with symmetric phase-space partitioning.

and blue lines is the dead zone, unpopulated by the normal parton shower.

Similar to the result in Section 2.1.2, we see that points in the ME corrected distribution are concentrated in the soft region as $x_g \to 0$, and along the upper boundary of the physical phase space where the emitted gluon is collinear to the up quark. However, in the normal parton-shower distribution fewer points lie along the upper physical phase-space boundary. Instead there is a concentration of points in the up squark emission region with $x_g \lesssim 0.85$ and along the lower boundary of the up quark emission region. In analogy to the case of top quark decay, these unphysical high density regions are understood to result from the parton-shower kernels overestimating the exact real-emission matrix element. Finally, we see that including the POWHEG style correction ensures that the region of phase space inaccessible to the normal parton shower is populated.

Differential distributions of the transverse momentum of the subleading jet[7], $p_{T,2}$, in each decay were also generated and are shown in Figure 2.5. The red solid line corresponds to the distribution generated using the uncorrected parton shower, while

[7]Jets are ordered in terms of their transverse momentum such that $p_{T,1} > p_{T,2} > p_{T,3}$ etc.

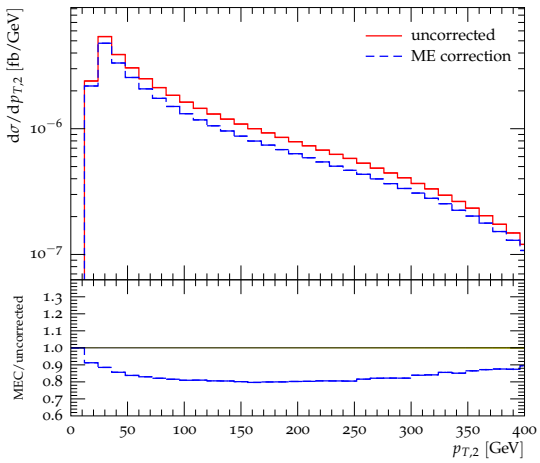

Figure 2.5: Transverse momentum distributions of the second hardest jet in the decay $\tilde{u}_L \to u\,\tilde{\chi}_1^0$, analysed in the rest frame of the $\tilde{u}_L$. Events were generated with (blue dashed line) and without (red solid line) the POWHEG style correction, using the CMSSM model with $m_0 = 1220\,\text{GeV}$, $m_{1/2} = 660\,\text{GeV}$, $\tan\beta = 10$, $A_0 = 0$ and $\mu > 0$ at the LHC with $\sqrt{s} = 8\,\text{TeV}$.

the blue dashed line shows the result with the ME correction to the decay applied. Error bars are included to indicate the statistical uncertainty in the distributions. As demonstrated in Figure 2.4, the parton shower tends to overpopulate the hard regions of phase space. Hence, including the POWHEG style correction reduces the p_T of the hardest emission in the decay. This is reflected in the ME corrected $p_{T,2}$ distributions which is softer that the uncorrected result. As such, we observe an $\mathcal{O}\,(20\%)$ reduction in the number of events passing the jet selection criterion $p_{T,j} > 20$ GeV when the correction is applied.

Matrix-element corrections to $\tilde{g} \to \tilde{t}_1\,\bar{t}$

Finally, we investigate the impact of the POWHEG style correction on the decay mode $\tilde{g} \to \tilde{t}_1\,\bar{t}$. The left and right-hand plots in Figure 2.6 show Dalitz distributions for this decay generated with and without the ME correction respectively. In both plots, the black outline indicates the kinematically allowed region phase space. The solid coloured lines show the boundaries of the parton-shower emission regions in the scenario where the $\bar{t}$ absorbs the transverse momentum recoil of the gluon emission

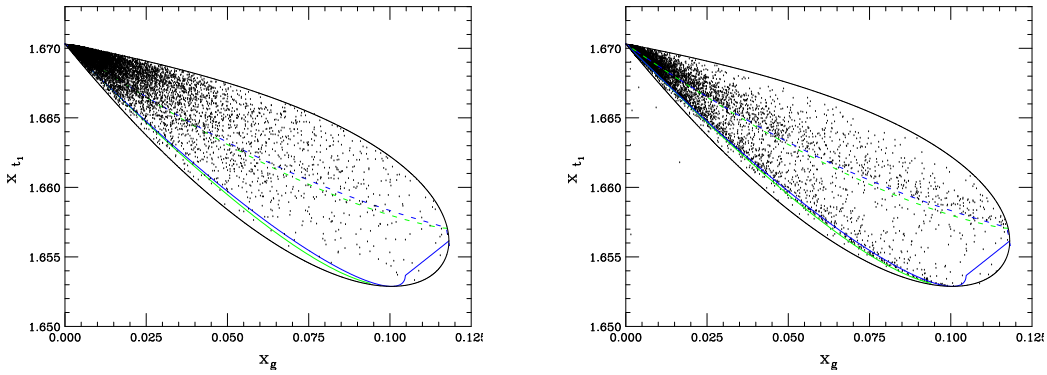

Figure 2.6: Dalitz distributions for the decay $\tilde{g} \to \tilde{t}_1\, \bar{t} g$ with (left) and without (right) the POWHEG style correction applied. The solid (dashed) coloured lines indicate the parton-shower emission regions when the $\bar{t}$ $\left(\tilde{t}_1\right)$ absorbs the transverse recoil of the emission. The solid (dashed) green line shows the lower (upper) boundary for radiation from the $\bar{t}$ $\left(\tilde{t}_1\right)$. The blue solid (dashed) lines are the equivalent upper (lower) boundaries for radiation from the $\tilde{g}$. All boundaries correspond to the case of symmetric phase-space partitioning and the black outline shows the kinematically allowed region of phase space.

and the $\tilde{t}_1$ is orientated along the negative z-axis in the $\tilde{g}$ rest frame. The region above the green (pale) solid line is populated by emissions from the $\bar{t}$ and the areas below the blue (dark) solid lines are filled by emissions from the $\tilde{g}$. In this case, the two emission regions overlap away from the soft limit and there is no region of phase space left unpopulated by the parton shower. The dashed coloured lines indicate the emission boundaries of the parton shower when instead the $\tilde{t}_1$ absorbs the transverse recoil of the emission and the $\bar{t}$ is aligned with the negative z-axis. The green (pale) dashed line is the upper limit for emissions coming from the $\tilde{t}_1$ and the blue (dark) dashed lines mark the lower boundaries for emissions from the $\tilde{g}$.

From the left-hand plot of Figure 2.6, we see that the majority of points in the ME corrected distribution are concentrated in the soft region of phase space. High density regions corresponding to emissions collinear to the $\bar{t}$ or $\tilde{t}_1$ are suppressed due to the massive nature of the decay products. In the parton-shower distribution, points are concentrated in the soft region and along the lower boundary of the $\bar{t}$ and dashed $\tilde{g}$ emission regions. The latter two unphysical regions of overpopulation

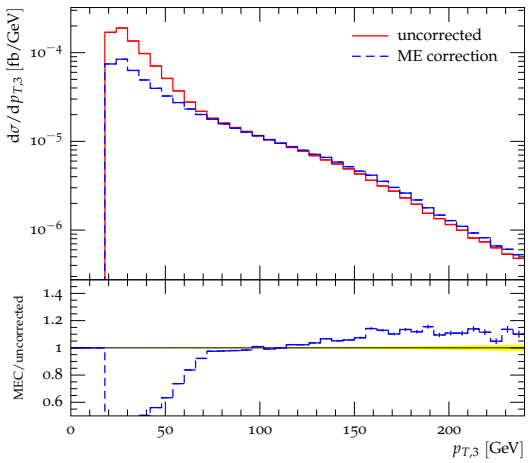

Figure 2.7: Transverse momentum distributions of the third hardest jet in the decay $\tilde{g} \to \tilde{t}_1\,\bar{t}$, analysed in the rest frame of the $\tilde{g}$ and with stable $\tilde{t}_1$ and $\bar{t}$. Events were generated with (blue dashed line) and without (red solid line) the POWHEG style correction, using the CMSSM model with $m_0 = 1220\,\text{GeV}$, $m_{1/2} = 660\,\text{GeV}$, $\tan\beta = 10$, $A_0 = 0$ and $\mu > 0$ at the LHC with $\sqrt{s} = 8\,\text{TeV}$.

again highlight the importance of correcting hard emissions in the parton shower using the exact real-emission matrix element.

Transverse momentum distributions of the third hardest jet in the rest frame of the $\tilde{g}$ were also plotted and are shown in Figure 2.7. To focus on the effect of the POWHEG style correction, the top quark and top squark produced in each decay were not allowed to decay further. The red solid and blue dashed lines in Figure 2.7 correspond to the uncorrected and ME corrected distributions respectively and error bars indicating the statistical uncertainty on the results are shown. As for the decay $\tilde{u}_L \to u\,\tilde{\chi}_1^0$, we find that the ME correction decreases the total number of events passing the jet p_T selection criterion. The effect is more pronounced in this case, with an $\mathcal{O}\,(40\%)$ reduction. The pure parton-shower distribution significantly exceeds the ME corrected result in the small $p_{T,3}$ limit, however in the high transverse momentum tail the two distributions are similar. This occurs because the POWHEG style correction softens the hardest emission in the decay, which in the low $p_{T,3}$ region forms the base of the third hardest jet. However, the maximum possible

p_T of the gluon generated by the ME correction is[8] $p_T^{\max} \approx 75\,\text{GeV}$. Jets contributing to the corrected $p_{T,3}$ distribution above this limit are sensitive to uncorrected shower emissions in addition to the hardest emission, therefore reducing the effect of the correction in the high p_T regime. As such, applying the ME correction will only impact significantly on the number of events passing a jet p_T selection criterion if the value of the p_T cut lies below $p_T^{\max}$ of the POWHEG corrected emission.

2.4 Summary

In this chapter, we have investigated the effect of using a POWHEG style ME correction to improve the simulation of hard QCD radiation in a range of particle decays. The implementation of this correction within the Herwig++ event generator was described in detail for the decay $t \to Wb$. Dalitz style distributions of the first emission from this decay in the uncorrected parton shower and ME corrected cases were produced, and showed that the parton shower has erroneous, unphysical areas of high emission density which result in the overpopulation of some high p_T regions of the emission phase space. This effect may be rectified by applying the POWHEG style correction, which ensures that the majority of emissions lie in the soft and collinear limits. Differential distributions of the minimum jet separation and logarithm of the jet measure were also generated with the POWHEG style correction and compared to those generated with the existing Herwig++ implementation of hard and soft matrix-element corrections. The two techniques exhibit a high level of agreement, therefore demonstrating the validity of our approach. In addition to this, distributions were generated using the normal parton shower. In agreement with the results from the Dalitz plots, these distributions were found to be considerably harder than those generated with the original or POWHEG style matrix-element corrections.

The impact of applying the POWHEG style ME correction to the decays of BSM particles was then studied in the context of the Randall-Sundrum and CMSSM models. In the former scenario, applying the matrix-element correction was found

[8]The value of $p_T^{\max}$ was calculated using the formula for $p_T^{\max}$ in top quark decay, given on page 53, with the replacements $m_t \to m_{\tilde{g}}$, $m_W \to m_{\tilde{t}_1}$ and $m_b \to m_t$.

to have a significant impact on the invariant mass distribution of dijets produced in the decay of the lightest RS graviton. The number of events passing selection criteria in the mass range $2.1\,\text{TeV} \leq m_{jj} \leq 2.3\,\text{TeV}$ was found to be $\mathcal{O}\,(40\%)$ less than in the uncorrected case, owing to the decreased fraction of the graviton's momentum accounted for by the two hardest jets when the correction is applied. The sizable impact of the correction in this scenario illustrates the importance of including higher-order corrections when optimising experimental searches.

The impact of the ME correction was also investigate for two decays in the CMSSM model by studying Dalitz plots and transverse momentum distributions. In general, applying the matrix-element correction was found to decrease the transverse momentum of the hardest parton-shower jet in each decay, leading to a reduction in the number of events passing the event selection criterion $p_{T,j} > 20$ GeV. However, no impact is expected in the case that the maximum transverse momentum of the POWHEG corrected emission does not exceed the lower bound on the jet transverse momentum set by the event selection criterion.

Chapter 3

Matrix-element corrections to stop-antistop production

To obtain an accurate simulation of radiation in BSM events, one must improve on the pure parton-shower description of hard emissions generated during both the production and decays of coloured particles. An improved treatment of the latter source of radiation was addressed in Chapter 2, where the impact of applying POWHEG style ME corrections was investigated for a number of BSM decay modes. In the following two chapters, we study the effect of applying POWHEG style ME corrections to radiation emitted during the production of BSM particles, specifically focusing on squark-antisquark production at the LHC.

To improve the description of hard radiation generated during production processes, our POWHEG style ME correction has been incorporated in Herwig++ through the MATCHBOX framework. The MATCHBOX framework provides NLO hard process calculations for a large range of Standard Model processes, with matching to the angular ordered and dipole showers [102] through both the MC@NLO and POWHEG formalisms. As such, it already contains the functionality required to implement ME corrections in squark-antisquark production, with only the Born and real-emission amplitudes missing. Typically, the MATCHBOX framework relies on interfaces to external matrix-element providers to obtain the necessary ampli-

tudes for calculations[1]. However, these interfaces exist only for SM processes and consequently the amplitudes used in this work were implemented manually, having been derived from those generated by MadGraph 5 [105] using the built-in MSSM model [109–112]. Extension of the Matchbox-MadGraph 5 interface to include BSM scenarios is however possible, and would allow ME corrections to alternative SUSY processes and BSM models to be included in a more automated way. Further details of the Matchbox framework can be found in Refs. [84, 102]. In addition, technical details of our ME correction implementation within the Matchbox framework are given in Appendix A.1.

In this chapter, the effect of applying our Powheg style ME correction is studied for the case of top squark-antisquark production. We begin in Section 3.1, with the validation of our implementation against the one available within the Powheg-Box program [5, 11, 79, 82]. The impact of the ME correction on parton-level distributions is investigated in Section 3.2, along with the significance of the truncated shower and the effects of different schemes for dividing the phase space of the Powheg emission. The combined impact of ME corrections applied during the production and decays of top squarks is also investigated in this section, considering benchmark scenarios with both compressed and well separated sparticle mass spectra. Finally, in Section 3.3 the impact of the Powheg style ME correction is studied in the context of an existing ATLAS search for top squarks [113], before concluding remarks are given in Section 3.4.

3.1 Validation

3.1.1 Setup

In the following section, we validate our implementation of Powheg style ME corrections for the production of top squark-antisquark pairs. To this end, LHC pp collisions were generated at a centre-of-mass energy of $\sqrt{s} = 14$ TeV. To focus on

[1]Interfaces to GoSam [103], HJets++ [104], MadGraph 5 [105], NJet [106], OpenLoops [107] and Vbfnlo [108] are available at present.

the impact of the correction, the effects of hadronization and the underlying event were not simulated and the top squarks and antisquarks were not allowed to decay. The mass of the top squark was set to $m_{\tilde{t}_1} = 700$ GeV. Histograms were plotted using the Rivet analysis framework [91] and, unless otherwise stated, all PDFs were taken from the LHAPDF package [114].

3.1.2 Validation of leading-order amplitudes

The leading-order amplitudes for top squark-antisquark production were validated by comparing results generated using the MATCHBOX framework to those produced using the internal Herwig++ setup. While these implementations are formally both part of the Herwig++ program, the MATCHBOX framework makes use of amplitudes derived using MADGRAPH 5 whereas the internal Herwig++ approach uses an independent implementation of the HELAS formalism [94]. The leading-order matrix elements were convoluted with the CTEQ6L1 PDF set [115], and the renormalization and factorization scales were set to $\mu_R = \mu_F = m_{\tilde{t}_1}$. The total cross sections calculated using MATCHBOX and the internal Herwig++ setup were found to exactly agree at $44.09^{+32\%}_{-23\%}$ fb. The percentile uncertainties indicate an estimate of the theoretical uncertainty on the predictions obtained by varying the renormalization and factorization scales simultaneously by a factor of two around the central value.

For further comparison, differential distributions of the invariant mass of the top squark pair[2], $m_{\tilde{t}_1\tilde{t}_1^*}$, and inclusive transverse momentum of the top squark[3], $p_{T,\tilde{t}_1}$, are shown in the left and right-hand plots of Figure 3.1. To focus on the validation of the matrix elements, no parton shower simulation has been included. The central results produced using the internal Herwig++ and MATCHBOX implementations are shown by the dashed blue and solid red lines respectively, with the uncertainty due to scale variation shown by the bands of corresponding colour. In both distributions, the two implementation are in excellent agreement.

[2]The invariant mass of the top squark pair is defined as $m_{\tilde{t}_1\tilde{t}_1^*} = \sqrt{(p_{\tilde{t}_1} + p_{\tilde{t}_1^*})^2}$, where $p_{\tilde{t}_1}$ and $p_{\tilde{t}_1^*}$ are the momenta of the top squark and antisquark respectively.

[3]We use $p_{T,\tilde{t}_1}$ to refer to transverse momentum distributions in which the contributions from both the $\tilde{t}_1$ and $\tilde{t}_1^*$ have been summed.

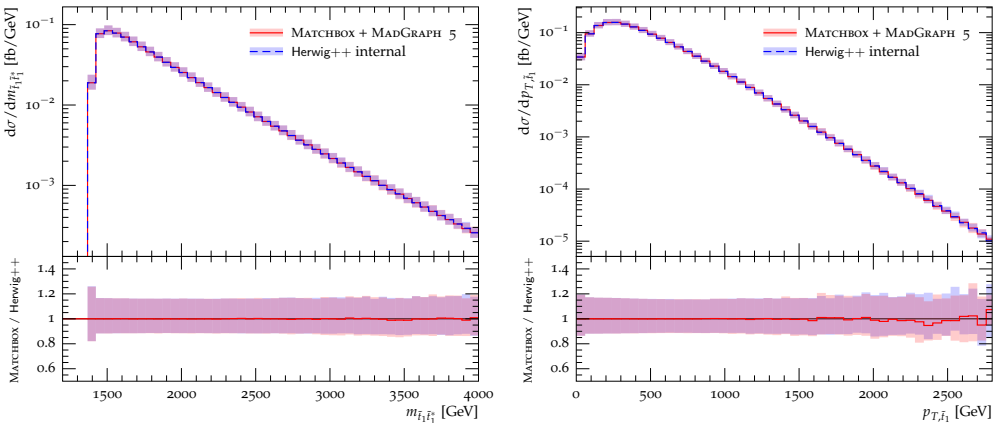

Figure 3.1: Distributions of the invariant mass of the top squark pair $m_{\tilde{t}_1\tilde{t}_1^*}$ (left) and the inclusive top squark transverse momentum $p_{T,\tilde{t}_1}$ (right) in simulations of LHC collisions at a centre-of-mass energy of 14 TeV. Events were generated using the LO MATCHBOX and internal Herwig++ setups, for top squarks of mass $m_{\tilde{t}_1} = 700$ GeV. For each line, the error band indicates the uncertainty arising from the variation of $\mu_R = \mu_F$ by a factor of two around the central value.

3.1.3 Validation of matrix-element corrections

To test the validity of our ME correction algorithm, results produced using the MATCHBOX implementation were compared to those generated using the POWHEG-BOX program [5, 11, 79, 82]. Events were simulated in which the parton shower was limited to the production of the hardest emission only, and the matrix elements were convoluted with the PDF set CTEQ6m [115][4]. To minimize differences between the implementations, the value of the strong coupling constant was set to the default Herwig++ value of the coupling evaluated at μ_R, including during the generation of the hardest emission. The factorization and renormalization scales were set and varied as with the LO validation described in Section 3.1.2. The POWHEGBOX program allows events to be generated both with the full POWHEG correction and in the case that the Born configuration is generated only at LO. The latter approach corresponds to our POWHEG style ME correction in the case that the real-emission configuration

[4]The CTEQ6m PDF set was used in this case as there exists an internal implementation of the set within the POWHEGBOX program.

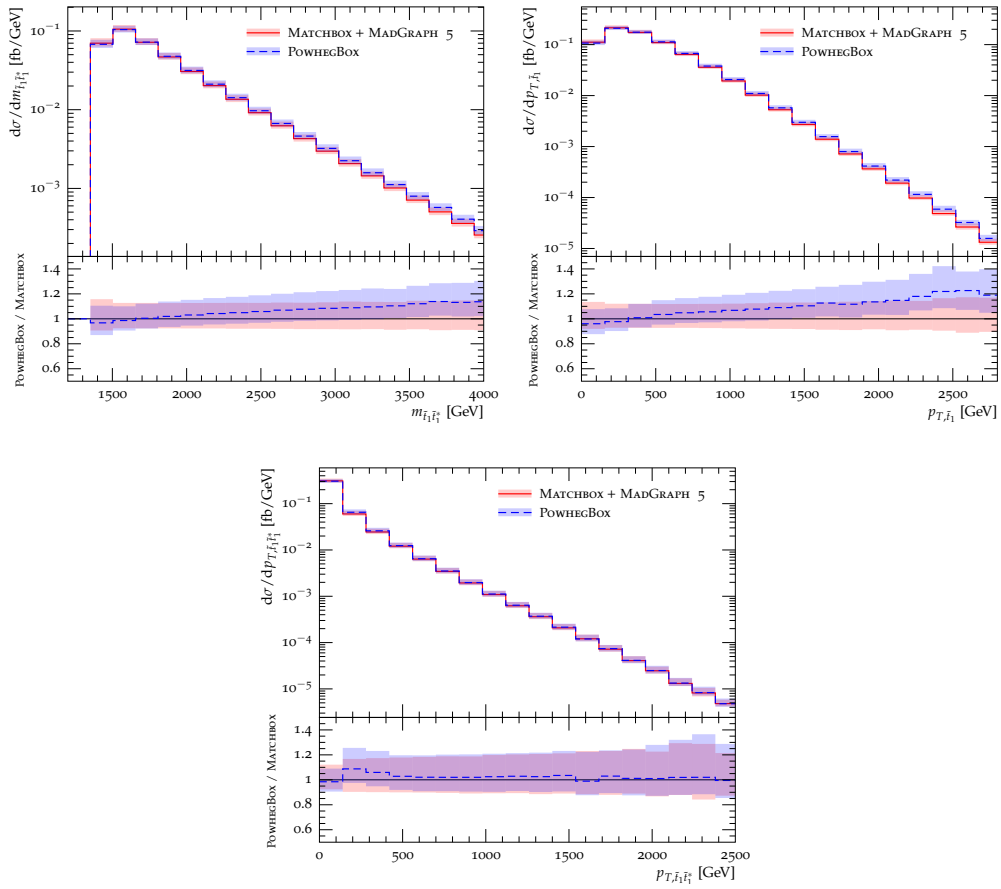

Figure 3.2: Distributions of the invariant mass of the top squark pair $m_{\tilde{t}_1\tilde{t}_1^*}$ (upper left), the inclusive top squark transverse momentum $p_{T,\tilde{t}_1}$ (upper right) and the transverse momentum of the top squark pair $p_{T,\tilde{t}_1\tilde{t}_1^*}$ (bottom) in simulations of LHC collisions at a centre-of-mass energy of 14 TeV. Events were generated using the matrix-element corrected MatchBox and PowhegBox setups detailed in the text, for top squarks of mass $m_{\tilde{t}_1} = 700$ GeV. For each line, the error band indicates the uncertainty arising from the variation of $\mu_R = \mu_F$ by a factor of two around the central value.

is not divided into S and H-events. Consequently, results were generated using this approach to allow for direct comparison between the implementations.

The total cross sections predicted by MatchBox and the PowhegBox program were found to be in good agreement at $59.01^{+32\%}_{-24\%}$ and $59.36^{+33\%}_{-23\%}$ fb respectively, where the indicted uncertainties were obtained by varying the renormalization and factorization scales simultaneously by a factor of two around the central value. Dif-

ferential distributions of $m_{\tilde{t}_1\tilde{t}_1^*}$ and $p_{T,\tilde{t}_1}$ were again produced and are shown in the upper left and right-hand plots of Figure 3.2. Distributions of the transverse momentum of the top squark-antisquark pair[5], $p_{T,\tilde{t}_1\tilde{t}_1^*}$, are shown in the bottom panel of Figure 3.2. The blue dashed and red solid lines show the central values calculated using PowhegBox and Matchbox respectively. The uncertainty resulting from the variation of μ_R and μ_F is indicated for each line by the band of corresponding colour. In all cases, the distributions produced with the Matchbox and PowhegBox implementations agree within the uncertainty bands. For the $m_{\tilde{t}_1\tilde{t}_1^*}$ and $p_{T,\tilde{t}_1}$ observables, differences are seen in the slopes of the distributions. This is due to the use of different kinematic mappings between the Born and real-emission phase space variables. The Matchbox implementation uses mappings which are consistent with the Catani-Seymour subtraction formalism, as described in Refs. [116] and [117] for massless and massive final-state particles respectively, while the PowhegBox implementation instead uses a mapping consistent with the FKS subtraction method, which is detailed in Ref. [79]. Some deviation is also seen in the $p_{T,\tilde{t}_1\tilde{t}_1^*}$ distribution, specifically in the low p_T region. This is to be expected given that the IR cutoff of the radiation phase space differs between the two implementations. In the region $p_T \gtrsim 500$ GeV, the shapes of the $p_{T,\tilde{t}_1\tilde{t}_1^*}$ distributions are in excellent agreement while the normalization shows an $\mathcal{O}(1\%)$ deviation consistent with the difference observed in the values of the total cross section. In general, the level of agreement observed between the results generated with Matchbox and the PowhegBox program is high, giving us confidence in the validity of the Matchbox implementation of Powheg style ME corrections.

[5] $p_{T,\tilde{t}_1\tilde{t}_1^*}$ is defined as the transverse component of the vectorial sum of the top squark and antisquark momenta.

3.2 Parton-level results

3.2.1 Setup

Having established the validity of the MATCHBOX ME correction algorithm in Section 3.1, we now go on to study its impact on parton-level events. To do so, pp collisions were simulated at $\sqrt{s} = 14$ TeV in which a top squark-antisquark pair was produced. Unless otherwise stated, the squarks were not allowed to decay. The CTEQ6L1 PDF set was used and the mass of the top squark was again $m_{\tilde{t}_1} = 700$ GeV. The renormalization and factorization scales were set to $\mu_R = \mu_F = \min(m_{T,\tilde{t}_1}, m_{T,\tilde{t}_1^*})$, where $m_{T,\tilde{t}_1}$ ($m_{T,\tilde{t}_1^*}$) is the transverse mass of the top (anti)squark. Simulations were considered in which either the parton shower was limited to the production of the POWHEG emission only, or the full parton-shower evolution took place. In the latter case, the truncated component of the parton shower required in ME corrected events is included by default, unless it is stated otherwise. In all simulations, the effects of hadronization and the underlying event were not generated.

Events were again analysed using the Rivet framework. For cases in which the full parton shower was simulated, all final-state particles excluding the stable top squarks were clustered into jets using the FASTJET [92] implementation of the anti-k_T algorithm [99] with the energy recombination scheme and a distance parameter $R = 0.4$. The resulting jets were required to have pseudorapidity and transverse momentum satisfying $|\eta_j| < 4.9$ and $p_{T,j} > 20$ GeV respectively. Unless otherwise stated, no additional event selection criteria have been imposed.

Throughout this section, by default, ME corrected results have been generated using the LoopSim method, *i.e.* by restricting the phase space accessible to shower-type POWHEG emissions, including the remaining hard real-emission contribution as a separate subprocess and restoring the unitarity of the parton shower by modifying the Born contribution. The division of the real-emission contribution was done using the resummation profile in Eq. 1.4.50 with the default parameter setting $\rho = 0.3$, and the natural starting scale of the shower set to $p_T^{\text{hard}} = \mu_F$. Finally, the uncertainty in results due to limited statistics is indicated by error bars in the distributions, except in the central values of ratio plots where it is instead shown by a yellow error band.

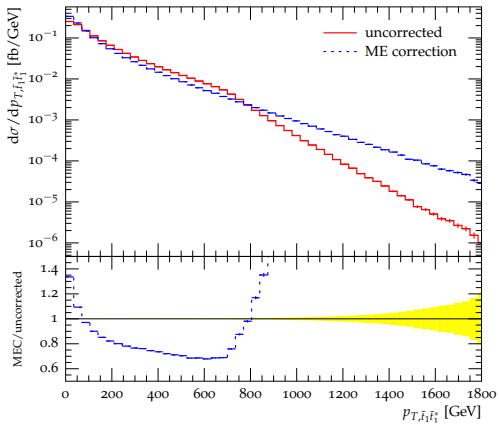

Figure 3.3: Distributions of the transverse momentum of the top squark pair, $p_{T,\tilde{t}_1\tilde{t}_1^*}$, in simulations of LHC collisions at $\sqrt{s} = 14$ TeV. Leading-order and matrix-element corrected MATCHBOX events, including simulation of the full parton shower, are compared for top squarks of mass $m_{\tilde{t}_1} = 700$ GeV.

3.2.2 Effect of the correction

We begin by comparing results generated with no correction with those produced when the POWHEG style ME correction is applied, in both cases including simulation of the full parton shower. Figure 3.3 shows the distributions of $p_{T,\tilde{t}_1\tilde{t}_1^*}$ corresponding to the uncorrected (solid red line) and ME corrected (dashed blue line) events. Two effects are evident in this plot. In the low p_T region, the distribution generated using the uncorrected parton shower is significantly harder than the ME corrected result. This is in agreement with the findings in Chapter 2 and is a consequence of the Herwig++ shower kernels overestimating the exact real-emission matrix element away from the strict soft-collinear limit. This causes the uncorrected Herwig++ parton shower to overpopulate some hard regions of the parton-shower phase space. In addition to this shift in the low p_T region, in the region $p_T \gtrsim m_{\tilde{t}_1}$ the ME corrected distribution significantly exceeds the uncorrected one. As was discussed in Section 1.3.2, the starting scale of the angular-ordered parton shower in Herwig++ is chosen such that the regions of phase space accessible to emissions from the various shower progenitors do not overlap. This construction is necessary to avoid double counting of radiation but also typically gives rise to a region of phase space which is

entirely unpopulated by the parton shower. This inaccessible dead zone corresponds to high p_T emissions and therefore we see a shortage of events in the hard tail of the uncorrected $p_{T,\tilde{t}_1\tilde{t}_1^*}$ distribution. In contrast, in the ME corrected approach the hardest emission in the shower is distributed according to the full real-emission matrix element and populates the entire available phase space. Therefore, we do not see this unphysical deficit of events in the high p_T region when the ME correction is included.

3.2.3 Effect of the truncated shower

In Section 1.4.5, the construction of the POWHEG formalism for angular-ordered parton showers was outlined. For this choice of ordering variable it is necessary to include a vetoed and truncated component of the parton shower. This simulates soft wide-angle radiation that would otherwise be missed by direct showering starting from the POWHEG corrected hard process. In previous studies, the inclusion of this truncated shower was found to have little impact on results generated using the POWHEG formalism.

In this section, we study the effect of including the truncated parton shower for the case of top squark-antisquark pair production. Furthermore, we provide a prescription by which events generated using specialist POWHEG matrix-element generators may be best interfaced with the Herwig++ angular-ordered parton shower.

To study the effects of the truncated shower, ME corrected events were generated as described in Section 3.2.1. Three parton-shower approaches were considered and are described below.

1. Truncated shower: In this setup, the vetoed-truncated shower required to ensure population of the entire shower phase space is included. The real-emission configuration generated by the matrix-element correction is reinterpreted in terms of a Born configuration and a parton-shower emission. In doing so, the emission is identified as being either initial-state radiation (ISR) or final-state radiation (FSR). This in turn dictates the exact form of the momentum reshuffling which is applied after the parton-shower evolution has

terminated in order to ensure energy-momentum conservation[6]. The inverse of this kinematic reconstruction procedure, along with the radiative variables of the POWHEG emission, is used to determine the value of the shower evolution variable corresponding to the POWHEG emission, $\tilde{q}_h$. Radiation is then generated by the conventional parton shower in the phase-space regions $\tilde{q}_0 > \tilde{q} > \tilde{q}_h$ and $\tilde{q}_h > \tilde{q} > \tilde{q}_{\min}$, in both cases requiring the transverse momentum of any splittings to be less than that of the POWHEG emission. Here $\tilde{q}_0$ and $\tilde{q}_{\min}$ are the maximum starting value and IR cutoff of the angular ordering parameter.

When the phase space of the POWHEG emission is divided such that there are both shower and hard real-emission events, the shower events are treated using the aforementioned prescription. Events generated using the hard component of the real-emission matrix element are showered directly, with each coloured leg in the hard process acting as a shower progenitor. The starting scale of the shower evolution variable is determined using the default Herwig++ convention. As such, the colour connected partner of a gluon emission, which is not uniquely defined, is assigned at random with equal probability of selecting each of the two possibilities. Finally, emissions generated by the conventional shower are not required to have transverse momentum less than that of the POWHEG emission. However, they are required to be softer than the maximum transverse momentum scale of the shower, which here has been set equal to the factorization scale.

2. No truncated shower: This approach proceeds as with the truncated shower case, with the real-emission configuration in S-events being used to define a parton-shower splitting. However, in this scheme radiation from the conventional shower is limited to the region $\tilde{q}_h > \tilde{q} > \tilde{q}_{\min}$. Hard real-emission events are treated as they were in the truncated shower case.

3. Direct shower: In this setup, the real-emission configuration in S-events is showered directly, using a similar approach to that applied to hard real-

[6]The momentum reshuffling procedure used in Herwig++ was outlined in Section 1.3.2 and more details can be found in Ref. [6].

emission configurations in the truncated shower case. Each coloured external leg is treated as a shower progenitor and the starting scale of the shower is determined using the default shower convention. As such, the value of the evolution variable corresponding to the POWHEG emission is determined without reinterpretation of the emission as a parton-shower splitting. Typically, this means that the region of phase space populated with parton-shower emissions in this procedure matches neither of the previous two cases. In addition, using the direct shower approach causes the default kinematic reconstruction procedure to treat all POWHEG emissions as FSR. Accordingly, at the end of the parton-shower evolution the momenta of the stop, antistop and POWHEG emission are boosted by a common factor to restore momentum conservation. If instead the radiation was treated as ISR, as should be the case in the majority of events, the momentum reshuffling would be performed in such a way that the invariant mass of the stop-antistop pair was preserved. Finally, as in the previous approaches, the transverse momenta of all subsequent shower emissions in S-events are required to be less than that of the POWHEG emission.

Events generated with the hard component of the real-emission matrix element are treated in the same way as the S-events, but with no requirement on subsequent emissions to be softer than the POWHEG one.

We note that this procedure corresponds to the approach taken when an external POWHEG matrix-element generator is interfaced to the Herwig++ angular-ordered parton shower[7]. While it is often considered to be an alternative to the approach which includes no truncated parton shower, there are clearly significant differences between the two procedures.

Figure 3.4 shows distributions of $m_{\tilde{t}_1\tilde{t}_1^*}$ (top left), $p_{T,\tilde{t}_1}$ (top right), $p_{T,\tilde{t}_1\tilde{t}_1^*}$ (bottom left) and $\Delta R(\tilde{t}_1\tilde{t}_1^*, j_1)$ (bottom right) generated using each of the shower procedures

[7]In fact, when an external POWHEG matrix-element generator is interfaced to the Herwig++ angular-ordered parton shower, all events are treated as S-events. However given the similarity in the treatment of S and H-events in this approach, this difference has negligible impact in practice.

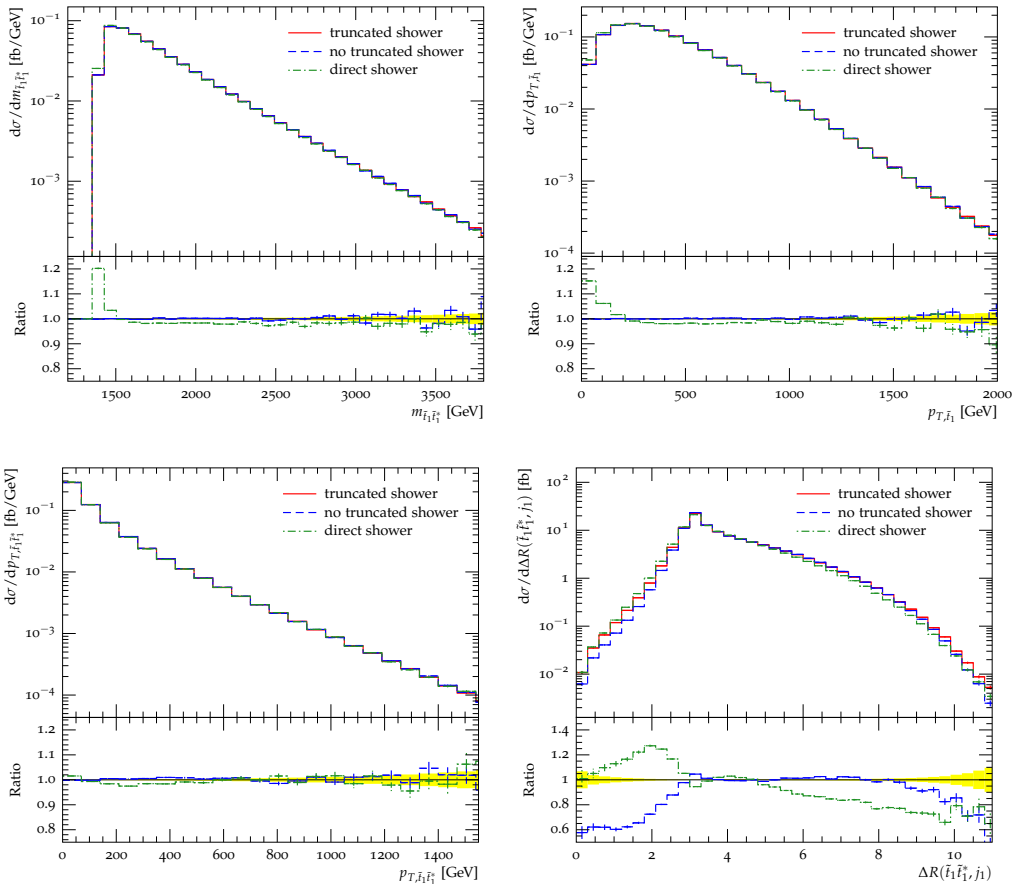

Figure 3.4: Distributions of the invariant mass of the top squark pair $m_{\tilde{t}_1\tilde{t}_1^*}$ (upper left), the inclusive top squark transverse momentum $p_{T,\tilde{t}_1}$ (upper right), the transverse momentum of the top squark pair $p_{T,\tilde{t}_1\tilde{t}_1^*}$ (bottom left) and separation of the hardest jet and $\tilde{t}_1\tilde{t}_1^*$ system $\Delta R(\tilde{t}_1\tilde{t}_1^*, j_1)$ (bottom right). Matrix-element corrected MATCHBOX events were generated at a centre-of-mass energy of 14 TeV for each of the three shower procedures described in Section 3.2.3.

outlined above. The $\Delta R(\tilde{t}_1\tilde{t}_1^*, j_1)$ variable is defined as

$$\Delta R(\tilde{t}_1\tilde{t}_1^*, j_1) = \sqrt{\Delta\phi^2_{\tilde{t}_1\tilde{t}_1^*,j_1} + \Delta\eta^2_{\tilde{t}_1\tilde{t}_1^*,j_1}}, \tag{3.2.1}$$

where $\Delta\phi_{\tilde{t}_1\tilde{t}_1^*,j_1}$ and $\Delta\eta_{\tilde{t}_1\tilde{t}_1^*,j_1}$ are the differences in azimuthal angle and pseudorapidity of the $\tilde{t}_1\tilde{t}_1^*$ system and the highest transverse momentum jet in each event. The lower panel in each plot shows the ratios of results generated with no truncated shower or with the direct shower procedure, to those which include the full truncated shower simulation.

Comparing the distributions generated with the truncated shower (solid red line) to those produced without the truncated shower (dashed blue line), we see negligible differences in the $m_{\tilde{t}_1\tilde{t}_1^*}$ and $p_{T,\tilde{t}_1}$ distributions. Radiation generated by the parton shower does not impact significantly on these observables since the majority of emissions are produced in the initial state. Accordingly, including or excluding the soft-wide angle radiation generated by the truncated shower has no effect. The $p_{T,\tilde{t}_1\tilde{t}_1^*}$ spectrum in the lower left-hand panel of Figure 3.4 also exhibits minimal sensitivity to the additional emissions produced by the truncated shower. In the $\Delta R(\tilde{t}_1\tilde{t}_1^*, j_1)$ distribution, the two shower procedures give similar results in the region $\Delta R > \pi$, where the distributions are predominantly sensitive to the configuration of the $\tilde{t}_1\tilde{t}_1^*$ system and the hardest jet. The hardest jet in each event should originate from the POWHEG emission and so is largely unaffected by the inclusion of the truncated shower. A small difference in the distributions is however seen in the large ΔR limit. This effect is due to the soft wide-angle emissions in the truncated shower causing the hardest jet in each event to be less central in rapidity than it would be if this component of radiation was not simulated. Furthermore, including the truncated shower also affects the softer jets produced by the parton shower. The amount of radiation in each event is increased, particularly when the transverse momentum of the POWHEG emission is low and therefore the phase space available for truncated emissions is at its largest. This leads to a slight hardening of all jets other than the hardest. This effect is evident in the region $\Delta R < \pi$, where the observable is sensitive to all radiation not contributing to j_1. When no truncated shower is simulated, less events are produced in which the $\tilde{t}_1\tilde{t}_1^*$ system and hardest jet deviate from a back-to-back configuration, and therefore less events populate the low ΔR bins.

Significant changes in the distributions in Figure 3.4 are observed when considering the results generated with the direct shower (dash-dotted green line). The $m_{\tilde{t}_1\tilde{t}_1^*}$ and $p_{T,\tilde{t}_1}$ distributions are consistently shifted to lower values when compared with the results generated both with and without the truncated shower. This is a result of the misinterpretation of ISR as FSR during the kinematic reshuffling, which causes the reconstruction procedure to have an unphysical impact on the momenta of the stop and antistop in the case that the emission was actually ISR.

In addition, the $p_{T,\tilde{t}_1\tilde{t}_1^*}$ spectrum generated with the direct shower displays a slight softening when compared with the other shower procedures, while the shape of the $\Delta R(\tilde{t}_1\tilde{t}_1^*, j_1)$ distribution shows more marked deviations, in general being shifted towards lower values. The overall impact of the parton shower does not different significantly for the three shower cases, however we clearly see that the distribution of the radiation in the event does. This is the result of not interpreting shower-type POWHEG emissions in terms of parton-shower splittings. Instead, the starting scale of the shower is calculated from the real-emission configuration in such a way that, for the dominant gluon emission contribution, the value will be maximized in 50% of events. This appears to produce more wide-angle radiation than would be present if the same real-emission configuration was treated as a parton-shower splitting. In general, this causes the hardest jet produced in the direct shower to be softer than in the other approaches, while the subleading shower jets become significantly harder.

The results presented in Figure 3.4 clearly illustrate that the direct shower approach, as it stands, does not provide an alternative to the case with no truncated shower. However, the behavior of the direct shower procedure may be improved through slight modification of the default Herwig++ shower setup. Firstly, the prescription for choosing the colour partner of gluon emissions may be modified so that the partner that minimises the starting value of the angular evolution parameter is always selected. In doing so, less wide-angle radiation is generated and the procedure more closely resembles the case that the real-emission configuration was interpreted as a shower splitting. In addition to this, the FSR kinematic reconstruction procedure may be modified so that the top squark and antisquark pair are treated as a single system. The reshuffling then proceeds via a rescaling of the momenta of the POWHEG emission and the $\tilde{t}_1\tilde{t}_1^*$ system, and therefore more closely reflects the procedure applied to ISR.

Figure 3.5 shows analogous distributions to those in Figure 3.4, now including the aforementioned modifications for the direct shower. Here we see excellent agreement between all three approaches in the $m_{\tilde{t}_1\tilde{t}_1^*}$ and $p_{T,\tilde{t}_1}$ distributions. In the $p_{T,\tilde{t}_1\tilde{t}_1^*}$ distribution, the direct shower procedure gives rise to slightly softer results due to the new kinematic reconstruction procedure. The direct shower $\Delta R(\tilde{t}_1\tilde{t}_1^*, j_1)$ distribution is

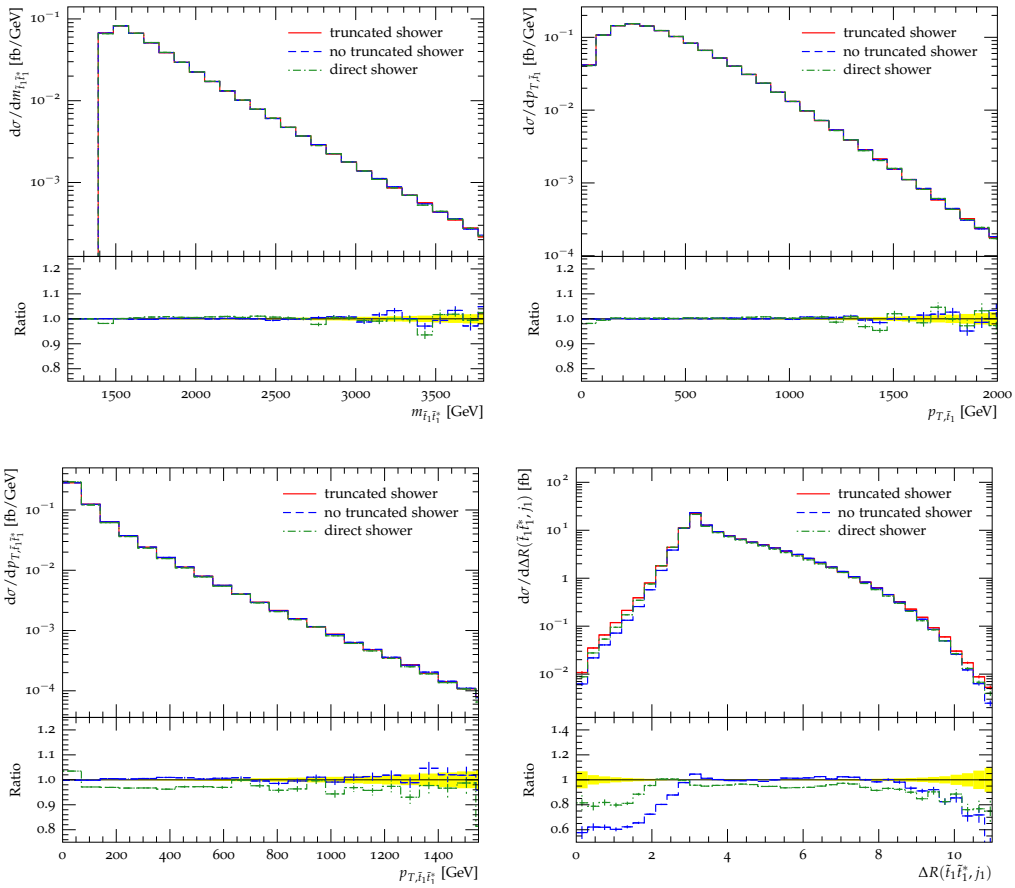

Figure 3.5: As in Figure 3.4, now including improvements to the kinematic reshuffling procedure and calculation of the parton-shower starting scale in the direct shower approach.

now in significantly better agreement with those generated using the other shower approaches, in particular with the case in which no truncated shower is simulated. A slight decrease in the normalization of the direct shower spectrum is observed, which is due to a reduction in the number of events which satisfy $p_{T,j_1} > 20$ GeV. Excluding this change, the direct and no truncated shower distributions are in excellent agreement in the region $\Delta R > \pi$. Some small discrepancy is still seen for $\Delta R < \pi$. However, we note that this region of phase space is sensitive to uncorrected parton-shower emissions and therefore has large associated uncertainties. In general, the modified direct shower approach does now provide a sensible alternative to the case in which no truncated shower is simulated.

Finally we note that here, and in the remainder of this work, we have used

the parton-shower setup that is the default choice in Herwig++ version 2.7.1. As such, the kinematics in processes with colour flows where no colour singlet can be constructed, *e.g.* $gg \to \tilde{t}_1\tilde{t}_1^*$, are reconstructed by treating first the final-state progenitors and then the initial-state progenitors, using the procedure outlined in Section 1.3.2. In Herwig++ version 3.0, a number of modifications will be made to the default parton-shower algorithm, including changes to the kinematic reconstruction procedure. In the new approach, the colour system containing the progenitor that radiated the highest transverse momentum emission is reconstructed first, again using the original procedure outlined in Section 1.3.2. This process is applied recursively, taking next the progenitor with the second hardest emission and so forth. One consequence of this modification is that the unphysical treatment of the stop and antistop momenta in the direct shower approach is corrected. As such once the procedure for choosing the colour connected partner of gluon emissions is modified, results generated using the direct shower in Herwig++ version 3.0 are in relatively good agreement with those generated with no truncated shower, although again exhibit a slightly softening of the $p_{T,\tilde{t}_i\tilde{t}_1^*}$ distribution.

3.2.4 Division of the real-emission phase space

In this section we investigate the impact of limiting the starting scale of shower-type POWHEG emissions using the phase-space restriction functions introduced in Section 1.4.3. To this end, matrix-element corrected events were generated using the setup described in Section 3.2.1, with the phase space accessible to S-events either maximal or restricted using the sharp, hfact or resummation profiles. The natural starting scale of the shower, p_T^{hard}, was set equal to the factorization scale in the sharp and resummation profiles, and in the latter the default setting $\rho = 0.3$ was used. As is typical, a fixed value of the natural scale was used in the hfact profile, which was chosen to be $p_T^{\text{hard}} = 350$ GeV. For each of the restricted phase space cases, LoopSim corrections were used to restore the unitarity of the parton shower.

Figure 3.6 shows distributions of $m_{\tilde{t}_1\tilde{t}_1^*}$, $p_{T,\tilde{t}_1}$, $p_{T,\tilde{t}_1\tilde{t}_1^*}$ and[8] $\Delta R(\tilde{t}_1, \tilde{t}_1^*)$ corresponding

[8]The variable $\Delta R(\tilde{t}_1, \tilde{t}_1^*)$ is defined as in Eq. 3.2.1, but replacing the momenta of the hardest

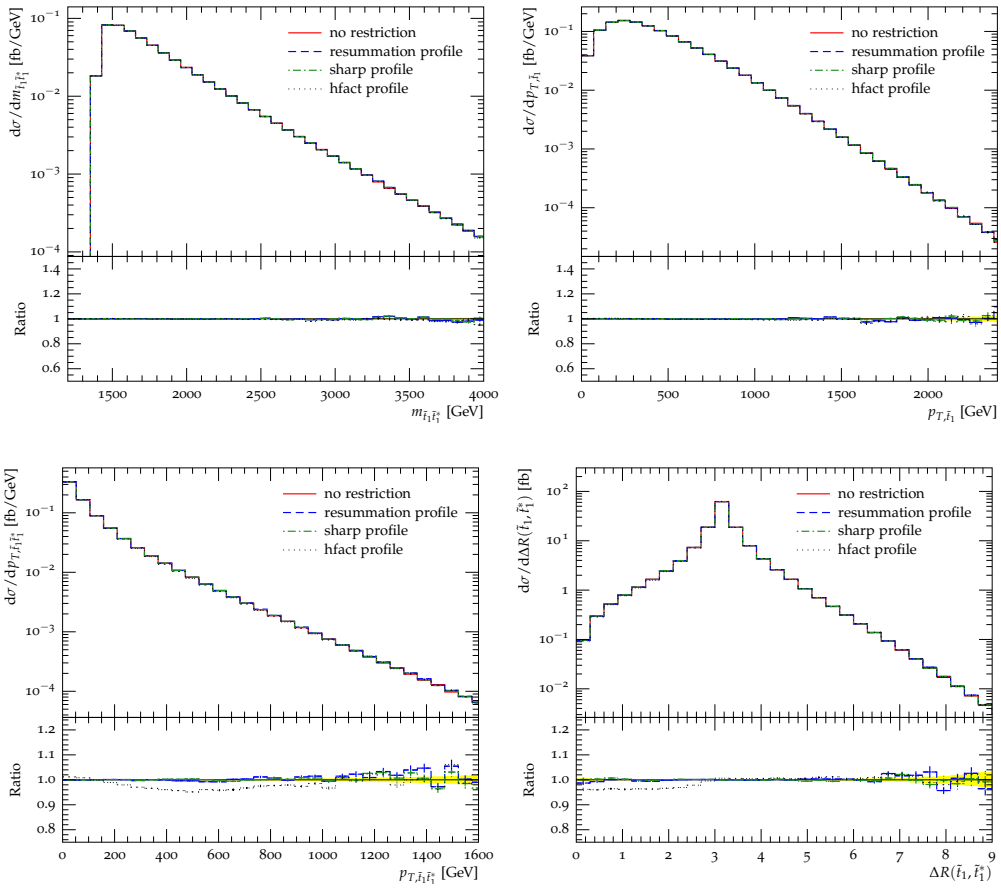

Figure 3.6: Distributions of the invariant mass of the top squark pair $m_{\tilde{t}_1\tilde{t}_1^*}$ (upper left), the inclusive top squark transverse momentum $p_{T,\tilde{t}_1}$ (upper right), the transverse momentum of the top squark pair $p_{T,\tilde{t}_1\tilde{t}_1^*}$ (bottom left) and separation of the top squark and antisquark $\Delta R(\tilde{t}_1, \tilde{t}_1^*)$ (bottom right). Matrix-element corrected distributions are shown for the cases in which the phase space of the shower-type POWHEG emission is either maximal or restricted using the sharp, hfact or resummation profiles.

to ME corrected events generated with the full phase space (red solid line), resummation (blue dashed line), sharp (green dot-dashed line) and hfact (black dotted line) phase-space restrictions. In this case, the parton-shower evolution has been limited to generating the POWHEG emission only. The lower panel in each plot shows the ratios of distributions generated with each form of phase-space restric-

jet and $\tilde{t}_1\tilde{t}_1^*$ system with the momenta of the top squark and antisquark.

tion, to the one generated with the full phase space available to the shower-type POWHEG emission.

For POWHEG emissions with transverse momentum $p_T < p_T^{\rm hard}$, restricting the phase space of the shower-type emissions affects both the normalization of the Born configuration and the exponent of the Sudakov form factor. The former is decreased by the restriction while the latter increases, and consequently no significant effect is expected in the distributions. For high transverse momentum emissions, the restricted phase space distributions are generated with the hard component of the real-emission matrix element only, whereas in the unrestricted case an additional Sudakov form factor multiplies this term. However, the Sudakov factor approaches unity in the high p_T limit and so again no significant difference between the restricted and unrestricted cases is expected.

As predicted, the sharp and resummation profile restrictions have minimal impact on all the distributions in Figure 3.6, as compared with the unrestricted case. However, some differences are seen in the $p_{T,\tilde{t}_1\tilde{t}_1^*}$ and $\Delta R(\tilde{t}_1, \tilde{t}_1^*)$ spectra generated with the hfact profile restriction. These distributions exhibit a softening of the POWHEG emission when compared to the other phase space options. This is a result of the lower value of $p_T^{\rm hard}$ used in the hfact restriction, which causes a larger fraction of the real-emission contribution to be included in the finite hard term and consequently a smaller exponent in the Sudakov form factor. It has been verified that distributions generated with the hfact profile with $p_T^{\rm hard} = 1$ TeV are in better agreement with those shown for the sharp, resummation and unrestricted cases.

It should be noted that a relatively large value of $p_T^{\rm hard}$ was chosen in this study, in an attempt to avoid causing problems with the Sudakov resummation in the singular regions of phase space. However, typically $p_T^{\rm hard}$ in the hfact approach is set to much lower values, see for example Ref. [22]. Given that deviations are seen in the Sudakov region already with $p_T^{\rm hard} = 350$ GeV, clearly the use of lower values is poorly motivated. However, with suitably large values of the natural starting scale, the hfact profile restriction is a reasonable alternative to the resummation profile restriction which is used by default in Herwig++[9].

[9]This conclusion pertains to the case of ME corrections only. When considering the full

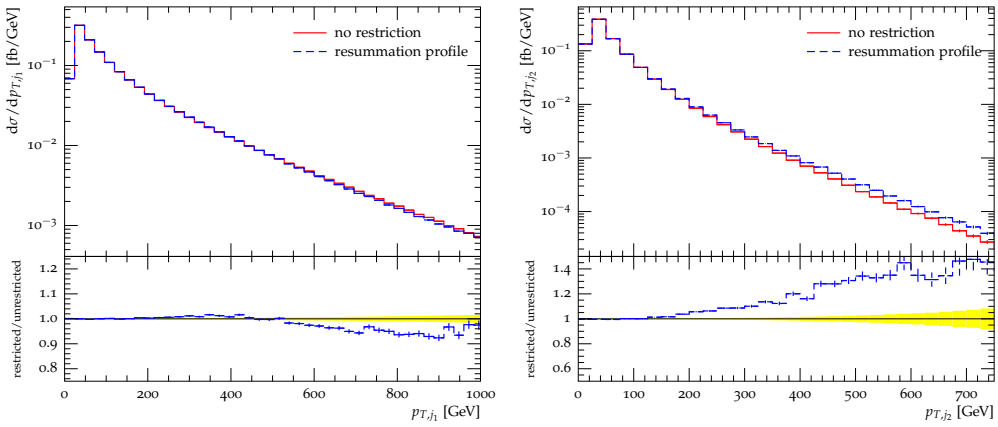

Figure 3.7: Distributions of the transverse momentum of the hardest p_{T,j_1} (left) and second hardest p_{T,j_2} (right) jet in each event. Matrix-element corrected distribution are shown for the cases in which the phase space of the shower-type POWHEG emission is either maximal or restricted using the resummation profile.

Restricting the phase space of the shower-type POWHEG emission has a more significant impact when the effect of the full parton shower is simulated. Figure 3.7 shows distributions of the transverse momentum of the hardest, p_{T,j_1}, and second hardest jet, p_{T,j_2}, in events generated with either unrestricted phase space (red solid line) or using the resummation profile restriction (blue dashed line). When the resummation profile restriction is applied, the transverse momentum of the hardest jet is reduced slightly. Conversely, the $p_{T,j2}$ distribution is shifted to higher values, an effect which prevails also in the subsequent softer jets. As was discussed in the previous section, hard real-emission events are showered directly with the starting scale of the parton shower governed by the default Herwig++ convention. This leads to the production of more wide-angle radiation than would otherwise be present if the event was treated as an S-event, as would be the case in the unrestricted phase space scenario. This causes the observed redistribution of radiation in the event, away from the hardest jet.

POWHEG correction, using the hfact profile leads to corrected emissions that are significantly harder than those produced in the other restricted phase space cases. Furthermore, uncertainties associated with varying the value of p_T^{hard} are unrealistically small for the hfact profile, see Ref. [84] for more details.

Here we show results for the resummation profile restriction only, since this approach will be used throughout the remainder of the thesis. However, the same effect is observed also when the real-emission phase space is divided using the hfact and sharp profiles, with the former showing more significant changes again due to the lower value of p_T^{hard}.

3.2.5 Combining corrections to stop production and decay

So far, in this chapter we have studied the impact of including POWHEG style ME corrections during the production stage of the event only. However, clearly it is desirable to combine this ME correction with the one studied in Chapter 2 which applies to the decays of new particles. In doing so, multiple hard emissions in each event are corrected to LO accuracy.

In this section, we study the effect of including both corrections by considering the case in which top squarks are pair produced, as described in[10] Section 3.2.1, and then decay via $\tilde{t}_1 \to b\tilde{\chi}_1^+$ or the equivalent conjugate mode. For simplicity, the charginos that are created are not allowed to decay further. We consider the benchmark scenarios with $(m_{\tilde{t}_1}, m_{\tilde{\chi}_1^+}) = (700, 200)$ GeV and $(225, 180)$ GeV. In both cases, the mixing matrices of both the top squarks and the charginos were maximized, and the width of the top squark was calculated internally by Herwig++. All final-state particles, excluding the $\tilde{\chi}_1^\pm$, were clustered into jets as described in Section 3.2.1. Jets were identified as b-tagged if they were found to lie within $\Delta R = 0.3$ of a final-state bottom quark[11]. The missing transverse momentum in each event was determined from the vector sum of the transverse momentum of all visible final-state particles[12]. The magnitude of this quantity, E_T^{miss}, was calculated and is

[10]For results shown in this and the next section, the event generation setup in Section 3.2.1 was modified slightly to include the correction to wide-angle gluon emissions described in Ref. [118]. This modification has negligible impact on results which have ME corrections applied during the production of the top squarks, but does have an $\mathcal{O}(20\%)$ effect of distributions generated without this ME correction, in general increasing the amount of radiation in events.

[11]$\Delta R = \sqrt{\Delta\eta^2 + \Delta\phi^2}$, where $\Delta\eta$ and $\Delta\phi$ are the differences in pseudorapidity and azimuthal angle of the jet and bottom quark, respectively.

[12]For the purpose of this analysis, the $\tilde{\chi}_1^\pm$ are treated as invisible.

plotted along with the transverse momentum distributions of the hardest b-tagged jet, p_{T,b_1} and the hardest, p_{T,j_1}, and second hardest, p_{T,j_2}, non b-tagged jets in each event. For each observable, results are shown for the cases in which either no ME corrections were applied (solid red line) or ME corrections were applied to the top squark decays (blue dashed line), production (green dot-dashed line) or to both the production and decays (dotted black line). The lower panel in each plot shows the ratio of results generated with one or both of the ME corrections to those which include no ME corrections.

Beginning with the high mass scenario with $(m_{\tilde{t}_1}, m_{\tilde{\chi}_1^+}) = (700, 200)$ GeV, the upper left-hand panel of Figure 3.8 show the transverse momentum distribution of the hardest non b-tagged jet in each event. Here we see that applying ME corrections to the decays of the top squarks causes a slight softening of the p_{T,j_1} distribution when compared with the uncorrected case. Including this ME correction reduces the transverse momentum of the hardest emission produced in the parton shower initiating from the decay. This is reflected in the soft region of the p_{T,j_1} distribution, while no significant change is seen in the high p_T regime. A much more dramatic effect is observed when ME corrections are applied to the production of the stop-antistop pair. In this case, a significant softening of the p_{T,j_1} distribution occurs in the low p_T region, while in the high p_T region we see the impact of populating the dead zone in the parton shower produced from the production process. This closely reflects the effects seen in Section 3.2.2. When the corrections to the production and decay stages are applied together, the transverse momentum of multiple emissions in each event will be reduced. Accordingly, we see further softening of the p_{T,j_1} distribution in the low p_T region when compared with the distribution generated with ME corrections in the production phase only.

Similar effects are seen in the upper right-hand panel of Figure 3.8, which shows the transverse momentum of the second hardest jet in each event. The POWHEG corrected emission will typically undergo further splittings during the remainder of the parton shower, meaning that the impact of the ME corrections are normally evident in several shower jets. Consequently, the same general effects seen in the p_{T,j_1} spectrum are observed also in the distributions of p_{T,j_2}.

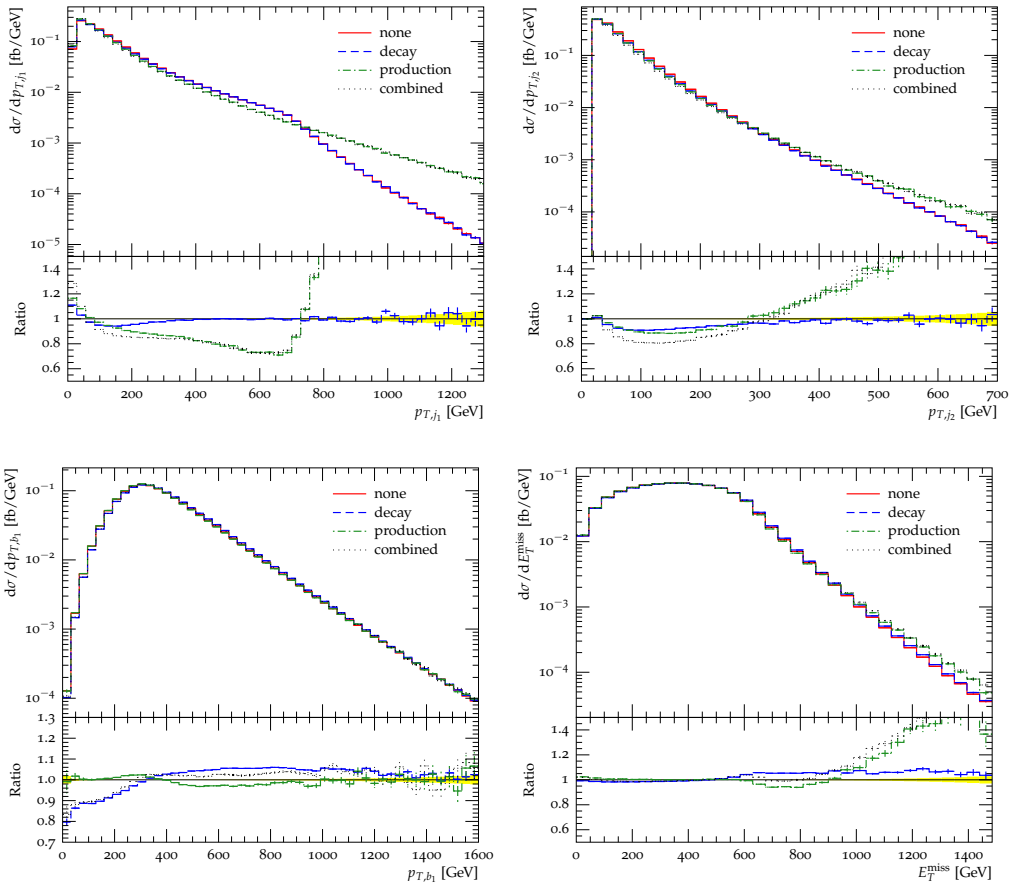

Figure 3.8: Distributions of the transverse momentum of the hardest p_{T,j_1} (upper left) and second hardest p_{T,j_2} (upper right) non b-tagged jets in each event, the transverse momentum of the hardest b-tagged jet p_{T,b_1} (lower left) and the missing transverse energy E_T^{miss} (lower right). Results are shown for the cases in which either no ME corrections have been applied or ME corrections have been applied to the top squark production, decays or both. Events were generated at a centre-of-mass energy of 14 TeV for the benchmark scenario with $(m_{\tilde{t}_1}, m_{\tilde{\chi}_1^+}) = (700, 200)$ GeV.

The transverse momentum distribution of the hardest b-tagged jet in each event is shown in the lower left-hand panel of Figure 3.8. For this observable, the most significant effect is seen when ME corrections are applied to radiation generated in the top squark decays. The softening of the hardest emission in the decay is compensated for by an increase in the transverse momentum of the decay products, and this is visible in the p_{T,b_1} spectrum. On the other hand, applying an ME correction to the production stage of the event causes only a very slight softening of

the p_{T,b_1} distribution. This is to be expected given that the transverse momentum distribution of the bottom quark largely reflects that of its parent top squark, which in turn displays little sensitivity to ME corrections applied during the production process. Correcting emissions both in the production and decay stages of the event leads to some cancellation between these two effects, but still results in significant deviation from the uncorrected distribution in the low p_T region. The same effect is seen also in the p_T spectrum of the second hardest b-tagged jet in each event.

Finally, the magnitude of the missing transverse momentum in each event is plotted in the lower right-hand panel of Figure 3.8. The shape of this distribution is largely governed by the momenta of the charginos produced in the top squark decays. Therefore, applying ME corrections in the decay stage of the event causes a slight shift of the E_T^{miss} spectrum to higher values, reflecting the hardening of the decay products. When a ME correction is applied in the production stage, we see a more significant shift from intermediate to high values of E_T^{miss}. Configurations with large values of E_T^{miss} arise when the top squark pair recoil against a high p_T initial-state emission. Therefore, the missing transverse energy distribution is directly affected by the hardest emission generated during the top squark production, such that the changes in the E_T^{miss} spectrum follow the same trend as those seen in the distributions of p_{T,j_1} and p_{T,j_2}. Combining corrections in the production and decay stages leads to a cancellation of effects at intermediate values of E_T^{miss} and a compound increase in the high E_T^{miss} region.

Equivalent distributions to those shown in Figure 3.8 are shown in Figure 3.9 for the compressed benchmark scenario with $(m_{\tilde{t}_1}, m_{\tilde{\chi}_1^+}) = (225, 180)$ GeV. Considering first the p_{T,j_1} distribution, we see that applying ME corrections to the decays of the top squarks has very little visible impact. This is because the maximum allowed transverse momentum of emissions in the decay shower is low, owing to the compressed nature of the mass spectrum. Therefore, the expected softening of the p_{T,j_1} distribution occurs at very low values of the transverse momentum where the selection criterion $p_{T,j} > 20$ GeV also applies. When ME corrections are applied during the production process, significant changes are seen which reflect those present in the $(m_{\tilde{t}_1}, m_{\tilde{\chi}_1^+}) = (700, 200)$ GeV scenario, but now with the effect of the parton-

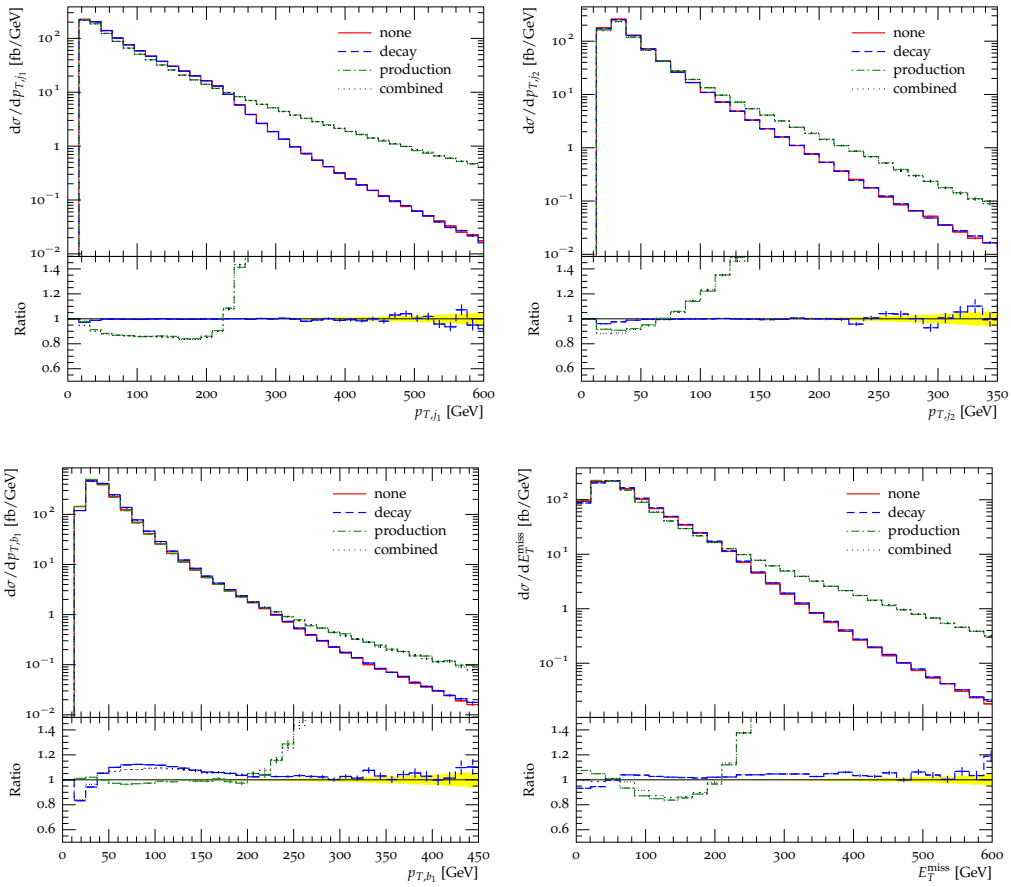

Figure 3.9: As in Figure 3.8, but for the compressed benchmark scenario with $(m_{\tilde{t}_1}, m_{\tilde{\chi}_1^+}) = (225, 180)$ GeV.

shower dead zone evident for lower values of p_{T,j_1}. The distribution generated with ME corrections in both the production and decay stages closely follows the case where only the former correction is included and, as with the high mass scenario, the changes in the p_{T,j_1} distributions are also seen in the p_{T,j_2} plot.

A significant effect is seen in the p_{T,b_1} spectrum when ME corrections are included during the decays. We see an increase in the transverse momentum of the decay products, which is compensating for the softening of the hardest emission in the decay, as was the case in the high mass scenario. However in contrast to the high mass scenario, a significant effect is also seen when ME corrections are applied in the production stage of the event. This is because b-tagged jets arising from the top squark decays are now softer than those originating from the hardest emission, either from direct production of a bottom quark or from the radiation of a gluon

followed by the splitting $g \to b\bar{b}$. Therefore, the softening of the hardest emission in the low p_T region and population of the parton shower dead zone of the production process is again visible. Applying the corrections to the hardest emissions in the production and decay stages results in a combination of these effects.

Finally in the E_T^{miss} distribution in Figure 3.9, we see that applying the ME corrections to the production and decay stages of the event has similar effects to those observed in the high mass scenario. The slight hardening of the chargino momenta is seen when ME corrections to the decays are included. In addition, applying the correction to the production process very clearly reflects the effects seen in the distribution of the hardest emission. The effect is more prominent here than in the high mass scenario because the inherent transverse momentum of the charginos is small, owing to the compressed nature of the mass spectrum, and therefore recoil arising from ISR has a greater impact on the distribution. Again when combining the corrections for the production and decay stages of the event, we see that the dominant effect comes from the correction to the production.

3.3 Effect of the correction on exclusion boundaries

In this section, the impact of including ME corrections to the production and subsequent decays of top squarks is studied within the context of an existing top squark search, described in Ref. [113], that was performed by the ATLAS collaboration using LHC Run 1 data. The search is sensitive to the direct production of a top squark-antisquark pair which decay via $\tilde{t}_1 \to b\tilde{\chi}_1^{\pm} \to b\tilde{\chi}_1^0 f f'$, giving rise to a signal of missing transverse energy and two b-tagged jets. The cases $\Delta m_{(\tilde{\chi}_1^{\pm}-\tilde{\chi}_1^0)} = 5$ GeV and 20 GeV were considered, making use of 20.1fb^{-1} of pp collision data at a centre-of-mass energy $\sqrt{s} = 8$ TeV. The set of selection criteria imposed in the study is summarized in Table 3.1 for the two distinct strategies referred to as signal region A (SRA) and signal region B (SRB), with more details available in Refs. [113, 119]. We note that the latter signal region is sensitive to events which have a hard jet originating from ISR radiation, in addition to the two b-tagged jets produced during the stop decays. Correspondingly, the selection criterion on the amount of missing

transverse energy is higher in this monojet-like search strategy than in the more conventional SRA approach.

To recreate the original analysis performed by the ATLAS collaboration, the selection criteria in Table 3.1 were implemented within the Rivet analysis framework. In order to validate this recast analysis, Herwig++ events were generated at a centre-of-mass energy of 8 GeV in which a top squark-antisquark pair was produced and decayed according to $\tilde{t}_1 \to b\tilde{\chi}_1^+ \to b\tilde{\chi}_1^0 f f'$. Events were generated without any POWHEG style ME corrections, and the branching ratio of the decay $\tilde{t}_1 \to b\tilde{\chi}_1^+$ was set to unity. The branching ratios of the 3-body decay $\tilde{\chi}_1^+ \to \tilde{\chi}_1^0 f f'$ were calculated internally in Herwig++, forcing the decay to proceed via an off-shell W-boson in order to be consistent with the decay channels considered in the original study. As in the original study, the effects of polarization due to the choice of top squark mixing were found to be negligible and so the mixing matrix was chosen to be maximal. In the absence of information about the electroweakino mixing matrices used in the ATLAS study, the lightest neutralino was chosen to be purely wino and the chargino to be a maximal admixture of the charged wino and higgsino interaction eigenstates. As in the original study, the PDF set CTEQ6L1 was used. The production cross-sections calculated by Herwig++ were corrected to NLO accuracy by applying a global renormalization factor calculated using the PROSPINO package [16, 17]. An indication of the uncertainty in this value was obtained by varying the factorization and renormalization scales simultaneously by a factor of two around the central value of $\mu_R = \mu_F = \min(m_{T,\tilde{t}_1}, m_{T,\tilde{t}_1^*})$. Events were simulated including the effects of parton showering, hadronization and the underlying event[13] but with no simulation of detector effects. The use of a b-tagging algorithm in the original study was, however, emulated by classifying jets as having originated from a b-quark if they were within $\Delta R = 0.3$ of a final-state B-hadron with $p_T > 5$ GeV. A p_T-dependent b-tagging efficiency was also imposed, having been obtained by fitting data in Ref. [123] and rescaling to account for differences in the average efficiency.

The correctness of our recast analysis was first verified by reproducing the cut

[13]The default set of tuned perturbative and non-perturbative parameters available in Herwig++ version 2.7.1 was used.

Selection criterion	Signal region A	Signal region B
E_T^{miss}	> 150 GeV	> 250 GeV
Leading jet, p_{T,j_1}	> 130 GeV	> 150 GeV
Subleading jet, p_{T,j_2}	> 50 GeV	> 30 GeV
Third jet, p_{T,j_3}	veto if > 50 GeV	> 30 GeV
$\Delta\phi(\mathbf{p}_T^{\text{miss}}, j_1)$	-	> 2.5
b-tagged jets	j_1 and j_2 b-tagged with $p_T > 50$ GeV, $\lvert\eta\rvert < 2.5$	j_2 and j_3 b-tagged with $p_T > 30$ GeV, $\lvert\eta\rvert < 2.5$
$\min_k(\Delta\phi(\mathbf{p}_T^{\text{miss}}, j_k))$ for $k \leq 3$	> 0.4	> 0.4
$E_T^{\text{miss}}/(\sum_{i=1}^{n} p_{T,j_i} + E_T^{\text{miss}})$	> 0.25, $n = 2$	> 0.25, $n = 3$
m_{CT} (see Refs. [120–122])	$> 150, 200, 250,$ $300, 350$ GeV	-
$H_{T,3} = \sum_i p_{T,j_i}$ for all $i > 3$	-	< 50 GeV
$m_{bb} = \sqrt{(p_{b,1} + p_{b,2})^2}$	> 200 GeV	-

Table 3.1: Summary of the selection criteria imposed in the ATLAS search for direct top squark pair production in final states with two b-tagged jets and missing transverse energy, E_T^{miss}. Shown separately are the criteria imposed in the signal regions A and B. Jets were ordered according to the magnitude of their transverse momentum, $p_{T,j}$, with $p_{T,j_1} > p_{T,j_2} > p_{T,j_3}$... and were required to fulfil $|\eta| < 2.8$. The difference in azimuthal angle between the missing transverse momentum vector, $\mathbf{p}_T^{\text{miss}}$, and the jet with the k-th highest transverse momentum, j_k, is written as $\Delta\phi(\mathbf{p}_T^{\text{miss}}, j_k)$. Finally, $p_{b,1}$ ($p_{b,2}$) represents the momentum of the leading (subleading) b-tagged jet. More details may be found in Ref. [113].

flow tables provided by the ATLAS collaboration in Ref. [119], and the m_{CT}, m_{bb}, E_T^{miss} and $H_{T,3}$ distributions in Ref. [113]. Some discrepancies were observed between results obtained using our recast analysis and those quoted in Ref. [119] for signal region B. However, this is to be expected given that simulation of the signal events in the original study was performed using MadGraph [124] interfaced to Pythia 6 [66]. In this setup, matrix-element level events are generated in which the top squark-antisquark pair is produced in association with different numbers of additional partons. The different event samples are then merged using the MLM prescription [74, 125, 126], before simulating the subsequent parton showering and hadronization stage of the event. By performing this matrix-element merging, a subset of the hard parton-shower emissions are corrected to LO accuracy. Therefore, we expect significant differences between results generated using this procedure and those produced with Herwig++, at least when considering search strategies that are sensitive to high p_T shower jets, like signal region B. With the exception of signal region B, good agreement was observed between the original ATLAS study and our recast results.

To further study the impact of the different simulation strategies, scans were performed in the $(m_{\tilde{t}_1}, m_{\chi_1^0})$ plane for both $\Delta m_{(\tilde{\chi}_1^\pm - \tilde{\chi}_1^0)} = 5$ GeV and 20 GeV. The 95% confidence level (CL) exclusion boundaries derived using our recast analysis were determined by comparing the number of Herwig++ events passing all selection criteria to the observed limit on the BSM event yield given in Ref. [113]. The resulting boundaries are shown in the left and right-hand plots of Figure 3.10, for $\Delta m_{(\tilde{\chi}_1^\pm - \tilde{\chi}_1^0)} = 5$ GeV and 20 GeV respectively. In each case, the red solid line shows the boundary derived in the original ATLAS analysis and the black dashed line is the result obtained using Herwig++ events. An estimation of the theoretical uncertainty on the Herwig++ results was obtained by varying the factorization and renormalization scales used by the Prospino package during the calculation of the total NLO cross section. The upper and lower boundaries arising from these variations are shown by the black dotted lines in Figure 3.10. Similarly, the edges of the 1σ uncertainty band quoted in the original ATLAS results are shown by the red dotted lines.

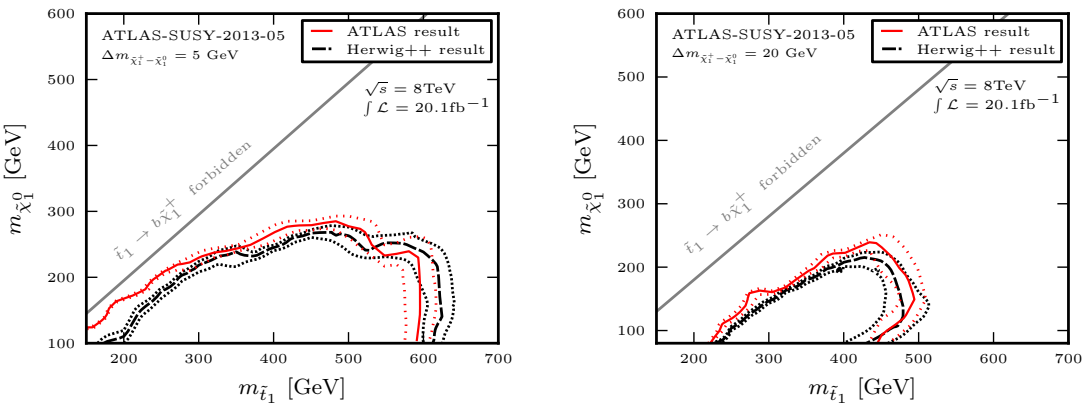

Figure 3.10: Observed 95% CL exclusion limit in the $(m_{\tilde{t}_1}, m_{\tilde{\chi}_1^0})$ mass plane for $\Delta m_{(\tilde{\chi}_1^\pm - \tilde{\chi}_1^0)} = 5$ GeV (left) and 20 GeV (right). The black dashed line indicates the boundaries derived using Herwig++ events as described in Section 3.3. The black dotted lines indicate the edges of an uncertainty band arising from scale variation in the NLO cross section calculation used to normalize the Herwig++ distributions. For comparison, the official ATLAS results from Figures 6c (left) and 6d (right) of Ref. [113] are shown by the red solid lines. In both cases, the red dotted lines show the edges of the associated $\pm 1\sigma$ uncertainty band. Results correspond to 20.1fb^{-1} of LHC collisions at a centre-of-mass energy of $\sqrt{s} = 8$ GeV.

The original and recast exclusion bounds for the $\Delta m_{(\tilde{\chi}_1^\pm - \tilde{\chi}_1^0)} = 5$ GeV scenario are consistent in the less compressed regions of phase space, *i.e.* when $m_{\tilde{t}_1} \gg m_{\tilde{\chi}_1^+} + m_b$. Approaching the limit $m_{\tilde{t}_1} = m_{\tilde{\chi}_1^+} + m_b$, we see that the exclusion boundary set in the original analysis is significantly more stringent than that determined using Herwig++ events. The most sensitive search strategy in this region is that of signal region B, and therefore this difference can be attributed to the differing treatments of hard parton-shower radiation in the signal events. Looking at the case with $\Delta m_{(\tilde{\chi}_1^\pm - \tilde{\chi}_1^0)} = 20$ GeV, better agreement is observed between the ATLAS and Herwig++ derived boundaries. The latter slightly underestimates the original result, most significantly in the low top squark mass region. However, the effect is less pronounced here owing to the negligible impact of the SRB search strategy in this case.

Having verified the accuracy of our recast analysis, we now study the impact

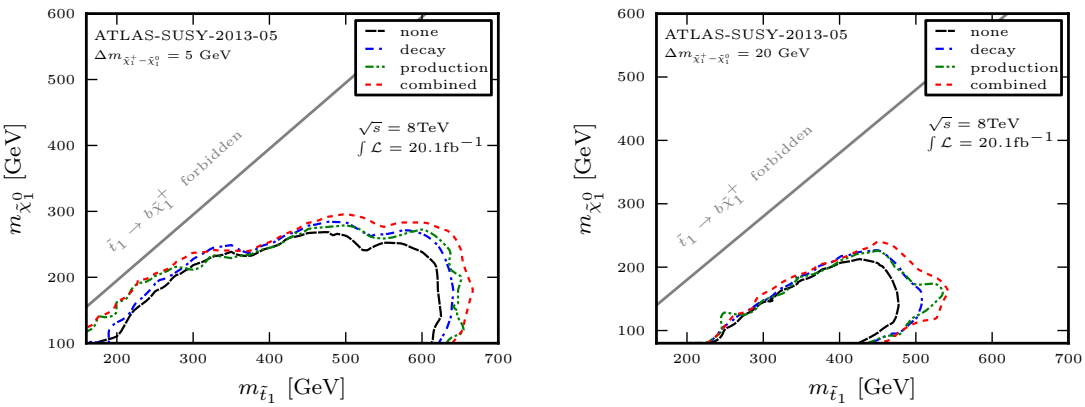

Figure 3.11: Observed 95% CL exclusion limit in the $(m_{\tilde{t}_1}, m_{\tilde{\chi}_1^0})$ mass plane for $\Delta m_{(\tilde{\chi}_1^\pm - \tilde{\chi}_1^0)} = 5$ GeV (left) and 20 GeV (right). The black dashed line indicates the boundaries derived using uncorrected Herwig++ events. Results obtained when POWHEG style ME corrections were applied to the top squark decays, production or in both stages of the event are shown respectively by the blue (dot-dashed), green (dot-dot-dashed) and red (dotted) lines. Results correspond to 20.1fb^{-1} of LHC collisions at a centre-of-mass energy of $\sqrt{s} = 8$ GeV.

of POWHEG style ME corrections on the exclusion boundaries derived using Herwig++. Figure 3.11 shows the exclusion boundaries set using Herwig++ events in the $\Delta m_{(\tilde{\chi}_1^\pm - \tilde{\chi}_1^0)} = 5$ GeV (left-hand panel) and $\Delta m_{(\tilde{\chi}_1^\pm - \tilde{\chi}_1^0)} = 20$ GeV (right-hand panel) scenarios. Results corresponding to events generated with either no ME corrections (black dashed line) or ME corrections applied during the top squark decays (blue dot-dashed line), production (green dash-dot-dot line) or in both stages of the event (red dotted line) are shown.

In the $\Delta m_{(\tilde{\chi}_1^\pm - \tilde{\chi}_1^0)} = 5$ GeV scenario, applying ME corrections to the hardest emission produced during the top squark decays causes an increase in the reach of the exclusion boundary in all regions of phase space. The most marked effect occurs in the high stop mass region where the SRA search strategy is setting the limit. Here the extension of the exclusion boundary is the result of a softening, in the low p_T region, of the transverse momentum spectrum of the hardest non b-tagged jet in each event. This in turn leads to a reduction in the number of events failing the selection criterion $p_{T,j_3} < 50$ GeV. Some increase in the sensitivity is also seen in

the more compressed regions of parameter space. In this case, the limit is being set by the SRB strategy and the increase in acceptance is due to an increase in the transverse momenta of the b-tagged jets, which in turn leads to more events passing the b-jet selection criteria. When instead the POWHEG style ME correction is applied during the production stage of the event, an extension of the exclusion boundary is again seen in the high stop mass region. This is similar to the effect observed when ME corrections were applied to the stop decays, and is also caused by an increase in the number of events passing the veto on the transverse momentum of the hardest non b-tagged jet. In addition, the exclusion boundary is significantly extended beyond the uncorrected result in the low stop mass region where SRB sets the limit. This is a consequence of the ME corrected emission in the production process populating the entire real-emission phase space, including the previously unpopulated dead zone. Crucially, this increases the number of events in which the top squark-antisquark pair recoils against a hard initial-state jet, and therefore the number passing the $E_T^{\text{miss}} > 250$ GeV requirement. Finally, when ME corrections are applied to radiation produced both in the top squark production and decays, the effects of the two corrections are combined. The exclusion boundary in the compressed region of parameter space predominantly follows the one generated with ME corrections in the production stage only. However in the high stop mass region, the effect of combining the corrections is significant, and the exclusion boundary is extended when compared with the results generated with a only one type of correction. This is a result of compound softening of the p_{T,j_3} distribution.

Considering now the scenario in which $\Delta m_{(\tilde{\chi}_1^\pm - \tilde{\chi}_1^0)} = 20$ GeV, in the high stop mass region of parameter space similar effects are observed to those seen in the $\Delta m_{(\tilde{\chi}_1^\pm - \tilde{\chi}_1^0)} = 5$ GeV case. Including the correction to either the production or the decays of the top squarks causes a reduction in the transverse momentum of the hardest non b-tagged jet in each event, therefore leading to an increase in the reach of the exclusion boundary. When both corrections are applied, this effect is again more pronounced due to composite softening of the p_{T,j_3} distribution. However, only a small effect is seen along the low mass edge of the exclusion boundary when any of the corrections are applied. This is because the search strategy setting the limit

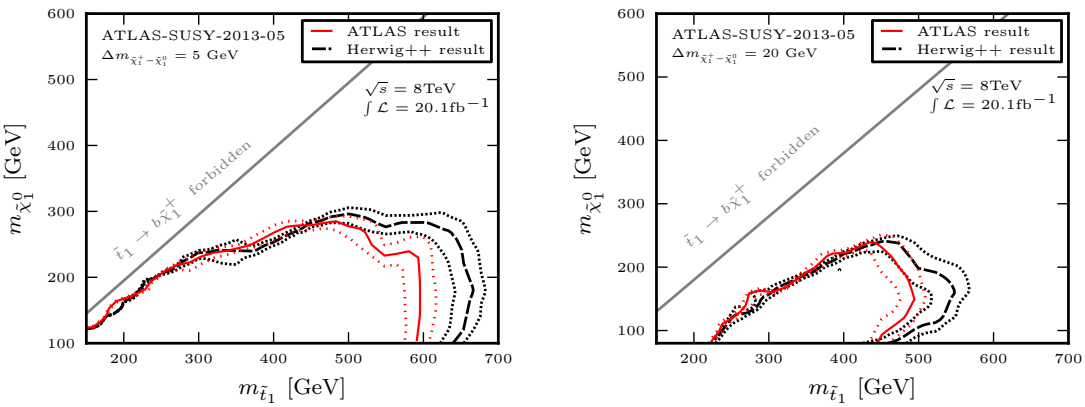

Figure 3.12: As in Figure 3.10, but with POWHEG style ME corrections applied during the production and decays of the top squarks in the Herwig++ events.

in this region is now SRA. Unlike the SRB strategy, the reach of signal region A is not significantly affected by the increased amount of E_T^{miss} in events generated with ME corrections in the production phase. In addition, the increase in acceptance due to the softening of the $p_{T,j3}$ spectrum is less pronounced in the compressed region, since in these scenarios the jets are typically already soft enough to pass the $p_{T,j3} < 50$ GeV selection criterion.

Finally, Figure 3.12 shows analogous plots to those in Figure 3.10, where now the Herwig++ events have been generated with ME corrections applied during both the production and decays of the top squarks. In both the $\Delta m_{(\tilde{\chi}_1^\pm - \tilde{\chi}_1^0)} = 5$ and 20 GeV scenarios, including ME corrections leads to excellent agreement between the original and recast exclusion limits in the compressed regions of parameter space. This is to be expected given that now both simulations of the signal process include improvements to the treatment of a number of hard emissions in each event. In the high stop mass region, the exclusion boundaries set using Herwig++ events is now more stringent than the original result. However, we note that in this region of parameter space the acceptance times the cross section is a relatively flat function, and so a small variation in either leads to a significant shift in the exclusion boundary. This is illustrated by the size of the uncertainty bands in this region. As such, it seems likely that differences between the Herwig++ and ATLAS results in this region are not significant, especially considering the lack of detector simulation in our study.

3.4 Summary

In this chapter we have presented an implementation of POWHEG style ME corrections to stop-antistop production at the LHC. The correction has been included within the MATCHBOX framework of the Herwig++ event generator, using MADGRAPH 5 derived amplitudes. Our implementation has been validated through comparison with results generated using the POWHEGBOX program, for which good agreement was observed in both the total cross sections and the differential distributions.

At parton level, it was found that including the POWHEG style ME correction to stop-antistop production has two significant and distinct effects on the hardest parton-shower emission. Firstly, as was found in Chapter 2, the uncorrected parton shower tends to overpopulate high p_T regions of the parton-shower phase space, and therefore including the ME correction reduces the transverse momentum of emissions in the soft and intermediate p_T regimes. In addition to this, the population of the dead zone in the parton-shower phase space now has a significant effect. As such, when the ME correction is included more emissions are produced in the high transverse momentum region than in the uncorrected case.

In this study, we have considered the matching of higher-order matrix elements with the Herwig++ angular-ordered parton shower, and as such it is necessary to include a truncated and vetoed component of the parton shower that simulates soft, wide-angle emissions. The impact of failing to include this component of radiation was studied and found to be largely insignificant, causing only a slight reduction in the transverse momentum of subleading shower jets. This reiterates the commonly held view that the effect of the truncated shower can often be safely neglected in POWHEG based approaches. A more striking effect was instead seen when ME corrected events were showered directly, using a procedure similar to the one employed when matrix-element level events are generated with a specialist POWHEG program and then interfaced to Herwig++ for the remainder of the shower evolution. It was found that this approach had an unphysical impact on distributions which should be insensitive to parton-shower radiation and also resulted in an increased amount of wide-angle radiation in events. Modifications to the Herwig++ angular-ordered

parton shower that correct this behaviour were also studied.

The effect of restricting the phase space of shower-type POWHEG emissions was investigated, both with the full parton shower simulation and when the evolution was limited to the production of the hardest emission only. In the latter case, a significant impact on results was only observed when the natural starting scale of the parton shower was chosen to be unphysically low, as is often the case when the hfact profile is used. In this case, the phase-space restriction was found to impact on the Sudakov region of the transverse momentum distribution of the hardest emission. In addition, when the full parton-shower evolution was included, differences were observed in the transverse momentum distributions of jets sensitive to parton-shower radiation. When the phase space of the POWHEG emission was divided, more wide-angle radiation was generated, leading to a softening of the hardest shower jet and an increase in the number of hard subleading jets.

Finally, having studied separately the impact of applying POWHEG style ME corrections during both the production and decays of sparticles, the effect of combining the corrections was investigated both at parton level and in the context of an existing search for top squarks performed by the ATLAS collaboration. In compressed regions of parameter space it was found that the impact of the combined corrections was largely driven by the one applied during the production of the top squarks. Including this correction was found to increase the number of events in which the stop-antistop pair recoiled against hard ISR, and therefore the number of events with a large the amount of missing transverse energy. Consequently, including the ME corrections resulted in significantly better agreement between the exclusion boundaries set using Herwig++ and those obtained in the original ATLAS study, where signal events were generated using MADGRAPH interfaced to PYTHIA 6 with MLM merging. Away from the compressed region, corrections applied during the production and decays of the top squarks were both found to have a significant impact. Separately each correction was found to extend the exclusion boundaries derived using Herwig++, with a cumulative effect seen when the corrections were applied together.

Chapter 4

Matrix-element corrections to squark-antisquark production

In this chapter we consider the generalization of our POWHEG style ME correction, studied in the previous chapter for stop-antistop production, to the remaining squark flavours. Higher-order QCD corrections to squark-antisquark production at the LHC in general have an additional degree of complexity when the squark in question is not the top squark. This is caused by new divergent contributions to the real-emission amplitude that arise when an intermediate s-channel gluino goes on-shell. These contributions may be interpreted as squark-gluino production followed by gluino decay, and therefore not as genuine NLO corrections to squark-antisquark production. As such, we wish to subtract them from the real-emission matrix element used in the POWHEG style ME correction.

The outline of this chapter is as follows. In Section 4.1, the different schemes for removing on-shell contributions to the real-emission matrix element will be outlined and technical details relevant to their implementation within a Monte Carlo event generator will be discussed. The MATCHBOX implementation of ME corrections to squark-antisquark production will be validated against results generated using the POWHEGBOX program in Section 4.2, with further results presented also in Appendix B.1. The different strategies available in MATCHBOX for removing on-shell contributions will then be tested and compared in Section 4.3. Having done so, in Section 4.4 we focus on a single on-shell subtraction procedure and study the impact

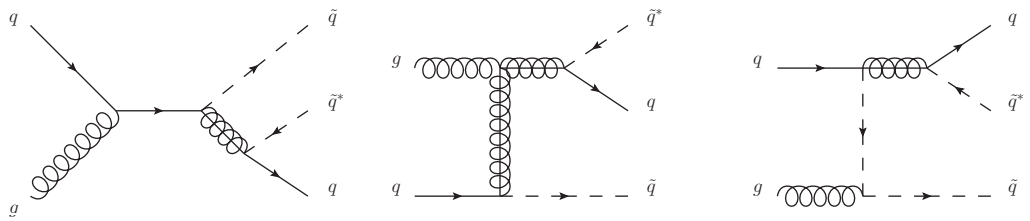

Figure 4.1: Feynman diagrams of the real-emission corrections to squark-antisquark production that lead to divergent contributions in the limit of on-shell gluinos.

of applying ME corrections using this prescription, relative to the uncorrected parton shower approach. In this section, the effect of combining ME corrections during the production and decays of squarks is also illustrated for benchmark scenarios with both compressed and well separated sparticle mass spectra. Finally, our findings are summarized in Section 4.5.

4.1 Treatment of on-shell contributions

The production of top squark-antisquark pairs, as was considered in the previous chapter, is a highly simplified case of general squark-antisquark pair production. For all flavours of squark other than the stop, the presence of quark content in the proton with corresponding flavour gives rise to new qg-initiated[1] contributions to the NLO real-emission process like those shown in Figure 4.1. When the sparticle mass hierarchy is such that $m_{\tilde{g}} > m_{\tilde{q}}$, the intermediate s-channel gluino in these diagrams may be produced on-shell. This leads to new potentially singular real-emission corrections to the Born process. This new type of divergence may be regulated by introducing a finite gluino width, $\Gamma_{\tilde{g}}$, in the offending propagator. However, a finite width is an all orders perturbative result, and therefore its introduction may violate the gauge invariance of the calculation. Moreover, the presence of such a large NLO contribution signals a break down in the validity of the perturbative expansion. These issues can be addressed by viewing the diagrams in Figure. 4.1

[1]Here we discuss the case of initial-state quarks only. However, equivalent new contributions arise also in $\bar{q}g$-initiated processes and the subsequent discussion is also valid in this case.

not as real-emission corrections to squark-antisquark pair production, but instead as the leading-order production $qg \to \tilde{q}\tilde{g}$ followed by the decay $\tilde{g} \to \tilde{q}^* q$. In a Monte Carlo event generator, squark-antisquark production and squark-gluino production would be simulated as separate processes, leading to double counting of the on-shell channel if the diagrams in Figure 4.1 were included in higher-order corrections to the former process. As such, it is clear that to avoid this double counting and maintain the convergence of the perturbative expansion, the on-shell contributions must be removed from the real-emission correction to squark-antisquark production.

Several methods have been proposed for performing this division into on-shell and what may be viewed as genuine NLO real-emission contributions. The most commonly employed methods, dubbed diagram removal (DR) and diagram subtraction (DS) in Ref. [127], are outlined below. Considering a generic qg-initiated channel, the squared matrix element may be written as

$$|\mathcal{M}|^2 = |\mathcal{M}_{\mathrm{R}}|^2 + 2\Re(\mathcal{M}_{\mathrm{R}}\mathcal{M}^*_{\mathrm{NR}}) + |\mathcal{M}_{\mathrm{NR}}|^2, \tag{4.1.1}$$

where $\mathcal{M}_{\mathrm{R}}$ denotes the amplitude arising from resonant diagrams, *i.e.* those in which an intermediate s-channel gluino may be on-shell, and $\mathcal{M}_{\mathrm{NR}}$ is the amplitude from the remaining non-resonant diagrams. In the diagram removal approach[2], contributions with on-shell gluinos are removed at the amplitude level. Consequently, both the resonant contribution and the interference terms are removed from Eq. 4.1.1 such that the real-emission matrix element squared becomes[3]

$$\mathcal{R} = |\mathcal{M}_{\mathrm{NR}}|^2. \tag{4.1.2}$$

This approach is straightforward to implement in Monte Carlo event generators however has the drawback that the interference terms are lost even when LO $\tilde{q}\tilde{g}$ production is included in the simulation. A variation of the diagram removal method was proposed in Ref. [128] which aims to combat this issue by dropping only the

[2]Diagram removal in the context of NLO matrix-element matching was first studied in Ref. [127], for the case of QCD corrections to tW production.

[3]As is Section 1.4, the relevant flux and parton luminosity factors are absorbed into the definition of $\mathcal{R}$. For simplicity, these factors are omitted in the following discussion.

resonant term and using

$$\mathcal{R} = |\mathcal{M}_{\rm NR}|^2 + 2\Re(\mathcal{M}_{\rm R}\mathcal{M}^*_{\rm NR}). \tag{4.1.3}$$

Both approaches, however, break gauge invariance and so in principle give arbitrary results.

In contrast, the diagram subtraction approach [127], often referred to as the "PROSPINO scheme" [15], keeps the full squared amplitude in Eq. 4.1.1 and introduces a subtraction term, $\mathcal{C}_{\rm sub}$, such that the real-emission matrix element squared is

$$\mathcal{R} = |\mathcal{M}_{\rm R}|^2 + 2\Re(\mathcal{M}_{\rm R}\mathcal{M}^*_{\rm NR}) + |\mathcal{M}_{\rm NR}|^2 - \mathcal{C}_{\rm sub}. \tag{4.1.4}$$

The subtraction term aims to locally cancel the contributions from on-shell gluinos. To achieve this without significantly modifying the genuine NLO contributions, the difference between the subtraction term and $|\mathcal{M}_{\rm R}|^2$ must be as close to zero as possible, in all regions of phase space. Therefore, the subtraction term most typically chosen, and which is used in this study, is

$$\mathcal{C}_{\rm sub} = \Theta(\sqrt{s} - m_{\tilde{g}} - m_{\tilde{q}})\Theta\left(m_{\tilde{g}} - m_{\tilde{q}^*}\right) \frac{m_{\tilde{g}}^2\Gamma_{\tilde{g}}^2}{\left((p_{\tilde{q}^*} + p_q)^2 - m_{\tilde{g}}^2\right)^2 + m_{\tilde{g}}^2\Gamma_{\tilde{g}}^2} |\mathcal{M}_{\rm R}(\phi_3^{'})|^2 d\phi_3^{'}. \tag{4.1.5}$$

Taking each component in turn:

- The function $\Theta(\sqrt{s} - m_{\tilde{g}} - m_{\tilde{q}})$ in Eq 4.1.5 ensures that no subtraction is performed when the centre-of-mass energy, $\sqrt{s}$, is insufficient for the on-shell production of a squark and gluino with masses $m_{\tilde{q}}$ and $m_{\tilde{g}}$ respectively.

- Similarly, the production of an on-shell gluino followed by the decay $\tilde{g} \to \tilde{q}^* q$ cannot occur for the mass ordering $m_{\tilde{g}} < m_{\tilde{q}^*}$. Therefore, the subtraction term must be zero in this case, which is guaranteed by the inclusion of the function $\Theta\left(m_{\tilde{g}} - m_{\tilde{q}^*}\right)$.

- Exact cancellation of the resonant contribution in the limit[4] $m_{\tilde{q}^* q} \to m_{\tilde{g}}$ is ensured by using an on-shell subtraction term that is proportional to $|\mathcal{M}_{\rm R}(\phi_3^{'})|^2$.

[4]We defined $m_{\tilde{q}^* q} = \sqrt{(p_{\tilde{q}^*} + p_q)^2}$, where p_q and $p_{\tilde{q}^*}$ are the momenta of the final-state quark and antisquark respectively.

- The subtraction term must only remove contributions with on-shell kinematics such that the procedure is gauge invariant in the small-width limit. Consequently, the amplitude in Eq. 4.1.5 is evaluated at the three-body phase-space point $\phi_3^{'}$, which is obtained by reshuffling the final-state kinematics of a general phase space point ϕ_3 such that they fulfil $m_{\tilde{q}^* q} = m_{\tilde{g}}$. The mapping between the full and restricted three-body configurations, $\phi_3 \to \phi_3^{'}$, must maintain energy-momentum conservation, preserve the on-shell conditions for the $\tilde{q}$ and $\tilde{q}^*$ and, crucially, reduce to the identity transformation when $m_{\tilde{q}^* q} = m_{\tilde{g}}$. These conditions can be met by employing the Catani-Seymour momentum reshuffling described in Ref. [56] for massive final-state particles. Using this formalism, the three-body phase space ϕ_3 is mapped to a two-body phase space with an on-shell gluino and final-state squark, which acts as the spectator particle. From this two-particle configuration, the momenta of the final-state quark and antisquark may be obtained in the rest frame of the on-shell gluino using the standard kinematics of a $1 \to 2$ decay, see *e.g.* Ref. [129]. The original direction of the antisquark in the rest frame of the off-shell gluino is used to set the azimuthal and polar angles of the decay. Finally, the momenta of the quark and antisquark are boosted from the gluino rest frame to the centre-of-mass frame to obtain the full set of transformed momenta.

- The momentum reshuffling procedure described above destroys the Breit-Wigner form of the gluino propagator in $|\mathcal{M}_{\mathrm{R}}(\phi_3^{'})|^2$. It is restored by including the factor
$$\frac{m_{\tilde{g}}^2 \Gamma_{\tilde{g}}^2}{\left((p_{\tilde{q}^*} + p_q)^2 - m_{\tilde{g}}^2\right)^2 + m_{\tilde{g}}^2 \Gamma_{\tilde{g}}^2}, \tag{4.1.6}$$
in the subtraction term, thus ensuring minimal differences between $\mathcal{C}_{\mathrm{sub}}$ and the resonant real-emission contribution.

- The Monte Carlo integration of the subtraction term is performed, as for the squared real-emission matrix element, by sampling the unrestricted phase space measure $d\phi_3$. As was discussed in Ref. [22], it is therefore necessary to include a Jacobian factor relating the restricted and unrestricted measures,

that is, in Equation 4.1.5 the substitution

$$d\phi_3' = \sqrt{\frac{\lambda(s, m_{\tilde{g}}^2, m_{\tilde{q}}^2)}{\lambda(s, m_{\tilde{q}^*q}^2, m_{\tilde{q}}^2)}} \frac{(m_{\tilde{g}}^2 - m_{\tilde{q}}^2) m_{\tilde{q}^*q}^2}{(m_{\tilde{q}^*q}^2 - m_{\tilde{q}}^2) m_{\tilde{g}}^2} \, d\phi_3, \tag{4.1.7}$$

is made.

- Finally, we note that the gluino width, $\Gamma_{\tilde{g}}$, must be exactly zero in the non-resonant amplitudes, so as not to disrupt the cancellation of the collinear singularities in the real-emission matrix element with those present in the Catani-Seymour dipole subtraction term. However, $\Gamma_{\tilde{g}}$ must take a non-zero value in all instances of the resonant amplitude, thereby avoiding divergences in the gluino propagator.

The diagram subtraction method as it is presented here only respects gauge invariance in the small-width limit, *i.e.* when $\Gamma_{\tilde{g}} \to 0$. Correspondingly, the parameter $\Gamma_{\tilde{g}}$ should take a very small but non-zero value and therefore may be viewed as a pure mathematical cutoff rather than the physical width of the gluino. A fully gauge invariant variation of the method can however be obtained. The construction of the subtraction term in this case requires the analytic expansion of Eq. 4.1.1 in terms of poles in $m_{\tilde{q}^*q} - m_{\tilde{g}}$, see Ref. [22] for details. As a result, this approach does not lend itself to the semi-automated nature in which we wish to add new processes to the MATCHBOX framework. Therefore, in this work we have implemented the original diagram subtraction approach and rely on the residual gauge dependence being small for sufficiently small values of $\Gamma_{\tilde{g}}$.

While being more complicated in terms of implementation within a Monte Carlo event generator, the diagram subtraction approach is clearly preferable to diagram removal. In addition to preserving gauge invariance in the small-width limit, the contribution removed through diagram subtraction closely mimics the term which would be included by simulating LO $\tilde{q}\tilde{g}$ production followed by gluino decay. As such, the full real-emission configuration with the resonant, non-resonant and interference contributions may be easily recovered in an inclusive simulation. Consequently, diagram subtraction will be implemented as the default procedure for dealing with the resonant real-emission diagrams in squark-antisquark production. However, the

original diagram removal method given in Eq. 4.1.2 is also made available to allow comparisons to be drawn and the impact of the interference term to be studied.

Generation of the hardest emission

Incorporating diagram removal into the POWHEG method is simple and amounts to making the replacement $\mathcal{M} \to \mathcal{M}_{\mathrm{NR}}$ in the squared real-emission matrix element, $\mathcal{R}$. However in the case of diagram subtraction, problems arise because the squared real-emission matrix element in Eq. 4.1.4 is not positive definite. The interference term is negative in some regions of phase space and, close to the resonance, the magnitude of this term can easily exceed the sum of the other contributions. These negative real-emission contributions affect the POWHEG procedure in two ways. Firstly, the function $\bar{\mathcal{B}}$, with which the Born configuration is generated, is not positive in all regions of phase space. This is easily dealt with by allowing Monte Carlo events to be generated with negative weights. As such, this does not introduce any additional complexity in the case of our POWHEG style ME corrections, since negatively weighted events were already required when considering unitarization of the correction using the LoopSim approach.

The second, somewhat more involved problem arises because the splitting kernel in the Sudakov form factor for the corrected emission is no longer positive definite. This leads to problems when generating the hardest emission, both for the full POWHEG and ME correction approaches. The simplest solution to this problem is to set all negative values of $\mathcal{R}$ in the splitting kernel equal to zero. In doing so however, negative contributions coming from interference effects are missed. Therefore, the result obtained by combining NLO squark-antisquark production with the LO production and decay of an on-shell gluino will not accurately reflect the full squared amplitude in Eq. 4.1.1. In addition, there is no obvious way of quantifying the effect of the missing negative phase-space points. This approach is straightforward to implement in a Monte Carlo event generator and will be referred to in the subsequent work as the **DS0** approach.

A second solution, considered in Ref. [130], is motivated by the observation that the majority of negative phase-space points lie close to the resonance. Therefore, by

making the substitution in the splitting kernel

$$\mathcal{R} \to \Theta(|m_{\tilde{q}^* q} - m_{\tilde{g}}| - \Delta)\mathcal{R}, \tag{4.1.8}$$

the problematic points are excluded. This introduces an artificial cutoff, Δ, in the radiation phase space which is typically chosen to be $\Delta = \mathcal{O}(\Gamma_{\tilde{g}})$. This method drops both positive and negative contributions to $\mathcal{R}$ close to the resonance. The effect of doing so may be quantified by varying the value of the cutoff parameter, and it was suggested in Ref. [130] that this approach is a reliable solution if the final observables exhibit negligible dependence on Δ. However by excluding all phase-space points near the resonance, one may in principle also be removing single logarithmically enhanced contributions arising from collinear $g \to q\bar{q}$ splittings, where the invariant mass of the quark-antisquark system by chance reproduces that of the gluino. As such, this approach impacts on the Sudakov region of the transverse momentum distribution of the hardest emission, a fact that will be illustrated in Section 4.3. Adopting the naming convention used in Ref. [22], this solution will be referred to as **DSI**.

An alternative method has been studied in Refs. [11, 22] in which only part of the real-emission matrix element is exponentiated, *i.e.* in analogy to the division of the real-emission phase space that was introduced in Section 1.4.3, the square matrix element is split into the components $\mathcal{R}^S$ and $\mathcal{R}^H$. One of the suggested combinations,

$$\mathcal{R}^S = |\mathcal{M}_{\rm NR}|^2 \quad \text{and} \quad \mathcal{R}^H = |\mathcal{M}_{\rm R}|^2 + 2\Re(\mathcal{M}_{\rm R}\mathcal{M}^*_{\rm NR}) - \mathcal{C}_{\rm sub}, \tag{4.1.9}$$

has been implemented within the MATCHBOX framework. This approach negates the need for the artificial phase-space cutoff and retains all positive and negative real-emission contributions. However, it has the disadvantage of being gauge dependent even in the limit $\Gamma_{\tilde{g}} \to 0$. This solution will be referred to as **DSII**.

Finally, in this study we propose an additional variant of the DSI method in Eq. 4.1.8 in which the near resonant configurations that are excluded in the splitting kernel are added back in as a hard finite contribution. To do so, we make use of the identity,

$$1 = \Theta_{\rm PS}\Theta_\Delta\Theta_{\rm col} + \Theta_{\rm PS}\Theta_\Delta(1-\Theta_{\rm col}) + (1-\Theta_{\rm PS}) + \Theta_{\rm PS}(1-\Theta_\Delta), \tag{4.1.10}$$

such that the real-emission matrix element may be divided into shower and hard emission components,

$$\mathcal{R}^S = (\Theta_\Delta \Theta_{\rm col} + (1 - \Theta_\Delta))\Theta_{\rm PS}\mathcal{R} \tag{4.1.11}$$

and

$$\mathcal{R}^H = (\Theta_{\rm PS}\Theta_\Delta(1 - \Theta_{\rm col}) + (1 - \Theta_{\rm PS}))\mathcal{R}, \tag{4.1.12}$$

where Θ_Δ is the Heaviside function $\Theta(\Delta - |m_{\tilde{q}^* q} - m_{\tilde{g}}|)$ which is unity for phase-space points that lie sufficiently close to the resonance. The function $\Theta_{\rm PS}$ corresponds to the function f in Section 1.4.3, *i.e.* it is zero when the transverse momentum of the POWHEG emission exceeds the natural starting scale of the parton shower and becomes unity for emissions below this cutoff, with the possibility of smoothing the transition between the two regimes. Phase-space configurations can occur in which both these resonant and low p_T conditions are fulfilled. To ensure that the hard component of the real-emission matrix element contains no logarithmically enhanced collinear contributions, the function $\Theta_{\rm col}$ is also introduced. It is defined as

$$\Theta_{\rm col} = \Theta\left(\frac{1}{p_T^2} - \frac{m_{\tilde{q}^* q}^2}{(m_{\tilde{q}^* q}^2 - m_{\tilde{g}}^2)^2 + m_{\tilde{g}}^2 \Gamma_{\tilde{g}}^2}\right). \tag{4.1.13}$$

As such, $\Theta_{\rm col}$ effectively decides whether the enhancement to the cross section due to the collinear nature of the emission is more or less significant than the enhancement due to the proximity of the phase-space point to the on-shell configuration. By performing the division in this way, $\mathcal{R}^S$ encapsulates emissions below the natural starting scale of the shower that are either far from the resonance, or close to the resonance and collinearly enhanced.

This approach, referred to as **DSI′**, has the advantages that it retains all positive and negative real-emission contributions and is gauge invariant in the limit $\Gamma_{\tilde{g}} \to 0$. As with the original DSI approach, the introduction of an artificial cutoff is necessary. However, as will be demonstrated in Section 4.3, negligible dependence on this parameter is evident, even at the level of the hard process.

Finally, when the DSII and DSI′ approaches are applied within the context of matrix-element corrections, the unitarity of the parton shower is violated. This can

be restored through the modification of the Born prefactor $\mathcal{B} \to \mathcal{B}'$, as described in Section 1.4.4.

4.2 Validation

4.2.1 Setup

Before studying the different methods for removing real-emission contributions with on-shell gluinos, we first validate our implementation of POWHEG style ME corrections for squark-antisquark pair production, for all squark flavours other than the stop. To this end, LHC pp collisions were generated at $\sqrt{s} = 14$ TeV in which stable squark-antisquark pairs were produced. In this section, results are shown for the case of left-handed up squark production where the masses of the up squark and potentially on-shell gluino were set to $m_{\tilde{u}_L} = 1.8$ TeV and $m_{\tilde{g}} = 2.4$ TeV respectively. Similar checks have also been performed for the production of all alternative squark-antisquark pairs[5] and in the scenario with $(m_{\tilde{g}}, m_{\tilde{q}}) = (1.9, 1.8)$ TeV. A limited number of these additional results are presented in Appendix B.1. During the validation the width of the gluino, which here acts to regulate the resonant contributions, was set to $\Gamma_{\tilde{g}}/m_{\tilde{g}} = 10^{-4}$. This choice is motivated by the observation that the real-emission cross section for channels with resonant contributions has negligible dependence on the value of the gluino width for $\Gamma_{\tilde{g}}/m_{\tilde{g}} \lesssim 10^{-2}$. This will be illustrated explicitly in Section 4.3. In all cases, the effects of hadronization and the underlying event were not simulated and, unless otherwise stated, PDF sets from the LHAPDF package were used. Distributions were created using the Rivet analysis framework and no event selection criteria were imposed.

4.2.2 Validation of leading-order amplitudes

The MATCHBOX implementation of left-handed up squark-antisquark production was validated at leading order through comparison with results produced using the internal Herwig++ implementation of the MSSM model. The leading-order matrix

[5] We consider only the production of same flavour squarks and antisquarks, *i.e.* $pp \to \tilde{q}_i \tilde{q}_i^*$.

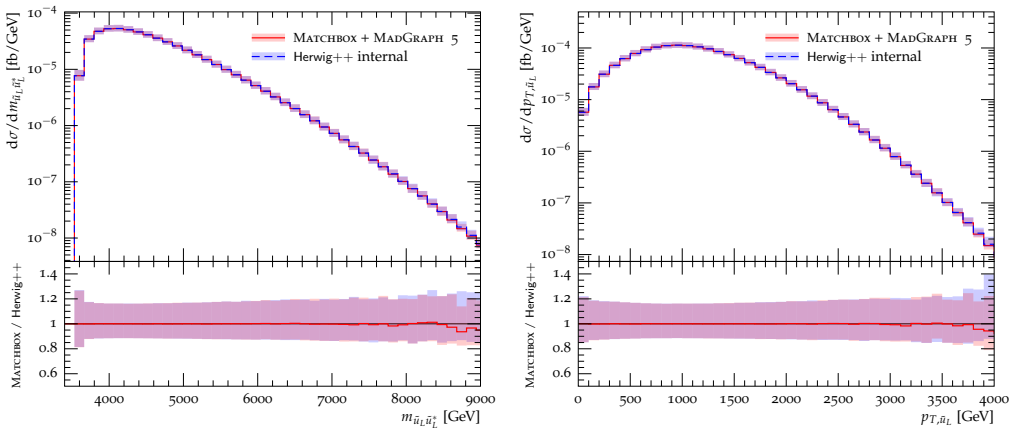

Figure 4.2: Distributions of the invariant mass of the up squark pair $m_{\tilde{u}_L\tilde{u}_L^*}$ (left) and the inclusive up squark transverse momentum $p_{T,\tilde{u}_L}$ (right) in simulations of LHC collisions at a centre-of-mass energy of 14 TeV. The production of left-handed up squark-antisquark pairs was simulated using the LO MATCHBOX and internal Herwig++ setups, in the scenario with $m_{\tilde{u}_L} = 1.8$ TeV. For each line, the error band indicates the uncertainty arising from the variation of $\mu_R = \mu_F$ by a factor of two around the central value.

elements were convoluted with the CTEQ6L1 PDF set and no parton shower effects were included in the simulation. The factorization and renormalization scales were set at $\mu_R = \mu_F = m_{\tilde{u}_L}$ and simultaneously varied by a factor of two around this central value to allow an estimation of the theoretical uncertainty to be obtained.

The total cross sections calculated using MATCHBOX and the internal Herwig++ setup were found to agree well at $71.45^{+34\%}_{-24\%}$ ab and $71.46^{+34\%}_{-24\%}$ ab respectively, where the percentile uncertainties correspond to those arising from scale variation. Distributions of the invariant mass of the up squark-antisquark pair, $m_{\tilde{u}_L\tilde{u}_L^*}$, and inclusive transverse momentum of the up squark, $p_{T,\tilde{u}_L}$, are shown in the left and right-hand plots of Figure 4.2. The central results generated with the MATCHBOX and Herwig++ implementations are shown by the red solid and blue dashed lines respectively, with the uncertainty due to scale variation indicated by the bands of corresponding colour. The MATCHBOX and Herwig++ results agree very well in both distributions, providing further confidence in our implementation of the leading-order amplitudes for squark-antisquark production.

4.2.3 Validation of matrix-element corrections

To test the correctness of our implementation of the diagram removal and subtraction procedures, along with the ME correction algorithm, events produced using MATCHBOX were compared to those generated with the POWHEGBOX program. The factorization and renormalization scales were set and varied as in the leading-order comparison in Section 4.2.2, and the PDF set CTEQ6m was used[6]. Events were generated in which the parton shower was limited to the production of the hardest emission and the strong coupling constant was fixed at the default Herwig++ value of the coupling evaluated at μ_R. Where possible, POWHEGBOX events were generated using the replacement $\bar{\mathcal{B}} \to \mathcal{B}$, to allow for direct comparison with our POWHEG style ME correction in the case that there is no division of the real-emission phase space.

We begin by considering events generated using the diagram removal approach in which the resonant contributions are removed at amplitude level. The total cross sections calculated by MATCHBOX and POWHEGBOX were found to agree well at $72.93^{+37\%}_{-25\%}$ ab and $72.94^{+36\%}_{-25\%}$ ab respectively, where the indicated uncertainty is the estimate arising from scale variation. For further comparison, differential distributions were generated and are shown in Figure 4.3. The blue dashed lines correspond to the results generated using POWHEGBOX and the red solid lines to those produced using MATCHBOX. In both cases, the band of corresponding colour indicates the scale variation uncertainty. The top left and right-hand panels of Figure 4.3 show distributions of $m_{\tilde{u}_L\tilde{u}_L^*}$ and $p_{T,\tilde{u}_L}$. As was observed for $\tilde{t}_1\tilde{t}_1^*$ production in the previous chapter, a slight difference in the slopes of the MATCHBOX and POWHEGBOX results is evident in these plots. This is caused by the use of different kinematic mapping procedures in the two implementations. Also shown, in the lower left-hand plot of Figure 4.3, are distributions of the transverse momentum of the up squark-antisquark pair, $p_{T,\tilde{u}_L\tilde{u}_L^*}$. Here the POWHEGBOX result is harder than the MATCHBOX distributions in the low p_T region. This effect was also observed for

[6]As in Section 3.1.3, this PDF set was used in order to simplify event generation with the POWHEGBOX program.

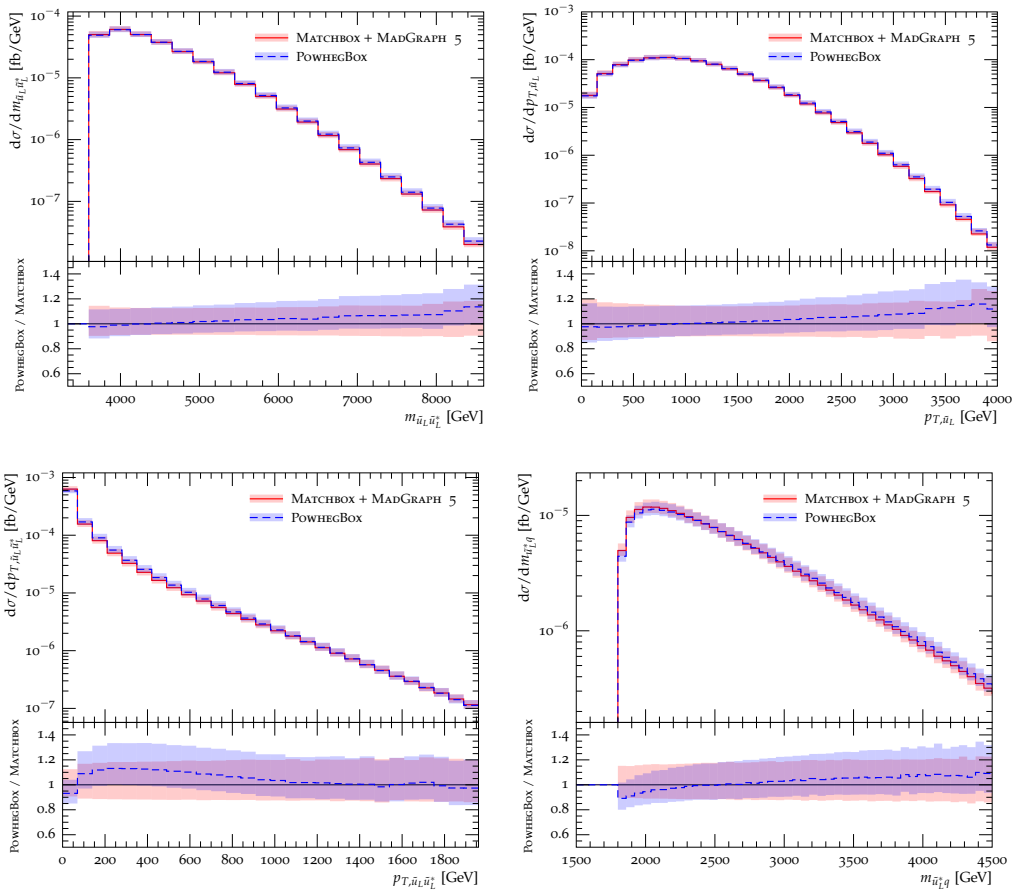

Figure 4.3: Distributions of the invariant mass of the up squark pair $m_{\tilde{u}_L\tilde{u}_L^*}$ (upper left), the inclusive up squark transverse momentum $p_{T,\tilde{u}_L}$ (upper right), the transverse momentum of the up squark pair $p_{T,\tilde{u}_L\tilde{u}_L^*}$ (bottom left) and invariant mass of the final state quark and up antisquark system $m_{\tilde{u}_L^*q}$ (bottom right). Events were generated at a centre-of-mass energy of 14 TeV using the matrix-element corrected MatchBox and PowhegBox setups detailed in the text with the diagram removal method. The mass of the up squark and gluino were $m_{\tilde{u}_L} = 1.8$ TeV and $m_{\tilde{g}} = 2.4$ TeV. For each line, the error band indicates the uncertainty arising from the variation of $\mu_R = \mu_F$ by a factor of two around the central value.

top squark-antisquark production and is attributed to the differing methods used to impose the IR cutoff of the radiation phase space. The results produced by the two implementation are in excellent agreement at high p_T. Finally, distributions of the

invariant mass of the final-state quark and up antisquark system[7], $m_{\tilde{u}_L^* q}$, are shown in the lower right-hand panel of Figure 4.3. Again, good agreement is observed between results generated using MATCHBOX and the POWHEGBOX program.

Comparing results generated using the diagram removal procedure allows the implementation of the non-resonant real-emission amplitudes and the total leading-order cross section to be validated. To test the correctness of the resonant real-emission amplitudes and on-shell subtraction term, we consider now the diagram subtraction approach of Eq. 4.1.4. To combat the non-positive definite nature of the splitting kernels we study both the case in which any negative values are set equal to zero, *i.e.* the DS0 method, and the case in which only the non-resonant term in the real-emission matrix element is exponentiated and the remaining terms are included as a hard finite contribution, *i.e.* the DSII approach. Analogous distributions to those in Figure 4.3 are shown in Figures 4.4 and 4.5 for the DS0 and DSII methods respectively. In the latter case, the substitution $\bar{\mathcal{B}} \to \mathcal{B}$ is not possible in the POWHEGBOX program and so the MATCHBOX distributions were normalized to account for the difference in the LO and NLO total cross sections.

Considering the DS0 results, as expected the $m_{\tilde{u}_L \tilde{u}_L^*}$ and $p_{T,\tilde{u}_L}$ distributions are consistent between the two implementations, with the POWHEGBOX results exhibiting a slight shift to higher values throughout. In addition, the MATCHBOX $p_{T,\tilde{u}_L \tilde{u}_L^*}$ distribution is in good agreement with the POWHEGBOX result in the high p_T region and shows the expected softening in the low p_T region. However, some discrepancy is observed between the implementations in the intermediate p_T range, where the resonant contributions have their most significant impact[8]. Disagreement between the $m_{\tilde{u}_L^* q}$ distributions is also evident close to the resonance, *i.e.* when $m_{\tilde{u}_L^* q} = m_{\tilde{g}}$. These differences are due to a combination of effects, the first of which relates to the treatment of the Jacobian factor in Equation 4.1.7 which accounts for the restricted on-shell phase space of the subtraction term. In the MATCHBOX implementation

[7]We define $m_{\tilde{u}_L^* q} = \sqrt{(p_{\tilde{u}_L^*} + p_q)^2}$, where $p_{\tilde{u}_L^*}$ and p_q are the momenta of the up antisquark and the final-state quark respectively. Only qg-initiated events impact on this observable, with the dominant contribution coming from events with an initial-state up quark.

[8]Resonant contributions impact in the region $p_{T,\tilde{u}_L \tilde{u}_L^*} \approx m_{\tilde{g}} - m_{\tilde{u}_L}$.

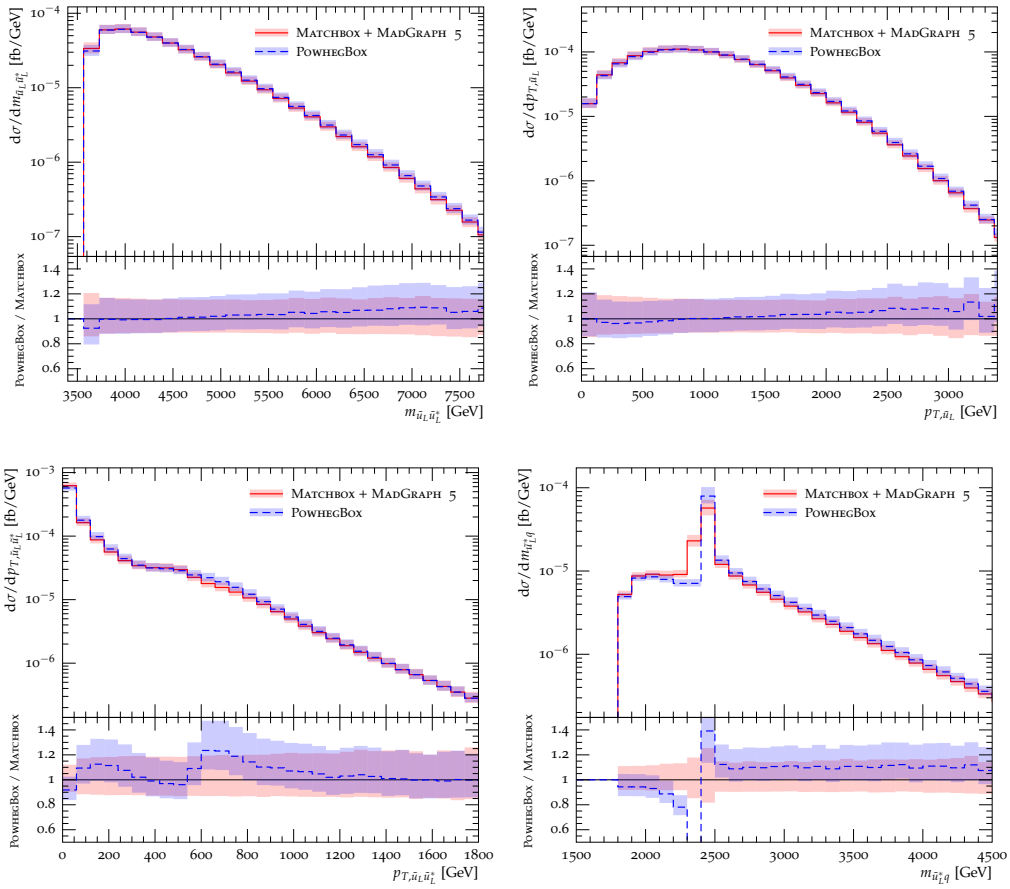

Figure 4.4: As in Figure 4.3, but using the DS0 diagram subtraction method to remove contributions with on-shell gluinos.

this factor has been included for all instances of the subtraction term, while in the PowhegBox program it is included only when the subtraction term appears in the hard component of the real-emission matrix element, not when it is utilized in the splitting kernel[9]. It has been confirmed that the two implementations are in significantly better agreement when the MatchBox treatment of the Jacobian is modified to reflect the PowhegBox approach. The second source of disagreement arises during the treatment of terms linear in $\Gamma_{\tilde{g}}$ that appear in the interference between the resonant and non-resonant amplitudes. These terms are discarded in the PowhegBox implementation but retained in the MatchBox approach[10]. Close

[9]The Jacobian factor is excluded in the splitting kernel of the PowhegBox implementation purely due to practical reasons, see Ref. [22].

[10]Discarding these terms in the MatchBox implementation would not be a straightforward

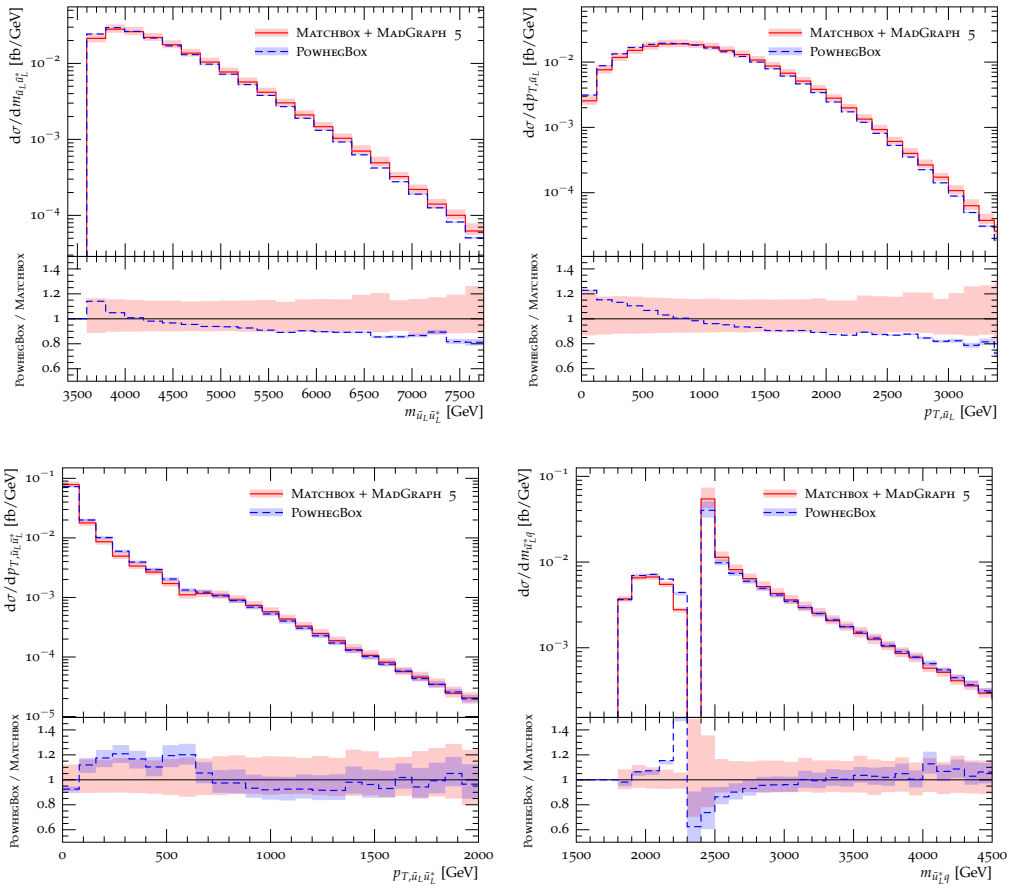

Figure 4.5: As in Figure 4.3, but using the DSII diagram subtraction method to remove contributions with on-shell gluinos.

to the resonance this leads to a difference in the implementations that scales as $m_{\tilde{g}}/\Gamma_{\tilde{g}}$. It has been verified that the observed differences in the $p_{T,\tilde{u}_L\tilde{u}_L^*}$ and $m_{\tilde{u}_L^*q}$ distributions do indeed decrease as $m_{\tilde{g}}/\Gamma_{\tilde{g}}$ is reduced.

Finally, considering the distributions generated using the DSII approach we see that the $m_{\tilde{u}_L\tilde{u}_L^*}$ and $p_{T,\tilde{u}_L}$ plots in Figure 4.5 are in relatively good agreement, however now with the PowhegBox results consistently shifted to slightly lower values. This change in slope arises because the Born configuration in the PowhegBox events is generated now with $\bar{\mathcal{B}}$ rather than $\mathcal{B}$. The $p_{T,\tilde{u}_L\tilde{u}_L^*}$ and $m_{\tilde{u}_L^*q}$ distributions shown in the bottom left and right-hand plots exhibit a good level of agreement between the two implementations, with only slight deviations in the intermediate p_T

matter due to the semi-automated method used to obtain the real-emission matrix elements.

region of the former and resonant region of the latter. In this scheme, the treatment of the on-shell phase space Jacobian factor is consistent between MATCHBOX and POWHEGBOX . Therefore, the observed discrepancy in these distributions is caused only by the differing treatment of terms linear in $\Gamma_{\tilde{g}}$ that appear in the interference contribution.

In general, the good level of agreement observed between the POWHEGBOX and MATCHBOX results presented in this section validates our implementation of ME corrections to squark-antisquark production, for both the diagram removal and subtraction procedures.

4.3 Comparison of on-shell subtraction methods

4.3.1 Setup

Having demonstrated the validity of the MATCHBOX implementation of diagram removal and subtraction in Section 4.2, in the following section we study in detail the different strategies for removing contributions with on-shell gluinos. To do so, we again rely predominantly on simulations of stable left-handed up squark-antisquark production at $\sqrt{s} = 14$ TeV, in a scenario with $(m_{\tilde{g}}, m_{\tilde{u}_L}) = (2.4, 1.8)$ TeV. When instructive, results will also be shown for alternative squark flavour and chirality combinations, and for the mass splitting $(m_{\tilde{g}}, m_{\tilde{q}}) = (1.9, 1.8)$ TeV. Unless otherwise stated, we consider ME corrected events in which the evolution of the parton shower was limited to the production of the POWHEG corrected emission only and the factorization and renormalization scales were set to $\mu_R = \mu_F = \min(m_{T,\tilde{u}_L}, m_{T,\tilde{u}_L^*})$. In all cases, the CTEQ6L1 PDF set was used and the effects of hadronization and the underlying event were not simulated. Differential distributions were created using the Rivet analysis framework, with no event selection criteria imposed. Finally, the uncertainty in results due to limited statistics is indicated by error bars in the distributions, except for the central values in ratio plots where this uncertainty is instead shown by a yellow error band.

4.3.2 Dependence on the width

Total cross section

In the diagram subtraction approach, $\Gamma_{\tilde{g}}$ does not correspond to the physical width of the gluino but is instead a regularizing parameter. Consequently, if predictions made using this approach are to be considered reliable they must be insensitive to the value of $\Gamma_{\tilde{g}}$, with any residual dependence on the width giving an indication of the size of gauge dependent contributions. To test the sensitivity of the MATCHBOX implementation of diagram subtraction to the value of the gluino width, we begin by studying the dependence on this parameter of contributions to the real-emission cross section arising from channels with resonant diagrams. In Figure 4.6, the numerical dependence of the combined $q_i g$ and $\bar{q}_i g$-initiated contributions to the real-emission cross section for the process $pp \to \tilde{q}_i \tilde{q}_i^*$ is shown, as a function of the ratio $\Gamma_{\tilde{g}}/m_{\tilde{g}}$, for $\tilde{q}_i = \tilde{u}_L$ (left) and $\tilde{d}_R$ (right). The mass of the squarks was set to $m_{\tilde{q}_i} = 1.8$ TeV, while the mass of the gluino was fixed at $m_{\tilde{g}} = 2.4$ TeV in the case of $\tilde{u}_L \tilde{u}_L^*$ production and at $m_{\tilde{g}} = 1.9$ TeV when considering $\tilde{d}_R \tilde{d}_R^*$ production. Results were obtained for fixed values of the factorization and renormalization scales, $\mu_R = \mu_F = m_{\tilde{q}_i}$.

For the squark flavour and chirality combinations in Figure 4.6, the cross sections calculated using diagram subtraction (red data points) are observed to be largely insensitive to the choice of regularizing parameter for values $\Gamma_{\tilde{g}}/m_{\tilde{g}} \lesssim 10^{-2}$. At larger values, the influence of gauge dependent contributions is visible and the diagram subtraction cross sections begin to decrease. In addition, in the very small-width limit, $\Gamma_{\tilde{g}}/m_{\tilde{g}} \lesssim 10^{-6}$, results can become numerically unstable. This leads us to concluded that widths in the range $10^{-4} \lesssim \Gamma_{\tilde{g}}/m_{\tilde{g}} \lesssim 10^{-2}$ are optimal for producing stable, gauge invariant results.

An analogous cross section calculated using diagram removal is also shown in each panel of Figure 4.6 by the blue data points. This value has no dependence on the gluino width and is included instead to illustrate the size of interference terms that are missed in this approach. To quantify the significance of the difference between the diagram subtraction and removal schemes, the full real-emission

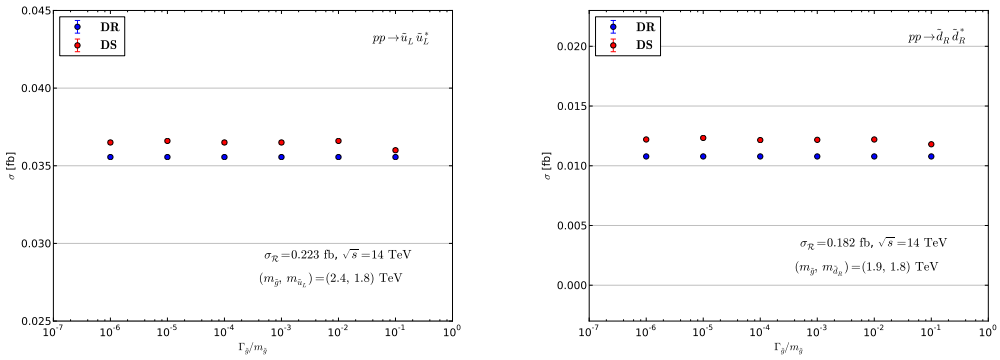

Figure 4.6: The dependence on the regularizing parameter $\Gamma_{\tilde{g}}/m_{\tilde{g}}$ of the combined $q_i g$ and $\bar{q}_i g$-initiated contributions to the real-emission cross section for the process $pp \to \tilde{q}_i \tilde{q}_i^*$, calculated using diagram subtraction (red points). Also shown is the width-independent diagram removal cross section (blue points) and the full real-emission cross section ($\sigma_{\mathcal{R}}$). Results are shown for $\tilde{u}_L \tilde{u}_L^*$ production in the scenario $(m_{\tilde{g}}, m_{\tilde{q}}) = (2.4, 1.8)$ TeV (left) and $\tilde{d}_R \tilde{d}_R^*$ production when instead $m_{\tilde{g}} = 1.9$ TeV (right).

cross section[11] for the process $pp \to \tilde{q}_i \tilde{q}_i^*$, calculated using diagram subtraction with $\Gamma_{\tilde{g}}/m_{\tilde{g}} = 10^{-4}$, is also indicated on each plot by $\sigma_{\mathcal{R}}$. Considering these values we see that, for processes in which there is valence quark content in the PDF with corresponding flavour to that of the produced squarks, the $q_i g$ and $\bar{q}_i g$-initiated channels contribute a significant fraction of the total real-emission cross section, for example 16% (7%) for $\tilde{u}_L \tilde{u}_L^*$ ($\tilde{d}_R \tilde{d}_R^*$) production in the scenario considered here. However, the interference terms omitted by the diagram removal approach amount to a less than 1% effect in the context of the full real-emission cross section in both cases[12]. The neglected interference terms are even less significant when considering the production of second generation squarks, where the $q_i g$ and $\bar{q}_i g$-initiated channels contribute to the real-emission cross section typically at the sub-percent level.

[11] The full real-emission cross section was regulated by imposing a transverse momentum cut on the final-state parton of $p_T > 1$ GeV.

[12] Although the interference terms have only a small impact at the level of the total cross section, in Section 4.3.4 we will show that for $\tilde{u}_L \tilde{u}_L^*$ production significant differences are present between differential distributions calculated with the diagram subtraction and removal procedures.

Differential distributions

Having previously demonstrated the stability of the real-emission cross section with respect to $\Gamma_{\tilde{g}}$, we study now the effect of the regularizing parameter in the context of differential distributions. To this end, we consider left-handed up squark-antisquark production, as described in Section 4.3.1, in the scenario with $(m_{\tilde{g}}, m_{\tilde{u}_L^*}) = (2.4, 1.8)$ TeV. We study separately the different diagram subtraction procedures and in each case consider distributions of $p_{T,\tilde{u}_L\tilde{u}_L^*}$ generated with $\Gamma_{\tilde{g}}/m_{\tilde{g}} = 10^{-2}$ (blue dashed line), 10^{-3} (red solid line) and 10^{-4} (green dot-dashed line). These are shown respectively for the DS0, DSI, DSI′ and DSII approaches in the upper left, upper right, lower left and lower right-hand panels of Figure 4.7. The bottom section of each plot shows the ratio of the distributions generated with $\Gamma_{\tilde{g}}/m_{\tilde{g}} = 10^{-2}$ and 10^{-4} to the one generated with the central value $\Gamma_{\tilde{g}}/m_{\tilde{g}} = 10^{-3}$. In the DSI′ approach, the cutoff on the radiation phase space used to define the resonant region was set to $\Delta = 0.4(m_{\tilde{g}} - m_{\tilde{q}})$, while in the original DSI scheme the smaller value of $\Delta = 0.05(m_{\tilde{g}} - m_{\tilde{q}})$ was used. The motivation for these values and dependence of the $p_{T,\tilde{u}_L\tilde{u}_L^*}$ distribution on this parameter will be discussed in the next section. Finally, in the DSI′ scheme the resummation profile with $\rho = 0.3$ was used to define the region of phase space below the natural starting scale of the parton shower, and in this and the DSII procedure LoopSim corrections were included to preserve the leading-order accuracy of the total cross section. This will be the case throughout the remainder of the chapter.

The upper left-hand panel of Figure 4.7 shows $p_{T,\tilde{u}_L\tilde{u}_L^*}$ distributions generated using the DS0 approach. In this scheme, the splitting kernel used to generate the hardest emission is set equal to zero at any problematic phase-space points where it would have otherwise been negative. As the value of $\Gamma_{\tilde{g}}$ decreases, the negative contributions discarded in this approach increase in size and become more localized around the resonant region $m_{\tilde{q}^*q} = m_{\tilde{g}}$. Consequently, the $p_{T,\tilde{u}_L\tilde{u}_L^*}$ distribution exhibits a significant dependence on the value of $\Gamma_{\tilde{g}}$ in the intermediate p_T region, where resonant contributions have their most significant effect. In the DSI scheme, the non-positive definite nature of the splitting kernel is dealt with by applying a cut to the phase space of the POWHEG corrected emission such that the region

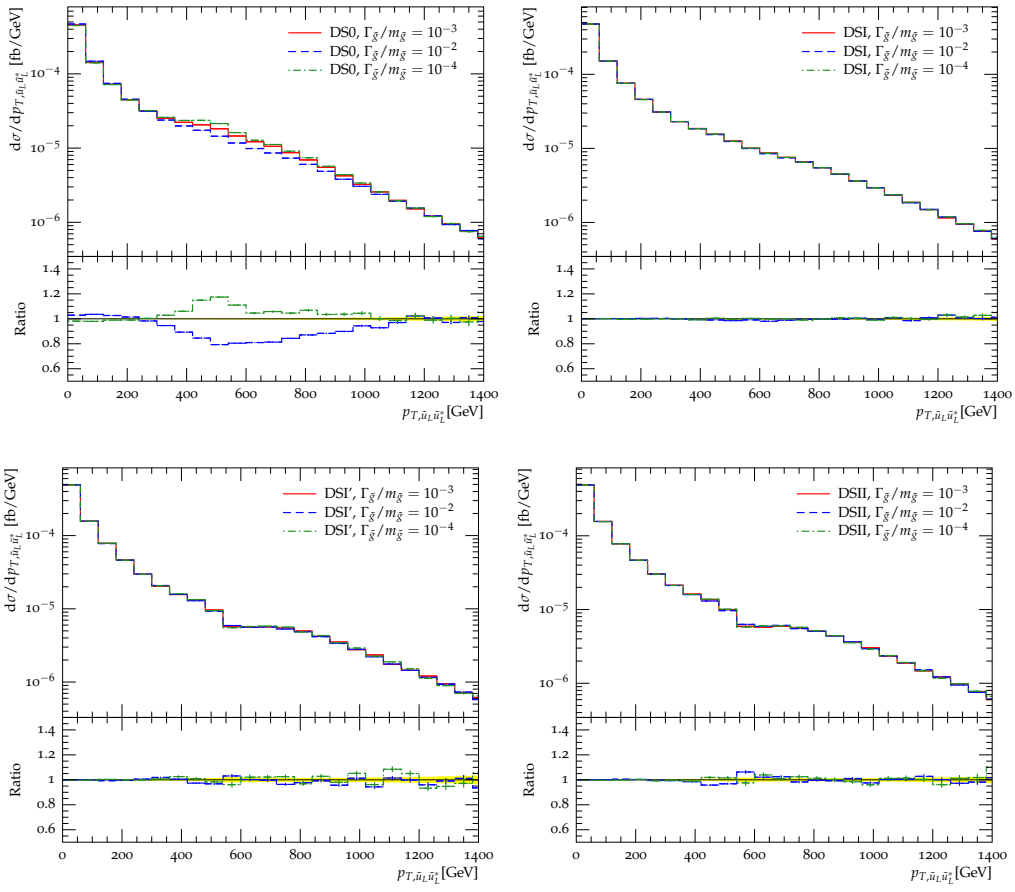

Figure 4.7: Dependence of the transverse momentum of the up squark-antisquark pair, $p_{T,\tilde{u}_L\tilde{u}_L^*}$, on the regularizing parameter $\Gamma_{\tilde{g}}/m_{\tilde{g}}$ in the DS0 (upper left), DSI (upper right), DSI′ (lower left) and DSII (lower right) schemes. Results were generated at a centre-of-mass energy $\sqrt{s} = 14$ TeV for a scenario with $(m_{\tilde{g}}, m_{\tilde{u}_L^*}) = (2.4, 1.8)$ TeV and $\Gamma_{\tilde{g}}/m_{\tilde{g}} = 10^{-2}$, 10^{-3} or 10^{-4}.

containing the majority of the negative contributions is removed. In doing so, both positive and negative contributions to the squared real-emission matrix element are discarded in the resonant region of phase space, where the choice of $\Gamma_{\tilde{g}}$ has most impact. Consequently, the $p_{T,\tilde{u}_L\tilde{u}_L^*}$ distribution generated with the DSI scheme exhibits no dependence on the gluino width. This lack of sensitivity to $\Gamma_{\tilde{g}}$ provides assurance that the region of phase space excluded by the cut does indeed contain the most significant negative contributions to the splitting kernel[13]. Finally, by

[13]In the DSI scheme, any negative contributions remaining after the phase-space cut are set to

introducing a hard real-emission contribution the DSI′ and DSII schemes take into account the negative contributions to the squared real-emission matrix element. As such, the corresponding $p_{T,\tilde{u}_L\tilde{u}_L^*}$ distributions in the lower left and right-hand panels of Figure 4.7 are largely insensitive to the value of the gluino width. A minor difference, inconsistent with pure statistical fluctuation, appears to be present in the DSII distribution generated with $\Gamma_{\tilde{g}}/m_{\tilde{g}} = 10^{-2}$ at $p_T \approx 600$ GeV. While the effect is small, we nevertheless aim to avoid it by using $\Gamma_{\tilde{g}}/m_{\tilde{g}} = 10^{-4}$ in the remainder of this section.

4.3.3 Dependence on the phase-space cutoff

In addition to the regularizing width $\Gamma_{\tilde{g}}$, the DSI and DSI′ methods also depend on the parameter Δ introduced in Eq. 4.1.8. In the DSI′ approach, schematically this parameter defines the region of phase space in which the squared non-resonant amplitudes are not the dominant term in the squared real-emission matrix element, and so real-emission configurations should be included as H-events rather than in the splitting kernel of the hardest emission[14]. Reasonable values for Δ in this approach[15] typically correspond to a significant fraction of $m_{\tilde{g}} - m_{\tilde{q}}$. In the original DSI method however, the parameter Δ is used to set the range of $m_{\tilde{q}^*q}$ values that are removed from the real-emission phase space in order to avoid encountering negative values of the splitting kernel. This excluded region is not taken into account elsewhere in the simulation. Therefore, it is desirable to choose the minimum possible value of Δ that ensures all significant negative contributions are removed. We choose $\Delta = 30$ GeV as the default setting in this scenario.

To assess the influence of the parameter Δ on results generated using the DSI

zero such that in the limit $\Delta \to 0$ the DSI and DS0 schemes are equivalent.

[14]In fact, some real-emission contributions in this resonant region must be treated as S-events so as to ensure that the hard real-emission term receives no contribution from logarithmically enhanced regions of phase space.

[15]Suitable values of Δ in the DSI′ scheme have been chosen by studying $m_{\tilde{u}_L^*q}$ distributions in LO $pp \to \tilde{u}_L\tilde{u}_L^*j$ events. Results generated using the diagram removal and subtraction methods were compared in order to determine the region of phase space in which there are significant real-emission contributions not arising from the squared non-resonant term.

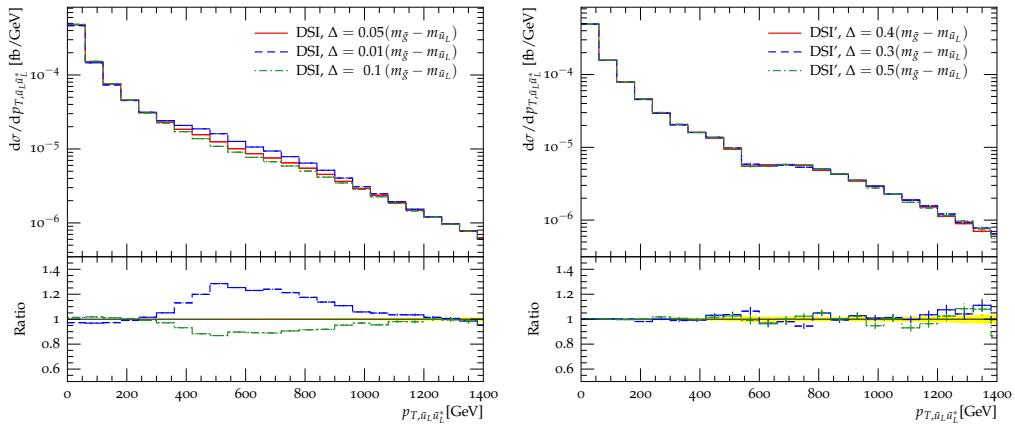

Figure 4.8: Dependence of the transverse momentum of the up squark-antisquark pair $p_{T,\tilde{u}_L\tilde{u}_L^*}$ on the parameter Δ for the DSI (left) and DSI′ (right) schemes in the benchmark scenario with $(m_{\tilde{g}}, m_{\tilde{u}_L^*}) = (2.4, 1.8)$ TeV.

and DSI′ prescriptions, matrix-element corrected events were generated as in Section 4.3.1, with the width of the gluino fixed at $\Gamma_{\tilde{g}} = 10^{-4} m_{\tilde{g}}$. Distributions of the transverse momentum of the up squark-antisquark system, $p_{T,\tilde{u}_L\tilde{u}_L^*}$, generated using the DSI and DSI′ schemes are shown respectively in the left and right-hand panels of Figure 4.8, for a benchmark scenario with $(m_{\tilde{g}}, m_{\tilde{u}_L}) = (2.4, 1.8)$ TeV. In both procedures, the value of Δ was parameterized according to $\Delta = x(m_{\tilde{g}} - m_{\tilde{u}_L})$. For the DSI approach, the values $x = 0.01$, 0.05 and 0.1 are shown, while in the DSI′ scheme x was taken to be 0.3, 0.4 or 0.5. Distributions corresponding to the highest, lowest and central values are shown in Figure 4.8 by the green (dot-dashed), blue (dashed) and red (solid) lines respectively. The lower panel in each plot shows the ratio of results generated with the highest and lowest values of x to those produced with the central value.

In the $p_{T,\tilde{u}_L\tilde{u}_L^*}$ distributions generated using the original DSI approach, a significant dependence on the value of Δ is observed. This is to be expected since in this procedure Δ directly controls the extent of the excluded phase-space region. In the DSI′ scheme, Δ instead affects the division of the real-emission matrix element between the splitting kernel and hard real-emission term. As such, its value does not impact significantly on the $p_{T,\tilde{u}_L\tilde{u}_L^*}$ distributions generated using this approach.

The insensitivity of results generated using the DSI′ procedure has been verified also for the benchmark scenario with $(m_{\tilde{g}}, m_{\tilde{u}_L}) = (1.9, 1.8)$ TeV.

4.3.4 Comparison of on-shell subtraction methods

In this section, we compare results generated using diagram removal (DR) and the DS0, DSI, DSI′ and DSII diagram subtraction procedures. To this end, events were generated as described in Section 4.3.1 with the gluino width set equal to $\Gamma_{\tilde{g}} = 10^{-4} m_{\tilde{g}}$. In the DSI and DSI′ methods the parameter Δ was set according to $\Delta = x(m_{\tilde{g}} - m_{\tilde{q}})$, with $x = 0.05$ and 0.4 respectively. Distributions of $m_{\tilde{u}_L \tilde{u}_L^*}$, $p_{T,\tilde{u}_L}$, $p_{T,\tilde{u}_L \tilde{u}_L^*}$ and $m_{\tilde{u}_L^* q}$ are shown in the upper left, upper right, lower left and lower right-hand panels of Figure 4.9. The results corresponding to the DR, DS0, DSI, DSI′ and DSII approaches are shown respectively by the red (solid), blue (dashed), green (dot-dot-dashed), yellow (dot-dashed) and black (dotted) lines. Ratios of distributions generated with the different diagram subtraction procedures to the one generated using diagram removal are shown in the lower portion of each plot.

The $m_{\tilde{u}_L \tilde{u}_L^*}$ and $p_{T,\tilde{u}_L}$ distributions in the upper panels of Figure 4.9 are largely insensitive to radiation emitted from the Born process and so also show minimal dependence on the choice of on-shell subtraction scheme. In the $p_{T,\tilde{u}_L \tilde{u}_L^*}$ and $m_{\tilde{u}_L^* q}$ distributions however, significant variations are observed between the different schemes. Considering first the latter observable, we see there is relatively good agreement between all five approaches at large values of $m_{\tilde{u}_L^* q}$. In this region, non-resonant terms provided the dominant contribution to the real-emission matrix element and therefore differing treatments of the interference between resonant and non-resonant amplitudes has little effect[16]. In the region where resonant amplitudes become significant, additional contributions arising from the interference term are evident in the diagram subtraction procedures. The interference term is positive in the region $m_{\tilde{u}_L^* q} > m_{\tilde{g}}$ and negative when $m_{\tilde{u}_L^* q} < m_{\tilde{g}}$, such that below the resonance there

[16]In the following discussion, we make the reasonable assumption that the cancellation between the resonant and subtraction terms is accurate and so only the non-resonant and interference terms are relevant.

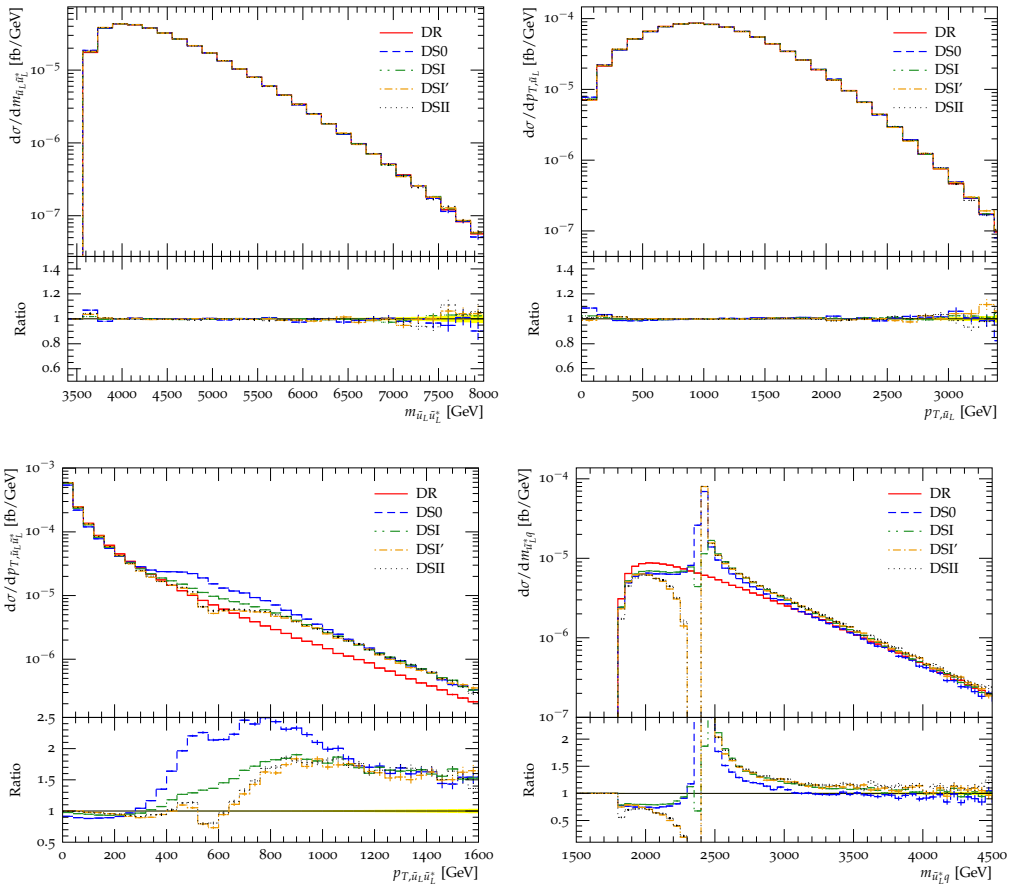

Figure 4.9: Distributions of the invariant mass of the up squark pair $m_{\tilde{u}_L\tilde{u}_L^*}$ (upper left), the inclusive up squark transverse momentum $p_{T,\tilde{u}_L}$ (upper right), the transverse momentum of the up squark pair $p_{T,\tilde{u}_L\tilde{u}_L^*}$ (bottom left) and invariant mass of the final state quark and antisquark system $m_{\tilde{u}_L^*q}$ (bottom right). Results are shown in which contributions from on-shell gluinos are removed using the diagram removal (DR) and the diagram subtraction procedures DS0, DSI, DSI′ and DSII introduced in Section 4.1. Events were generated at a centre-of-mass energy of 14 TeV for a scenario with $(m_{\tilde{g}}, m_{\tilde{u}_L^*}) = (2.4, 1.8)$ TeV.

are real-emission configurations which contribute to the total squared matrix element with negative weights. In the DS0 scheme, these negative contributions, which cause difficulties in the splitting kernel of the hardest emission, are simply set to zero. Consequently, the resulting $m_{\tilde{u}_L^*q}$ distribution is positive in all regions of phase space and significantly exceeds the DR result in the region of positive interference contributions, *i.e.* $m_{\tilde{u}_L^*q} > m_{\tilde{g}}$. In the DSI scheme, a region around the resonance is

excluded from the phase space of the splitting kernel thereby removing the most significant negative contributions. The effect of the phase-space restriction can be seen in the resonant region of the $m_{\tilde{u}_L^* q}$ spectrum, however the distribution does not fall to zero due to additional sub-dominant contributions from qg-initiated processes with $q \neq u$. In the DSII approach, all positive and negative interference contributions are retained as a hard real-emission contribution, and only the non-resonant component of the real-emission amplitude is used in the splitting kernel[17]. As a result, the DSII distribution is less than the DS0 result in the region where negative interference contributions are significant, becoming negative at $m_{\tilde{u}_L^* q} \lesssim m_{\tilde{g}}$. The DSI′ approach, which also takes into account both positive and negative interference contributions, exhibits very similar behaviour to the DSII result[18].

In the limit $m_{\tilde{u}_L^* q} \to m_{\tilde{u}_L}$, the interference term is small compared with the non-resonant contribution, leading to the expectation that the diagram removal and diagram subtraction approaches should yield similar results. However, we observe that the $m_{\tilde{u}_L^* q}$ distributions generated using diagram subtraction are suppressed with respect to the DR result. In the DS0 and DSI schemes, the integrated splitting kernel in the Sudakov form factor is substantially larger than in the case of diagram removal, explaining the observed difference. In the DSII approach, the observed suppression is instead due to the negative interference contributions, which are significant in this case since they contribute to the distribution without being multiplied by the Sudakov form factor. Finally for the DSI′ scheme, the suppression comes from the modified Born configuration used in the LoopSim approach.

Considering now the $p_{T,\tilde{u}_L \tilde{u}_L^*}$ distribution in the lower left-hand panel of Figure 4.9, we see that in the high p_T limit the four diagram subtraction procedures are in relatively good agreement and consistently exceed the diagram removal result.

[17]In addition, in the DSII scheme the Born-level matrix element undergoes the modification $\mathcal{B} \to (\mathcal{B} - \int(|\mathcal{M}_{\mathrm{R}}|^2 + 2\Re(\mathcal{M}_{\mathrm{R}}\mathcal{M}_{\mathrm{NR}}^*) - C_{\mathrm{sub}}))$ such that the unitarity of the parton shower is maintained. However, it has been verified that in this case the effect of the modification is small.

[18]It has been verified that results produced using the DSI′ and DSII methods agree well, not only in this scenario, but also for alternative squark flavour and chirality combinations and for different mass splittings between the squark and gluino.

Clearly the interference term missing from the latter scheme contributes significantly in this region. In addition, the agreement of the DS approaches implies that negative contributions to the squared real-emission matrix element are not important in this limit. Moving to lower values of $p_{T,\tilde{u}_L\tilde{u}_L^*}$, the negative contributions do however become relevant, causing the DS0 approach to overestimate the other diagram subtraction results. The DSI′ and DSII schemes again produce very similar results, and both exhibit behaviour consistent with the transition of the interference term from positive to negative values. The original DSI approach, which removes all negative and some positive contributions in the resonant region, exceeds the DSI′ and DSII results although not as significantly as the DS0 case. Finally, in the low $p_{T,\tilde{u}_L\tilde{u}_L^*}$ limit, the distributions generated with the DR, DSI′ and DSII approaches are similar. This is because the interference term is negligible in this region when compared with the enhanced non-resonant contribution. As such, the DSII and DR procedures should coincide exactly, while the DSI′ approach will have an additional term proportional to $\int_{p_T\approx p_T^{\min}}^{p_T^{\max}} 2\Re(\mathcal{M}_{\mathrm{R}}\mathcal{M}_{\mathrm{NR}}^*)dp_T$ in the exponent of the Sudakov form factor. This integral is insignificant when compared with the equivalent term arising from the squared non-resonant amplitudes if all the negative contributions to the integrand are taken into account, as is the case in the DSI′ procedure. However, when large negative contributions are excluded, as in the DS0 and DSI procedures, the integral can be significant resulting in a suppression of the $p_{T,\tilde{u}_L\tilde{u}_L^*}$ distribution in the low p_T limit. This effect is particularly significant in the DS0 scheme.

To summarize, we find that the choice of on-shell subtraction technique impacts considerably on distributions sensitive to the POWHEG corrected emission. In contrast to Section 4.3.2, significant differences are seen between distributions generated using diagram removal and those which use diagram subtraction. Of the studied diagram subtraction procedures, the DS0 and DSI approaches exhibit significant shortcomings. Both procedures fail to take into account negative contributions to the real-emission matrix element, which has a non-negligible impact in the Sudakov region of the transverse momentum distribution of the corrected emission. In addition, the former approach exhibits a significant dependence on the value of $\Gamma_{\tilde{g}}$ used, while the latter technique is sensitive to the choice of Δ. On the other hand, the DSII

and new DSI′ schemes take into account both positive and negative contributions to the real-emission matrix element and as a consequence result in sensible treatment of the on-shell contributions. The DSI′ scheme will be implemented in MATCHBOX as the default choice and the impact of applying matrix-element corrections using this scheme will be studied in more detail in the next section.

4.4 Parton-level results

4.4.1 Setup

In this section, we study the impact of the POWHEG style ME correction to squark-antisquark production on hard parton-shower radiation, using the DSI′ approach to subtract contributions from intermediate on-shell gluinos. To this end, $\sqrt{s} = 14$ TeV parton-level events were simulated in which left-handed up squark-antisquark pairs were produced. The factorization and renormalization scales were set equal to $\mu_R = \mu_F = \min(m_{T,\tilde{u}_L}, m_{T,\tilde{u}_L^*})$ and the CTEQ6L1 PDF set was used. In matrix-element corrected events, the regularizing width was set to $\Gamma_{\tilde{g}} = 10^{-4} m_{\tilde{g}}$ and the phase space cutoff parameter was $\Delta = 0.4(m_{\tilde{g}} - m_{\tilde{u}_L})$. In both corrected and uncorrected events, the full evolution of the parton shower was generated, including the truncated component of the shower where relevant. However, the effects of hadronization and the underlying event were not simulated. Distributions were plotted using the Rivet analysis framework and, unless otherwise stated, no event selection criteria were imposed. Finally, the uncertainty on the resulting distributions due to limited statistics is indicated with error bars, as in Section 4.3.1.

4.4.2 Effect of the correction

We begin by considering the case in which the produced up squarks are stable, and compare in Figure 4.10 the transverse momentum distributions of the up squark-antisquark pair generated with (blue dashed line) and without (red solid line) the POWHEG style ME correction. In the left-hand panel, results are shown for a benchmark scenario with $(m_{\tilde{g}}, m_{\tilde{u}_L}) = (700, 650)$ GeV. Similar effects to those seen in the

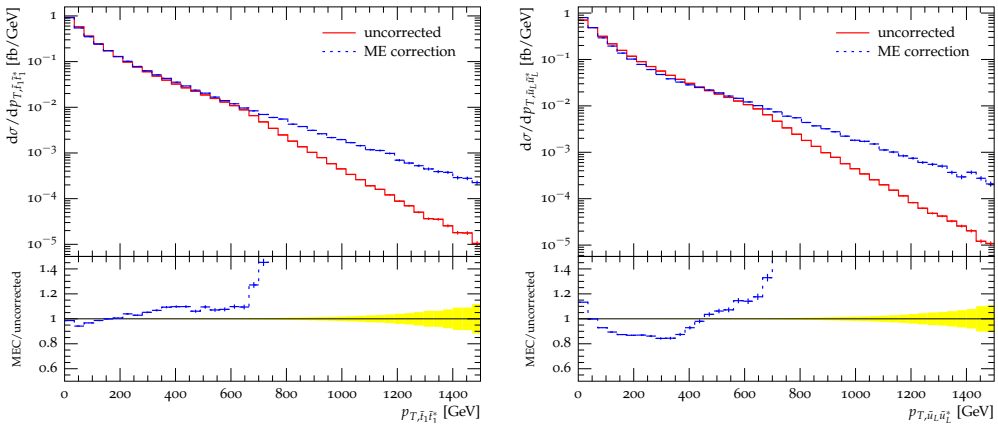

Figure 4.10: Distributions of the transverse momentum of the up squark pair $p_{T,\tilde{u}_L\tilde{u}_L^*}$ in simulations of LHC collisions at $\sqrt{s} = 14$ TeV. Leading-order and matrix-element corrected MATCHBOX events, including simulation of the full parton shower, are compared for benchmark scenarios with $(m_{\tilde{g}}, m_{\tilde{u}_L}) = (700, 650)$ GeV (left) and $(m_{\tilde{g}}, m_{\tilde{u}_L}) = (1000, 650)$ GeV (right).

case of top squark-antisquark production in Figure 3.3 are also observed in this distribution. When the ME correction is applied, we see an increase in the number of events in the high p_T tail, which is caused by the hardest emission populating the dead zone of the parton-shower phase space, and at very low values of $p_{T,\tilde{u}_L\tilde{u}_L^*}$ the distribution is shifted slightly towards softer emissions. In addition to these changes, a new effect is observed at intermediate values of the transverse momentum. The squared real-emission matrix element used to generate the hardest emission in the ME corrected events now has a contribution arising from the interference of resonant and non-resonant diagrams. No approximation of this term is included in the parton-shower splitting kernels, and therefore when the ME correction is applied we see an increase in the number of events in the region where the resonant amplitudes are significant. Similar effects are also seen in the right-hand panel of Figure 4.10, which shows $p_{T,\tilde{u}_L\tilde{u}_L^*}$ distributions in a benchmark scenario with $(m_{\tilde{g}}, m_{\tilde{u}_L}) = (1000, 650)$ GeV. In this case, the interference contribution in the ME corrected distribution now has an effect at higher values of p_T, close to the region where the effect of the dead zone becomes apparent, such that the softening in the low p_T region is more pronounced.

4.4.3 Combining corrections to squark production and decay

In analogy to Section 3.2.5, we now study the effect of applying separate and combined POWHEG style ME corrections to the production and decays of the up squarks. Events were simulated as in Section 4.4.1, with the up squarks decaying via the mode $\tilde{u}_L \to u\tilde{\chi}_1^0$. All visible final-state particles were clustered into jets using the implementation of the anti-k_T algorithm within the FASTJET program, with the energy recombination scheme and a distance parameter $R = 0.4$. The resulting jets were required to have pseudorapidity and transverse momentum satisfying $|\eta_j| < 4.9$ and $p_{T,j} > 20$ GeV respectively. The missing transverse momentum in each event was determined from the vector sum of the transverse momentum of all visible final-state particles. Distributions of the magnitude of this quantity, E_T^{miss}, and the transverse momentum of the three hardest jets, p_{T,j_i} for $i = 1, 2, 3$, are plotted in Figures 4.11 and 4.12 for benchmark scenarios with $(m_{\tilde{g}}, m_{\tilde{u}_L}) = (2.4, 1.8)$ TeV and $(m_{\tilde{g}}, m_{\tilde{u}_L}) = (700, 650)$ GeV respectively. In both cases, the mass of the neutralino was $m_{\tilde{\chi}_1^0} = 600$ GeV. Results generated with no ME correction (solid red line) are compared to those generated with ME corrections applied to the up squark decays (blue dashed line), production (green dot-dash line) or in both stages of the event (black dotted line). The lower panel in each plot shows the ratio of results generated with one or both ME correction to those which were produced with no corrections.

In the scenario with $(m_{\tilde{g}}, m_{\tilde{u}_L}) = (2.4, 1.8)$ TeV, the large difference in mass between the squark and its decay products means that up quarks produced in the decay will typically be very energetic and form the basis of the hardest jets in the event. Applying POWHEG style ME corrections during the squark decays therefore has a significant impact on the p_{T,j_1} and p_{T,j_2} distributions in Figure 4.11, shifting both towards higher values. This is caused by the correction softening the hardest emission in the parton shower initiated by each decay, resulting in the decay products themselves having higher transverse momentum. When instead the POWHEG style correction is applied to the production stage of the event, no significant effect is observed. This correction effects the momentum of the combined squark-antisquark system and has only a negligible impact on the individual momenta of the up squarks. Consequently the p_T distributions of the separate up

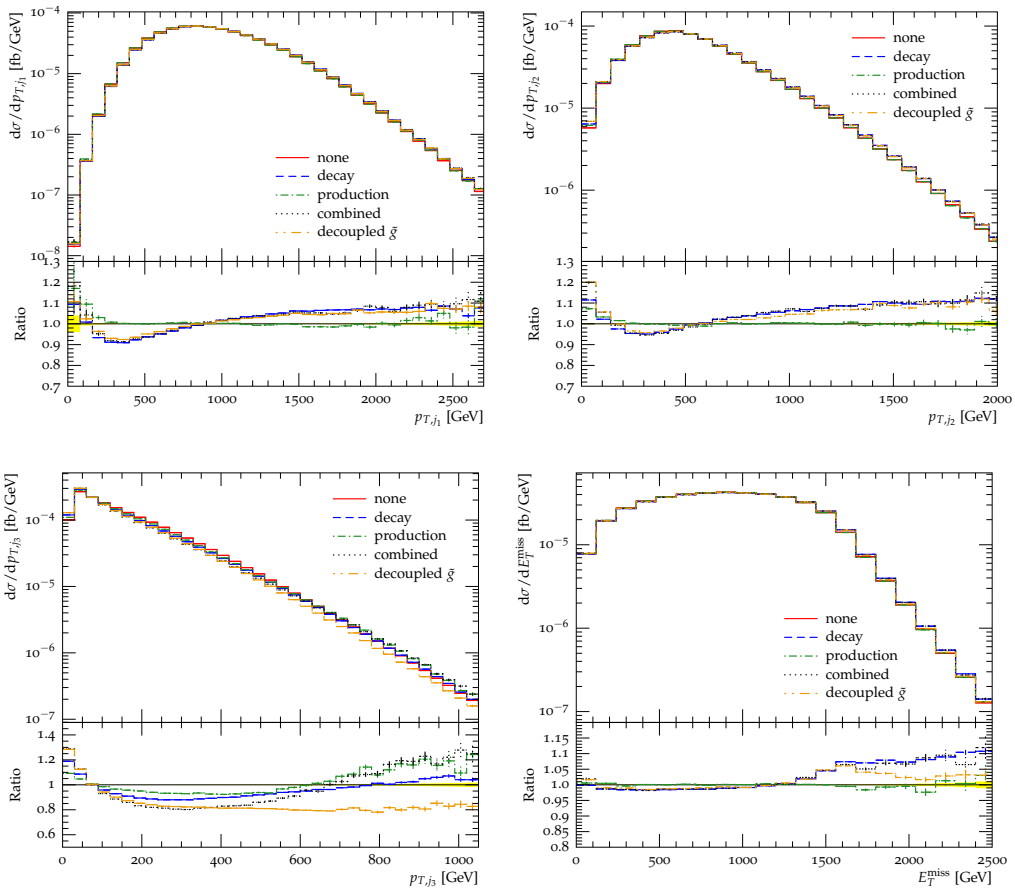

Figure 4.11: Distributions of the transverse momentum of the first $p_{T,j1}$ (upper left), second $p_{T,j2}$ (upper right) and third $p_{T,j3}$ (lower left) hardest jet in each event and the missing transverse energy E_T^{miss} (lower right). Results are shown for the cases in which either no ME corrections have been applied or ME corrections have been applied to the up squark production (using the DSI′ procedure), decays or both. Events were generated in the benchmark scenario with $(m_{\tilde{g}}, m_{\tilde{q}}) = (2.4, 1.8)$ TeV and $m_{\tilde{\chi}_1^0} = 600$ GeV. Also shown are distributions generated with combined ME corrections in the case that the gluino is decoupled.

squark decay products, p_{T,j_1} and p_{T,j_2}, show no change.

While similar effects are observed in the p_{T,j_1} and p_{T,j_2} spectra, the p_{T,j_3} plot in Figure 4.11 exhibits different trends. This distribution is sensitive to hard parton shower emissions and so is shifted towards lower values when ME corrections are applied to the decays of the up squarks. Similarly, when the correction is applied during the production stage of the event the p_{T,j_3} distribution is again softened,

reflecting the tendency of the uncorrected parton shower to overpopulate the hard regions of the shower phase space. In the high p_T region, the corrected distribution begins to exceed the uncorrected result. However, the drop-off in the uncorrected distribution, characteristic of the dead zone in the parton-shower phase space, occurs at $p_T \approx m_{\tilde{u}_L}$ and so is not evident in this case. Combining the two ME corrections leads to further softening in the low p_T region of the distribution.

Finally, in the E_T^{miss} distribution of Figure 4.11 we find that applying ME correction to the decays of the up squarks has a significant impact. This distribution is largely governed by the momentum of the pair of neutralinos produced in each event and so is shifted to higher values when this correction is applied. In contrast, no effect is seen when the ME correction is applied in the production stage of the event, implying that increasing the number of events in which the squark-antisquark pair recoils against very hard ISR does not have a significant impact in this scenario.

Also shown on each plot in Figure 4.11 is the distribution obtained when both ME corrections are applied in a benchmark scenario with $m_{\tilde{u}_L} = 1.8$ TeV and the gluino too massive to be kinematically accessible at this centre-of-mass energy (yellow dot-dot-dashed line). Comparing this to the case with $m_{\tilde{g}} = 2.4$ TeV, we see that decoupling the gluino only has a substantial effect in the tail of the $p_{T,j3}$ distribution. The difference is caused by the absence of the real-emission interference term between resonant and non-resonant diagrams when the gluino is decoupled. While the effect is of the order of 50% in the high p_T region, it amounts to only a sub-percent change in the number of events which would pass a event selection criterion $p_{T,j_3} > 200$ GeV.

Equivalent distributions to those in Figure 4.11 are shown in Figure 4.12 for the benchmark scenario with $(m_{\tilde{g}}, m_{\tilde{u}_L}) = (700, 650)$ GeV and $m_{\tilde{\chi}_1^0} = 600$ GeV. Considering first the p_{T,j_1} distribution in the upper left-hand panel we see that the momentum distribution is much softer than in the previous high mass scenario. The compressed nature of the mass splitting between the squark and neutralino means that jets originating from the up squark decays are significantly less energetic. Nevertheless, the up quarks produced in the decays still contribute significantly in the low p_T region of this distribution. Therefore, the distribution is shifted towards

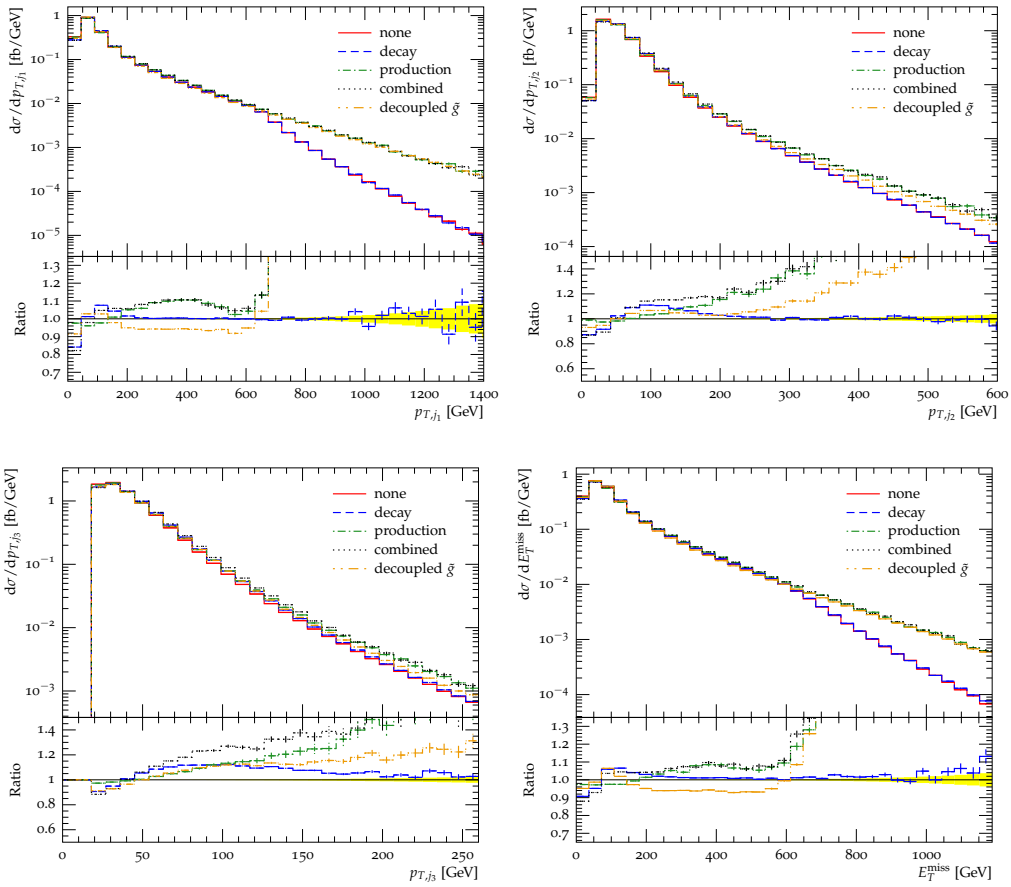

Figure 4.12: As in Figure 4.11, but for the compressed benchmark scenario with $(m_{\tilde{g}}, m_{\tilde{q}}) = (700, 650)$ GeV.

higher values when ME corrections are applied to the decays of the up squarks. No change occurs in the high p_T region, where the spectrum is mainly sensitive to parton-shower radiation. Applying the ME correction to the production of the up squark-antisquark pair has a much more dramatic effect. The p_{T,j_1} distribution is now largely governed by the distribution of the hardest parton-shower emission produced during the showering of the hard scattering process. As such, we see changes in the distribution similar to those in Figure 4.10. The ME corrected distribution exceeds the uncorrected one in the high p_T region due to the formers ability to the fill the parton-shower dead zone. Furthermore, an increase in the number of events is also seen at intermediate values of p_T, which is caused by the additional interference term in the splitting kernel of the POWHEG corrected emission. However, the softening of the corrected result with respect to the uncorrected case that is present

in the low p_T region of Figure 4.10 is not evident in this distribution. This is because the change occurs at values of the transverse momentum below the event selection criterion $p_{T,j_1} > 20$ GeV.

The changes seen in the p_{T,j_1} distribution are observed also in the p_T spectra of the second and third hardest jet in each event, p_{T,j_2} and p_{T,j_3}, which will typically originate from splittings of the hardest parton-shower emission. Similar trends to those in p_{T,j_1} are also evident in the distribution of the missing transverse energy in Figure 4.12, although in this case the shift in the distribution seen when ME corrections are applied to the up squark decays is due to increases in the p_T of the neutralinos, rather than the up quarks. In contrast to the high mass benchmark point, the recoil of squark-antisquark pairs against hard ISR does have a substantial effect on the shape of the distribution, with more events populating the high E_T^{miss} region when ME corrections are applied to the production stage of the event.

As in Figure 4.11, results are also shown which correspond to the same benchmark scenario with a decoupled gluino, including ME corrections during both the production and decays of the squarks. Decoupling the gluino has a significant impact on all the distributions. The change is driven by the fact that real-emission interference terms between resonant and non-resonant diagrams are negligible in the case of a very high mass gluino. As such, the transverse momentum spectrum of the POWHEG corrected emission now exhibits softening in the intermediate and low p_T limits. This effect causes a 13% reduction in the number of events passing an event selection cut of $p_{T,j_1} > 200$ GeV, or equivalently $E_T^{\text{miss}} > 200$ GeV. Experimental searches for squarks at the LHC are often interpreted in terms of simplified models with decoupled gluinos. By doing so, the search is likely to be less sensitive to compressed regions of parameter space than it would be in a scenario with a heavy but accessible gluino.

4.5 Summary

In this chapter we have studied the effect of applying POWHEG style ME corrections to squark-antisquark production, having extended the correction to stop-antistop production introduced in the previous chapter to treat general squark flavours. For the production of all squark flavours other than the stop, an additional complication arises in scenarios with $m_{\tilde{q}} < m_{\tilde{g}}$ due to the presence of divergent real-emission amplitudes containing an intermediate s-channel gluino. These contributions occur also in the leading-order production of a squark and a gluino, where the gluino then decays to a quark and an antisquark. As such, they must be removed from the real-emission amplitude to avoid double counting. Several previously proposed methods for removing this contribution have been implemented within the MATCHBOX framework, along with a new approach which we have dubbed the DSI′ method. Where possible, our implementation has been validated against results generated using the POWHEGBOX program.

We have focused predominantly on left-handed up squark-antisquark pair production and, working at parton level, have studied the different schemes for removing on-shell contributions. The sensitivity of each approach to the width of the gluino has been studied both at the level of total cross sections and in differential distributions. In addition, the dependence of results on restrictions applied to the real-emission phase space, which are necessary in some schemes but nevertheless unphysical, has also been investigated. From the information gained in these studies, we conclude that the new DSI′ and previously proposed DSII [22] schemes provide the most consistent and well-motivated treatments of on-shell contributions.

Having verified the behaviour of the newly proposed DSI′ scheme, the effect of applying POWHEG style ME corrections using this prescription was studied. Applying the ME correction was found to have similar effects on distributions sensitive to the hardest parton-shower emission to those observed in stop-antistop production. We find that there is a softening of distributions in the low transverse momentum region and a significant increase in the number of events which contain very high transverse momentum radiation. In addition to these effects, a previously unseen increase in the number of events in the intermediate p_T region was also observed. This feature is

caused by additional contributions to the splitting kernel of the POWHEG corrected emission arising from the interference of resonant and non-resonant real-emission amplitudes.

Finally, the effect of combining ME corrections during the production and decay stages of the event was studied, again for the case of left-handed up squark production. We find that both ME corrections can have a substantial effect on distributions, but that the most marked impact occurs when the ME correction is applied to the production of the squark-antisquark pair in scenarios featuring small mass splittings between the different superparticles. Furthermore, we find that in such cases the mass of the gluino impacts significantly on the shapes of distributions, and results in a more than 10% reduction in the number of events passing a typical event selection criterion of $E_T^{\text{miss}} > 200$ GeV when the gluino is decoupled, as compared with the case in which the gluino is heavier than the squark but easily accessible at LHC energies.

Chapter 5

Constraining compressed SUSY scenarios with monotop signatures

The search for monojet signatures has proven to be an effective way of constraining the compressed regions of SUSY parameter space and other new physics scenarios. Inspired by this approach, monotop signals of a single top quark together with missing transverse momentum have been proposed as a means of constraining a number of BSM models, see Refs. [131, 132] for early work investigating the sensitivity of the LHC to monotop signals using a simplified model approach. Since then monotops have become increasingly well studied, see for example Refs. [133–139], and are predicted to be observable at the LHC for a large range of new physics masses and couplings. Consequently, experimental searches for monotop signatures have been performed using data recorded at the Tevatron [140] and LHC [141–143], but have found no evidence of new physics to date.

In this chapter we consider the possibility of accessing the compressed regions of SUSY parameter space using monotop probes. The production of a superpartner pair in association with a top quark can manifest itself as a monotop signature when the decay of each superpartner gives rise to a small amount of missing transverse energy and soft SM objects. We use Monte Carlo simulations to determine the projected sensitivity of the LHC with 300 fb^{-1} of 14 TeV collision data to two simplified compressed scenarios.

The chapter is organised as follows. In Section 5.1, our simplified compressed

scenarios are outlined along with the technical setup for the simulation of both the new physics signals and the relevant sources of background. Analysis strategies based on both leptonic and hadronic monotop decays have been developed and are detailed in Section 5.2. In Section 5.3, the results for specific benchmark scenarios are presented and the sensitivity of monotop probes is compared with the projected reach of alternative analysis strategies at the LHC. Finally, some concluding remarks are given in Section 5.4.

5.1 Monte Carlo simulations

5.1.1 Signal processes

In our simplified model framework, we first consider the production of a top quark in association with the lightest top squark $\tilde{t}_1$ and the gluino $\tilde{g}$, for the case in which both sparticles decay into the lightest neutralino $\tilde{\chi}_1^0$ and Standard Model particles. All other superpartners are decoupled, with masses that are inaccessible at the LHC. We consider the scenario in which the masses of the stop and gluino are similar and not significantly larger than that of the neutralino, such that the additional Standard Model objects produced during the superparticle decays are soft and invisible. Monotop systems may also be produced in scenarios where the gluino is significantly heavier than the stop, which is again not much heavier than the neutralino. In this case, monotop production relies on the associated production of a heavy gluino and a light top squark, the gluino decays into a top quark and a stop, while both stops decay invisibly. Such a process occurs at tree level when considering flavour mixings of the up-type squarks that, for instance, occurs in minimally-flavor-violating SUSY models. Production cross sections in such models are highly suppressed given that all flavour-violating effects are driven by the CKM matrix, however could be enhanced in non-minimal flavour violation scenarios [144–146]. Nevertheless, we study only the first class of models.

In addition to the case in which a top squark and top quark are produced along with a gluino, we consider also the signal in which they are produced in association

with the lightest neutralino[1]. Again, here we focus on the scenario in which the top squark is not significantly heavier than the neutralino. For both signal scenarios, the stop is chosen to be a maximal admixture of the left-handed and right-handed stop gauge eigenstates. For the signal scenario in which a gluino is produced with a top squark and top quark, the lightest neutralino is assumed to be purely bino. When instead a neutralino is produced directly, it is assumed to be predominantly higgsino[2]. This enhances the production cross section as compared with the purely bino neutralino scenario.

Event generation for the hard scattering signal process was performed using the MadGraph 5 [105] implementation of the MSSM model [109–112]. Using this setup, the CTEQ6L1 PDF set [115] was convoluted with hard matrix elements describing the production of a pair of strong superpartners in association with either a leptonically or a hadronically decaying top quark. The decays of the superparticles and matching of the parton-level hard events with a parton shower and hadronization infrastructure was performed with Herwig++ version 2.7 [6,7]. The accessible decay modes of the final-state superparticles and associated branching ratios were calculated internally by Herwig++ . No 4-body modes were considered, and therefore in the highly compressed region with $m_{\tilde{t}_1} < m_b + m_W + m_{\tilde{\chi}_1^0}$ the dominant decay channel of the stop was[3] $\tilde{t}_1 \to c\,\tilde{\chi}_1^0$. In regions of phase space where $m_{\tilde{t}_1} > m_b + m_W + m_{\tilde{\chi}_1^0}$,

[1]In this scenario, the gluino is now decoupled.

[2]The neutralino mixing matrix is chosen such that the lightest neutralino is 99% higgsino and 1% bino. In doing so, the production cross section is enhanced while still leaving all top squark decay modes accessible. In scenarios with a predominantly higgsino $\tilde{\chi}_1^0$, the lightest chargino and neutralino will be near degenerate in mass. As such, the production of a top squark and bottom quark in association with the lightest chargino will lead to a "mono b-jet" signature that could be used to constrain the same region of parameter space as the monotop probe. This signature provides an interesting alternative to monotop signals, however, its investigation goes beyond the scope of this work.

[3]In the MSSM, the decay $\tilde{t}_1 \to c\,\tilde{\chi}_1^0$ proceeds via a loop and CKM suppressed channel only. Therefore, the width of the top squark is sufficiently small that hadronization occurs before the top squark decays. However, the lifetime of the top squarks is still short when compared with detector time scales and so we assume the final observables do not differ significantly from the situation in which the top squarks decay promptly, before hadronization.

the decay mode $\tilde{t}_1 \to W^+ b \tilde{\chi}_1^0$ was found to dominate. For all mass scenarios considered in this study, the dominant gluino decay channel was $\tilde{g} \to q\,\bar{q}\,\tilde{\chi}_1^0$. Finally, a global normalization factor of $K = 1.4$ was included when simulating the production of a top squark, top quark and neutralino. This factor aims to account for the large next-to-leading order contributions to this process [147].

Signal cross sections for the example scenarios of top squark, top quark and gluino production with $(m_{\tilde{t}_1} = m_{\tilde{g}}, m_{\tilde{\chi}_1^0}) = (200, 190)$ GeV and top squark, top quark and neutralino production with $(m_{\tilde{t}_1}, m_{\tilde{\chi}_1^0}) = (145, 75)$ GeV are given in Table 5.1. Comparing with the expected monojet cross sections of 12.5 pb (for $m_{\tilde{t}_1} = m_{\tilde{g}} = 200$ GeV after imposing a typical monojet requirement on the jet transverse momentum of $p_{T,j} > 450$ GeV) and 0.7 pb (for $m_{\tilde{t}_1} = 145$ GeV again after imposing a requirement on the jet transverse momentum of $p_{T,j} > 450$ GeV), one can expect these scenarios to be sensitive to both monotop and monojet probes. However, the competitive cross section in the case of top quark, top squark and neutralino production is strongly affected by the composition of the neutralino. In scenarios with a lightest neutralino that is predominately bino or wino, the cross section drops to 0.09 pb and 0.2 pb respectively when $(m_{\tilde{t}_1}, m_{\tilde{\chi}_1^0}) = (145, 75)$ GeV, with no selection criteria imposed. In these cases, it is unlikely that monotop probes could provide comparable limits to those derived using monojet searches.

5.1.2 Background processes

Leptonically decaying monotop states result in event topologies with a single hard lepton, a jet originating from the fragmentation of a b-quark and missing transverse energy. As such, the main sources of background events are the production of a $t\bar{t}$ pair where one of the top quarks decays leptonically and the other one hadronically, and the production of a single-top quark in association with a W-boson where either the top quark or the W-boson decays leptonically. We also consider extra background processes expected to have subdominant contributions, namely the two other single-top production modes and W-boson plus jets, γ^*/Z-boson plus jets and diboson production.

Turning to hadronically decaying monotops, the above signal final-state is altered

with the hard lepton being replaced by a pair of hard jets. In this case, the dominant contributions to the background events come from fully hadronic $t\bar{t}$ events, Z-boson plus jets events in which the Z-boson decays invisibly and W-boson plus light-jets events in which the W-boson decays leptonically but where its decay products escape identification[4]. Additionally, single-top, W-boson plus b-jets and diboson production processes are also expected to contribute, in a less significant way, to the total number of monotop background events.

In the simulation of the Standard Model backgrounds for both the leptonic and hadronic monotop analyses, QCD multijet production processes have been neglected. We instead assume the related background contributions will be under good control after the selection criteria detailed in Section 5.2 have been applied. Finally, no detector effects other than a b-tagging efficiency (see Section 5.2) have been simulated in this work. Consequently, all possible sources of instrumental background have been ignored.

Parton-level production of top-antitop pairs, including the top decays, was simulated by convoluting NLO matrix elements with the CTEQ6M PDF set [115] using the PowhegBox program [5, 79, 82, 148]. These events were then matched to Herwig++ for parton showering and hadronization. Owing to the angular-ordered nature of the Herwig++ parton shower, it is in principle necessary to include a truncated component of the parton shower which simulates emissions with a smaller transverse momentum than those described by the NLO matrix elements, but a larger value of the shower evolution variable. However, the corresponding effects are typically small and so here have been omitted[5]. The same machinery was used to generate single-top events [130, 149], suppressing resonant contributions related

[4]The production of a hadronically decaying W-boson in association with jets does not induce a significant background contribution due to the small expected amount of missing transverse energy in this case.

[5]As was found in Chapter 3, some modification of the default Herwig++ shower setup is required to render the direct showering of externally generated Powheg events equivalent to the case in which no truncated shower is simulated. These modification have not been included in the following, however it has been verified that excluding them has negligible impact on the number of events passing the event selection criteria.

Process	σ[pb]	$N_{\text{event}}^{\text{SRL1}}$	$N_{\text{event}}^{\text{SRL2}}$	$N_{\text{event}}^{\text{SRH1}}$	$N_{\text{event}}^{\text{SRH2}}$
$W(\to l\nu)$ + light jets	67453	≈ 0	3150	4500	9030
$\gamma^*/Z(\to l\bar{l})$ + jets	26603	≈ 0	≈ 0	-	-
$\gamma^*/Z(\to \nu\bar{\nu})$ + jets	12387	≈ 0	≈ 0	23160	36390
$t\bar{t}$	781	43230	292500	35190	80040
Single top [t-channel]	7320	36.6	4650	250.8	762
Single top [s-channel]	312	6.3	244.8	35.7	75.3
tW production	2313	4890	42570	3480	7560
$Wb\bar{b}$ with $W \to l\nu$	3660	≈ 0	549	134.1	158.7
Diboson	158	31.5	268.8	205.5	315
Total background	107834	48190	343900	66960	134330
$(m_{\tilde{g}} = m_{\tilde{t}_1}, m_{\tilde{\chi}_1^0}) = (200, 190)$ GeV	2.54	8430	17280	12690	14700
$(m_{\tilde{t}_1}, m_{\tilde{\chi}_1^0}) = (145, 75)$ GeV	2.37	3180	7773	6796	9840

Table 5.1: Cross sections for the simulated background processes and two representative signal scenarios, including an NLO K-factor of 1.4 for the signal scenario in which the stop and top are produced in association with a neutralino. Also shown are the number of events, N_{events}, surviving all selection criteria in the leptonic (SRL1, SRL2) and hadronic (SRH1, SRH2) signal regions. Results correspond to 300 fb^{-1} of LHC collisions at a centre-of-mass energy of 14 TeV.

to the tW mode following the diagram subtraction prescription of Ref. [130], as implemented in the PowhegBox.

In order to simulate the production of a W-boson with light-flavour jets (u, d, s, c) or a γ^*/Z-boson with both light and heavy-flavour jets (u, d, s, c, b), the Sherpa 2.0 [150, 151] package was used. We have followed the MENLOPS prescription to match an event sample based on NLO matrix elements related to the production of a single gauge boson to LO samples describing the production of the same gauge boson with one and two extra jets [152, 153]. In all cases, the vector bosons were forced to decay

either leptonically or invisibly, including all three flavours of leptons, and matrix elements were convoluted with the CTEQ6M PDF set. Moreover, the invariant masses of lepton pairs produced via a γ^*/Z-boson s-channel diagram were required to exceed 10 GeV.

The production of a W-boson with heavy-flavour jets was simulated separately using MadGraph 5 and its built-in Standard Model implementation. We have generated LO matrix elements that have been convoluted with the LO PDF set CTEQ6L1. Parton-level events were simulated including the leptonic decay of the W-boson and then showered and hadronized with Herwig++.

Finally, diboson production was simulated at NLO accuracy and matched to the Herwig++ parton shower using its built-in Powheg implementation [154]. In this case, the component of radiation corresponding to the truncated shower was included, and the matrix elements were convoluted with the CTEQ6M PDF set.

The total cross sections for all considered background processes are shown in Table 5.1.

5.2 Event selection strategies

5.2.1 Object reconstruction

The objects used as inputs for the leptonic and hadronic monotop search strategies of the next two subsections were reconstructed as in typical single-top studies performed by the ATLAS collaboration (see for example Ref. [155]). Electron (muon) candidates were required to have transverse momentum $p_{T,\ell} > 10$ GeV, pseudorapidity satisfying $|\eta_\ell| < 2.47$ (2.5) and to be isolated, such that the sum of the transverse momenta of all charged particles in a cone of radius[6] $\Delta R < 0.2$ centered on the lepton was less than 10% of its transverse momentum.

Jets were reconstructed from all visible final-state particles with pseudorapidity satisfying $|\eta| < 4.9$ by applying an anti-k_T jet algorithm [99] with a radius param-

[6]The angular distance between two particles is defined as $\Delta R = \sqrt{\Delta\phi^2 + \Delta\eta^2}$, where $\Delta\phi$ and $\Delta\eta$ are their differences in azimuthal angle and pseudorapidity respectively.

eter $R = 0.4$, as implemented in the FastJet program [92]. Reconstructed jet candidates were required to not overlap with candidate electrons within a distance of $\Delta R < 0.2$, and to have transverse momentum $p_{T,j} > 20$ GeV and pseudorapidity $|\eta_j| < 2.5$. Any lepton candidate within a distance $\Delta R < 0.4$ to the closest of the selected jets was then discarded. We further identified jets as originating from a b-quark if their angular distance to a B-hadron satisfies $\Delta R < 0.3$ and imposed a p_T-dependent b-tagging probability derived from the data in Ref. [123]. This corresponds to an average efficiency of 70% in the case of $t\bar{t}$ events.

5.2.2 Leptonic monotops

The preselection of events possibly containing a leptonically decaying monotop signal was designed to reflect the expected final-state particle content. As such, events were required to contain exactly one lepton candidate with transverse momentum $p_{T,\ell} > 30$ GeV and one b-jet with transverse momentum $p_{T,b} > 30$ GeV. To reflect the expectation that the produced superparticles (and their decay products) are largely invisible, any event containing an extra jet with transverse momentum $p_{T,j} > \min(p_{T,b}, 40\,\text{GeV})$ was discarded. After these basic requirements, a number of additional selection steps were implemented in order to increase the sensitivity s of the analysis to the signal, where $s = S/\sqrt{S+B}$ and S and B are the number of signal and background events passing all selection criteria, respectively. Two signal regions were defined, SRL1 and SRL2, with the former dedicated to the high mass regions of the superparticle parameter space and the latter to the low mass regions.

Starting with the signal region SRL1, the missing transverse momentum $\mathbf{p}_T^{\text{miss}}$ in the event, determined from the vector sum of the transverse momenta of all visible final-state particles, was required to have a magnitude $E_T^{\text{miss}} > 150\,\text{GeV}$. The orientation of the missing transverse momentum with respect to the identified lepton was also constrained by imposing a minimum value for the W-boson transverse mass,

$$m_T^W = \sqrt{2p_{T,\ell}E_T^{\text{miss}}\left[1 - \cos\left(\Delta\phi(\ell, \mathbf{p}_T^{\text{miss}})\right)\right]}\,, \tag{5.2.1}$$

where $\Delta\phi(\ell, \mathbf{p}_T^{\text{miss}})$ is the difference in azimuthal angle between the lepton and the missing transverse momentum. Selected events were required to satisfy $m_T^W >$

120 GeV. This is motivated by the observation that the peak of the m_T^W distribution occurs at lower values in events in which the missing transverse momentum originates solely from the leptonic decay of a W-boson than it does when both a neutrino from the W-boson decay and a pair of invisible sparticles contribute to $\mathbf{p}_T^{\text{miss}}$ (like in the signal case). This last selection ensures that the non-simulated QCD multijet background is negligible [156, 157].

The second signal region, SRL2, was optimized for lower mass scenarios where E_T^{miss} is typically very small due to a low neutralino mass. Instead of constraining the individual quantities E_T^{miss} and m_T^W, events satisfying

$$E_T^{\text{miss}} + m_T^W > 220\,\text{GeV}, \tag{5.2.2}$$

were instead selected. In doing so, signal events with low values of E_T^{miss} are retained by the selection process provided they have a suitably large value of m_T^W. This ensures that the QCD multijet background contributions are small [158].

In both search strategies, the following additional selection criteria were imposed. Firstly, in order to reduce the number of background events in which the identified lepton and b-jet did not originate from a single top quark, a restriction on the invariant mass of the lepton plus b-jet system was imposed,

$$m_{b\ell} = \sqrt{(p_b + p_\ell)^2} < 150\,\text{GeV}. \tag{5.2.3}$$

This leads to a reduction in background contributions from semi-leptonically decaying $t\bar{t}$ and s-channel single-top events in which one of the b-jets was not identified. Finally, a minimum value for the invariant mass of the monotop system, or equivalently for the invariant mass of the system comprised of the missing transverse momentum, the identified lepton and b-jet,

$$m\left(\mathbf{p}_T^{\text{miss}}, \ell, b\right) = \sqrt{(\mathbf{p}_T^{\text{miss}} + p_\ell + p_b)^2} > 700\,\text{GeV}, \tag{5.2.4}$$

was enforced.

5.2.3 Hadronic monotops

In the hadronic case, final states arising from the production of a pair of strong superpartners together with a top quark contain one heavy-flavour and two light

jets associated with the top decay, as well as missing transverse energy and extra soft objects arising from the decays of the superparticles. Therefore, events that contained no candidate leptons and exactly one b-jet with $p_{T,b} > 30$ GeV were selected. In addition, we have demanded the presence of exactly three light jets in each event. This requirement was found to slightly increase the analysis sensitivity over the case in which only two light jets were required.

Two search strategies referred to as SRH1 and SRH2 were designed, the former to be sensitive to scenarios with higher superparticle masses and the latter to lower mass cases. The missing transverse energy in events was required to satisfy $E_T^{\text{miss}} > 200\,\text{GeV}$ and $E_T^{\text{miss}} > 150\,\text{GeV}$ in the SRH1 and SRH2 regions respectively. While an even looser missing energy selection might increase the sensitivity in the SRH2 case, this would no longer ensure sufficient control of the non-simulated QCD multijet background and furthermore not be sensible in the context of event triggers. To improve the trigger efficiency associated with the SRH2 region, the hardest non b-tagged jet in each event was required to fulfil $p_{T,j_1} > 80\,\text{GeV}$, such that a trigger based on the selection of a hard jet in association with missing transverse energy may be used. In contrast, no selection on the hardest jet was imposed for the SRH1 region, since it is likely that triggers based on the amount of missing transverse energy only could be used in this case.

A number of selection criterion were imposed for both strategies to improve the sensitivity of the analysis. Firstly, the invariant mass of a light dijet system, m_{jj}, was required to be consistent with the mass of the W-boson,

$$50\,\text{GeV} < m_{jj} < 100\,\text{GeV}, \tag{5.2.5}$$

where the pair of light jets was chosen such that the quantity $|m_W - m_{jj}|$ was minimized. This pair of light jets was then combined with the b-tagged jet to fully reconstruct the hadronically decaying top quark, and the resulting system was constrained to have an invariant mass in the range

$$100\,\text{GeV} < m_{bjj} < 200\,\text{GeV}. \tag{5.2.6}$$

This eliminates a large number of background events which do not contain a hadronically decaying top quark. In particular, it leads to a significant reduction of the W-

and γ^*/Z-boson plus jet background contributions.

Next, several restrictions were applied based on the kinematic configuration of the events. The azimuthal angle between the missing transverse momentum and both the b-tagged and hardest non b-tagged jet in the event were required to be suitably large,

$$\Delta\phi\left(\mathbf{p}_T^{\text{miss}}, \mathbf{p}_{j1}\right) > 0.6 \quad \text{and} \quad \Delta\phi\left(\mathbf{p}_T^{\text{miss}}, \mathbf{p}_b\right) > 0.6 \ . \tag{5.2.7}$$

These selection criteria were designed to rejected events in which the missing transverse energy originates from the mismeasurement of jets or semi-leptonic decays of heavy-flavour hadrons. Including these requirements is also expected to reduce background contributions originating from QCD multijet events with large instrumental missing transverse energy. Finally to reflect the topology of signal events, the reconstructed top quark was required to be well separated from the missing transverse momentum, with the difference in azimuthal angle exceeding

$$\Delta\phi\left(\mathbf{p}_T^{\text{miss}}, \mathbf{p}_t\right) > 1.8 \ . \tag{5.2.8}$$

5.3 Results

5.3.1 Leptonic monotops

The numbers of events populating both leptonic monotop signal regions defined in Section 5.2.2 are listed in the third and fourth columns of Table 5.1 separately for the different background contributions and for the two compressed spectra scenarios mentioned in Section 5.1.1. The first of these scenarios is a representative high mass setup for top squark, top quark and gluino production where the relevant masses are $(m_{\tilde{t}_1}{=}m_{\tilde{g}}, m_{\tilde{\chi}_1^0}) = (200, 190)$ GeV. The second is an example low mass scenario with $(m_{\tilde{t}_1}, m_{\tilde{\chi}_1^0}) = (145, 75)$ GeV where the gaugino produced in association with the top squark and top squark is now the lightest neutralino. The SRL1 analysis strategy is illustrated in Figure 5.1 where we present the m_T^W (left panel) and E_T^{miss} (right panel) distributions after applying all SRL1 selection requirements, except $m_T^W > 120\,\text{GeV}$ and $E_T^{\text{miss}} > 150$ GeV respectively. Results are shown for the two

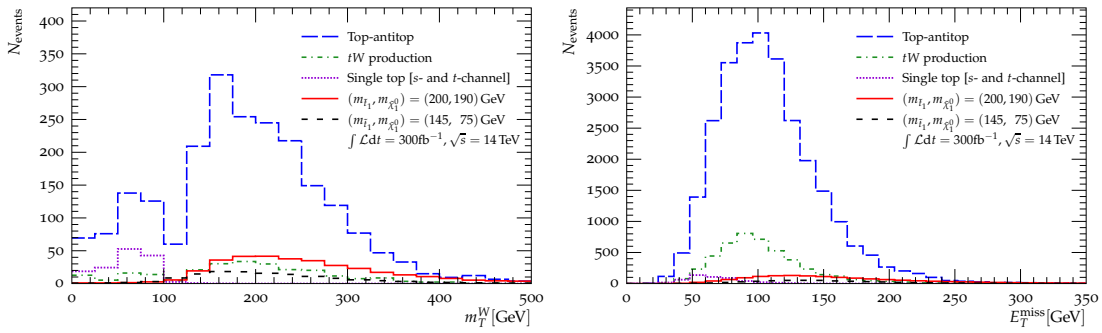

Figure 5.1: Distributions of the W-boson transverse mass m_T^W (left) and the missing transverse energy E_T^{miss} (right), normalized to 300 fb^{-1} of LHC collisions at a centre-of-mass energy of $\sqrt{s} = 14$ TeV. Results are shown for the dominant background contributions after all selection criteria defining the SRL1 region have been applied, except $m_T^W > 120\,\text{GeV}$ (left) and $E_T^{\text{miss}} > 150\,\text{GeV}$ (right). Also shown are the spectra for the example signal scenarios of Section 5.1.1.

considered signal scenarios and the prevailing components of the Standard Model background, *i.e.* for $t\bar{t}$, tW and single-top (in the s- and t-channel) production.

The m_T^W distributions for the background contributions exhibit peaks in the region $m_T^W \simeq 80\,\text{GeV}$, which correspond to events in which both the lepton and all the missing transverse momentum originate from a W-boson decay. In contrast, both signal distributions feature a suppression for $m_T^W < 120$ GeV, which motivates the m_T^W selection criterion of the SRL1 strategy. Despite the large number of remaining background events, the sensitivity of the SRL1 analysis to the high mass $(\tilde{t}_1, t, \tilde{g})$ and low mass $(\tilde{t}_1, t, \tilde{\chi}_1^0)$ signal scenarios reaches 36σ and 14σ respectively. The SRL1 search strategy was designed to probe higher mass spectra, and so is by construction less sensitive to scenarios with light neutralinos where a comparatively smaller amount of E_T^{miss} is present, as seen in the right panel of Figure 5.1. This drop in the sensitivity is alleviated through the inclusion of the SRL2 analysis strategy. This strategy exhibits a reduced sensitivity to the high mass benchmark point of 29σ. The sensitivity to the lower mass $(\tilde{t}_1, t, \tilde{\chi}_1^0)$ example scenario is in fact also slightly reduced to 13σ. However, it has been confirmed that in even less compressed scenarios the sensitivity of the SRL2 analysis exceeds that of the SRL1 analysis, a

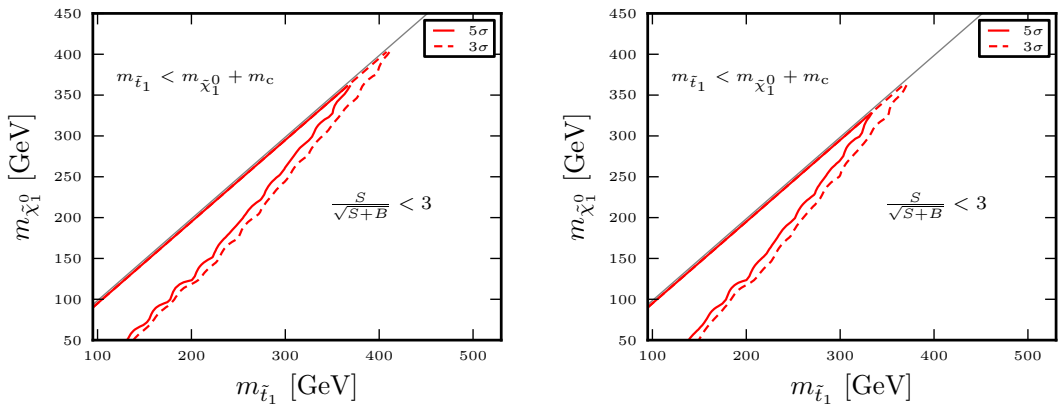

Figure 5.2: LHC sensitivity to a leptonically decaying monotop signal induced by a compressed supersymmetric scenario, adopting either the SRL1 (left) or SRL2 (right) search strategy. Results are shown in the $(m_{\tilde{t}_1}, m_{\tilde{\chi}_1^0})$ plane for $(\tilde{t}_1, t, \tilde{g})$ production in scenarios with $m_{\tilde{t}_1} = m_{\tilde{g}}$. Results are based on the simulation of 300 fb^{-1} of LHC collisions at a centre-of-mass energy of $\sqrt{s} = 14$ TeV.

feature that is evident in the discovery bounds presented in Figure 5.3.

To study more extensively the LHC sensitivity to different compressed supersymmetric scenarios, we perform a scan of the $(m_{\tilde{t}_1}, m_{\tilde{\chi}_1^0})$ plane, enforcing $m_{\tilde{t}_1} = m_{\tilde{g}}$ for the $(\tilde{t}_1, t, \tilde{g})$ signal scenario, and derive contours corresponding to different observation boundaries. The 5σ and 3σ regions for top quark, top squark and gluino production are shown respectively by solid and dashed red lines in Figure 5.2 for the SRL1 (left panel) and SRL2 (right panel) search strategies. Equivalent boundaries are shown in Figure 5.3 for the case of direct neutralino production in association with a top and stop. As a result of the design, the SRL1 analysis is found to be more sensitive to higher mass setups for both signal scenarios. Conversely, the SRL2 search strategy is more sensitive to scenarios featuring smaller superpartner masses and possibly less compressed spectra, as can be seen for both $(\tilde{t}_1, t, \tilde{g})$ and $(\tilde{t}_1, t, \tilde{\chi}_1^0)$ production with the latter exhibiting a more significant improvement in the less compressed regions of parameter space.

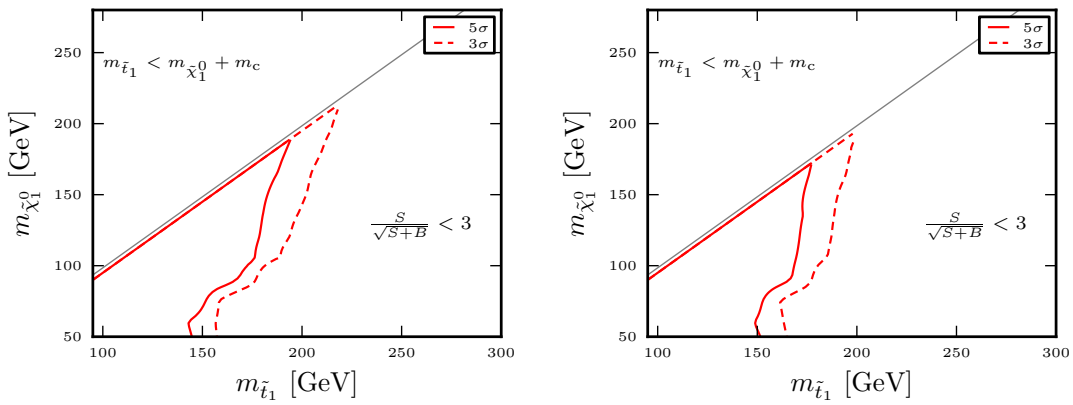

Figure 5.3: LHC sensitivity to a leptonically decaying monotop signal induced by a compressed supersymmetric scenario, adopting either the SRL1 (left) or SRL2 (right) search strategy. Results are shown in the $(m_{\tilde{t}_1}, m_{\tilde{\chi}_1^0})$ plane for $(\tilde{t}_1, t, \tilde{\chi}_1^0)$ production with 300 fb^{-1} of LHC collisions at a centre-of-mass energy of $\sqrt{s} =$ 14 TeV.

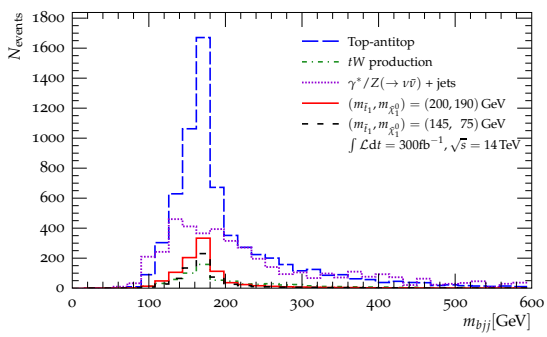

Figure 5.4: Distributions of the invariant mass of the reconstructed top quark m_{bjj}, normalized to 300 fb^{-1} of LHC collisions at a centre-of-mass energy of $\sqrt{s} = 14$ TeV. Results are shown for the dominant background contributions after all selection criteria defining the SRH2 region have been applied, except $m_{bjj} \in [100, 200]$ GeV. Also shown are the spectra for the example signal scenarios of Section 5.1.1.

5.3.2 Hadronic monotops

We again focus on the high mass and low mass example scenarios of Section 5.1.1 and apply the hadronic monotop selection requirements outlined in Section 5.2.3. The number of signal events populating the SRH1 and SRH2 regions are given in the fifth and sixth columns of Table 5.1, together with the different background contributions. The results indicate that the Standard Model background is largely composed of events originating from $t\bar{t}$, γ^*/Z-boson plus jets, tW and W-boson plus light jet production for both search regions.

Our hadronic monotop selection strategy is illustrated in Figure 5.4 which shows the distribution of the invariant mass of the reconstructed top quark after applying all SRH2 requirements, except the one on m_{bjj}. Results are shown for the two considered signal scenarios and the dominant background sources. In principle, the W-boson plus light jet results should also be represented. However, only a very small fraction of the $\sim 10^8$ simulated events pass all selection criteria, so that after normalizing to the large associated total cross section and an integrated luminosity of 300 fb^{-1} the resulting statistical uncertainty is important. The W-boson plus light jets curve has therefore been omitted.

From Figure 5.4 we see that imposing the constraint $m_{bjj} \in [100, 200]$ GeV will retain the majority of the signal events while reducing the number of background events, particularly in the case of γ^*/Z plus jets production for which the distribution does not peak significantly at the top mass. As such, after applying this final selection criterion the sensitivity of the SRH2 strategy to the high mass $(\tilde{t}_1, t, \tilde{g})$ and low mass $(\tilde{t}_1, t, \tilde{\chi}_1^0)$ signal benchmark points is found to be 38σ and 26σ respectively. The SRH1 strategy has a significantly improved sensitivity to the high mass scenario of 45σ, whilst the sensitivity to the low mass point drops slightly to 25σ.

As in Section 5.3.1, we perform a scan in the $(m_{\tilde{t}_1}, m_{\tilde{\chi}_1^0})$ plane, with the equality $m_{\tilde{t}_1} = m_{\tilde{g}}$ enforced for the case of $(\tilde{t}_1, t, \tilde{g})$ production. The results are given in Figures 5.5 and 5.6 which show the 5σ and 3σ contours found after applying the SRH1 (left panel) and SRH2 (right panel) search strategies for $(\tilde{t}_1, t, \tilde{g})$ and $(\tilde{t}_1, t, \tilde{\chi}_1^0)$ production respectively. By design, the SRH1 analysis has an enhanced sensitivity to compressed scenarios with relatively large sparticle masses, while the SRH2 strategy

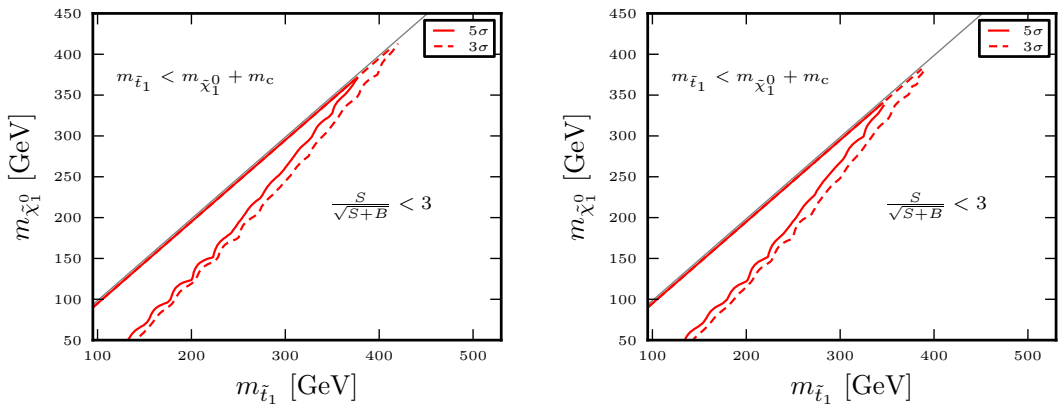

Figure 5.5: Same as Figure 5.2, but for the SRH1 (left) and SRH2 (right) search strategies.

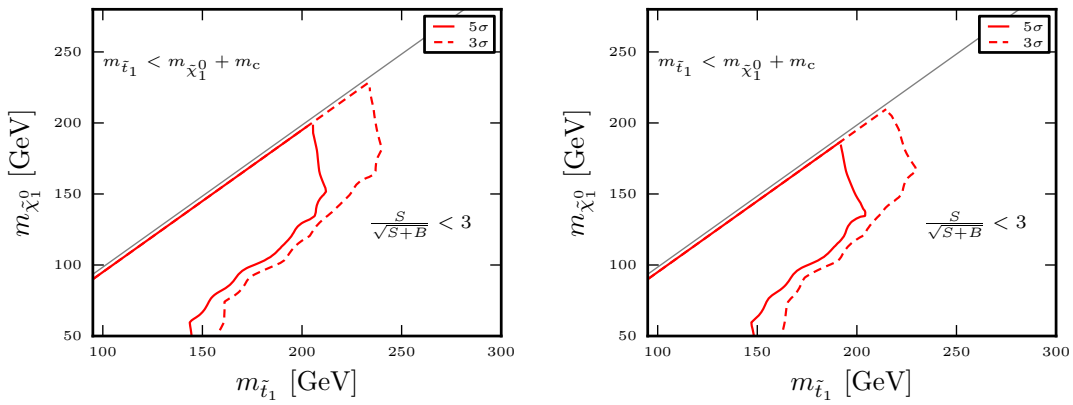

Figure 5.6: Same as Figure 5.3, but for the SRH1 (left) and SRH2 (right) search strategies.

is instead more tuned to situations with smaller superparticle masses and a less compressed spectrum. The reach of SRH2 improves over that of SRH1 in the low mass region of parameter space for the case of $(\tilde{t}_1, t, \tilde{\chi}_1^0)$ production. However, no significant extension of the observation boundaries is seen in the case of $(\tilde{t}_1, t, \tilde{g})$ production in Figure 5.5.

Finally, we note that the contours derived by considering hadronic monotop decays in $(\tilde{t}_1, t, \tilde{g})$ production exceed the limits set by the leptonic monotop search strategies in all regions of the $(m_{\tilde{t}_1}, m_{\tilde{\chi}_1^0})$ plane. For the case of $(\tilde{t}_1, t, \tilde{\chi}_1^0)$ production, hadronic monotop decays provide the most extensive reach in high mass scenarios,

while considering leptonic decays leads to more stringent limits in low mass and less compressed regions of the $(m_{\tilde{t}_1}, m_{\tilde{\chi}_1^0})$ plane.

5.3.3 Comparison to existing bounds

For the signal scenario in which a gluino is produced in association with the top squark and top quark, the search strategies presented here have the capability of discovering a significant region of the $(m_{\tilde{t}_1}, m_{\chi_1^0})$ plane. However, these scenarios are in fact already excluded. By requiring $m_{\tilde{g}} = m_{\tilde{t}_1}$ the signal is subject to constraints derived from direct LHC searches for light gluinos [37, 159]. These rule out at the 95% confidence level the existence of gluinos with mass less than $\mathcal{O}(600)$ GeV in highly compressed scenarios. Even with 300 fb^{-1} of LHC collisions at a centre-of-mass energy of $\sqrt{s}$ =14 TeV, our monotop based search strategy does not have comparable sensitivity to these higher mass gluino scenarios.

For our second signal scenario in which a top squark and top quark are produced in association with the lightest neutralino, the gluino mass bounds are no longer applicable. As such, we investigate whether the monotop based search strategy presented here can place competitive exclusion limits when compared with previously exploited analysis strategies that, for example, search for monojet events or make use of charm-flavour identification techniques. To do so, we approximate the 95% CL exclusion limit of our search strategy with the 2σ discovery bound, and plot this contour in the left-hand panel of Figure 5.7 for the combined hadronic monotop search strategies[7]. Superimposed on Figure 5.7 are the current 95% CL exclusion limits set by the ATLAS [160] and CMS [161] collaborations. We see that our monotop based search strategy can provide comparable exclusion bounds in the region with $m_{\tilde{t}_1} < m_{\tilde{\chi}_1^0} + m_b + m_W$. However, we note that our bounds make use of 300 fb^{-1} of LHC data at $\sqrt{s}$ = 14 TeV while the existing limits are based on $\mathcal{O}(20)$ fb^{-1} of data recorded at $\sqrt{s} = 8$ TeV.

The right-hand panel of Figure 5.7 instead shows a comparison between the 5σ

[7]We find in this case that the discovery bounds derived from studying hadronic monotop decays exceed those set by leptonically decaying monotops searches in all regions of the parameter space.

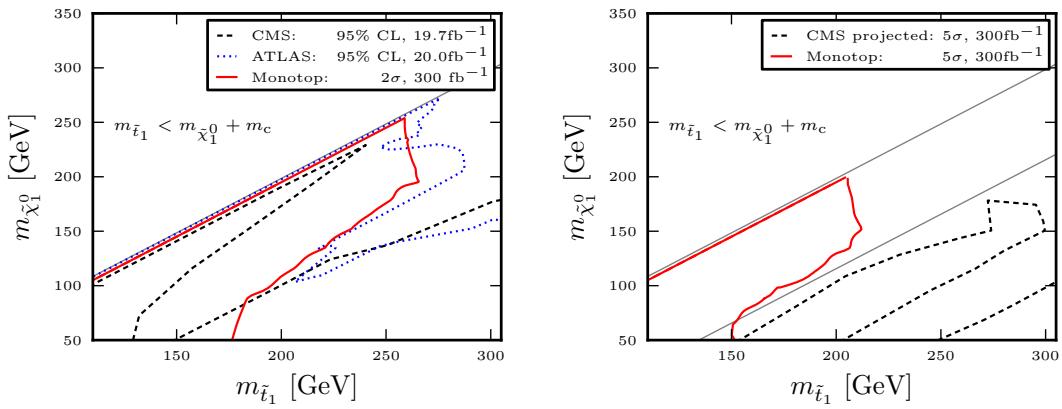

Figure 5.7: Left: Comparison of the current 95% CL exclusion boundaries set by the ATLAS and CMS collaborations with $\mathcal{O}(20)$ fb^{-1} of data recorded at $\sqrt{s}$ = 8 TeV and the 2σ sensitivity of the LHC to a monotop signal arising from $(\tilde{t}_1, t, \tilde{\chi}_1^0)$ production for 300 fb^{-1} of LHC collisions at a centre-of-mass energy of $\sqrt{s} = 14$ TeV. Right: Comparison of the 5σ sensitivity of the LHC to hadronically and leptonically decaying monotop signals arising from $(\tilde{t}_1, t, \tilde{\chi}_1^0)$ production and the extrapolated 5σ discovery bound derived from a CMS search for stops in events with electrons and muons. Both results correspond to 300 fb^{-1} of LHC data at $\sqrt{s} = 14$ TeV.

discovery reach of our monotop analysis[8] and the 5σ discovery boundary arising from a CMS search for top squarks in events with final-state electrons or muons [162], extrapolated to 300 fb^{-1} of LHC data taken at $\sqrt{s} = 14$ TeV [163]. For the latter, we show the boundary corresponding to the less conservative scenario where the uncertainty on the background is assumed to be dominated by the statistical precision. Here we observe that the monotop analysis sets stronger limits in the region $m_{\tilde{t}_1} \approx m_{\tilde{\chi}_1^0} + m_b + m_W$ for $m_{\tilde{t}_1} \lesssim 150$ GeV. However, the comparison is again not ideal given that extrapolated boundaries are not available for the search strategies that set the most stringent limits in the compressed regions of phase space with $\sqrt{s} = 8$ TeV data.

[8] We show the result obtained by combining the hadronic and leptonic monotop search strategies in the most naïve way, making use of the most sensitive strategy at each parameter space point. While a more sophisticated combination might expand the observation boundaries, our simplistic approach provides a conservative estimate.

5.4 Summary

In this chapter we have investigated the feasibility of using monotop probes to constrain supersymmetric scenarios with near mass-degenerate accessible sparticles. We have considered the production of a pair of superparticles in association with a top quark in LHC collisions at a centre-of-mass energy of 14 TeV. Since the sparticle mass spectrum is compressed, both superpartners decay into missing transverse energy carried by the lightest neutralino and a collection of Standard Model objects too soft to be reconstructed. The resulting new physics signal consequently consists of a monotop signature.

Both the leptonic and hadronic decays of the top quark have been investigated and two pairs of analysis strategies, respectively dedicated to the low and high mass regions of the parameter space, have been designed.

It was found that monotop signals arising from the production of a top squark, top quark and gluino in a compressed supersymmetric setup are in principle reachable with 5σ sensitivity at the future Run 2 of the LHC. With a luminosity of 300 fb^{-1}, scenarios in which the top squark and gluino have masses below 380 GeV are discoverable. As such, we find the monotop based search strategy is not competitive with current bounds set by direct searches for light gluinos.

In addition, we have studied the production of a top squark and top quark in association with the lightest neutralino. In this case, 5σ sensitivity is obtained for compressed scenarios with $m_{\tilde{t}_1} \lesssim 200$ GeV and also in the region $m_{\tilde{t}_1} \approx m_{\tilde{\chi}_1^0} + m_b + m_W$ for $m_{\tilde{t}_1} \lesssim 150$ GeV. The latter region is not excluded by any existing extrapolations of current searches to 300 fb^{-1} of $\sqrt{s} = 14$ TeV data.

Chapter 6

Summary and conclusions

In this thesis we have presented an implementation of matrix-element corrections based on the POWHEG formalism through which QCD real-emission matrix elements may be consistently matched with parton-shower algorithms. These corrections have been implemented within the Herwig++ Monte Carlo event generator for a wide range of decays that occur in most of the well studied new physics scenarios and for the production of squark-antisquark pairs at the LHC. In the latter case, a number of methods for removing real-emission contributions with on-shell intermediate gluinos have been implemented, including a new variation of the diagram subtraction procedure.

Applying matrix-element corrections to the decays of new particles was found to reduce the transverse momentum of distributions sensitive to the hardest emission in the decay-initiated parton shower, correcting the tendency of the parton-shower splitting kernels to overpopulate some hard regions of phase space. A similar effect was observed for the matrix-element correction to squark-antisquark production, augmented with a substantial increase in the number of events containing very high transverse momentum parton-shower jets. The latter effect is caused by the matrix-element correction populating the dead zone in the parton-shower phase space.

For the case of squark-antisquark production, we have separately studied the effect of applying matrix-element corrections to the production and decay stages of the event, along with the impact of combining the two corrections. This was studied both at parton level and in the context of an existing ATLAS search for the

direct production of top squarks at the LHC. In either case, it was found that corrections to the squark production and decays were both important in scenarios with well separated superparticle mass spectra, while in compressed regions of parameter space the effect of the former correction dominates. In addition, by applying these corrections we achieve good agreement with the original ATLAS analysis which was performed using matrix-element merging. The agreement between the two signal simulation strategies gives us further confidence in the limits being set using this analysis.

The matrix-element corrections to the decays of BSM particles are provided in Herwig++ version 2.7 onwards, while corrections to the production of Standard Model particles will become available in Herwig++ version 3.0. The matrix-element correction to squark-antisquark production will, however, not be included in this version. Instead, it will be made available once the capability to include POWHEG style matrix-element corrections for a range of new physics production processes is present. In this sense, the correction to squark-antisquark production presented in this thesis marks the beginning of an exciting new implementation of higher-order corrections to BSM particle production within the Herwig++ event generator. Furthermore, as NLO virtual corrections to new physics processes become available in independent matrix-element generators, our correction may be easily promoted to the full POWHEG correction using existing elements of the MATCHBOX framework.

Finally, we have also investigated a novel alternative strategy for accessing compressed regions of the supersymmetric parameter space which relies on the production of a monotop signature. We have designed search strategies for both leptonic and hadronic monotop decays and found them to be sensitive to scenarios with small splittings between the masses of accessible superparticles.

A.1 Matrix-element corrections in the MATCHBOX framework

In the following, we expand on the discussion in Section 1.4.4 and give a more in-depth description of our POWHEG style ME correction as it is implemented within the MATCHBOX framework. Details are given for the case of LoopSim corrections in which the phase space of the hardest emission is divided into shower and hard real-emission components, and the weight of the Born configuration has been modified to restore the unitarity of the parton shower. The formulae relevant to ME corrections without phase-space division can be obtained from those below by setting $\mathcal{R}^H = 0$.

Including the LoopSim correction, the inclusive cross section for the hardest emission is

$$d\sigma^{\mathrm{ME}} = \mathcal{B}'\left(\Phi_n\right) d\Phi_n \left[\Delta\left(p_T^{\max}, p_T^{\min}\right) + d\Phi_R \frac{\mathcal{R}^S\left(\Phi_{n+1}\right)}{\mathcal{B}\left(\Phi_n\right)} \Delta\left(p_T^{\max}, p_T\right)\right] + \mathcal{R}^H\left(\Phi_{n+1}\right) d\Phi_{n+1}, \tag{A.1.1}$$

where

$$\mathcal{B}'(\Phi_n) = \mathcal{B}(\Phi_n) - \int_{p_T^{\min}}^{p_T^{\max}} d\Phi_R \mathcal{R}^H\left(\Phi_{n+1}\right). \tag{A.1.2}$$

Beginning with the third term in Eq. A.1.1, which corresponds to the finite real contribution, we have in more detail,

$$\mathcal{R}^H\left(\Phi_{n+1}\right) d\Phi_{n+1} = d\sigma_R \theta_{\mathrm{cuts}}(\Phi_{n+1}) d\Phi_{n+1} - \sum_\alpha d\sigma_R w_\alpha \left[f(p_T^\alpha, p_T^{\max}, p_T^{\mathrm{hard}})\theta(p_T^\alpha - p_T^{\min}) + \theta(p_T^{\min} - p_T^\alpha)\right] \theta_{\mathrm{cuts}}(\Phi_n^\alpha) d\Phi_{n+1}. \tag{A.1.3}$$

Taking each component of Eq. A.1.3 in turn:

- $d\sigma_R$ is the NLO real-emission contribution to the differential hadronic cross section,

$$d\sigma_R = \frac{|\mathcal{M}_R|^2}{2s_R} x_a^R x_b^R f_a^{h_1}(x_a^R, \mu_F^R) f_b^{h_2}(x_b^R, \mu_F^R), \tag{A.1.4}$$

  where $\mathcal{M}_R$ and s_R are the amplitude and partonic centre-of-mass energy of the real-emission process. The PDF factors are represented by $f_a^{h_1}(x_a, \mu_F)$ and

$f_b^{h_2}(x_b, \mu_F)$, where x_a and x_b are the momentum fractions of the incoming partons and μ_F is the factorization scale. The values of the momentum fractions and factorization scale can differ between the Born and real-emission configurations. We use superscripts R and B to indicate whether the quantities have been evaluated with the real-emission or Born kinematics respectively. Along with the momentum fraction, the flavour of one of the initial-state partons may also change during the splitting. Parton flavours before and after the emission are indicated by primed and unprimed subscripts respectively.

- The $n+1$ parton phase-space element is defined as

$$d\Phi_{n+1} = \frac{dx_a^R}{x_a^R}\frac{dx_b^R}{x_b^R}\,(2\pi)^4\,\delta^4\left(\sqrt{s_R} - \sum_{i=1}^{n+1} p_i\right)\prod_{i=1}^{n+1}\frac{d^3\vec{p}_i}{2E_i(2\pi)^3}, \tag{A.1.5}$$

  where $p_i = (E_i, \vec{p}_i)$ is the momentum of the outgoing particle i.

- The weight of each splitting channel is

$$w_\alpha = \frac{\mathcal{D}_\alpha}{\sum_\beta \mathcal{D}_\beta}, \tag{A.1.6}$$

  where $\mathcal{D}_\alpha$ is a dipole function that encapsulates the singular structure of the real-emission matrix element in the splitting channel α. Dipoles based on the Catani-Seymour formalism [55,56] have been implemented within the MATCHBOX framework. However for the case of ME corrections, the full dipole functions are not required since it is never necessary to integrate them analytically over the phase space of the unresolved parton. As such, simple functions of the momenta of the emission p_j, the emitting particle p_i and the spectator particle p_k have been used for the dipole functions in Eq. A.1.6. When the emitted parton is a gluon

$$\mathcal{D}_i = C\frac{p_i.p_k}{p_i.p_j(p_i.p_j + p_j.p_k)}, \tag{A.1.7}$$

  where the colour factor is $C = (N_c^2 - 1)/2N_c$ ($C = N_c$) when the emitting particle transforms under the fundamental (adjoint) representation of $SU(N_c)$. When instead the emitted parton is a quark or antiquark, the form of the dipole is

$$\mathcal{D}_i = \frac{C}{p_i.p_j}, \tag{A.1.8}$$

where here the colour factor is $C = \frac{1}{2}$, the trace invariant of the fundamental representation of $SU(N_c)$.

- Mapping between the $n+1$ and n particle configurations is done using the schemes described in Refs. [116] and [117] for massless and massive final-state particles respectively. A different mapping prescription is required for each type of splitting channel, and therefore the transverse momentum of the emission, p_T^α, depends on the particular channel through which the emission took place.

- The function $f(p_T^\alpha, p_T^{\max}, p_T^{\text{hard}})$, as defined in Section 1.4.3, specifies the restricted phase space of shower-type hardest emissions. The sharp, hfact and resummation profiles are all available in the MATCHBOX framework. Phase-space restriction with the resummation profile is applied by default when either the full POWHEG or POWHEG style ME correction is used in the simulation.

- Finally, $\theta(p_T^\alpha - p_T^{\min})$ imposes an IR cutoff on the transverse momentum of the additional emission and $\theta_{\text{cuts}}(\Phi_n^\alpha)$ ($\theta_{\text{cuts}}(\Phi_{n+1})$) indicates any event selection criteria that have been applied to the Born (real-emission) configuration during event generation.

Within the MATCHBOX framework, the contribution in Eq. A.1.3 is contained within a `SubtractedME` object. The first term in Eq. A.1.3, corresponding to the full real-emission contribution, is the *head* object, while each term in the sum over α provides a separate *dependent* object. The first term in the dependent object subtracts the double counted contribution from the parton-shower splitting kernel. The second term corresponds to the bridging cross section and is included to cancel the full real-emission contribution in the divergent regions of phase space.

The modified Born configuration in Eq. A.1.2 contains both the true Born contribution, defined in direct analogy to the first term in Eq. A.1.3, and an additional term which ensures that the total integrated cross section is unaffected by the ad-

ditional parton-shower emission. The exact form of the integrand of this term is

$$\begin{aligned}\mathcal{R}^H\left(\Phi_{n+1}\right) d\Phi_R = \sum_\alpha d\sigma_R w_\alpha \big[&\theta(p_T^\alpha - p_T^{\min}) \\ &- f(p_T^\alpha, p_T^{\max}, p_T^{\text{hard}})\theta(p_T^\alpha - p_T^{\min})\big]\, \theta_{\text{cuts}}(\Phi_n^\alpha)\frac{d\Phi_{n+1}}{d\Phi_n},\end{aligned} \tag{A.1.9}$$

where $d\Phi_n$ is defined as in Eq. A.1.5 with the replacements $n+1 \to n$, $s_R \to s_B$ and x_a^R, $x_b^R \to x_{a'}^B$, $x_{b'}^B$.

The contribution in Eq. A.1.9 is also included in MATCHBOX as a `SubtractedME` object. Each term in the sum again provides a separate dependent contribution and no head object is present in this case. To improve efficiency, the summation over α is performed as a Monte Carlo sum. This requires only a single real-emission phase space configuration to be generated. By contrast, in the conventional approach a point in the $n+1$ body phase space must be generated for each of the possible splitting channels that, starting from a given Born configuration, give rise to the required real-emission configuration. Consequently, this approach is more computationally expensive.

Finally, the splitting kernel appearing in Eq. A.1.1, which is also used in the Sudakov form factor, is more precisely expressed as

$$\begin{aligned}\frac{\mathcal{R}^S}{\mathcal{B}} d\Phi_R = \sum_\alpha \Bigg[&w_\alpha f(p_T^\alpha, p_T^{\max}, p_T^{\text{hard}})\, \frac{\alpha_s(p_T^\alpha)\, \alpha_s(\mu_R^B)^k}{\alpha_s(\mu_R^R)^{k+1}}\, \frac{|\mathcal{M}_R|^2}{|\mathcal{M}_B|^2} \\ &\cdot \frac{f_a^{h_1}(x_a^R, p_T^\alpha)\, f_b^{h_2}(x_b^R, p_T^\alpha)}{f_{a'}^{h_1}(x_{a'}^B, p_T^\alpha)\, f_{b'}^{h_2}(x_{b'}^B, p_T^\alpha)}\theta(p_T^\alpha - p_T^{\min})\frac{d\Phi_{n+1}^\alpha}{d\Phi_n}\Bigg],\end{aligned} \tag{A.1.10}$$

where k is the order in α_s of the Born cross section. The ratio of coupling constants in Eq. A.1.10 cancels with those included implicitly in the ratio of squared matrix elements and leaves an overall factor of $\alpha_s(p_T^2)$. By using transverse momentum as the argument of the strong coupling constant in the parton shower, a subleading but numerically relevant class of logarithms are resummed [69], see Ref. [6] for more details of this scale choice in the context of the Herwig++ event generator. The ratio of PDF functions in Eq. A.1.10 simplifies to unity in the case of final-state emissions, and for initial-state emissions guides the evolution of the backwards parton shower as described in Section 1.3.2.

In MATCHBOX, the splitting kernel for the hardest emission is computed in the `MEMatching` class for both POWHEG and POWHEG style ME corrections. This class inherits from a more general `ShowerApproximation` object which facilitates the division of the phase space of the hardest emission. The generation of the hardest emission is performed by the `ShowerApproximationGenerator`.

B.1 Validation of matrix-element corrections to $\tilde{q}\tilde{q}^*$ production

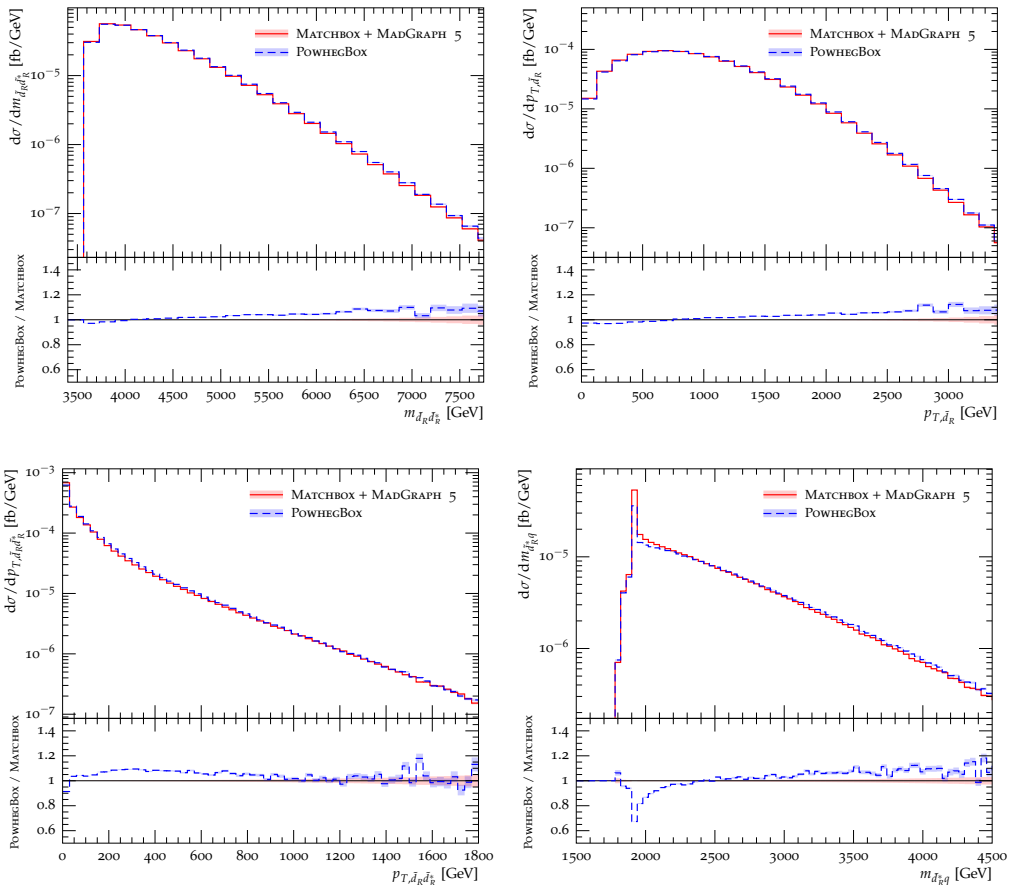

Figure B.1: Comparison of $m_{\tilde{d}_R\tilde{d}_R^*}$, $p_{T,\tilde{d}_R}$, $p_{T,\tilde{d}_R\tilde{d}_R^*}$ and $m_{\tilde{d}_R^*q}$ distributions generated using the MatchBox and PowhegBox implementations of Powheg style ME corrections with the DS0 diagram subtraction scheme. The mass of the down squark and gluino were $m_{\tilde{d}_R} = 1.8$ TeV and $m_{\tilde{g}} = 1.9$ TeV.

With the aim of further validating our MatchBox implementation of ME corrections to squark-antisquark production, here we present additional plots comparing distributions generated using MatchBox to those produced with the PowhegBox program. Events were generated as in Section 4.2.3, using the DS0 approach to remove real-emission contributions with on-shell gluinos. Analogous plots to those in Figure 4.4 are shown in Figures B.1, B.2 and B.3 for $\tilde{d}_R\tilde{d}_R^*$, $\tilde{c}_R\tilde{c}_R^*$ and $\tilde{s}_L\tilde{s}_L^*$ production respectively. In the first two cases, the mass hierarchy between the squark and

gluino was $(m_{\tilde{g}}, m_{\tilde{q}}) = (1.9, 1.8)$ TeV, while for strange squark production the gluino mass was instead $m_{\tilde{g}} = 2.4$ TeV. In each plot, error bands indicate the uncertainty in the distributions due to limited statistics.

In general, the distributions generated using the MATCHBOX and POWHEGBOX implementations agree well, with similar differences to those seen for $\tilde{u}_L\tilde{u}_L^*$ production in Section 4.2.3. More specifically, slight differences are observed in the slopes of the $m_{\tilde{q}\tilde{q}^*}$ and $p_{T,\tilde{q}}$ distributions, which as before is attributed to the different kinematic mapping procedures used in the two implementations. In addition, the two implementations agree well in the high p_T region of the $p_{T,\tilde{q}\tilde{q}^*}$ distribution, with the MATCHBOX generated spectra exhibiting a slight softening in the low p_T region when compared with the POWHEGBOX results. This is due to the different methods of imposing the IR cutoff on the radiation phase space.

In Section 4.2.3, discrepancies were observed between the POWHEGBOX and MATCHBOX results in the $p_{T,\tilde{u}_L\tilde{u}_L^*}$ distribution at $p_T \approx m_{\tilde{g}} - m_{\tilde{u}_L}$ and in the resonant region of the $m_{\tilde{u}_L^* q}$ plot. These are caused by differing treatments of the Jacobian factor in the phase space of the subtraction term and contributions to the interference term that are linear in $\Gamma_{\tilde{g}}$. The same differences are also present in the implementations of $\tilde{d}_R\tilde{d}_R^*$ production, but their effects are less visible in the $p_{T,\tilde{d}_R\tilde{d}_R^*}$ distribution of Figure B.1 than they were for $\tilde{u}_L\tilde{u}_L^*$ production. This is partially a consequence of the compressed mass spectrum, $(m_{\tilde{g}}, m_{\tilde{d}_R}) = (1.9, 1.8)$ TeV, which means that resonant contributions affect the low p_T region of the distribution where non-resonant channels are enhanced due to soft and collinear logarithms. This causes the overall impact of terms involving the resonant amplitudes, and therefore the difference between the MATCHBOX and POWHEGBOX implementations, to be less evident in this scenario. In addition, the parton luminosity factors are such that channels with resonant amplitudes account for less of the real-emission cross section than in $\tilde{u}_L\tilde{u}_L^*$ production. This reduces the visible impact of differences between the MATCHBOX and POWHEGBOX implementations in both the $p_{T,\tilde{d}_R\tilde{d}_R^*}$ and $m_{\tilde{d}_R^* q}$ distributions in Figure B.1. Similar arguments may also be applied to explain the reduced visibility of differences between the MATCHBOX and POWHEGBOX results in the $p_{T,\tilde{q}\tilde{q}^*}$ and $m_{\tilde{q}^* q}$ distributions in Figures B.2 and B.3.

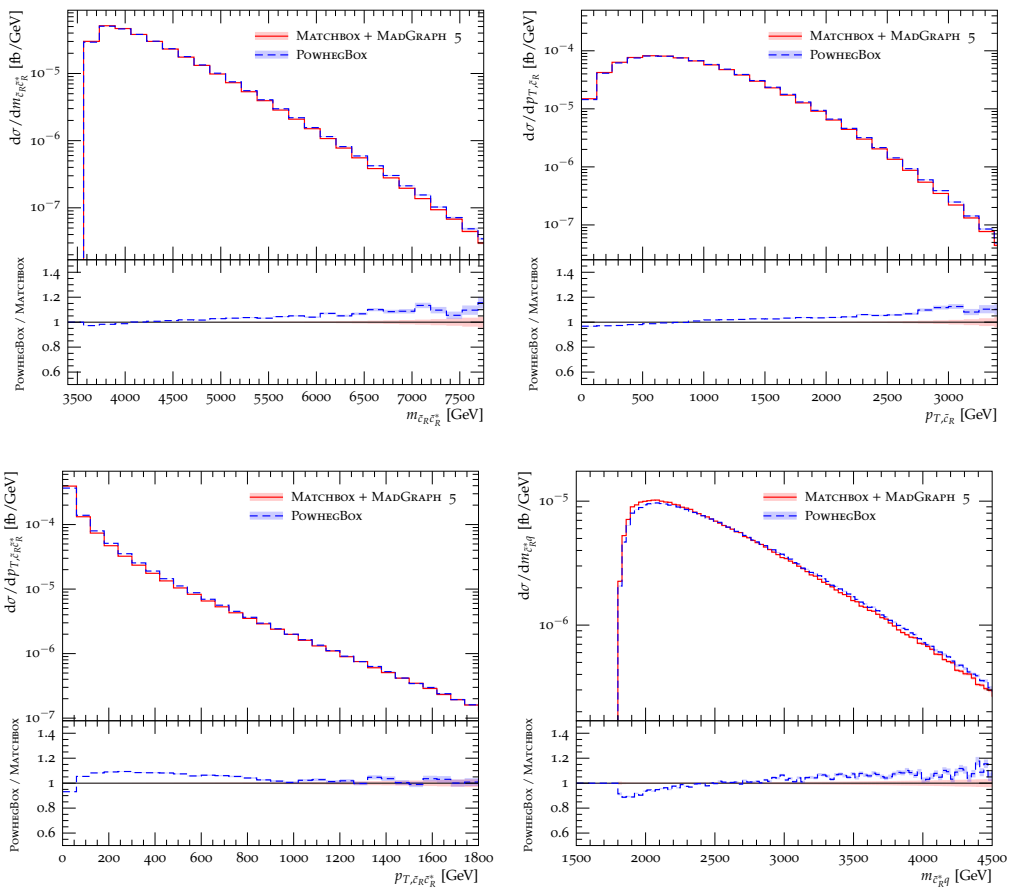

Figure B.2: As in Figure B.1, but for $\tilde{c}_R\tilde{c}_R^*$ production with the mass splitting $(m_{\tilde{g}}, m_{\tilde{c}_R}) = (1.9, 1.8)$ TeV.

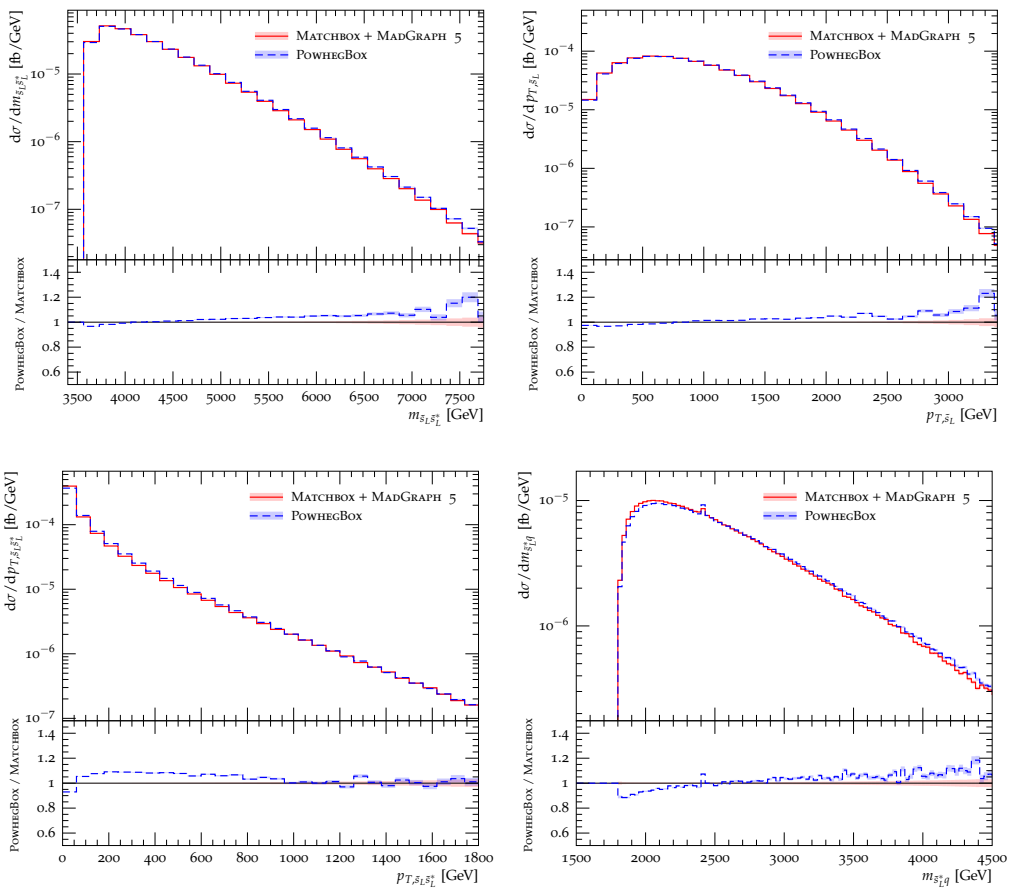

Figure B.3: As in Figure B.1, but for $\tilde{s}_L\tilde{s}_L^*$ production with the mass splitting $(m_{\tilde{g}}, m_{\tilde{s}_L}) = (2.4, 1.8)$ TeV.

Bibliography

[1] H. P. Nilles, *Supersymmetry, Supergravity and Particle Physics*, *Phys.Rept.* **110** (1984) 1–162.

[2] H. E. Haber and G. L. Kane, *The Search for Supersymmetry: Probing Physics Beyond the Standard Model*, *Phys.Rept.* **117** (1985) 75–263, [UM-HE-TH-83-17, SCIPP-85-47].

[3] **ATLAS** Collaboration, *ATLAS Supersymmetry (SUSY) searches*, https://twiki.cern.ch/twiki/bin/view/AtlasPublic/SupersymmetryPublicResults.

[4] **CMS** Collaboration, *CMS Supersymmetry Physics Results*, https://twiki.cern.ch/twiki/bin/view/CMSPublic/PhysicsResultsSUS.

[5] P. Nason, *A New method for combining NLO QCD with shower Monte Carlo algorithms*, *JHEP* **0411** (2004) 040, [hep-ph/0409146].

[6] M. Bahr, S. Gieseke, M. Gigg, D. Grellscheid, K. Hamilton, et al., *Herwig++ Physics and Manual*, *Eur.Phys.J.* **C58** (2008) 639–707, [arXiv:0803.0883]. 143 pages, program and additional information available from http://projects.hepforge.org/herwig.

[7] J. Bellm, S. Gieseke, D. Grellscheid, A. Papaefstathiou, S. Platzer, et al., *Herwig++ 2.7 Release Note*, arXiv:1310.6877.

[8] O. Latunde-Dada, *Applying the POWHEG method to top pair production and decays at the ILC*, *Eur.Phys.J.* **C58** (2008) 543–554, [arXiv:0806.4560].

[9] P. Richardson and D. Winn, *Investigation of Monte Carlo Uncertainties on Higgs Boson searches using Jet Substructure*, *Eur.Phys.J.* **C72** (2012) 2178, [arXiv:1207.0380].

[10] J. M. Campbell, R. K. Ellis, P. Nason, and E. Re, *Top-pair production and decay at NLO matched with parton showers*, *JHEP* **1504** (2015) 114, [arXiv:1412.1828].

[11] R. Gavin, C. Hangst, M. Kramer, M. Muhlleitner, M. Pellen, et al., *Squark Production and Decay matched with Parton Showers at NLO*, *Eur.Phys.J.* **C75** (2015), no. 1 29, [arXiv:1407.7971].

[12] E. Norrbin and T. Sjostrand, *QCD radiation off heavy particles*, *Nucl.Phys.* **B603** (2001) 297–342, [hep-ph/0010012].

[13] S. Dawson, E. Eichten, and C. Quigg, *Search for Supersymmetric Particles in Hadron - Hadron Collisions*, *Phys.Rev.* **D31** (1985) 1581.

[14] W. Beenakker, R. Hopker, M. Spira, and P. Zerwas, *Squark production at the Tevatron*, *Phys.Rev.Lett.* **74** (1995) 2905–2908, [hep-ph/9412272].

[15] W. Beenakker, R. Hopker, M. Spira, and P. Zerwas, *Squark and gluino production at hadron colliders*, *Nucl.Phys.* **B492** (1997) 51–103, [hep-ph/9610490].

[16] W. Beenakker, R. Hopker, and M. Spira, *PROSPINO: A Program for the production of supersymmetric particles in next-to-leading order QCD*, hep-ph/9611232.

[17] W. Beenakker, M. Kramer, T. Plehn, M. Spira, and P. Zerwas, *Stop production at hadron colliders*, *Nucl.Phys.* **B515** (1998) 3–14, [hep-ph/9710451].

[18] D. Goncalves-Netto, D. Lopez-Val, K. Mawatari, T. Plehn, and I. Wigmore, *Automated Squark and Gluino Production to Next-to-Leading Order*, *Phys.Rev.* **D87** (2013), no. 1 014002, [arXiv:1211.0286].

[19] E. Bagnaschi, G. Degrassi, P. Slavich, and A. Vicini, *Higgs production via gluon fusion in the POWHEG approach in the SM and in the MSSM*, *JHEP* **1202** (2012) 088, [arXiv:1111.2854].

[20] I. Fridman-Rojas and P. Richardson, *Next-to-Leading Order Simulation of Slepton Pair Production*, arXiv:1208.0279.

[21] B. Jager, A. von Manteuffel, and S. Thier, *Slepton pair production in the POWHEG BOX*, *JHEP* **1210** (2012) 130, [arXiv:1208.2953].

[22] R. Gavin, C. Hangst, M. Kramer, M. Muhlleitner, M. Pellen, et al., *Matching Squark Pair Production at NLO with Parton Showers*, *JHEP* **1310** (2013) 187, [arXiv:1305.4061].

[23] B. Jager, A. von Manteuffel, and S. Thier, *Slepton pair production in association with a jet: NLO-QCD corrections and parton-shower effects*, *JHEP* **1502** (2015) 041, [arXiv:1410.3802].

[24] I. Fridman-Rojas, *Beyond the Standard Model Phenomenology at Next-to-Leading Order at the LHC*, PhD thesis, Institute for Particle Physics Phenomenology, University of Durham, 2014.

[25] L. Randall and R. Sundrum, *A Large mass hierarchy from a small extra dimension*, *Phys.Rev.Lett.* **83** (1999) 3370–3373, [hep-ph/9905221].

[26] S. Glashow, *Partial Symmetries of Weak Interactions*, *Nucl.Phys.* **22** (1961) 579–588.

[27] S. Weinberg, *A Model of Leptons*, *Phys.Rev.Lett.* **19** (1967) 1264–1266.

[28] A. Salam, *Weak and Electromagnetic Interactions*, *Conf.Proc.* **C680519** (1968) 367–377.

[29] S. P. Martin, *A Supersymmetry primer*, *Adv.Ser.Direct.High Energy Phys.* **21** (2010) 1–153, [hep-ph/9709356].

[30] **ATLAS, CMS** Collaboration, G. Aad et al., *Combined Measurement of the Higgs Boson Mass in pp Collisions at $\sqrt{s} = 7$ and 8 TeV with the ATLAS and CMS Experiments*, `arXiv:1503.0758`.

[31] A. Signer, *ABC of SUSY*, *J.Phys.* **G36** (2009) 073002, [`arXiv:0905.4630`].

[32] R. Haag, J. T. Lopuszanski, and M. Sohnius, *All Possible Generators of Supersymmetries of the s Matrix*, *Nucl.Phys.* **B88** (1975) 257.

[33] S. R. Coleman and J. Mandula, *All Possible Symmetries of the S Matrix*, *Phys.Rev.* **159** (1967) 1251–1256.

[34] J. Gunion and H. E. Haber, *Higgs Bosons in Supersymmetric Models. 1.*, *Nucl.Phys.* **B272** (1986) 1.

[35] H. E. Haber, *The Status of the minimal supersymmetric standard model and beyond*, *Nucl.Phys.Proc.Suppl.* **62** (1998) 469–484, [`hep-ph/9709450`].

[36] **Super-Kamiokande** Collaboration, K. Abe et al., *Search for proton decay via $p \to \nu K^+$ using 260âĂĽâĂĽkilotonÂůyear data of Super-Kamiokande*, *Phys.Rev.* **D90** (2014), no. 7 072005, [`arXiv:1408.1195`].

[37] **ATLAS** Collaboration, G. Aad et al., *Search for squarks and gluinos with the ATLAS detector in final states with jets and missing transverse momentum using $\sqrt{s} = 8$ TeV proton–proton collision data*, *JHEP* **1409** (2014) 176, [`arXiv:1405.7875`].

[38] **CMS** Collaboration, V. Khachatryan et al., *Searches for supersymmetry using the M_{T2} variable in hadronic events produced in pp collisions at 8 TeV*, `arXiv:1502.0435`.

[39] **ATLAS** Collaboration, *Missing Energy Trigger Public Results*, `https://twiki.cern.ch/twiki/bin/view/AtlasPublic/MissingEtTriggerPublicResults`.

[40] **CMS** Collaboration, *Private Communication.*

[41] **UA1** Collaboration, G. Arnison et al., *Experimental Observation of Events with Large Missing Transverse Energy Accompanied by a Jet Or a Photon(s) in p anti-p Collisions at s**(1/2)=540-GeV*, *Phys.Lett.* **B139** (1984) 115.

[42] H. E. Haber and G. L. Kane, *Signatures and Possible Evidence for Supersymmetry at the CERN Collider*, *Phys.Lett.* **B142** (1984) 212.

[43] J. F. Gunion and S. Mrenna, *A Study of SUSY signatures at the Tevatron in models with near mass degeneracy of the lightest chargino and neutralino*, *Phys.Rev.* **D62** (2000) 015002, [`hep-ph/9906270`].

[44] H. K. Dreiner, M. Kramer, and J. Tattersall, *How low can SUSY go? Matching, monojets and compressed spectra*, *Europhys.Lett.* **99** (2012) 61001, [`arXiv:1207.1613`].

[45] **ATLAS** Collaboration, G. Aad et al., *Search for pair-produced third-generation squarks decaying via charm quarks or in compressed supersymmetric scenarios in pp collisions at $\sqrt{s} = 8$ TeV with the ATLAS detector*, `arXiv:1407.0608`.

[46] **CMS** Collaboration, V. Khachatryan et al., *Searches for third generation squark production in fully hadronic final states in proton-proton collisions at sqrt(s)=8 TeV*, `arXiv:1503.0803`.

[47] **CMS** Collaboration, V. Khachatryan et al., *Search for dark matter, extra dimensions, and unparticles in monojet events in protonâĂŞproton collisions at $\sqrt{s} = 8$ TeV*, *Eur.Phys.J.* **C75** (2015), no. 5 235, [`arXiv:1408.3583`].

[48] **ATLAS** Collaboration, G. Aad et al., *Search for new phenomena in final states with an energetic jet and large missing transverse momentum in pp collisions at $\sqrt{s} = 8$ TeV with the ATLAS detector*, `arXiv:1502.0151`.

[49] V. N. Gribov and L. N. Lipatov, *Deep inelastic e p scattering in perturbation theory*, *Sov. J. Nucl. Phys.* **15** (1972) 438–450. [Yad. Fiz.15,781(1972)].

[50] Y. L. Dokshitzer, *Calculation of the Structure Functions for Deep Inelastic Scattering and e+ e- Annihilation by Perturbation Theory in Quantum*

Chromodynamics., *Sov. Phys. JETP* **46** (1977) 641–653. [Zh. Eksp. Teor. Fiz.73,1216(1977)].

[51] G. Altarelli and G. Parisi, *Asymptotic Freedom in Parton Language*, *Nucl. Phys.* **B126** (1977) 298.

[52] F. Bloch and A. Nordsieck, *Note on the Radiation Field of the electron*, *Phys.Rev.* **52** (1937) 54–59.

[53] T. Kinoshita, *Mass singularities of Feynman amplitudes*, *J.Math.Phys.* **3** (1962) 650–677.

[54] T. Lee and M. Nauenberg, *Degenerate Systems and Mass Singularities*, *Phys.Rev.* **133** (1964) B1549–B1562.

[55] S. Catani and M. Seymour, *A General algorithm for calculating jet cross-sections in NLO QCD*, *Nucl.Phys.* **B485** (1997) 291–419, [hep-ph/9605323].

[56] S. Catani, S. Dittmaier, M. H. Seymour, and Z. Trocsanyi, *The Dipole formalism for next-to-leading order QCD calculations with massive partons*, *Nucl.Phys.* **B627** (2002) 189–265, [hep-ph/0201036].

[57] S. Frixione, Z. Kunszt, and A. Signer, *Three jet cross-sections to next-to-leading order*, *Nucl.Phys.* **B467** (1996) 399–442, [hep-ph/9512328].

[58] D. A. Kosower, *Antenna factorization of gauge theory amplitudes*, *Phys.Rev.* **D57** (1998) 5410–5416, [hep-ph/9710213].

[59] J. M. Campbell, M. Cullen, and E. N. Glover, *Four jet event shapes in electron - positron annihilation*, *Eur.Phys.J.* **C9** (1999) 245–265, [hep-ph/9809429].

[60] A. Buckley, J. Butterworth, S. Gieseke, D. Grellscheid, S. Hoche, et al., *General-purpose event generators for LHC physics*, *Phys.Rept.* **504** (2011) 145–233, [arXiv:1101.2599].

[61] M. Gigg and P. Richardson, *Simulation of Finite Width Effects in Physics Beyond the Standard Model*, `arXiv:0805.3037`.

[62] P. Richardson, *Spin correlations in Monte Carlo simulations*, *JHEP* **0111** (2001) 029, [`hep-ph/0110108`].

[63] M. Bahr, S. Gieseke, and M. H. Seymour, *Simulation of multiple partonic interactions in Herwig++*, *JHEP* **0807** (2008) 076, [`arXiv:0803.3633`].

[64] B. Webber, *A QCD Model for Jet Fragmentation Including Soft Gluon Interference*, *Nucl.Phys.* **B238** (1984) 492.

[65] D. Grellscheid and P. Richardson, *Simulation of Tau Decays in the Herwig++ Event Generator*, `arXiv:0710.1951`.

[66] T. Sjostrand, S. Mrenna, and P. Z. Skands, *PYTHIA 6.4 Physics and Manual*, *JHEP* **0605** (2006) 026, [`hep-ph/0603175`].

[67] G. Marchesini and B. Webber, *Simulation of QCD Jets Including Soft Gluon Interference*, *Nucl.Phys.* **B238** (1984) 1.

[68] G. Marchesini and B. Webber, *Monte Carlo Simulation of General Hard Processes with Coherent QCD Radiation*, *Nucl.Phys.* **B310** (1988) 461.

[69] D. Amati, A. Bassetto, M. Ciafaloni, G. Marchesini, and G. Veneziano, *A Treatment of Hard Processes Sensitive to the Infrared Structure of QCD*, *Nucl.Phys.* **B173** (1980) 429.

[70] S. Gieseke, P. Stephens, and B. Webber, *New formalism for QCD parton showers*, *JHEP* **0312** (2003) 045, [`hep-ph/0310083`].

[71] P. Nason, *Presentation at the TOP LHC Working Group 2014*, `https://indico.cern.ch/event/301787/session/10/contribution/23/material/slides/0.pdf`.

[72] S. Catani, F. Krauss, R. Kuhn, and B. Webber, *QCD matrix elements + parton showers*, *JHEP* **0111** (2001) 063, [`hep-ph/0109231`].

[73] L. Lonnblad, *Correcting the color dipole cascade model with fixed order matrix elements*, *JHEP* **0205** (2002) 046, [hep-ph/0112284].

[74] J. Alwall, S. Hoche, F. Krauss, N. Lavesson, L. Lonnblad, et al., *Comparative study of various algorithms for the merging of parton showers and matrix elements in hadronic collisions*, *Eur.Phys.J.* **C53** (2008) 473–500, [arXiv:0706.2569].

[75] S. Mrenna and P. Richardson, *Matching matrix elements and parton showers with HERWIG and PYTHIA*, *JHEP* **0405** (2004) 040, [hep-ph/0312274].

[76] S. Frixione and B. R. Webber, *Matching NLO QCD computations and parton shower simulations*, *JHEP* **0206** (2002) 029, [hep-ph/0204244].

[77] S. Frixione, P. Nason, and B. R. Webber, *Matching NLO QCD and parton showers in heavy flavor production*, *JHEP* **0308** (2003) 007, [hep-ph/0305252].

[78] M. H. Seymour, *Matrix element corrections to parton shower algorithms*, *Comput.Phys.Commun.* **90** (1995) 95–101, [hep-ph/9410414].

[79] S. Frixione, P. Nason, and C. Oleari, *Matching NLO QCD computations with Parton Shower simulations: the POWHEG method*, *JHEP* **0711** (2007) 070, [arXiv:0709.2092].

[80] S. Platzer, *Parton Showers and Radiative Corrections in QCD*, PhD thesis, Karlsruhe Institute of Technology (KIT), 2010.

[81] S. Alioli, P. Nason, C. Oleari, and E. Re, *NLO Higgs boson production via gluon fusion matched with shower in POWHEG*, *JHEP* **0904** (2009) 002, [arXiv:0812.0578].

[82] S. Alioli, P. Nason, C. Oleari, and E. Re, *A general framework for implementing NLO calculations in shower Monte Carlo programs: the POWHEG BOX*, *JHEP* **1006** (2010) 043, [arXiv:1002.2581].

[83] P. Nason and B. Webber, *Next-to-Leading-Order Event Generators*, *Ann.Rev.Nucl.Part.Sci.* **62** (2012) 187–213, [arXiv:1202.1251].

[84] S. Platzer et al., *Precision LHC Event Generation with Herwig++ (in preparation).*

[85] M. Rubin, G. P. Salam, and S. Sapeta, *Giant QCD K-factors beyond NLO*, *JHEP* **1009** (2010) 084, [arXiv:1006.2144].

[86] M. Bengtsson and T. Sjostrand, *A Comparative Study of Coherent and Noncoherent Parton Shower Evolution*, *Nucl.Phys.* **B289** (1987) 810.

[87] M. Bengtsson and T. Sjostrand, *Coherent Parton Showers Versus Matrix Elements: Implications of PETRA - PEP Data*, *Phys.Lett.* **B185** (1987) 435.

[88] J. Tully, *Monte Carlo simulations of hard QCD radiation*, PhD thesis, Institute for Particle Physics Phenomenology, University of Durham, 2009.

[89] K. Hamilton and P. Richardson, *A Simulation of QCD radiation in top quark decays*, *JHEP* **0702** (2007) 069, [hep-ph/0612236].

[90] K. Arnold, L. d'Errico, S. Gieseke, D. Grellscheid, K. Hamilton, et al., *Herwig++ 2.6 Release Note*, arXiv:1205.4902.

[91] A. Buckley, J. Butterworth, L. Lonnblad, D. Grellscheid, H. Hoeth, et al., *Rivet user manual*, *Comput.Phys.Commun.* **184** (2013) 2803–2819, [arXiv:1003.0694].

[92] M. Cacciari, G. P. Salam, and G. Soyez, *FastJet User Manual*, *Eur.Phys.J.* **C72** (2012) 1896, [arXiv:1111.6097].

[93] S. Catani, Y. L. Dokshitzer, M. Olsson, G. Turnock, and B. Webber, *New clustering algorithm for multi - jet cross-sections in e+ e- annihilation*, *Phys.Lett.* **B269** (1991) 432–438.

[94] H. Murayama, I. Watanabe, and K. Hagiwara, *HELAS: HELicity amplitude subroutines for Feynman diagram evaluations*, .

[95] M. Gigg and P. Richardson, *Simulation of beyond standard model physics in Herwig++*, *Eur.Phys.J.* **C51** (2007) 989–1008, [hep-ph/0703199].

[96] **ATLAS** Collaboration, G. Aad et al., *Search for Extra Dimensions in diphoton events using proton-proton collisions recorded at $\sqrt{s} = 7$ TeV with the ATLAS detector at the LHC*, arXiv:1210.8389.

[97] **CTEQ** Collaboration, H. Lai et al., *Global QCD analysis of parton structure of the nucleon: CTEQ5 parton distributions*, *Eur.Phys.J.* **C12** (2000) 375–392, [hep-ph/9903282].

[98] **ATLAS** Collaboration, G. Aad et al., *ATLAS search for new phenomena in dijet mass and angular distributions using pp collisions at $\sqrt{s} = 7$ TeV*, arXiv:1210.1718.

[99] M. Cacciari, G. P. Salam, and G. Soyez, *The Anti-k(t) jet clustering algorithm*, *JHEP* **0804** (2008) 063, [arXiv:0802.1189].

[100] **ATLAS** Collaboration, *Search for squarks and gluinos with the ATLAS detector using final states with jets and missing transverse momentum and 5.8 fb^{-1} of $\sqrt{s}$=8 TeV proton-proton collision data*, .

[101] F. E. Paige, S. D. Protopopescu, H. Baer, and X. Tata, *ISAJET 7.69: A Monte Carlo event generator for pp, anti-p p, and e+e- reactions*, hep-ph/0312045.

[102] S. Platzer and S. Gieseke, *Dipole Showers and Automated NLO Matching in Herwig++*, *Eur.Phys.J.* **C72** (2012) 2187, [arXiv:1109.6256].

[103] G. Cullen, N. Greiner, G. Heinrich, G. Luisoni, P. Mastrolia, et al., *Automated One-Loop Calculations with GoSam*, *Eur.Phys.J.* **C72** (2012) 1889, [arXiv:1111.2034].

[104] F. Campanario, T. M. Figy, S. Platzer, and M. Sjodahl, *Electroweak Higgs Boson Plus Three Jet Production at Next-to-Leading-Order QCD*, *Phys.Rev.Lett.* **111** (2013), no. 21 211802, [arXiv:1308.2932].

[105] J. Alwall, R. Frederix, S. Frixione, V. Hirschi, F. Maltoni, et al., *The automated computation of tree-level and next-to-leading order differential cross sections, and their matching to parton shower simulations*, `arXiv:1405.0301`.

[106] S. Badger, B. Biedermann, P. Uwer, and V. Yundin, *Numerical evaluation of virtual corrections to multi-jet production in massless QCD*, *Comput.Phys.Commun.* **184** (2013) 1981–1998, [`arXiv:1209.0100`].

[107] F. Cascioli, P. Maierhofer, and S. Pozzorini, *Scattering Amplitudes with Open Loops*, *Phys.Rev.Lett.* **108** (2012) 111601, [`arXiv:1111.5206`].

[108] K. Arnold, M. Bahr, G. Bozzi, F. Campanario, C. Englert, et al., *VBFNLO: A Parton level Monte Carlo for processes with electroweak bosons*, *Comput.Phys.Commun.* **180** (2009) 1661–1670, [`arXiv:0811.4559`].

[109] N. D. Christensen, P. de Aquino, C. Degrande, C. Duhr, B. Fuks, et al., *A Comprehensive approach to new physics simulations*, *Eur.Phys.J.* **C71** (2011) 1541, [`arXiv:0906.2474`].

[110] C. Duhr and B. Fuks, *A superspace module for the FeynRules package*, *Comput.Phys.Commun.* **182** (2011) 2404–2426, [`arXiv:1102.4191`].

[111] C. Degrande, C. Duhr, B. Fuks, D. Grellscheid, O. Mattelaer, et al., *UFO - The Universal FeynRules Output*, *Comput.Phys.Commun.* **183** (2012) 1201–1214, [`arXiv:1108.2040`].

[112] A. Alloul, N. D. Christensen, C. Degrande, C. Duhr, and B. Fuks, *FeynRules 2.0 - A complete toolbox for tree-level phenomenology*, *Comput.Phys.Commun.* **185** (2014) 2250–2300, [`arXiv:1310.1921`].

[113] **ATLAS** Collaboration, G. Aad et al., *Search for direct third-generation squark pair production in final states with missing transverse momentum and two b-jets in $\sqrt{s} = 8$ TeV pp collisions with the ATLAS detector*, *JHEP* **1310** (2013) 189, [`arXiv:1308.2631`].

[114] M. Whalley, D. Bourilkov, and R. Group, *The Les Houches accord PDFs (LHAPDF) and LHAGLUE*, hep-ph/0508110.

[115] J. Pumplin, D. Stump, J. Huston, H. Lai, P. M. Nadolsky, et al., *New generation of parton distributions with uncertainties from global QCD analysis*, *JHEP* **0207** (2002) 012, [hep-ph/0201195].

[116] S. Platzer and S. Gieseke, *Coherent Parton Showers with Local Recoils*, *JHEP* **1101** (2011) 024, [arXiv:0909.5593].

[117] M. Stoll, *Parton Shower for Massive Fermions*, Diploma thesis, Karlsruhe Institute of Technology (KIT), 2012.

[118] A. Schofield and M. H. Seymour, *Jet vetoing and Herwig++*, *JHEP* **1201** (2012) 078, [arXiv:1103.4811].

[119] **ATLAS** Collaboration, https://atlas.web.cern.ch/Atlas/GROUPS/PHYSICS/PAPERS/SUSY-2013-05.

[120] D. R. Tovey, *On measuring the masses of pair-produced semi-invisibly decaying particles at hadron colliders*, *JHEP* **0804** (2008) 034, [arXiv:0802.2879].

[121] G. Polesello and D. R. Tovey, *Supersymmetric particle mass measurement with the boost-corrected contransverse mass*, *JHEP* **1003** (2010) 030, [arXiv:0910.0174].

[122] *MctLib*, https://mctlib.hepforge.org.

[123] **ATLAS** Collaboration, *Calibrating the b-Tag Efficiency and Mistag Rate in* $35pb^{-1}$ *of Data with the ATLAS Detector*, ATLAS-CONF-2011-089, ATLAS-COM-CONF-2011-082.

[124] J. Alwall, M. Herquet, F. Maltoni, O. Mattelaer, and T. Stelzer, *MadGraph 5 : Going Beyond*, *JHEP* **1106** (2011) 128, [arXiv:1106.0522].

[125] M. L. Mangano, *Presentation at the FNAL Matrix Element/Monte Carlo Tuning Working Group 2002*, `http://www-cpd.fnal.gov/personal/mrenna/tuning/nov2002/mlm.pdf`.

[126] J. Alwall, S. de Visscher, and F. Maltoni, *QCD radiation in the production of heavy colored particles at the LHC*, *JHEP* **0902** (2009) 017, [`arXiv:0810.5350`].

[127] S. Frixione, E. Laenen, P. Motylinski, B. R. Webber, and C. D. White, *Single-top hadroproduction in association with a W boson*, *JHEP* **0807** (2008) 029, [`arXiv:0805.3067`].

[128] W. Hollik, J. M. Lindert, and D. Pagani, *NLO corrections to squark-squark production and decay at the LHC*, *JHEP* **1303** (2013) 139, [`arXiv:1207.1071`].

[129] T. Han, *Collider phenomenology: Basic knowledge and techniques*, `hep-ph/0508097`.

[130] E. Re, *Single-top Wt-channel production matched with parton showers using the POWHEG method*, *Eur.Phys.J.* **C71** (2011) 1547, [`arXiv:1009.2450`].

[131] J. Andrea, B. Fuks, and F. Maltoni, *Monotops at the LHC*, *Phys.Rev.* **D84** (2011) 074025, [`arXiv:1106.6199`].

[132] J. F. Kamenik and J. Zupan, *Discovering Dark Matter Through Flavor Violation at the LHC*, *Phys.Rev.* **D84** (2011) 111502, [`arXiv:1107.0623`].

[133] B. Fuks, *Beyond the Minimal Supersymmetric Standard Model: from theory to phenomenology*, *Int.J.Mod.Phys.* **A27** (2012) 1230007, [`arXiv:1202.4769`].

[134] A. Kumar, J. N. Ng, A. Spray, and P. T. Winslow, *Tracking down the top quark forward-backward asymmetry with monotops*, *Phys.Rev.* **D88** (2013), no. 7 075012, [`arXiv:1308.3712`].

[135] E. Alvarez, E. C. Leskow, J. Drobnak, and J. F. Kamenik, *Leptonic Monotops at LHC*, *Phys.Rev.* **D89** (2014) 014016, [`arXiv:1310.7600`].

[136] J.-L. Agram, J. Andrea, M. Buttignol, E. Conte, and B. Fuks, *Monotop phenomenology at the Large Hadron Collider*, *Phys.Rev.* **D89** (2014) 014028, [arXiv:1311.6478].

[137] I. Boucheneb, G. Cacciapaglia, A. Deandrea, and B. Fuks, *Revisiting monotop production at the LHC*, arXiv:1407.7529.

[138] B. Fuks, J. Proudom, J. Rojo, and I. Schienbein, *Characterizing New Physics with Polarized Beams at High-Energy Hadron Colliders*, *JHEP* **1405** (2014) 045, [arXiv:1403.2383].

[139] J. N. Ng and A. de la Puente, *Probing Radiative Neutrino Mass Generation through Monotop Production*, *Phys.Rev.* **D90** (2014), no. 9 095018, [arXiv:1404.1415].

[140] **CDF** Collaboration, T. Aaltonen et al., *Search for a dark matter candidate produced in association with a single top quark in $p\bar{p}$ collisions at $\sqrt{s} = 1.96$ TeV*, *Phys.Rev.Lett.* **108** (2012) 201802, [arXiv:1202.5653].

[141] **CMS** Collaboration, *Search for new physics with monotop final states in pp collisions at sqrt(s) = 8 TeV*, CMS-PAS-B2G-12-022.

[142] **CMS** Collaboration, V. Khachatryan et al., *Search for Monotop Signatures in Proton-Proton Collisions at $\sqrt{s} = 8$ TeV*, *Phys.Rev.Lett.* **114** (2015), no. 10 101801, [arXiv:1410.1149].

[143] **ATLAS** Collaboration, G. Aad et al., *Search for invisible particles produced in association with single-top-quarks in proton-proton collisions at $\sqrt{s} = 8$ TeV with the ATLAS detector*, *Eur.Phys.J.* **C75** (2015), no. 2 79, [arXiv:1410.5404].

[144] G. Bozzi, B. Fuks, B. Herrmann, and M. Klasen, *Squark and gaugino hadroproduction and decays in non-minimal flavour violating supersymmetry*, *Nucl.Phys.* **B787** (2007) 1–54, [arXiv:0704.1826].

[145] B. Fuks, B. Herrmann, and M. Klasen, *Flavour Violation in Gauge-Mediated Supersymmetry Breaking Models: Experimental Constraints and*

Phenomenology at the LHC, *Nucl.Phys.* **B810** (2009) 266–299, [arXiv:0808.1104].

[146] B. Fuks, B. Herrmann, and M. Klasen, *Phenomenology of anomaly-mediated supersymmetry breaking scenarios with non-minimal flavour violation*, *Phys.Rev.* **D86** (2012) 015002, [arXiv:1112.4838].

[147] C. Degrande, B. Fuks, V. Hirschi, J. Proudom, and H.-S. Shao, *Automated next-to-leading order predictions for new physics at the LHC: the case of colored scalar pair production*, *Phys.Rev.* **D91** (2015), no. 9 094005, [arXiv:1412.5589].

[148] S. Frixione, P. Nason, and G. Ridolfi, *A Positive-weight next-to-leading-order Monte Carlo for heavy flavour hadroproduction*, *JHEP* **0709** (2007) 126, [arXiv:0707.3088].

[149] S. Alioli, P. Nason, C. Oleari, and E. Re, *NLO single-top production matched with shower in POWHEG: s- and t-channel contributions*, *JHEP* **0909** (2009) 111, [arXiv:0907.4076].

[150] T. Gleisberg, S. Hoeche, F. Krauss, A. Schalicke, S. Schumann, et al., *SHERPA 1. alpha: A Proof of concept version*, *JHEP* **0402** (2004) 056, [hep-ph/0311263].

[151] T. Gleisberg, S. Hoeche, F. Krauss, M. Schonherr, S. Schumann, et al., *Event generation with SHERPA 1.1*, *JHEP* **0902** (2009) 007, [arXiv:0811.4622].

[152] K. Hamilton and P. Nason, *Improving NLO-parton shower matched simulations with higher order matrix elements*, *JHEP* **1006** (2010) 039, [arXiv:1004.1764].

[153] S. Hoche, F. Krauss, M. Schonherr, and F. Siegert, *NLO matrix elements and truncated showers*, *JHEP* **1108** (2011) 123, [arXiv:1009.1127].

[154] K. Hamilton, *A positive-weight next-to-leading order simulation of weak boson pair production*, *JHEP* **1101** (2011) 009, [arXiv:1009.5391].

[155] **ATLAS** Collaboration, G. Aad et al., *Measurement of the t-channel single top-quark production cross section in pp collisions at $\sqrt{s} = 7$ TeV with the ATLAS detector*, *Phys.Lett.* **B717** (2012) 330–350, [arXiv:1205.3130].

[156] **ATLAS** Collaboration, G. Aad et al., *Measurement of WZ production in proton-proton collisions at $\sqrt{s} = 7$ TeV with the ATLAS detector*, *Eur.Phys.J.* **C72** (2012) 2173, [arXiv:1208.1390].

[157] **CMS** Collaboration, S. Chatrchyan et al., *Measurement of the sum of WW and WZ production with W+dijet events in pp collisions at $\sqrt{s} = 7$ TeV*, *Eur.Phys.J.* **C73** (2013) 2283, [arXiv:1210.7544].

[158] B. Radics, *Observation of top quark pair production and estimation of W+jets background with ATLAS at the LHC*, CERN-THESIS-2010-237, BONN-IR-2010-14.

[159] **CMS** Collaboration, S. Chatrchyan et al., *Search for new physics in the multijet and missing transverse momentum final state in proton-proton collisions at $\sqrt{s}$= 8 TeV*, *JHEP* **1406** (2014) 055, [arXiv:1402.4770].

[160] **ATLAS** Collaboration, G. Aad et al., *ATLAS Run 1 searches for direct pair production of third-generation squarks at the Large Hadron Collider*, arXiv:1506.0861.

[161] **CMS** Collaboration, *Search for top squarks decaying to a charm quark and a neutralino in events with a jet and missing transverse momentum*, .

[162] **CMS** Collaboration, *Search for top-squark pair production in the single lepton final state in pp collisions at 8 TeV*, CMS-PAS-SUS-13-011.

[163] **CMS** Collaboration, *Projected Performance of an Upgraded CMS Detector at the LHC and HL-LHC: Contribution to the Snowmass Process*, arXiv:1307.7135.